# DEVELOPMENT OF DURABLE ANTIBACTERIAL STAINLESS STEEL SURFACES THROUGH PLASMA NITRIDING AND ULTRASHORT PULSED LASER TEXTURING

by

BEHNAM DASHTBOZORG




A thesis submitted to the University of Birmingham

for the degree of

DOCTOR OF PHILOSOPHY

School of Metallurgy and Materials

College of Engineering and Physical Sciences

University of Birmingham

December 2020

UNIVERSITY OF
BIRMINGHAM

## University of Birmingham Research Archive

### e-theses repository

This unpublished thesis/dissertation is copyright of the author and/or third parties. The intellectual property rights of the author or third parties in respect of this work are as defined by The Copyright Designs and Patents Act 1988 or as modified by any successor legislation.

Any use made of information contained in this thesis/dissertation must be in accordance with that legislation and must be properly acknowledged. Further distribution or reproduction in any format is prohibited without the permission of the copyright holder.

# ABSTRACT

Owing to their excellent corrosion resistance, austenitic stainless steels (ASS) have become an important material within the food and medical industries. In particular, the AISI 316L alloys (which are used in this study) are abundantly found in applications where harsh chemical environments are unavoidable. However, due to their poor wear resistance and susceptibility to bacterial colonisation, there are concerns for their further uptake in the future. Low-temperature plasma nitriding can address the poor durability of the ASS alloys by forming the S phase on the surface of the materials, and therefore, providing combined improvement in hardness, wear resistance and corrosion resistance. However, this does not alleviate the worries for biofouling of the surface. Pulsed laser texturing presents a promising and scalable approach for the introduction of functional antibacterial properties on surfaces. However, due to the thermal nature of laser patterning and the thermodynamic metastability of the S phase, almost no research has been conducted prior to this study on the combination of these technologies.

Therefore, in this thesis, detailed characterisation of the response of S phase treated surfaces to ultrashort (nano and femtosecond) laser texturing has been carried out. The results within this study have shown that it is possible to texture S phase treated surfaces using femtosecond (fs) pulsed laser texturing with no discernible decomposition or detrimental consequences to the layer structure, hardness or corrosion resistance of the S phase.

Given these new findings, and the need to produce durable antibacterial ASS alloys, the focus of this study was then directed towards the identification of bio-inspired surface textures with strong antibacterial efficacy. Four biomimetic fs laser produced structures inspired by features found on lotus leaves, shark skin and springtails were compared to identify an optimal texture. Measurement of the antimicrobial efficacy against *S. aureus* demonstrated that the springtail inspired triangular LIPSS (laser-induced periodic surface structures) possessed the strongest resistance (over 90 % reduction of viable bacteria).

Finally, to fully examine the antibacterial durability of the surfaces, comparisons of wear resistance, texture integrity and long-term antibacterial efficacy against *S. aureus* and *E. coli* were carried out on triangular LIPSS textures formed on untreated and S phase treated AISI 316L alloys. Significant improvements of all properties were found with S phase hardened and triangular LIPSS textured surfaces. Using a novel, yet simple, approach to produce uniformly worn textures, which has been a challenge for researchers thus far, it has been possible, within this study, to examine the antibacterial performance of the textured surfaces as a function of surface damage. Almost instantaneous removal of the fine features of the triangular LIPSS, and associated antibacterial efficacy, was observed on untreated samples. On the other hand, retention of texture features and long-lasting antibacterial performance, with at least two fold increase in antibacterial durability when compared to untreated equivalent surfaces, was found on triangular LIPSS textures produced on S phase treated surfaces.

Thus, the findings of this thesis are hoped to pave the way towards the generation of long-lasting antibacterial, and possibly multi-functional, stainless steel surfaces for use in the food and medical industries.

# ACKNOWLEDGEMENTS

First and foremost, I would like to express my deepest gratitude to my supervisors, Prof Hanshan Dong, Dr Xiaoying Li and Dr Rachel Sammons for their support and help throughout this study. Without our regular meaningful discussions, combined with your advice and guidance, this project would not have been possible. I would also like to thank all three of them for their help during the application stages for joining this PhD degree.

I would also like to thank everyone involved in the Innovative Metal Processing (IMPaCT) Centre for Doctoral Training, both staff and students. I would also like to send my appreciations to the Engineering and Physical Sciences Research Council (EPSRC; EP/F006926/1) for their financial support throughout this study.

I would like to thank all the members, past and present, of the surface engineering group, including Yana Liang, Dr Shaojun Qi, Dr Mario Coseglio, Dr Tatiana Mukinay, Zhiyuan Jing, Yingdi Feng and Chang Che. I would like to also send my thanks to all the staff within the School of Metallurgy and Materials & School of Dentistry, especially Jaswinder Singh, Paul Stanley and Gay Smith. Special thanks also go to Dr Valter Jantara Junior and James Alexander for their meaningful discussion, help with lab experiments and overall support throughout this study.

I would also like express my thanks to the laser texturing group in the school of mechanical engineering, including Prof Stefan Dimov, Dr Jean-Michel Romano, Dr Antonio Garcia-Giron and Dr Pavel Penchev for their help in creating all the patterns used within this study.

Finally, I want to also thank my friends and family for their kindness, support and help throughout the entirety of my time in university, both as an undergraduate and as a PhD student.

# PUBLICATIONS AND AWARDS

## Published Articles

Sawyer, V., Tao, X., Dong, H., **Dashtbozorg, B.,** Li, X., Sammons, R. and Dong, H.S., 2020. Improving the Tribological Properties and Biocompatibility of Zr-Based Bulk Metallic Glass for Potential Biomedical Applications. *Materials*, 13(8), pp.1960.

**Dashtbozorg, B.**, Li, X.Y., Romano, J.M., Garcia-Giron, A., Sammons, R.L., Dimov, S.S. and Dong, H. 2020. A study on the effect of ultrashort pulsed laser texturing on the microstructure and properties of metastable S phase layer formed on AISI 316L surfaces. *Applied Surface Science,* 511, 145557.

Romano J.M., Fantova Sarasa J., Concheso C., Gulcur M., **Dashtbozorg B.**, Garcia-Giron A., Penchev P., Dong H., Whiteside B.R. and Dimov S.S. 2020. Effects of mould wear on hydrophobic polymer surfaces replicated using plasma-treated and laser-textured stainless steel inserts. *Tribology-Materials, Surfaces & Interfaces*, 14(4), pp.240-252.

Garcia-Giron, A., Romano, J.M., Batal, A., **Dashtbozorg, B.,** Dong, H., Solanas, E.M., Angos, D.U., Walker, M., Penchev, P. and Dimov, S.S., 2019. Durability and wear resistance of laser-textured hardened stainless steel surfaces with hydrophobic properties. *Langmuir*, 35(15), pp.5353-5363.

Joshi, G.S., **Dashtbozorg, B.**, Romano, J.M., Garcia-Giron, A., Gaudiuso, C., Dong, H., Dimov, S.S. and Carbone, G. 2018. Experimental investigation of the tribological and wettability properties of laser-textured martensitic steel surfaces. *Proceedings of LPM2018 – the 19th International Symposium on Laser Precision Microfabrication*.

Garcia-Giron, A., Romano, J.M., Liang, Y., **Dashtbozorg, B.**, Dong, H., Penchev, P. and Dimov, S.S., 2018. Combined surface hardening and laser patterning approach for functionalising stainless steel surfaces. *Applied Surface Science*, 439, pp.516-524.

# Awards

**Best Oral Presentation** at the International Conference on Surface Engineering Applications on “the response of nitrogen S phase to ultrashort pulsed laser texturing for the production of durable antibacterial surfaces”, September 2019.

**Best Oral Presentation** at the 7th Materials Forum at the School of Metallurgy and Materials on “plasma nitriding and femtosecond LIPSS texturing for durable antibacterial stainless steel surfaces”, January 2019.

**Best Poster Presentation** at the 6th Materials Forum at the School of Metallurgy and Materials, February 2018.

**2nd Best Poster Presentation** at the National Student Conference in Metallic Materials, July 2017.

**Best Poster Presentation** at the School of Metallurgy and Materials Postgraduate Junior Poster Competition, June 2017.

# CONTENTS

**LIST OF FIGURES ..... I**

**LIST OF TABLES ..... XI**

**ABBREVIATIONS ..... XIII**

**CHAPTER 1 INTRODUCTION ..... 1**

**CHAPTER 2 LITERATURE REVIEW ..... 4**

**2.1. Stainless Steel ..... 4**

*2.1.1. Classification ..... 5*

*2.1.2. Types of Stainless Steel ..... 7*

*2.1.3. Ferritic Stainless Steel ..... 7*

*2.1.4. Austenitic Stainless Steel ..... 9*

*2.1.5. Duplex Stainless Steel ..... 11*

*2.1.6. Martensitic Stainless Steel ..... 12*

*2.1.7. Precipitation-Hardening Stainless Steel ..... 14*

**2.2. AISI 316L Austenitic Stainless Steel ..... 16**

*2.2.1. Composition ..... 17*

*2.2.2. Corrosion Properties ..... 20*

*2.2.3. Mechanical Properties ..... 30*

*2.2.4. Tribological Properties ..... 32*

*2.2.5. Applications & Drawbacks ..... 42*

**2.3. Surface Engineering ..... 43**

*2.3.1. Classification ..... 44*

*2.3.2. Nitriding of Austenitic Stainless Steel ..... 45*

*2.3.3. Plasma Nitriding ..... 47*

**2.4. S Phase ..... 62**

*2.4.1. Formation* ..... *64*
*2.4.2. Metallurgical Characteristics* ..... *66*
*2.4.3. Thermodynamic Metastability* ..... *70*
*2.4.4. Properties* ..... *71*
*2.4.5. Limitations* ..... *74*
**2.5. Antibacterial Surfaces ..... 75**
*2.5.1. Demand for Antibacterial Surfaces* ..... *76*
*2.5.2. Current Control Measures & their Limitations* ..... *77*
*2.5.3. Future Preventative Measures* ..... *79*
*2.5.4. Anti-Biofouling Surfaces* ..... *79*
**2.6. Surface Texturing ..... 81**
*2.6.1. Ultrashort Pulsed Laser Texturing* ..... *82*
*2.6.2. Femtosecond Pulsed Laser Texturing* ..... *86*
**2.7. Summary ..... 88**

**CHAPTER 3 MATERIALS & METHODS ..... 89**

**3.1. Materials and Sample Preparation ..... 89**
*3.1.1. Cross-Section Preparation* ..... *89*
*3.1.2. Plasma Surface Treatment* ..... *90*
*3.1.3. Laser Texturing* ..... *91*
*3.1.4. Sample Coding* ..... *94*
**3.2. Characterisation ..... 95**
*3.2.1. Material Characterisation* ..... *95*
*3.2.2. Texture Characterisation* ..... *97*
**3.3. 1-D Surface Temperature Modelling ..... 97**
**3.4. Electrochemical Corrosion Testing ..... 99**
*3.4.1. Potentiodynamic Anodic Polarisation* ..... *99*
*3.4.2. Electrochemical Impedance Spectroscopy* ..... *100*
**3.5. Wettability Testing ..... 101**
**3.6. Tribological Testing ..... 101**
*3.6.1. Reciprocating Sliding Wearing* ..... *101*

*3.6.2. Pattern Durability Testing ..... 102*
**3.7. Antimicrobial Testing ..... 104**
**3.8. Statistical Analysis ..... 105**

**CHAPTER 4 EXPERIMENTAL RESULTS ..... 107**

**4.1. ASPN Surface Layer ..... 107**
**4.2. Nano- and Femtosecond Pulsed Channel Textures ..... 109**
*4.2.1. Morphology of Textured Surfaces ..... 110*
*4.2.2. Cross-Sectional Layer Structure ..... 112*
*4.2.3. Predicted Surface Temperatures ..... 116*
*4.2.4. Corrosion Behaviour ..... 119*
**4.3. Antibacterial S Phase Texturing ..... 126**
*4.3.1. Texture Morphology ..... 126*
*4.3.2. Cross-Sectional Layer Structure ..... 129*
*4.3.3. Antimicrobial Efficacy ..... 132*
**4.4. Triangular LIPSS Textures ..... 133**
*4.4.1. Texture Morphology ..... 134*
*4.4.2. Cross-Sectional Layer Structure ..... 137*
*4.4.3. Corrosion Behaviour ..... 141*
*4.4.4. Surface Wettability ..... 144*
*4.4.5. Antimicrobial Efficacy ..... 146*
**4.5. Texture Durability ..... 148**
*4.5.1. Dry Sliding Reciprocating Wear ..... 148*
*4.5.2. Ringer's Lubricated Reciprocating Wear ..... 151*
*4.5.3. Antibacterial Durability ..... 154*

**CHAPTER 5 DISCUSSION ..... 160**

**5.1. S Phase & Its Thermostability ..... 160**
*5.1.1. Characterisation & Properties of S Phase ..... 160*
*5.1.2. Thermostability & Laser Texturing of S Phase ..... 161*

**5.2. Response of S Phase to Ultrashort Pulsed Laser Texturing 162**
*5.2.1. Effect of Nanosecond Laser Texturing.....162*
*5.2.2. Effect of Femtosecond Laser Texturing .....168*
**5.3. Antibacterial Texturing ..... 170**
*5.3.1. Optimising Femtosecond Textures.....170*
*5.3.2. Properties of Triangular LIPSS Textures .....173*
**5.4. Assessing Antibacterial Durability of Triangular LIPSS ..... 178**
*5.4.1. Difficulties Associated with Assessing Texture Durability.....178*
*5.4.2. Antimicrobial Durability of Textured Surfaces.....180*
**5.5. Future Perspective ..... 182**
*5.5.1. Proposed Future Work on Antibacterial Textures.....182*
*5.5.2. Future Use of Texture Channel Spacing.....184*

**CHAPTER 6 CONCLUSIONS ..... 187**

**REFERENCES ..... 190**

# LIST OF FIGURES


| | | |
|---|---|---|
| Fig. 2-1 | *Passive oxide film on AISI 316 stainless steel revealed using atom probe tomography (a) and chemical composition depth profiling (b) [29, 30].* | 4 |
| Fig. 2-2 | *Schaeffler diagram showing expected microstructure at room temperature with changing chromium and nickel equivalent alloying elements (in wt%) [27, 32].* | 6 |
| Fig. 2-3 | *Iron-chromium phase diagram. The labelled phases are as follows: liquid (L), ferrite (α), austenite (γ) and iron-chromium intermetallic compounds (σ) [30].* | 8 |
| Fig. 2-4 | *Chromium-depleted zones adjacent to nitride or carbide precipitates (Redrawn from [28]).* | 9 |
| Fig. 2-5 | *Visualisation of the austenite to martensite transformation, where (a) is a single slip dislocation, (b) is many slip dislocations, (c) is a 1 direction expansion (uniaxial dilatation), (d) a simple shear and (e) is the invariant plane strain (IPS) caused by the combined 1-directional expansion and shearing [30].* | 14 |
| Fig. 2-6 | *Stainless steel family composition and property linkages [42].* | 17 |
| Fig. 2-7 | *Summary of autocatalytic events during pitting corrosion [33].* | 24 |
| Fig. 2-8 | *Hydrogen evolution reactions in the event of corrosion of iron in hydrochloric acid [33].* | 25 |
| Fig. 2-9 | *Schematic diagram of crevice corrosion [33].* | 27 |
| Fig. 2-10 | *Galvanic series in sea water. For active-passive alloys, black boxes indicate the active state, while white boxes indicate passive state [27].* | 29 |
| Fig. 2-11 | *Galvanic series, containing AISI 316L (passive), in sea water at 10 and 40 ˚C [63].* | 30 |
| Fig. 2-12 | *Different types of contact: (a) Point, (b) Plane and (c) Plate [74].* | 34 |

| | | |
|---|---|---|
| Fig. 2-13 | *Ball-on-plate point contact with labelling for Hertz contact theory calculations [74].* | 35 |
| Fig. 2-14 | *Contact types during abrasive wear: (a) open two-body, (b) closed two-body, (c) open three-body and (d) closed three-body [76].* | 40 |
| Fig. 2-15 | *Adhesive wear mechanism [81].* | 41 |
| Fig. 2-16 | *Fe-N phase diagram, where α is alpha ferrite, γ is austenite, γ' is $Fe_4N$ and ε is $Fe_{2-3}N$ [91].* | 46 |
| Fig. 2-17 | *Types of DC glow-discharge: (A) DC electrical discharge tube, (B) parallel plate plasma reactor, (C) co-planar magnetron reactors and (D) co-axial electron bombardment discharge chamber [98].* | 50 |
| Fig. 2-18 | *Influence of pressure on the formation and stabilisation of plasma. (a) At atmospheric pressure there is almost no mean free path for molecules. (b) At very low pressures (e.g. 0.0001 mbar (0.01 Pa)) there is a very long mean free path but limited gas molecules to collide with to create sustained usable plasma energy. (c) At low pressures (e.g. 0.1 mbar) the gas molecules have a sizable mean free path and plenty of molecules to collide with, and therefore form a usable plasma energy [82].* | 50 |
| Fig. 2-19 | *Townsend avalanche event with cascading events of electron-induced ionisation events [106].* | 51 |
| Fig. 2-20 | *Paschen curve of the voltage to current density relationship for low pressure DC plasma discharge. [98].* | 54 |
| Fig. 2-21 | *Electron and ion distributions across the electrodes in the dark discharge plasma regimes [106].* | 54 |
| Fig. 2-22 | *Glow-discharge formation in a typical DC plasma nitriding treatment.* | 55 |
| Fig. 2-23 | *Koelbel's model for the DC glow-discharge plasma nitriding of ferrous alloys [92].* | 57 |
| Fig. 2-24 | *Schematic drawing of the regions of normal glow-discharge plasma [98].* | 58 |

| | | |
|---|---|---|
| Fig. 2-25 | *Typical surface morphology after (A) DC glow-discharge nitriding and (B) active screen plasma nitriding. The edge effects are prevalent in DC plasma nitriding, while uniform treatment is seen in active screen plasma nitriding. Material in image is M2 tool steel.* | 60 |
| Fig. 2-26 | *Active screen plasma nitriding of steels. Samples inside the mesh cage (cathodic potential) were at a floating potential. Core temperatures were measured during treatment using a thermocouple inserted into a dummy sample.* | 61 |
| Fig. 2-27 | *Hollow cathode formation on active screen.* | 61 |
| Fig. 2-28 | *Optical micrograph of 450 °C plasma nitrided AISI 316 ASS for 5 hours [123].* | 63 |
| Fig. 2-29 | *XRD patterns following active screen plasma nitriding of AISI 316 ASS for 20 hours at 420 °C [115].* | 63 |
| Fig. 2-30 | *Elemental depth profile of nitrogen following plasma nitriding treatment of AISI 316 at 400 °C for 15 hours and 440 °C for 20 hours. Line labelled maximum N denotes the approximate maximum possible nitrogen solid solubility in austenite [125].* | 65 |
| Fig. 2-31 | *Gibbs free energy (per mole of chromium atoms) of chromium nitrides and carbides at different temperatures. Note the significantly lower energy and therefore thermodynamically more stable state of the CrN precipitates at all plotted temperatures [91, 146].* | 68 |
| Fig. 2-32 | *EXAFS study on untreated (unnitrided), S phase treated (nitrided) and denitrided S phase (using $H_2$ gas). Following nitriding, the distance to the nearest metal-metal atom (vertical dotted line) shifts for Fe, Ni and Cr in comparison to the untreated samples. Following denitriding, only shifting of the metal-metal spacing for Cr is seen. Following nitriding, all elements show somewhat similar nearest neighbour interstitial occupancy, whereas following denitriding, only Cr shows strong nearest neighbour occupancy [91, 140].* | 69 |
| Fig. 2-33 | *Isothermal stability plot (line shows 50 % decomposition) of S phase formed on AISI 304L and 316L using isochronal annealing data [91, 149].* | 71 |
| Fig. 2-34 | *Hardness profiles of AISI 316L samples plasma nitrided at 400 °C for 20 hours in 25% $N_2$ (HN) and 20% $N_2$ (LN) [155].* | 72 |

| | | |
|---|---|---|
| Fig. 2-35 | *Anodic polarisation curve on untreated, 360 °C nitrided and 380 °C nitrided AISI 316L surfaces in 5 % NaCl media [161].* | 74 |
| Fig. 2-36 | *Electron micrographs demonstrating antimicrobial effect of nanopillars found on cicada wings. Image A (scale bar = 1 µm) shows Pseudomonas aeruginosa cells on the surface of cicada wings, with clear signs of nanopillar penetration. Image B (scale bar = 200 nm) is an angled higher magnification image showing the penetration more clearly [169].* | 76 |
| Fig. 2-37 | *Periodicity and aspect ratio effect on the available surface area for bacterial (E. coli) attachment on untreated (Ti NT), Hydrothermally treated A (TiA) and hydrothermally treated B (TiB) commercially pure titanium [201].* | 81 |
| Fig. 2-38 | *Scanning electron microscope image showing both (a) low spatial frequency LIPSS and (b) high spatial frequency LIPSS formed on the surface of titanium samples [205].* | 83 |
| Fig 2-39 | *Schematic diagram of the phenomena observed in long pulsed thermal laser machining and athermal femtosecond laser ablation. Original diagram from Clark-MXR Inc (original source material not available) [213].* | 85 |
| Fig. 2-40 | *Fabrication of a cantilever through nanosecond (a-d) and femtosecond (e-h) laser processing. The scan patterns (a and e), magnified top views (b and f), magnified cut edges (c and g) and electron backscatter diffraction analysis of the cross sections (d and h) at positions D-D and H-H, respectively, are shown. The inset at the top right corresponds to the colour coding of the grain orientation with respect to an external reference. Note the lack of coarsening and variation in the grain structure following femtosecond laser processing (h) in comparison with nanosecond laser processing (d) [212].* | 85 |
| Fig. 2-41 | *Electron microscope image (main image) showing triangular LIPSS formed on steel using femtosecond pulsed laser texturing (310 fs, 500 kHz). Top right image is a fast Fourier transform taken of the same image, showing the multi-directional ordering in the texture [206].* | 87 |
| Fig. 3-1 | *Schematic diagram of active screen plasma treatment setup.* | 90 |
| Fig. 3-2 | *Schematic diagram of the rastering strategy used during the laser texturing. With labels for grid/hatch spacing (h) and Gaussian spot beam diameter ($2*\omega_0$) [206].* | 92 |

| | | |
|---|---|---|
| Fig. 3-3 | *Illustration of the large area wear testing. Image on the left shows the setup for the test. Image on the right shows the sliding trajectory and distance travelled per rotation.* | 103 |
| Fig. 3-4 | *Overview of antimicrobial testing procedure.* | 106 |
| Fig. 4-1 | *Characterisation of the ASPN sample type. (A) shows elemental depth profiling and (B) shows the cross sectional morphology of the S phase. Although only three elements are displayed in the elemental depth profiling, all elements present in the alloy were measured.* | 108 |
| Fig. 4-2 | *XRD phase comparison of Unt and ASPN samples.* | 109 |
| Fig. 4-3 | *Surface morphology of the ASPN treated and channel textured samples. (A1-3) 310 fs samples, (B1-3) 15 ns samples and (C1-3) 220 ns samples. Hatch spacing (a) was also measured to be 300.6 ± 1.1 µm. Arrows indicate areas where cracks are present and where channels have closed in on themselves.* | 111 |
| Fig. 4-4 | *Surface morphology of 310 fs textured samples. The fine sub-micron ripple textures along each channel can be seen in image A, with some inconsistencies in the texturing process (a). Image B shows the back-sputtered particulates (b) found adjacent to the channels.* | 112 |
| Fig. 4-5 | *Secondary (A1-A2, B1-B2 and C1-C2) and backscattered (A3, B3 and C3) electron images of cross-sectional layer structures of the channel textured samples. (A1-A3) 310 fs samples, (B1-B3) 15 ns samples and (C1-C3) 220 ns samples. Areas of material cracking are indicated with an arrow. Labels (a, b and c) indicate locations of elemental spot analysis listed in Table 4 1.* | 114 |
| Fig. 4-6 | *Backscattered electron imaging (top row) and EDS elemental mapping through the cross-sectional areas of each sample type: (A) ASPN samples, (B) 310 fs textured samples, (C) 15 ns textured samples and (D) 220 ns textured samples. Samples are organised in columns, with each row representing a different element (as labelled). Colour intensity mapping used is relative to each individual element map. Arrows correspond to sites of precipitation that match elemental composition changes in the related maps.* | 115 |

| | | |
|---|---|---|
| Fig. 4-7 | *Cross-sectional TEM sample preparation and characterisation of the 310 fs textured sample: (A) SEM image of FIB cutting and milling of the sample for thin TEM specimen preparation; (B) TEM image of the S phase layer, showing the surface texture contour line; (C) enlarged 310 fs textured top surface, and (D) selected area diffraction pattern from S phase area shown in (C).* | 116 |
| Fig. 4-8 | *Single pulse surface temperature modelling following 15 ns and 220 ns laser pulses.* | 118 |
| Fig. 4-9 | *Multiple pulse surface temperature modelling following 15 ns and 220 ns laser pulses. Dash and dot lines indicate the peak temperatures, while the dotted lines show the saturation temperatures.* | 118 |
| Fig. 4-10 | *Polarisation curves of the different channel textured sample types in Ringer's solution.* | 120 |
| Fig. 4-11 | *Secondary and backscattered electron imaging following anodic polarisation testing of (A) 310 fs, (B) 15 ns and (C) 220 ns textured samples. Arrows indicate areas of material damage or profound corrosion attack.* | 121 |
| Fig. 4-12 | *Bode phase (top) and magnitude (bottom) plots of the channel textured sample types. Fitted lines were made according to the equivalent circuit models in Fig. 4-14.* | 124 |
| Fig. 4-13 | *Nyquist plot of impedance of the channel textured sample types. Fitted lines were made according to the equivalent circuit models in Fig. 4-14. Inset magnifies the $Z_{real}$ region between 0-30 x$10^3$ Ω to show the 220 ns plot more clearly.* | 124 |
| Fig. 4-14 | *Equivalent circuit models used for EIS analysis where $R_s$ is solution resistance, $R_f$ (resistance to polarisation) & $Q_f$ (double layer capacitance) relate to the outer electrolyte-sample interface layer, $R_p$ & $Q_p$ relate to the S phase-untreated bulk interface, and W relates to the Warburg impedance associated with diffusion resistance. Model A was used for ASPN and 310 fs textured samples. Model B was used for 15 ns and 220 ns textured samples.* | 125 |
| Fig. 4-15 | *Raman spectroscopy of all the channel textured sample types. Peaks relating to surface carbon deposition and surface oxidation ($Cr_2O_3$ and $CrO_2$) are labelled accordingly.* | 125 |

| | | |
|---|---|---|
| Fig. 4-16 | *Surface morphology of the (A) ASPNL1 and (B) ASPNL2 textures. Labels (also used in Table 4 4) correspond to the 90 ° peak spacing (a), 45 ° peak spacing (b), tip diameter (c) and channel spacing (S1). Arrow indicates location of severe back-sputtering.* | 128 |
| Fig. 4-17 | *Surface morphology of the (A) ASPNS and (B) ASPNΔ textures. Labels (also used in Table 4 4) correspond to the 90 ° spacing (a), 45 ° inner spacing (b), channel width (c) and channel spacing (S1). Labelling and in-depth detail of the ASPNΔ sample can be found in section 4.4.* | 128 |
| Fig. 4-18 | *Cross-sectional electron microscopy imaging of the (A) ASPNL1, (B) ASPNL2, (C) ASPNS and (D) ASPNΔ sample types.* | 130 |
| Fig. 4-19 | *Backscattered electron imaging (top row) and EDS elemental mapping through the cross sectional areas of the (A) ASPN, (B) ASPNL1, (C) ASPNL2, (D) ASPNS and (E) ASPNΔ sample types. Samples are organised in columns, with each row representing a different element (as labelled). Colour intensity mapping is relative to each individual element map. It should be noted that a different magnification was used in E.* | 131 |
| Fig. 4-20 | *Antimicrobial efficacy of the different textured sample types against S. aureus. Dotted line corresponds to the efficacy for the ASPN sample type. Other than the labelled comparisons, all other comparison were found to be significantly different to each other ($p<0.05$).* | 133 |
| Fig. 4-21 | *Camera pictures of the surface colours and uniformity of Unt (A), UntΔ (B), ASPN (C) and ASPNΔ (D) samples.* | 135 |
| Fig. 4-22 | *Surface morphology of the different sample types: Unt (A), UntΔ (B1-2), ASPN (C) and ASPNΔ (D1-2). Lines labelled S1 and S2 depict the two types of channel spacing present within the textured surface.* | 136 |
| Fig. 4-23 | *Pattern periodicity (labelled as a, b and c) of UntΔ (A) and ASPNΔ (B) sample types revealed by surface micrographs (labelled 1) and image FFTs (labelled 2). Hexagonal structuring is demonstrated by both sample types, and consequently, 3 orders of symmetry are found with angles α1 and α2 (where α1 = α2 = 60 °).* | 137 |

| | | |
|---|---|---|
| Fig. 4-24 | *Cross-sectional secondary electron micrographs of the different sample types: Unt (A), UntΔ (B), ASPN (C) and ASPNΔ (D). Arrows indicate the surface of the texture, while the * represents the nickel protective plating layer on the UntΔ sample type. Scale bar is the same for all images.* | 140 |
| Fig. 4-25 | *XRD phase analysis of Unt, ASPN and ASPNΔ samples.* | 140 |
| Fig. 4-26 | *Hardness depth profiling of Unt, ASPN and ASPNΔ samples.* | 141 |
| Fig. 4-27 | *Bode phase (top) and magnitude (bottom) plots of the Unt, UntΔ, ASPN and ASPNΔ sample types. Fitted lines were made according to the equivalent circuit models in Fig. 4-29.* | 143 |
| Fig. 4-28 | *Nyquist plot of impedance of the Unt, UntΔ, ASPN and ASPNΔ sample types. Fitted lines were made according to the equivalent circuit models in Fig. 4-29.* | 143 |
| Fig. 4-29 | *Equivalent circuits models used for EIS analysis where $R_s$ is solution resistance, $R_f$ (resistance to polarisation) & $Q_f$ (double layer capacitance) relate to the outer electrolyte-S phase interface, and $R_p$ & $Q_p$ relate to the S phase-untreated bulk interface. Model A was used for Unt & UntΔ samples. Model B was used for ASPN & ASPNΔ samples.* | 144 |
| Fig. 4-30 | *Surface free energy calculations of the Unt, UntΔ, ASPN and ASPNΔ sample types.* | 145 |
| Fig. 4-31 | *Antimicrobial efficacy of the Unt, UntΔ, ASPN and ASPNΔ sample types against S. aureus. Other than the labelled comparisons, all other comparison were found to be significantly different to each other.* | 147 |
| Fig. 4-32 | *Antimicrobial efficacy of the Unt, UntΔ, ASPN and ASPNΔ sample types against E. coli. All samples were found to be significantly different to each other.* | 147 |
| Fig. 4-33 | *Camera pictures demonstrating the number of colony forming units of S. aureus (images on the left) and E. coli (images on the right) present following contact with each sample type: Unt (A), UntΔ (B), ASPN (C) and ASPNΔ (D).* | 148 |
| Fig. 4-34 | *Wear Factor of the Unt, UntΔ, ASPN and ASPNΔ surfaces following dry sliding reciprocating wear testing under 3 different loads: 50 gf, 300 gf and 500 gf.* | 150 |

| | | |
|---|---|---|
| Fig. 4-35 | *Electron micrographs of the resulting wear tracks following dry sliding wear of the UntΔ surface under a load of 50 gf (A) and ASPNΔ surface under a load of 500 gf (B).* | 151 |
| Fig. 4-36 | *Wear Factor of the Unt, UntΔ, ASPN and ASPNΔ surfaces following Ringer's lubricated sliding reciprocating wear testing under 3 different loads: 50 gf, 300 gf and 500 gf.* | 152 |
| Fig. 4-37 | *Electron micrographs of the resulting wear tracks following Ringer's lubricated wearing of the UntΔ (A) and ASPNΔ (B) surfaces under loads of 50 gf (1), 300 gf (2) and 500 gf (3). Insets at the top left of each image are lower magnification micrographs taken at the same spot.* | 153 |
| Fig. 4-38 | *Surface morphology of UntΔ surfaces at different stages of large area wearing: untouched surface (A1-2) and low cycle wearing (B1-2).* | 155 |
| Fig. 4-39 | *Surface morphology of ASPNΔ at different stages of large area wearing: untouched surface (A1-2), low cycle wearing (B1-2), medium cycle wearing (C1-2) and high cycle wearing (D1-2).* | 156 |
| Fig. 4-40 | *Antimicrobial efficacy against S. aureus before and after large area wearing of the triangular LIPSS textured surfaces. Other than the three labelled ones, the antimicrobial efficacy was found to be significantly different ($p<0.05$) for all comparisons. Efficacy of the untextured surfaces are represented by dashed (Unt) and dotted (ASPN) lines.* | 158 |
| Fig. 4-41 | *Antimicrobial efficacy against E. coli before and after large area wearing of the triangular LIPSS textured surfaces. Other than the three labelled ones, the antimicrobial efficacy was found to be significantly different ($p<0.05$) for all comparisons. Efficacy of the untextured surfaces are represented by dashed (Unt) and dotted (ASPN) lines.* | 159 |
| Fig. 5-1 | *Different set ups for wear testing. Image A represents ball-on-plate contact (e.g. Fig. 4-35) with a single point/small area of contact. Image B represents plane/surface-on-surface contact with localised points of contact due to irregularities in the texture (B1), uneven surface on the sample (B2) and uneven counterpart surface (B3). Image C represents diamond suspension large area wearing where conformation of the liquid allows for equal pressure and the homogeneous spread of the diamond particles for controlled damage of the texture under all conditions (irregularities in the texture (C1), uneven counterpart surface (C2) and uneven surface on the sample (C3)).* | 179 |

Fig. 5-2 *Changing surface morphology and availability for bacterial (b) attachment. Images B1 and B2 describe the available surface with reducing periodicity (Λ). Images C1 and C2 describe the available surface with increasing tip diameter (d). Note that only channel spacing (S) changes with both periodicity and tip diameter.* 186

# LIST OF TABLES


| | | |
|---|---|---|
| Table 3-1 | *Chemical composition of AISI 316L coupons measured using average glow-discharge optical emission spectroscopy depth readings* | 89 |
| Table 3-2 | *Pulsed laser texturing settings for channel textured sample types.* | 92 |
| Table 3-3 | *Sample codes, treatment condition and texturing condition of all sample types.* | 94 |
| Table 3-4 | *Load and maximum Hertzian contact pressures during reciprocating sliding wear testing.* | 102 |
| Table 3-5 | *Total sliding distances of the large area wear testing with changing cycle counts.* | 103 |
| Table 4-1 | *Elemental concentrations (wt%) from the location shown in Fig. 4-5. ASPN spots were taken from the surface.* | 114 |
| Table 4-2 | *Quantitative corrosion measurements of the channel textured sample types.* | 119 |
| Table 4-3 | *Measurements of resistance (Ω) to polarisation of the channel textured sample types.* | 123 |
| Table 4-4 | *Pattern spacing, tip diameter and channel spacing of the ASPNL1, ASPNL2 and ASPNS textures.* | 127 |
| Table 4-5 | *S phase layer thickness on textured peaks and valleys.* | 130 |
| Table 4-6 | *Pattern periodicity, channel spacing and surface roughness (pre-texturing) for the Unt, UntΔ, ASPN & ASPNΔ samples.* | 135 |
| Table 4-7 | *Measurements of resistance (Ω) to polarisation of the 310 fs, Unt, UntΔ, ASPN and ASPNΔ sample types. The lack of $R_p$ value for the Unt and UntΔ samples related to the equivalent circuit models in Fig. 4-29.* | 142 |

| | | |
|---|---|---|
| Table 4-8 | *Contact angle measurements of the Unt, UntΔ, ASPN and ASPNΔ sample types.* | 145 |
| Table 5-1 | *Total distance of chromium diffusion for any surface spot following nanosecond laser texturing.* | 166 |

# ABBREVIATIONS

| | |
|---|---|
| α | Alpha Iron/Ferrite |
| γ | Austenite |
| γ’ | $Fe_4N$ |
| δ | Delta Iron/Ferrite |
| ε | $Fe_{2-3}N$ |
| σ | Iron-Chromium Intermetallic Compounds |
| $\omega_0$ | Gaussian Beam Spot Radius |
| AISI | American Iron and Steel Institute |
| ANOVA | Analysis of Variance |
| ASPN | Active Screen Plasma Nitriding |
| ASTM | American Society for Testing and Materials |
| ASS | Austenitic Stainless Steel |
| at% | Atomic Percentage |
| BCC | Body Centred Cubic |
| BCT | Body Centred Tetragonal |
| CVD | Chemical Vapour Deposition |
| CFU | Colony Forming Units |
| D | Diffusion coefficient of Cr in austenite |
| DC | Direct Current |
| *E. coli* | *Escherichia coli* |
| $E_{Corr}$ | Corrosion Potential of Surface |
| EDS | Energy Dispersive X-ray Spectroscopy |
| EDTA | Ethylenediaminetetraacetic Acid |
| EIS | Electrochemical Impedance Spectroscopy |
| $E_{oc}$ | Open Circuit Potential |
| EPS | Extracellular Polysaccharide |
| EXAFS | Extended X-ray Absorption Fine Structure |

| | |
|---|---|
| FCC | Face Centred Cubic |
| FFT | Fast Fourier Transform |
| FIB | Focus Ion Beam |
| $f$ | Fraction Transformed |
| fs | Femtosecond |
| GDOES | Glow-Discharge Optical Emission Spectroscopy |
| gf | Gram force |
| GDP | Gross Domestic Product |
| GP | Guinier-Preston zones |
| HAI | Healthcare-Acquired Infections |
| HCP | Hexagonal Closed Packing |
| HSFL | High Spatial Frequency LIPSS |
| HV | Vickers Hardness |
| I | Current |
| $I_{Corr}$ | Corrosion Current Density |
| IPS | Invariant Plane Strain |
| L | Liquid |
| LASER | Light Amplification by Stimulated Emission of Radiation |
| LIPSS | Laser-Induced Periodic Surface Structures |
| LSFL | Low Spatial Frequency LIPSS |
| $M^+$ | Metal Cation |
| $M_f$ | Martensite Finish Temperature |
| MRSA | Methicillin Resistant *Staphylococcus aureus* |
| $M_s$ | Martensite Start Temperature |
| MSSA | Methicillin Susceptible *Staphylococcus aureus* |
| *N. nucifera* | *Nelumbo nucifera* |
| NHS | National Health Service |
| ns | Nanosecond |
| $P_0$ | Maximum Hertzian Contact Pressure |

| | |
|---|---|
| PBS | Phosphate Buffered Saline |
| PEG | Polyethylene Glycol |
| PREN | Pitting Resistance Equivalent with Nitrogen |
| PVD | Physical Vapour Deposition |
| $Q_f$ | Double Layer Capacitance Related to the Outer Liquid Interface Layer |
| $Q_p$ | Double Layer Capacitance Related to the S Phase/Untreated Bulk Barrier |
| $R_a$ | Mean Deviation Away from the Mean Profile |
| $R_f$ | Resistance to Polarisation Related to the Electrolyte-Surface/S Phase Interface Layer |
| $R_p$ | Resistance to Polarisation Related to the S Phase-Untreated Bulk Interface Layer |
| *S. aureus* | *Staphylococcus Aureus* |
| S1 | Channel Spacing 1 |
| S2 | Channel Spacing 2 |
| SCE | Saturate Calomel Electrode |
| SEM | Secondary Electron Microscopy |
| SRO | Short Range Ordering |
| TEM | Transmission Electron Microscopy |
| $T_{peak}$ | Peak Temperature |
| TSA | Tryptone Soya Agar |
| $T_{sat}$ | Saturation Temperature |
| TSB | Tryptone Soya Broth |
| UV | Ultraviolet |
| V | Voltage |
| $V_B$ | Breakdown Voltage |
| W | Warburg Impedance |
| wt% | Weight Percentage |
| XRD | X-ray Diffraction |
| XPS | X-ray Photoelectron Spectroscopy |

# CHAPTER 1 INTRODUCTION

Owing to their superior corrosion resistance, bio-inert nature and excellent formability, austenitic stainless steels (ASS) have become one of the most important materials used in the food and the medical industries [1]. They have found widespread applications as medical scalpels, bone saws, surgical sutures, bone fixation pins, pressure vessels, storage containers, cutlery, and piping [2-6]. Although ASS alloys are currently the materials of choice for these applications, there are still concerns over their use. The first concern relates to their relatively low hardness and poor wear resistance, which limits their longevity and necessitates regular in-service maintenance [7-9]. However, the largest worry for their use relates to their high susceptibility to the attachment and growth of bacteria [4, 10, 11], which has led to serious complications involving healthcare-acquired infections (HAI) and cross contamination of foods [12]. These issues present serious public health (over 300,000 cases of HAIs and over 500,000 cases of foodborne illnesses each year in the UK [13]) and economical (combined estimate of £3 billion annually in the UK [14, 15]) challenges that require addressing.

Low-temperature plasma nitriding has been shown to address the poor durability of the ASS alloys by forming the thermodynamically metastable S phase on the surface, and therefore, providing combined improvements in hardness, wear resistance and corrosion resistance of the alloys [16-18]. However, this does not alleviate the concerns related to the biofouling of the surfaces [11, 19]. Pulsed laser texturing presents a promising and scalable approach for the introduction of functional antibacterial properties on surfaces [20]. However, due to the

thermal nature of laser patterning and the metastable state of the S phase, almost no research has been conducted prior to this study on the combination of these technologies [21, 22].

Fortunately, the recent development and increased availability of ultrashort nanosecond ($10^{-9}$ s) and femtosecond ($10^{-15}$ s) pulsed lasers has created new opportunities for the antibacterial functionalisation of S phase treated surfaces [23]. Ultrashort pulsed lasers have shown potential for texturing of surfaces through rapid annealing or athermal approaches, respectively, and have therefore given new hope for the production of durable antibacterial stainless steel surfaces for use in the food and medical industries [23-25].

## Aims & Objectives

The aim of this study was to examine the potential to produce long-lasting antibacterial surfaces on AISI 316L austenitic stainless steel surfaces through combined ultrashort laser texturing and S phase surface treatments. In order to tackle this broad and challenging aim, the study can be broken down into the following objectives:

1. Examination of the response to, and feasibility of, ultrashort (nano and femtosecond) laser texturing of S phase treated AISI 316L surfaces using a mixture of materials characterisation techniques (e.g. crystal structure and microstructural analysis), functional performance evaluation (e.g. electrochemical corrosion resistance) and 1-D surface temperature modelling. Successful combination of the two technologies was deemed to have been achieved when no discernible deterioration of the original

properties of the untreated alloy or the S phase treated layer had developed following laser texturing of the surface [26].

2. Exploration of the antibacterial performance of various biologically inspired textures produced on S phase treated AISI 316L surfaces. Optimal texture structuring was determined through the measurement of the inherent antibacterial performance of each bioinspired texture following exposure to *S. aureus*. Additional microstructural analysis (e.g. cross-sectional elemental mapping) of each textured surface was also undertaken to ensure that the previous objective (precipitate-free S phase layer) was still being maintained following the different textures.
3. To examine the mechanical and antibacterial durability of the chosen texture (optimal texture from previous objective) produced on untreated and S phase treated AISI 316L surfaces, with specific comparisons of wear resistance, texture durability, texture structural integrity and long-lasting antibacterial efficacy against *S. aureus* and *E. coli*.

# CHAPTER 2 LITERATURE REVIEW

## 2.1. Stainless Steel

Stainless steels are a family of ferrous alloys which contain more than 50 wt% iron and contain at least 12 wt% chromium [1]. They are renowned for their excellent corrosion resistance, which is achieved through the formation of a tightly adherent and continuous surface chromium oxide ($Cr_2O_3$; Fig. 2-1) film. In the presence of oxygen, any disruption to this oxide film is instantaneously and passively repaired. Thus, owing to their excellent corrosion resistance, stainless steels have found a wide variety of uses, ranging from open air architectural applications to chemically active product streams in the chemical processing industry. In line with the focus of this study, stainless steels have also found extensive applications as materials for domestic appliances, food industry equipment and medical instruments & devices [27, 28].

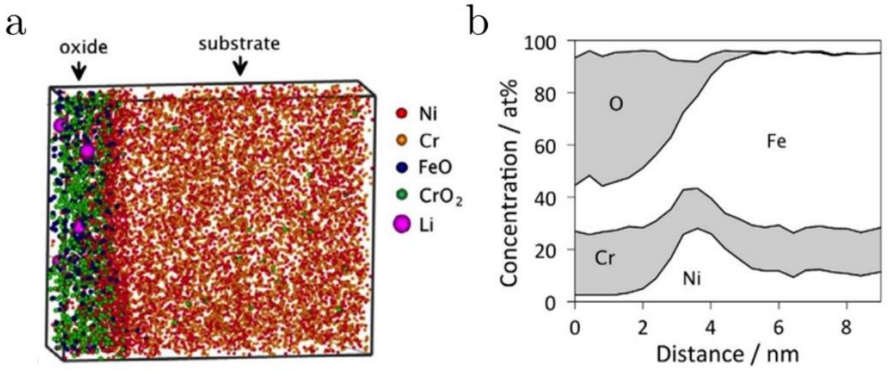



*Fig. 2-1 Passive oxide film on AISI 316 stainless steel revealed using atom probe tomography (a) and chemical composition depth profiling (b) [29, 30].*

### 2.1.1. Classification

To appreciate the nomenclature, phases present, and alloying elements used in stainless steels, it is important to understand the metallurgy of iron, that builds the foundation for all stainless steel alloys.

Upon cooling of pure molten iron, the first solid phase, observed at the melting temperature of iron (1540 °C), is a body-centred cubic (BCC) structured known as delta iron/ferrite (δ). Further cooling leads to a transformation to a face-centred cubic (FCC) crystal structured phase called austenite (γ) at 1394 °C. At 912 °C, the FCC austenite reverts to a BCC phase known as alpha iron/ferrite (α). Although no more crystallographic changes are observed upon further cooling, there are changes in the magnetic properties, with the initially nonmagnetic (paramagnetic) α phase becoming magnetic (ferromagnetic) below 769 °C (also known as the Curie temperature) [28, 31].

When homogeneously and slowly cooled, all matter tends to arrange to reduce free energy in the system. Therefore, since the crystal structure of iron interchanges between FCC and BCC during cooling, it is accurate to assume that the free energies associated with the austenite and ferrite phases are similar [28]. Alloying elements that promote either phase can dictate the predominate structure of the material at room temperature. Consequently, alloying elements are classified as either ferrite or austenite stabilisers. Since chromium (ferrite stabiliser) and nickel (austenite stabiliser) are the main alloying elements of stainless steels, it is convenient to give the total contributions of the alloying elements as a value of the combined chromium or nickel equivalence according to equations 2-1 and 2-2, respectively. A plot of the

nickel equivalent elements against chromium equivalent elements, called a Schaeffler diagram (Fig. 2-2), can then map the expected phases for a given composition [27, 30].

$$Total\ Cr\ equivalents = Cr + 2 \cdot Si + 1.5 \cdot Mo + 5 \cdot V\ (in\ wt\%) \quad \text{(equation 2-1)}$$

$$Total\ Ni\ equivalents = Ni + Co + 0.5 \cdot Mn + 30 \cdot C + 30 \cdot N\ (in\ wt\%) \quad \text{(equation 2-2)}$$

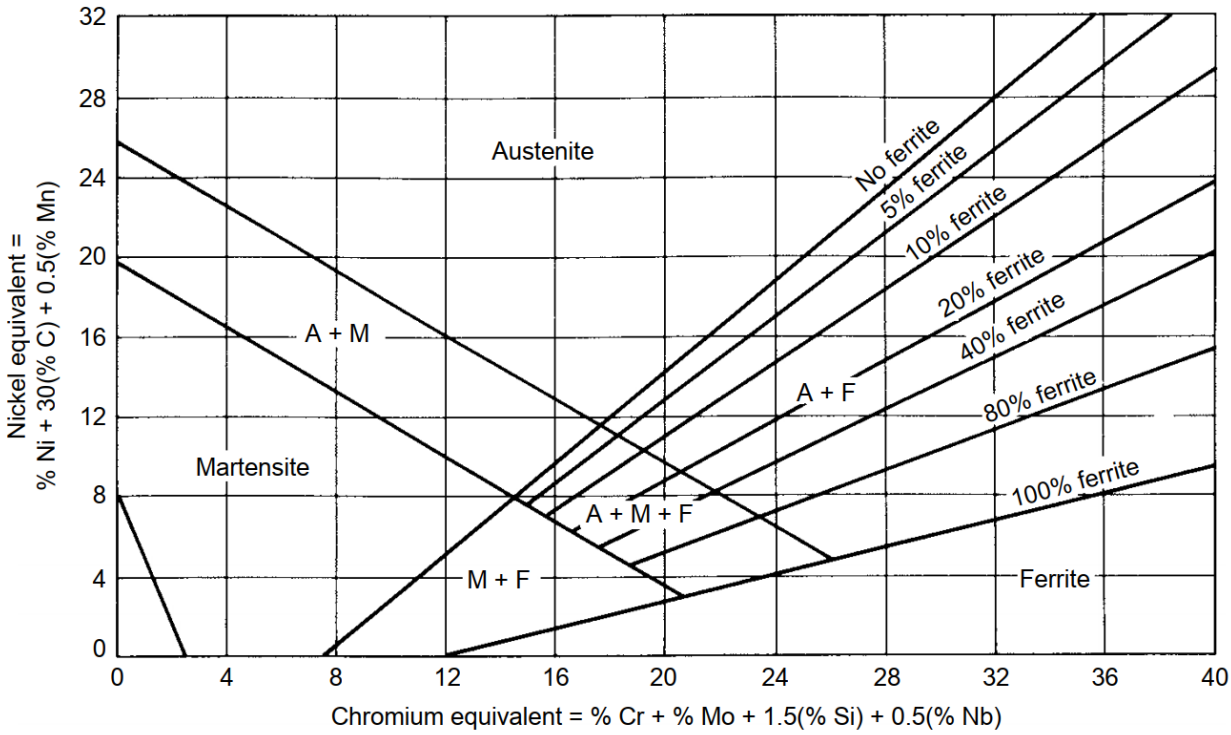



*Fig. 2-2 Schaeffler diagram showing expected microstructure at room temperature with changing chromium and nickel equivalent alloying elements (in wt%) [27, 32].*

### 2.1.2. Types of Stainless Steel

Five major families of stainless steels exist. Four of the classifications are based on the crystallographic structure of the phases, these are the austenitic (FCC), ferritic (BCC), martensitic (body-centred tetragonal (BCT)) and duplex (FCC & BCC) stainless steels [27]. The other class of stainless steels, the precipitation-hardening stainless steels, are instead defined by their ability to be age (precipitation) hardened, and can be further sub-categorised based on the microstructure of the solution-annealed alloy (martensitic, austenitic and austenitic-martensitic) [28, 33, 34].

### 2.1.3. Ferritic Stainless Steel

Since chromium is a strong ferrite phase stabilising element, ferritic stainless steels are essentially iron-chromium alloys, and therefore, widely regarded as the simplest type of stainless steel. With increasing chromium content, the temperature range whereby the ferritic phase is stable increases, and at approximately 12 wt% chromium, the ferritic phase becomes the dominant phase at all temperature (Fig. 2-3). At room temperature, the ferrite phase has a relatively high yield strength, low ductility, low work hardenability, and is ferromagnetic [28, 31]. Ferritic stainless steels are generally regarded to have inferior corrosion resistance in comparison with austenitic stainless steels. This is largely due to the poor solubility of carbon and nitrogen within the BCC lattice, especially at colder temperatures, which consequently lead to the expulsion and precipitation of these interstitial atoms to grain boundaries or dislocations [33]. Due to the favourable thermodynamic driving forces, the formation of chromium carbides and/or nitrides are preferred at these sites, and subsequently lead to the

depletion of free (unbound) chromium in the matrix of adjacent regions (Fig. 2-4), and therefore, cause localised breakdowns of the passive film, leading to a loss of overall corrosion resistance [28]. To overcome this, modern methods attempt to reduce the carbon and/or nitrogen content, and to incorporate alloying elements that can preferentially form thermodynamically favourable benign carbides and/or nitrides (e.g. titanium or niobium), thus retaining the homogeneous spread of chromium in the matrix [27].

As a result of not requiring the austenite phase stabilising and costly nickel alloying, ferritic stainless steels provide considerable economic advantages over austenitic stainless steels. Combined with their resistance to stress corrosion and temperature-induced fatigue, ferritic stainless steels are commonly utilised in less corrosively critical applications such as car exhaust systems, kitchen appliances, cookware and storage tanks [27, 30].

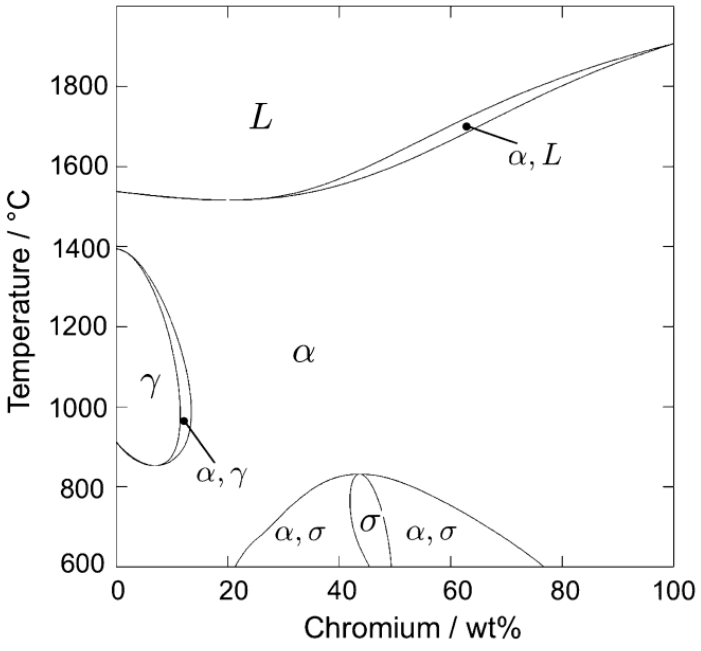



*Fig. 2-3 Iron-chromium phase diagram. The labelled phases are as follows: liquid (L), ferrite (α), austenite (γ) and iron-chromium intermetallic compounds (σ) [30].*

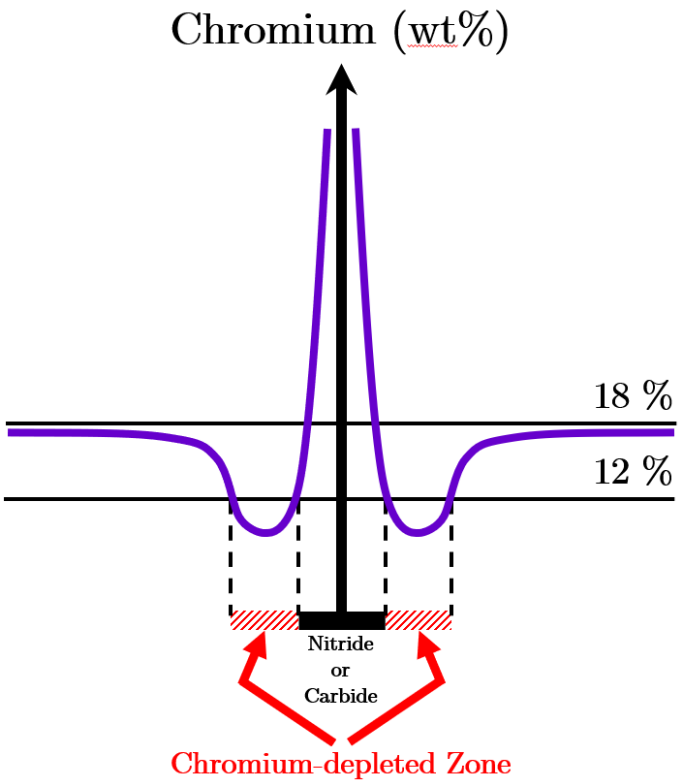



*Fig. 2-4 Chromium-depleted zones adjacent to nitride or carbide precipitates (Redrawn from [28]).*

### 2.1.4. Austenitic Stainless Steel

Owing to their superior corrosion resistance, even within stainless steels, austenitic stainless steels are currently the most widely used family of stainless steel alloys and account for approximately 70 % of all steels in use [35, 36].

To overcome the problems related to the precipitation of carbides and/or nitrides in ferritic stainless steel alloys, it is necessary to change the crystal structure to the FCC austenite, in order to increase the interstitial solubility of carbon and/or nitrogen. The stabilisation of the austenite phase at room temperature is primarily achieved through the addition of nickel, and nickel alternative (see equation 2-2), which aid in opening the austenite loop to lower

temperatures [30, 33]. The leanest compositions for austenitic stainless steels (ASS) are the 18-8 or AISI (American Iron and Steel Institute) 304 alloys, which contain 18-20 wt% chromium and 8-10 wt% nickel [37].

ASS can be classified into two subgroups, the AISI 200 and the AISI 300 series, which differ in their primary approach to stabilisation of the austenite phase. In the 200 series, austenite phase stabilisation is largely achieved through the addition of manganese and nitrogen, with only small additions of nickel, whereas, in the 300 series it is accomplished primarily through the addition of nickel [38]. The addition of nickel improves the formability of the alloys, while the addition of manganese and nitrogen increase the mechanical strength of the resulting alloys [39].

ASS are non-magnetic alloys that cannot be hardened by heat treatment; however, given the low stacking fault energies, they can be readily work hardened. In practice, this results in relatively low as-cast yield strength, in the region of 200-400 MPa, but potentially higher than 2000 MPa yield strength following cold working of the material [28]. They are also characterised with high ductility and toughness, at all temperature ranges, even close to absolute zero [35, 37]. However, due to their higher expansion coefficient, in comparison with ferritic stainless steels, they possess poorer cyclic oxidation resistance (spallation of the protective oxide film) and are more prone to fatigue, especially thermal fatigue [37]. Additionally, impurities such as sulphur, which can form inclusions in ASS alloys, act to increase susceptibility to pitting corrosion and stress corrosion cracking in chloride containing media [28].

Prolonged exposure of ASS at elevated temperatures (> 400 ˚C) can enable the precipitation of chromium carbides at grain boundaries, thus making the alloys sensitive to intergranular corrosion (through the same mechanism as explained in section 2.1.3). Prevention or delay of the precipitation can be achieved through either reduction of carbon content (hence the formation of low carbon, 'L', alloys) or through additions of alloying elements that form preferential benign carbides (similar to section 2.1.3) [27, 33, 38].

### 2.1.5. Duplex Stainless Steel

Duplex stainless steels are typically characterised with having an equal microstructure ratio of austenite to ferrite, which is achieved through careful balancing of alloying elements to expand the α + γ portion of the iron-chromium phase diagram (Fig. 2-3) [30]. To obtain an equal volume fraction of the two phases, it is usually necessary to incorporate at least 20 wt% chromium in the alloys (Fig. 2-2), and consequently, duplex stainless steels possess excellent corrosion resistance [28]. Additionally, due to the lesser requirements for nickel, duplex stainless steels also have economic advantages over fully austenitic stainless steel alloys [37]. Resulting from the dual phase structure, these alloys also provide a good combination of improved mechanical properties and corrosion resistance when compared with either phase alone. The improvements in yield strength, toughness and fatigue are accomplished through the simultaneous presence of both phases (refine grain size), solid solution hardening (increased alloying of substitutional and interstitial elements) and increased fatigue limit [28, 36]. The excellent corrosion resistance of duplex stainless steels arises from the synergetic combination

of resistance to stress corrosion cracking in the ferrite phase and the higher general corrosion resistance of the austenitic phase [38].

The greatest limitation of duplex stainless steels arises due to the increased use of alloying elements and presence of both phases, which can give rise to an increased number of embrittling secondary phases. Consequently, to avoid the precipitation of the secondary phases, duplex stainless steels are not recommended for use above 300 ˚C. Additionally, given that they have a ductile-to-brittle transition, they are also not suited for cryogenic use [28, 30].

Owing to the historic difficulties associated with the formation and microstructural control of duplex stainless steels, there still exists a lot of hesitancy over the long-term availability of the alloys, and therefore, their industrial uptake has not yet reached its full potential. However, given their many advantages over single phase stainless steels, and the improved understanding and reliability of their manufacture, uptake of these alloys is steadily increasing [28].

### 2.1.6. Martensitic Stainless Steel

Martensite is a thermodynamically metastable phase found in iron, steel and stainless steel alloys, which arises from the rapid phase transformation from austenite to ferrite in the absence of diffusion [31]. Due to the non-equilibrium state of martensite, it is not found in the iron-chromium phase diagram (Fig. 2-3). As previously described in section 2.1.1, the free energy driving force for the transformation of austenite to ferrite increases with cooling, and below a certain temperature, known as the martensite start temperature ($M_s$), it is possible for austenite grains to spontaneously begin transforming as a result of deformation [28].

Quenching at temperatures below the $M_s$, leads to the phase transformation without diffusion of either substitutional or interstitial elements, and subsequently causes slip dislocation of planes (shearing) in order to facilitate the transformation (Fig. 2-5) [30]. Consequently, a BCC structure is obtained with supersaturated concentrations of interstitial elements that, due to the reduced interstitial spacing within the BCC structure, distort the unit cell to a BCT structure. Moreover, the reduced solubility of interstitial elements within the BCT structure leads to colossal interstitial supersaturation of the martensite lattice, and hence expansion of the phase [28]. Although as-quenched martensite has very high hardness, it suffers from poor toughness and ductility, and tempering is required to alleviate the high strains through controlled diffusion of interstitial elements to the phase boundaries in the form of carbide precipitates [34, 36].

Therefore, martensitic stainless steels are essentially ferritic stainless steels that are austenised (heated to fully transform into austenite) and then quenched to produce the thermodynamically metastable martensite phase [36]. Due to the need for these alloys to transform into austenite at elevated temperatures, martensitic stainless steels characteristically contain the lowest levels of chromium, a ferrite phase stabiliser, and thus, typically possess the weakest corrosion resistance of the different microstructured stainless steel families [27]. Moreover, the high carbon contents and the tempering typically associated with martensitic stainless steels, promote the formation of chromium carbides that further reduce the corrosion resistance of the alloys. Hence, martensitic stainless steels are usually only found in mildly corrosive applications, such as cutlery or tooling [28].

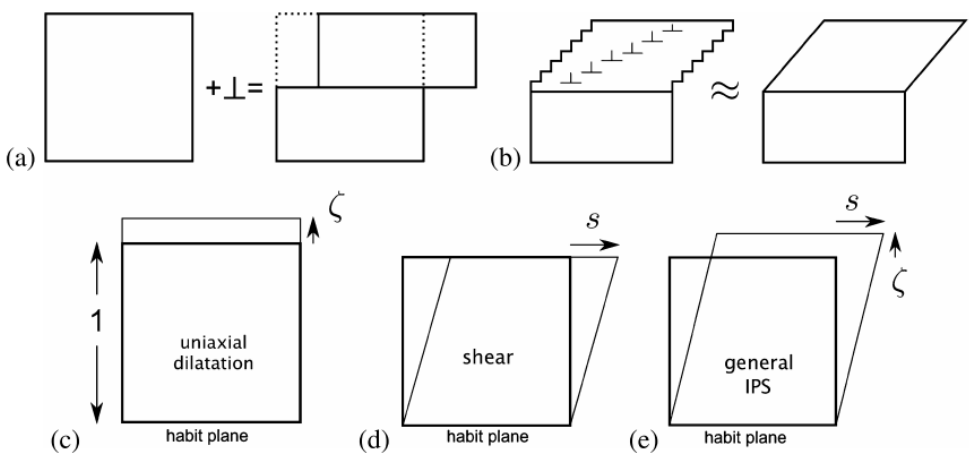



*Fig. 2-5 Visualisation of the austenite to martensite transformation, where (a) is a single slip dislocation, (b) is many slip dislocations, (c) is a 1 direction expansion (uniaxial dilatation), (d) a simple shear and (e) is the invariant plane strain (IPS) caused by the combined 1-directional expansion and shearing [30].*

### 2.1.7. Precipitation-Hardening Stainless Steel

Precipitation-hardening stainless steels are characterised by their ability to be age hardened through the addition of alloying elements such as copper, aluminium and titanium [38]. The incorporation of these elements in the alloy has two advantages, the first being to enable the precipitation of multiple hard phases below the phase transformation temperatures of the alloys, thereby allowing age hardening, and the second being to detract from the formation of chromium containing phases in order to retain the corrosion resistance of the alloy [40].

During age hardening, the driving forces (e.g. solid solubility) for the formation of the intermetallic phases containing the alloying elements (e.g. $Ni_3Ti$) promote the gathering of many evenly spread nanoscale clusters, known as Guinier-Preston (GP) 1 zones, which are rich in the alloying elements. With time, the elements within each cluster align to form organised

10-50 nm sized, and 1 or 2 atomic planes thick, regions containing the solutes, known as GP 2 zones, that are still coherent with the substrate crystal structure. If the dimensions of the precipitating phases and the substrate match closely (usually <1 % difference), then coherency can still exist beyond the initial formation of the phase [41]. Whilst coherency with the substrate matrix is retained, strengthening of the alloy is achieved at every stage of the development (GP 1 to GP 2 to coherent particles) through induced strains and barriers created to the movement of dislocations in the material. Beyond a certain precipitate size, breakdown in coherency follows, known as overaging, which results in the loss of the hardening effect due to the relaxation of the stresses induced on the lattice [28]. At this point, only Orowan hardening (dislocation looping) mechanisms remain in the alloy, which provide a reduced hardening effect, and increasingly lower effectiveness with precipitate coarsening [41].

Due to the reduced presence of chromium containing secondary phases, precipitation-hardening stainless steels possess higher corrosion resistance than martensitic stainless steels, while still providing great strength (up to 1.7 GPa yield strength) and higher ductility [34]. Moreover, since there is only limited dimensional change following age hardening, fabrication of the alloys into the final form can be done in the relatively softer state before final hardening [28].

Martensitic precipitation-hardening stainless steels are the most common and widely used type of precipitation-hardening stainless steel. Due to the low carbon content (<0.05 wt%), these alloys, in their annealed state, are relatively soft in comparison with the typical high carbon martensitic stainless steels [34]. If the content of austenite stabilising elements is increased, then it can be made possible for the austenite structure to be maintained at room

temperature in a metastable state. This can then facilitate easier fabrication of the final product in the softer austenitic structure, followed by cryogenic treatment, cold working, or heat treatment to transform to martensite; hence, these are named austenitic-martensitic precipitation-hardening stainless steels [42]. Further austenite stabilisation gives rise to austenitic precipitation-hardening stainless steels, which are fully austenitic in both the solution annealed and age hardened state. This provides the benefit of easier fabrication, combined with the ability to employ these alloys in higher temperature applications (e.g. up to 700 ˚C) with reduced risk of phase transformation or overaging [27]. Moreover, the nonmagnetic nature of the austenite phase also create new areas for application of these alloys in comparison with the other precipitation-hardening stainless steel types [28].

## 2.2. AISI 316L Austenitic Stainless Steel

As previously described in section 2.1.4, the AISI 304 alloys constitute the most basic composition for austenitic stainless steels (ASS), and therefore, create the basis for the development of almost all other austenitic stainless steel alloys. The alloy of focus within this study is the AISI 316L ASS, and as shown in Fig. 2-6, these can be traced back to the AISI 304 alloys through the AISI 316 composition. Due to their favourable corrosion resistance and bio-inert nature, these three alloy compositions account for the majority of stainless steels currently in use in the food and medical industries [6, 43]. Therefore, the physical metallurgy and composition of the AISI 316L ASS alloys will be detailed in chronological order, going from the AISI 304 to 316 to 316L alloys, before property analysis relating to the corrosion resistance, mechanical properties and tribological properties of the alloys is discussed.

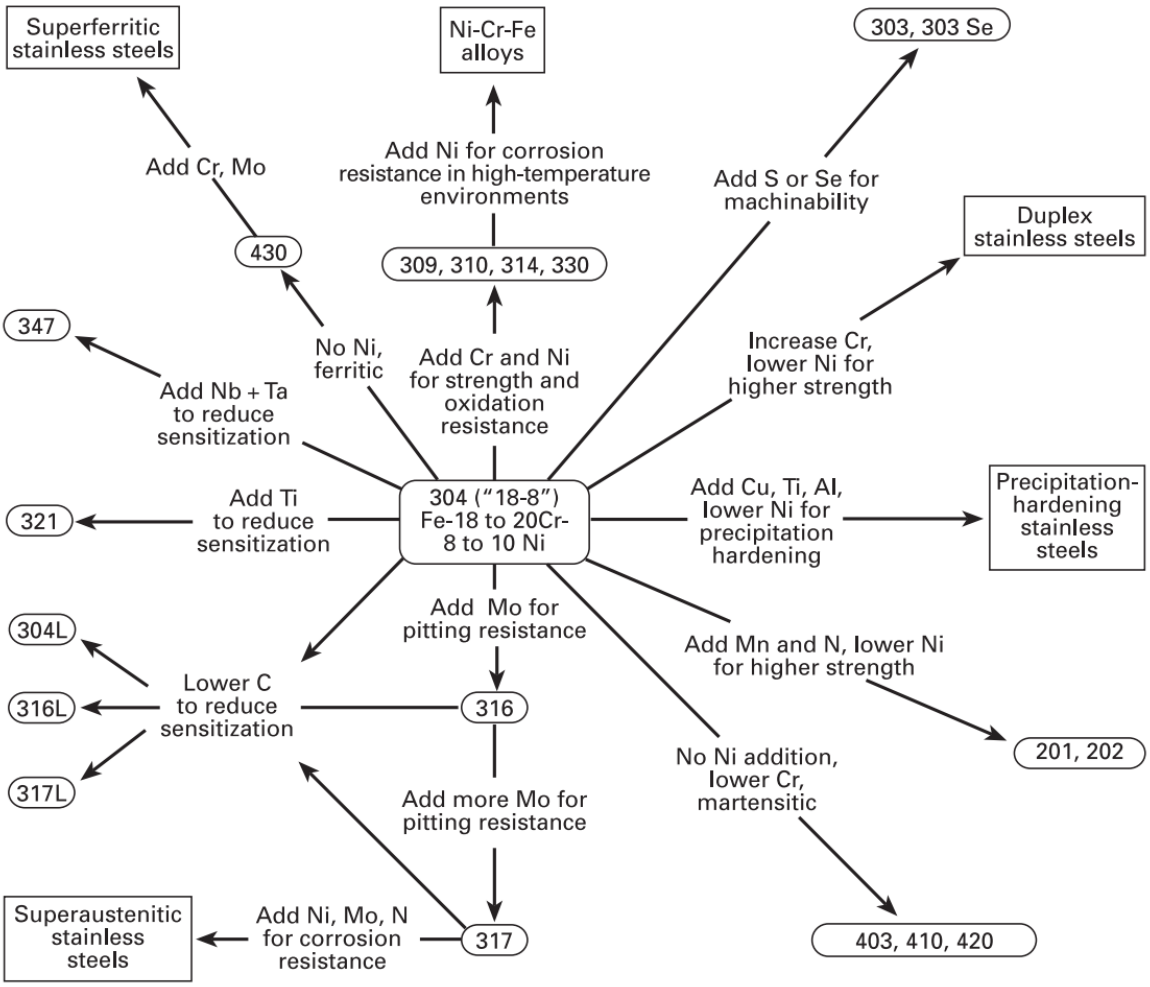



*Fig. 2-6 Stainless steel family composition and property linkages [42].*

## 2.2.1. Composition

Depending on the ASTM (American Society for Testing and Materials) standard followed by the supplier, each of which relate to specific applications of the material, slightly different accepted ranges for the alloying elements of an indexed alloy can exist. The overall accepted composition range in AISI 304 stainless steels are as follow: 17.50-20.00 wt% Cr, 8.00-11.00

wt% Ni, ≤2.00 wt% Mn, ≤1.00 wt% Si, ≤0.10 wt% N, ≤0.08 wt% C, ≤0.045 wt% P, ≤0.03 wt% S [44].

As expected, and previously explained in section 2.1, the additions of the carbon, chromium and nickel are the main alloying elements, and respectively, each aid in forming the steel base, the corrosion resistant surface oxide and the fully austenitic structure of the alloy [37]. The inclusion of manganese in the alloy serves to enhance the strength and toughness of the alloy, whilst also indirectly increasing the stability of the austenite phase by increasing the solubility of nitrogen, a strong austenite stabiliser (like the AISI 200 series) [28]. Additionally, manganese can act as a scavenging element for residual oxygen and sulphur within the alloy, by forming manganese sulphide and manganese oxide inclusions, and therefore, helping to avoid the formation of the more harmful oxides and sulphides of iron [36]. These inclusions, particularly manganese sulphide, can also improve machinability of the alloy at the cost of fracture toughness, weldability and corrosion resistance [45]. Phosphorous has a similar effect to sulphur (improve machinability), while also positively influencing the strength of the alloy. As a result of the negative influences of sulphur and phosphorous on the corrosion resistance, toughness and weldability of the alloy, they are regularly regarded as undesirable impurities in steel alloys; however, small quantities of these elements are commonly intentionally added to reduce material processing costs [46].

The strongest deoxidising element in these alloys is silicon, and additions of this element help to prevent the formation of crack-inducing carbon monoxide bubbles that can form during the casting of the alloys, while at the same time improving the oxidation resistance of the alloy.

However, due to the ferrite stabilising effect of silicon, only limited quantities can be added [36, 47].

Nitrogen, as a solid solution, can be extremely beneficial to austenitic stainless steel alloys (see section 2.4); however, at concentrations high enough to cause incoherent precipitation of nitrides, it can adversely affect the corrosion resistance (as previously described in section 2.1.4). Therefore, production controls, such as alloying with titanium or niobium, are necessary to capture any nitrogen not present as an interstitial solid solution, before the deleterious chromium nitrides can form [28].

As shown in Fig. 2-6, the only difference between the AISI 304 and AISI 316 alloys is the addition of molybdenum (2.00-3.00 wt%), which improves the pitting corrosion resistance of the alloy. However, since molybdenum is a ferrite stabiliser, a slight reduction in chromium (down to 16.00-18.00 wt%) and increase in nickel (up to 10.00-14.00 wt%) content is necessary to maintain the alloy as fully austenitic [28, 34]. The exact mechanisms behind the improved pitting corrosion resistance imparted by the addition of molybdenum are still not well characterised; however, current results suggest that there may be a multitude of roles that molybdenum may play. Studies have suggested that molybdenum can reduce the passive oxide dissolute rate [48], increase the thickness of the passive film [49], improve bonding in the passive oxide [50], inhibit the growth of trenches formed at MnS inclusions [51, 52], reduce the local pH [53], and promote the repair of the passive oxide [54].

Although carbon is an excellent interstitial solid solution element, and can effectively increase the strength of iron-based alloys, it is also a strong precipitate forming element and can give

rise to sensitisation at grain boundaries (section 2.1.4) [31]. For applications containing harsh chemical environments, such as body implants or acidic liquid storage containers (e.g. lemon juice), it is necessary to reduce the carbon content of alloys in order to improve intergranular corrosion resistance (by eliminating/delaying carbide formation) [2, 34, 42]. Subsequently, low carbon versions of common alloys exist, including AISI 304L and AISI 316L, whereby the carbon content is reduced to a maximum content of 0.03 wt%, down from a maximum content of 0.08 wt%, with no other compositional changes [55].

### 2.2.2. Corrosion Properties

With the current rapid development of technology and science, it is often easy to forget or underappreciate many monumental discoveries throughout history. This is particularly visible with the normalisation of the availability and global widespread use of stainless steel alloys, even with the alloys having only been industrially produced for little over 100 years. It is often forgotten that it was widely regarded that iron-based alloys would never be corrosion resistant, with the journal *The Corrosion and Preservation of Iron and Steel* stating in 1910 that "the tendency to rust is a characteristic inherent in the element known as iron, and will, in all probability, never be totally overcome"; however, as we now know, this can, for all intents and purposes, be readily overcome [47]. Therefore, it is important to appreciate that the stainless steel alloys that are currently readily available did not always exist, and that their excellent corrosion resistance should not be ignored or trivialised. To this end, stainless steels are now some of the most popular materials utilised across the globe [1, 56].

Austenitic stainless steels, despite their relatively poor mechanical and tribological properties, are still the most widely used form of stainless steel, with most of the credit being given to their corrosion resistance, which is superior, even against other types of stainless steels [28]. As has been previously introduced in section 2.1, the excellent corrosion resistance of austenitic stainless steels is primarily achieved through the passive formation of a thin chromium oxide ($Cr_2O_3$) layer at the surface of specimens, which acts to isolate the core material from the external environment. In the presence of oxygen (e.g. air), instantaneous repair of the oxide can also occur, helping to 'self-heal' the surface and retain the corrosion resistance indefinitely [27]. This phenomenon relies on the availability of enough chromium across all exposed surfaces to both provide full oxide coverage and to facilitate re-passivation of the surface. Therefore, to retain its stainless nature, it is necessary for all stainless steel alloys to possess at least 12 wt% chromium; however, in more severe corrosive environments, it is commonly necessary to alloy 17-20 wt% chromium (e.g. 18-8 stainless steels) [28].

Although this chromium oxide layer is resilient against most chemicals, it can be prone under attacks by specific acids such as sulphuric acid and hydrochloric acid. In fact, this weakness is one of the biggest contributors to the delayed discovery of stainless steels. In the 1890's, high chromium steels were examined by multiple researchers, including Robert Hadfield, for the purpose of developing steels with better corrosion resistance; however, the testing of corrosion resistance in those times was typically carried out against sulphuric acid, and therefore resulted in very poor results (complete sample dissolution with overnight exposure), and ultimately ceased further examination. Luckily, work on these steels did eventually persist

in the early 20th century, with the discovery of these steels by Harry Brearley (martensitic), Benno Strauss (austenitic), Christian Dantsizen (ferritic) and Frederick Becket (ferritic) [47].

In most cases, total loss of the surface oxide is rare, and typically can only occur in extreme conditions; instead, localised breakdowns of the surface oxide, that expose the susceptible bulk, are more common. Once exposed, the bulk corrodes much like low-alloy or carbon steels, and therefore is subject to the different forms of corrosive attack [27]. This, therefore, demonstrates the need for homogeneity across the samples, to equally protect every surface, and reveals the importance of avoiding elemental segregation and precipitation (Fig. 2-4). As previously discussed in section 2.2.1, cases can be made for the effect of every alloying element, and their respective roles on the improvement or susceptibility against different forms of attack. The most common forms of corrosion faced by these alloys are general, intergranular, pitting, crevice, and galvanic corrosion [33, 57].

#### 2.2.2.1. General Corrosion

General corrosion, which is also commonly referred to as uniform corrosion, occurs in the presence of acids, and leads to the gradual, and uniform, removal of material across all exposed surfaces. This form of attack is not usually of great concern, this is due to the passive nature of austenitic stainless steels, as well as, the progressive development of the attack, making it easy to measure, track and to take action on before catastrophic failure can occur [58].

#### 2.2.2.2. Intergranular Corrosion

Intergranular corrosion, as the name suggests, occurs in the regions between grains, rather than within the grains. Sensitisation (e.g. carbide precipitation) of the stainless steel alloys can make them vulnerable to this form of attack (as previously described in sections 2.1.3, 2.1.4 & 2.2.1). Luckily, the low carbon nature of the AISI 316L alloys reduces the risk of carbide precipitation, even under welding conditions, and helps to minimise or prevent this form of attack [33, 35, 58].

#### 2.2.2.3. Pitting Corrosion

Pitting is an extremely localised form of corrosion attack that produces holes, or "pits", at the surface of samples. Pitting occurs when either one area of a sample becomes anodic with respect to the rest of the surface, or when there is a localised change of the corrosive agent (chemical composition or concentration). In stainless steels, the formation of pits is typically associated with localised breakdowns in the passive oxide film, which can arise adjacent to precipitates (e.g. carbides), at sites of inclusions (e.g. MnS), in crevices (oxygen starvation), and at grain boundaries [33, 57].

Due to the need for a localised weakness on the surface of samples, delayed formation of pits is common, and therefore, make them unpredictable and dangerous. Additionally, pitting is self-propagating, especially in chloride containing solutions, and once initiated, the rate of material removal accelerates with time. This arises due to multiple synergetic and autocatalytic events (Fig. 2-7) such as: (1) freshly exposed stainless steel surfaces react with chloride ions in the media to release metal chlorides (equation 2-3). (2) The release of the metal cations ($M^+$)

produces a localised positive charge at the site of the pit, (3) that then attract more chloride ions to the pit to neutralise the charge, (4) thus increasing the chloride concentration, and accelerating material removal in the localised region. (5) The hydrolysis reaction of the metal chlorides within the pit forms metal hydroxides and hydrochloric acid (equation 2-4), therefore reducing the local pH and further increasing the dissolution rate. (6) The highly concentrated solution within the pit prevents oxygen migration in the media, therefore preventing passivation of newly exposed surfaces and enabling widening (undercutting) of the pit below the surface [33, 35].

$$M + 2HCl \rightarrow M^{2+}2Cl^{-} + H_2 \qquad \text{(equation 2-3)}$$

$$M^{2+} + 2Cl^{-} + 2H_2O \rightarrow M(OH)_2 + 2H^{+} + 2Cl^{-} \qquad \text{(equation 2-4)}$$

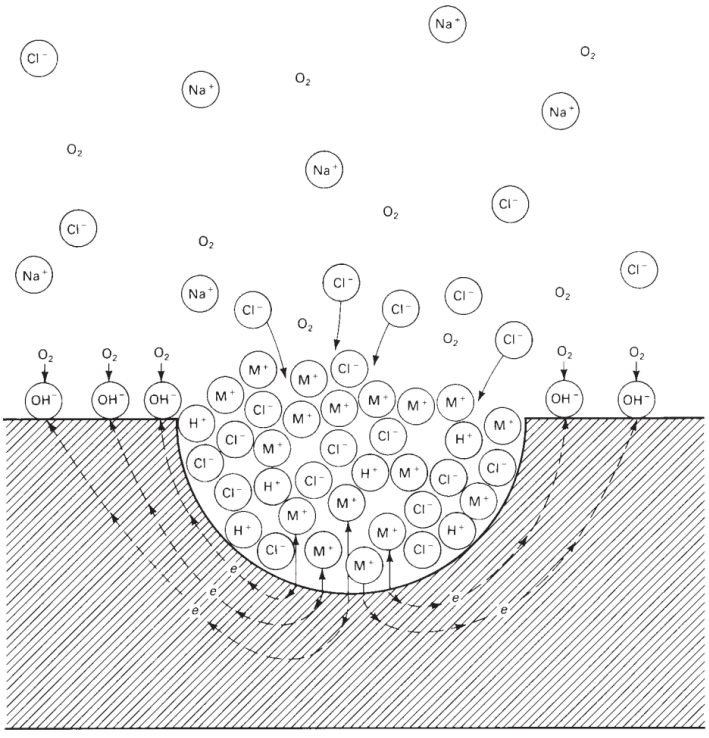



*Fig. 2-7 Summary of autocatalytic events during pitting corrosion [33].*

Moreover, the electrons released from the oxidation reactions that produce the metal cations are driven by potential difference, through the material, towards the relatively cathodic adjacent surfaces. The build-up electrons at the cathode drives the residual $H^+$ ions in the pits towards the cathodic areas, therefore allowing for reduction reactions such as the hydrogen evolution (equation 2-5; Fig. 2-8), oxygen reduction (equations 2-6 & 2-7) and metal-ion reduction (equation 2-8) [33, 58].

$$2H^+ + 2e^- \rightarrow H_2 \qquad \text{(equation 2-5)}$$

$$O_2 + 4H^+ + 4e^- \rightarrow 2H_2O \qquad \text{(equation 2-6)}$$

$$O_2 + 2H_2O + 4e^- \rightarrow 4OH^- \qquad \text{(equation 2-7)}$$

$$M^{3+} + e^- \rightarrow M^{2+} \qquad \text{(equation 2-8)}$$

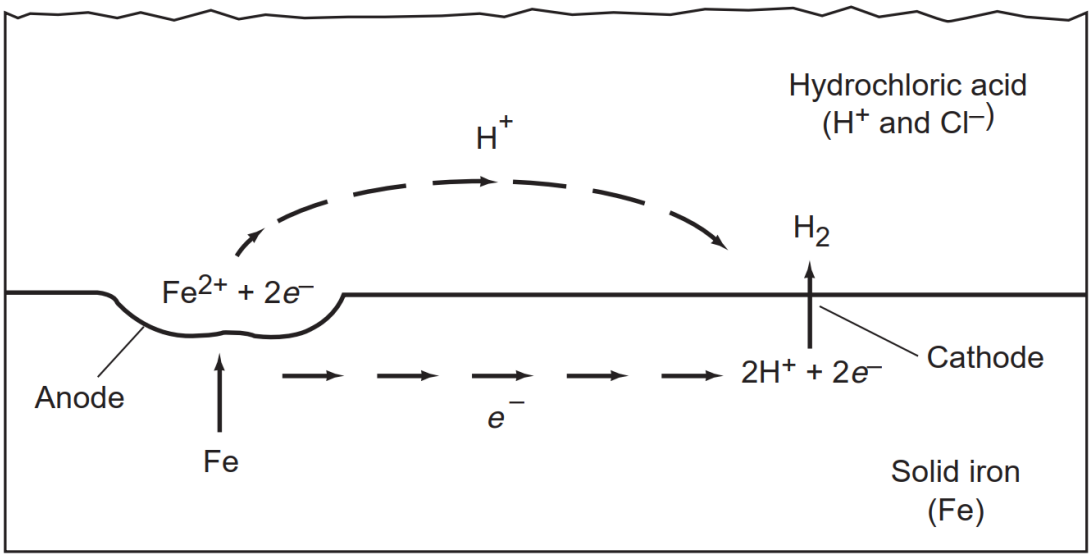



*Fig. 2-8 Hydrogen evolution reactions in the event of corrosion of iron in hydrochloric acid [33].*

The main concerns with pitting relate to the unpredictable initiation, difficulties associated with detecting the initiation and development of pits (commonly masked by other forms of ongoing corrosion & negligible weight loss), and rapid acceleration deep into the material [33, 35].

As has already been stated in section 2.2.1, the composition of the alloys can play a major role in the formation, thickness and repair of the passive surface film. Consequently, an equation (equation 2-9) has been developed, known as the pitting resistance equivalent with nitrogen (PREN), which helps to rank different alloys and give an idea of their susceptibility to the formation of pits [27]. The inclusions of chromium and molybdenum in the PREN equation are obvious and their influence on the surface film has already been discussed; however, the inclusion of nitrogen, especially with such a large coefficient, has not been previously discussed. The exact mechanisms involved in the improvement of pitting corrosion resistance that occurs following the introduction of nitrogen are still not well characterised, and like the effect of molybdenum, the influence is still a subject of debate [27]. Current theories suggest that nitrogen may play a role in: (1) forming ammonium ions that increase the pH of the surface (including within pits) and impede the oxidation reaction involving the metal ions [59], (2) stabilising the passive film, thus hindering attacks from chloride ions [60], (3) occupying active sites at the surface (e.g. kinks and steps) [59], and (4) stabilising the austenite phase [56, 61, 62].

$$PREN = Cr + 3.3 \cdot Mo + 30 \cdot N \ (in\ wt\ \%) \qquad \text{(equation 2-9)}$$

#### 2.2.2.4. Crevice Corrosion

Crevice corrosion is another localised form of corrosion that is difficult to avoid and is very similar in development to pitting corrosion. As the name suggests, this form of attacks occurs at narrow or restricted regions, where the media can become stagnant. Over time, due to the chemical attack and migration by the corrosive agent, depletion of the oxygen within the crevice can arise, which for stainless steels causes the loss of passivity and reduction of corrosion resistance. Once the protective film is penetrated, corrosion can commence almost identically to pitting, with the crevice acting as the anode & the material adjacent to the crevice acting as the cathode. Preventing or delaying crevice corrosion can be achieved in two main ways, the first being to modify the chemical composition of the alloy (increase PREN elements & reduce inclusions and carbides), and the second is to improve the design and fitting of tools and modular components to limit the presence and size of crevices [33, 57, 58].

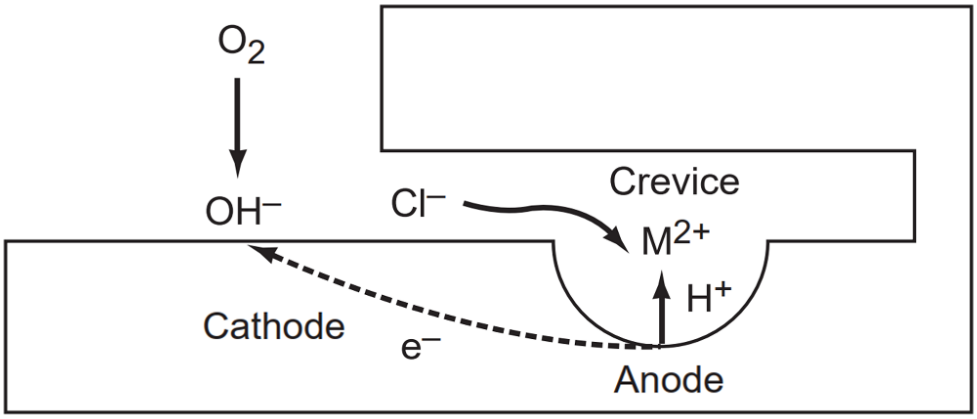



*Fig. 2-9 Schematic diagram of crevice corrosion [33].*

#### 2.2.2.5. Galvanic Corrosion

Galvanic corrosion arises when multiple electrically conductive materials are coupled together in the same electrolyte media. This form of attack occurs due to the potential difference between the two coupled materials, therefore forming a galvanic cell, whereby each material acts as an electrode [33]. The flow of electrons depends on the behaviour of each material, with the more active (more corrosion prone) material becoming the anode, and the more passive or noble (more corrosion resistant) material becoming the cathode. It is possible to predict the direction and potential of galvanic corrosion using a galvanic series, where the electrical potential (voltage; also known as corrosion potential) of each material can be individually examined, and compared with a saturate calomel electrode (SCE), within a specific electrolyte (e.g. sea water) [35]. Stainless steels are interestingly found twice in the galvanic series (Fig. 2-10), once with the protective oxide layer present (passive), and then again with the oxide layer absent (active). Although the galvanic series does not give information about the corrosion rate, it is useful for predicting the corrosion potential of a metal, and further demonstrates the importance of the passive oxide layer to the excellent corrosion resistance of stainless steels [33]. As is shown in Fig. 2-11, AISI 316L alloys in the passive state are extremely noble, with similar potentials to pure titanium alloys (passive) at elevated temperatures (40 ˚C) [63].

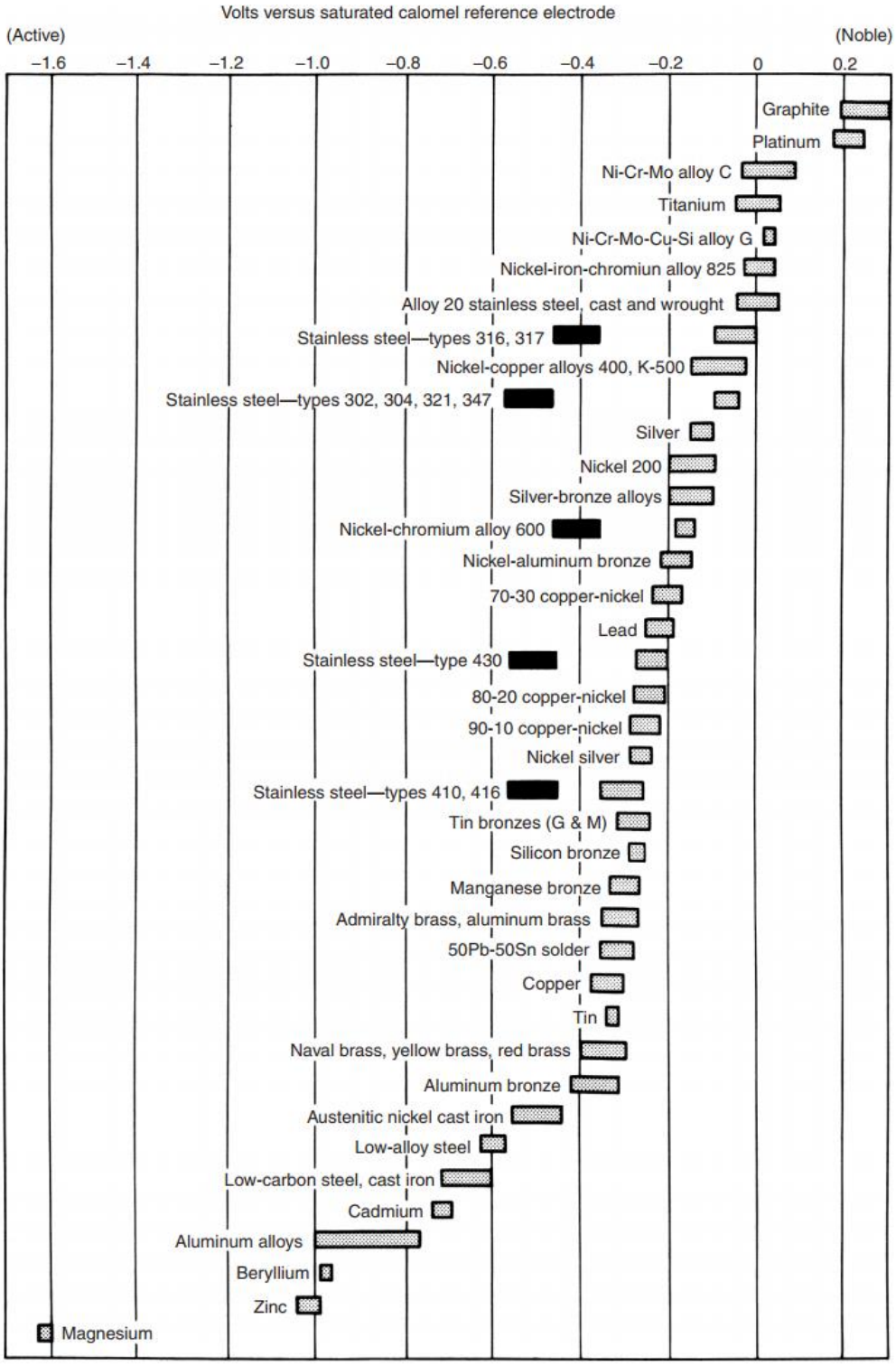



*Fig. 2-10 Galvanic series in sea water. For active-passive alloys, black boxes indicate the active state, while white boxes indicate passive state [27].*

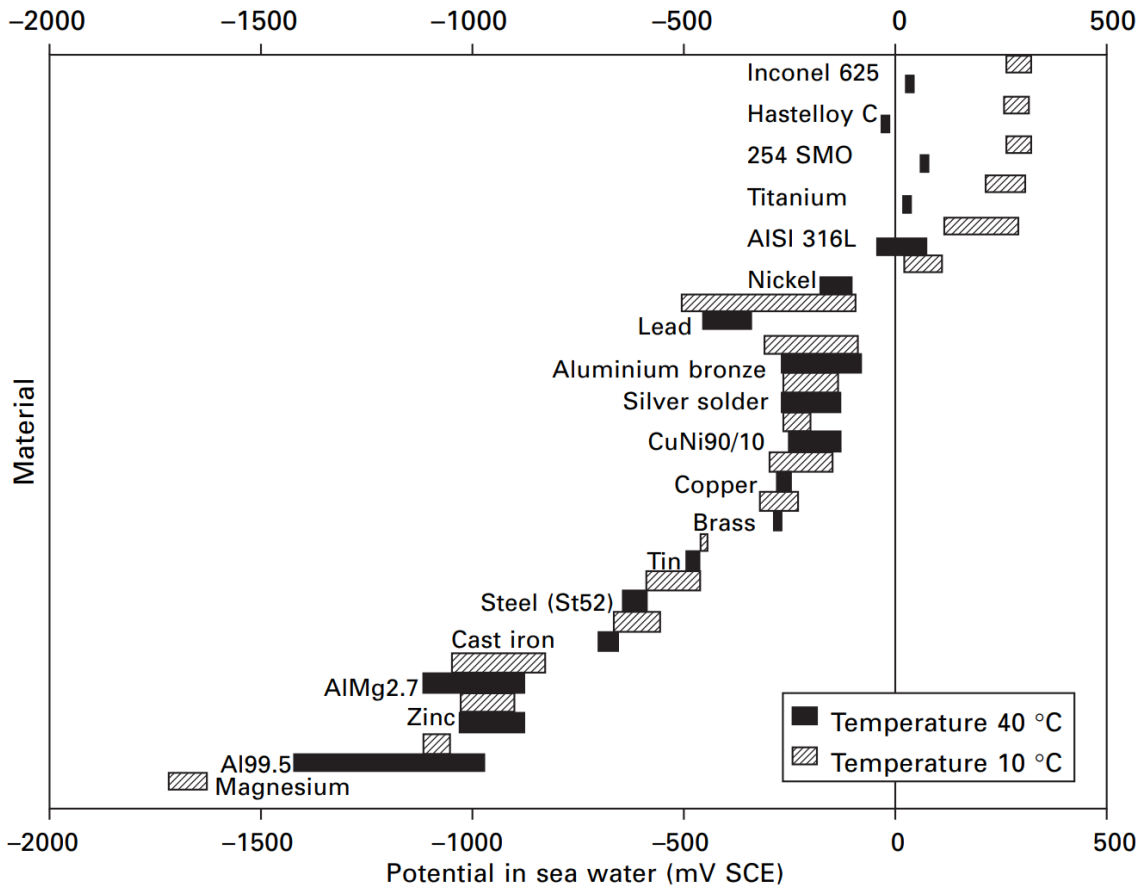



*Fig. 2-11 Galvanic series, containing AISI 316L (passive), in sea water at 10 and 40 ˚C [63].*

### 2.2.3. Mechanical Properties

As mentioned in section 2.2.2, austenitic stainless steels possess poor mechanical and tribological properties, yet they are still regularly utilised in applications where interacting surfaces (e.g. sliding motion) are unavoidable [64-66]. This uptake comes from their excellent resistance to corrosion attack, which often makes them the only steel material of choice for demanding applications. Austenitic stainless steels are by far the most widely used type of stainless steel, and within the food and medical industries, the AISI 304, 316 and 316L alloys

dominate. In terms of overall applications, the 304 alloys, which are for general use, are the most popular alloy, and account for almost 50% of the total austenitic stainless steel production [37]. However, in medical applications where direct long-term or permanent contact with the body is necessary, the AISI 316L alloys become the only acceptable choice capable of dealing with the harsh corrosive environments [42]. Similarly, the AISI 316/316L alloys are the only choice for low pH applications (e.g. acidic liquids) in the food industry [6]. Therefore, since these alloys are widely used, and currently irreplaceable for certain applications, it is important to understand the mechanical properties of the chosen material to enable better understanding of the performance, longevity and potential premature failures that may arise in service.

Relative to other steels, austenitic stainless steels are mechanically soft (≈ 250 Vickers Hardness (HV)), have a low fatigue limit (30% of tensile strength) and a low proof stress (170-310 MPa). Consequently, they are subject to a high degree of wearing, and therefore, show poor tribological properties [18, 30, 67, 68].

Although ASS alloys are generally regarded as having poor mechanical properties, they do still possess some desirable properties which make them ideal for specific applications. ASS have a good range of yield strengths (0.2-2GPa), good formability and good toughness [16, 28]. Moreover, ASS alloys are very versatile with respect to temperature, and are viable for use at both low (cryogenic) and high temperatures [37]. With reducing temperatures, ASS alloys become harder, and inevitably, lose ductility; however, even at the lowest temperatures possible (close to absolute zero), the ductility (and toughness) remains high. This is particularly true for the AISI 316L alloy and can be attributed to the increased stability of the austenite

phase, thus slowing the strain-induced transformation to the more brittle BCT martensitic phase (α') [69-71]. On the other hand, at high temperatures, ASS alloys are also superior in strength, corrosion resistance and oxidation resistance [72]. Their desirable strength at elevated temperatures arises due to their high temperature phase stability and high interstitial solid solubility, which improve the overall strength (particularly creep strength) in comparison to other forms of stainless steels. At high temperatures, where solution annealing and precipitate coarsening regularly proceed, alloys whose strength depends on the formation and retention of fine dispersed precipitates or cold work hardening suffer greatly, therefore meaning that interstitial solid solution hardening, which austenitic stainless steels excel at, becomes the beneficial form of hardening for high temperature applications. Additionally, the presence of the $Cr_2O_3$ passive film provides a sufficient barrier to both the external corrosive environment and to further uptake of oxygen. Ultimately, this has led to austenitic stainless steels finding many applications as super heaters, boilers, steam lines and heat exchangers [28, 73].

### 2.2.4. Tribological Properties

Tribology is the multidisciplinary science of surfaces interacting with one another under relative motion, and includes the studies of contact mechanics, friction, wear, and lubrication. Although each individual element within tribology has been studied for hundreds or thousands of years, the combined study of tribology is still relatively new, with the term having only been first used in 1966 [74]. Consequently, it is still a developing science, and some of the fundamental elements and testing approaches are still subject to regular change and debate.

Nevertheless, tribology is well established as an important science that, when well understood and optimised, can significantly reduce operating costs, decrease equipment downtime, and increase component longevity. Even with the current science and knowledge, tribology is still regularly poorly accounted for, and it is estimated to cost each country approximately 1.6 % of their total GDP (gross domestic product) as a result of inefficiencies. In 2008, in the US alone, this cost was estimated to be around $186 billion [75].

#### 2.2.4.1. Contact Mechanics

There are many different forms of contact that can occur between two surfaces, including point, plane, and plate contacts (Fig. 2-12). In application, the contact conditions are dynamic, and can change over time depending on many factors such as material properties, operating conditions, and surface geometries. Under elastic conditions, it is common to describe the contact using Hertz contact theory, which takes into account the Young's moduli and Poisson's ratios of the two materials, in combination with the contact area and force between them to give a stress distribution (Fig. 2-13). Equations 2-10 to 2-13 and Fig. 2-13 demonstrate how the stress distribution can be calculated for a point-on-plate contact, with $P_0$ denoting the maximum pressure, which arises at the centre of contact (x = 0) [74].

$$P(x) = P_0 \sqrt{1 - \left[\frac{x}{a}\right]^2} \qquad \text{(equation 2-10)}$$

where P(x) is the calculated pressure as a function of distance away from the centre (Pa), $P_0$ is the maximum Hertz pressure (Pa; calculated by equation 2-11), x is distance away from the point

of loading (m) and a is the radius of the circular contact area formed (m; calculated by equation 2-12).

$$P_0 = \frac{1.5 \cdot F}{\pi \cdot a^2} \quad \text{(equation 2-11)}$$

where F is the normal force applied to the surface (N).

$$a = \left[\frac{3 \cdot F \cdot R}{4 \cdot E}\right]^{\frac{1}{3}} \quad \text{(equation 2-12)}$$

where R is the radius of the spherical counterpart (m) and E is the ratio of elastic moduli to Poisson coefficient of the two materials (Pa; calculated using equation 2-13).

$$\frac{1}{E} = \frac{1 - \nu_1^2}{E_1} + \frac{1 - \nu_2^2}{E_2} \quad \text{(equation 2-13)}$$

where $\nu_1$ and $\nu_2$ are the Poisson coefficients of the sample and spherical counterpart, and $E_1$ and $E_2$ are the Young's moduli of the sample and spherical counter (Pa).

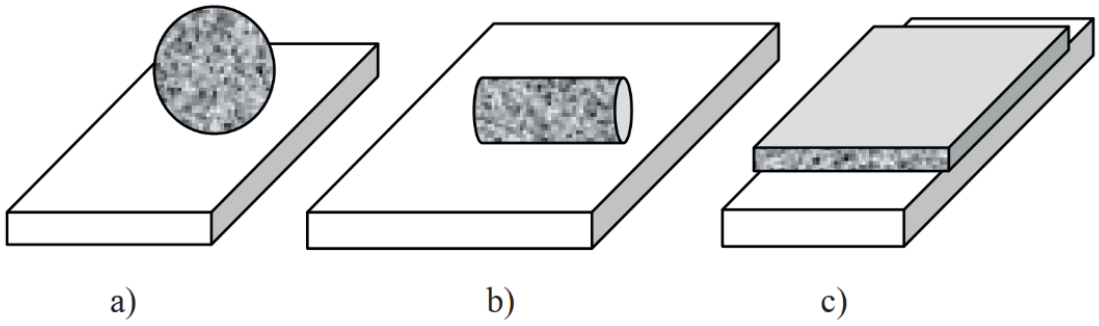



*Fig. 2-12 Different types of contact: (a) Point, (b) Plane and (c) Plate [74].*

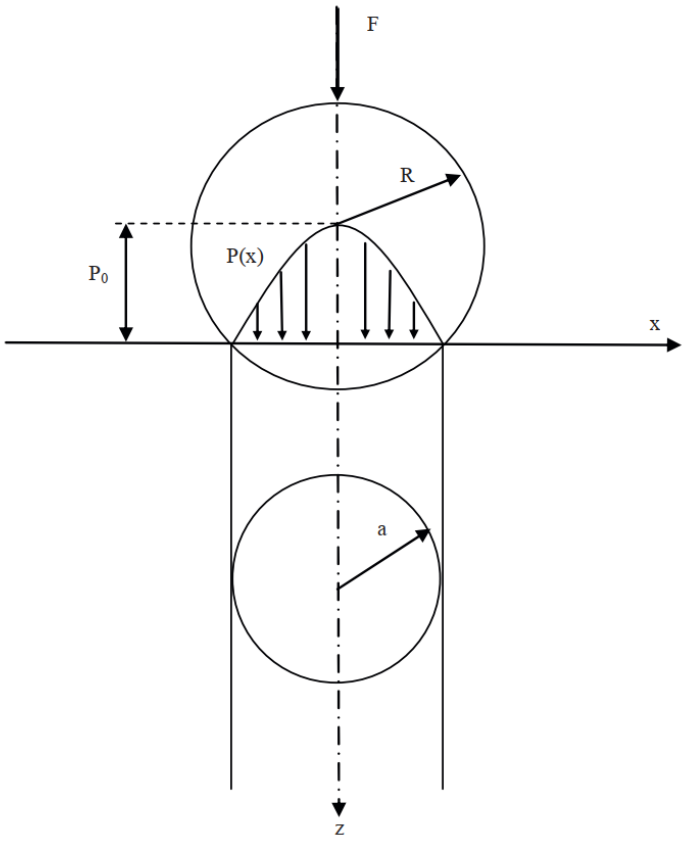



*Fig. 2-13 Ball-on-plate point contact with labelling for Hertz contact theory calculations [74].*

Although pure elastic deformation is uncommon in service, calculations of the maximum Hertzian contact pressures ($P_0$), beyond which plastic yield proceeds, can still give important information about material properties and feasibility for different applications [76]. This is a particularly useful concept for carrying out small scale analysis of material properties for high load applications, whereby realistic testing is expensive, especially if the material fails, or is lost, during/following testing. Therefore, using smaller contact areas and counterparts with high Young's moduli, it is possible to reproduce the initial contact stresses on samples, that resemble in-service conditions, with only moderate loads or risks of material loss. However,

care should always be taken to mimic the intended application environment (e.g. temperature, lubrication state), relative motion (e.g. unidirectional sliding, reciprocating sliding, rolling-sliding) and operating conditions (e.g. temperature, velocity, time, humidity). It should also be noted that the true contact area is different to the contact area typically used in the Hertzian contact calculations. This arises due to the inevitable plastic deformation of the material in combination with most of the force being distributed through small asperities at the surface. Consequently, the true initial contact stresses may be many orders of magnitude greater than expected, which is particularly prevalent with hard materials that can retain the structural integrity of the asperities for longer [76, 77].

#### 2.2.4.2. Friction

The resistance to movement of one surface over another is known as friction. Although friction can arise between, as well as within, all types of matter (e.g. gases, liquids, and solids), within this description, only friction between two solid objects, with or without lubricating agents, will be discussed. Friction is directly influenced by the surface topography, environment, and forces during motion. During frictional interactions, dissipation of the energy generates heat that can significantly change the subsequent lubricating environment (e.g. viscosity), material properties (e.g. phase changes), and surface topography (e.g. melting/deforming). In applications where the intended work is achieved through the movement of surfaces across one another (e.g. railway wheels on the railway track), friction can cause significant losses of energy, with estimations pointing towards 20 % of all energy consumption being used to overcome friction [58, 78]. However, in some cases, utilisation of the effects of frictions has created new application, such as friction welding, which intentionally produce and maximises

frictional interactions. In most cases though, more attention is paid to reducing or minimising friction, with lubrication being the most common approach [76].

The friction coefficient value of AISI 316L alloys can vary depending on the testing conditions (e.g. load, temperature, counterpart material, counterpart size); however, under room temperature conditions and dry lubrication, the stable friction coefficient value is typically found to be between 0.6 and 0.7 [64, 79, 80].

#### 2.2.4.3. Lubrication

As previously introduced in section 2.2.4.1, when surfaces are in motion against each other, the load is carried through asperities, leading to high tangential contact stresses, and giving rise to aggravated wear and damage. Through the use of a lubricant, which can take the form of a solid (e.g. silver), liquid (e.g. engine oil) or gas (e.g. air), it is possible distribute the applied stresses across a large surface (e.g. using hydrodynamic pressure), thereby effectively minimising localised wear and friction [76]. The phenomena described within this section will largely relate to liquid lubrication; however, in some cases the principles are universal.

Depending on the degree of lubrication, it may be possible to fully (thick-film lubrication) or partially (thin-film or mixed lubrication) separate two surfaces. Under severe thin-film conditions, only a molecularly thick film forms on surfaces (boundary lubrication), and therefore, the entire load is carried by the asperities. Wear can still occur even within a well lubricated system; however, the debris produced is typically reduced in size, and therefore able to be kept suspended in the lubricant, and away from the interacting surfaces [58].

The resistance to motion, i.e. friction within the contacting surfaces, also changes depending on the lubricating regime present. Under thick-film lubrication, friction is directly related to the internal shearing stresses of the lubricant, which is also known as the hydrodynamic friction. Under thin-film lubrication, the overall friction coefficient is a mixture of the hydrodynamic friction and the friction generated from the motion of the two surfaces against one another. Boundary lubrication, on the other hand, is a product of the dry friction between the surfaces (see section 2.2.4.2) and any thin film or surface adsorbed layer that may be present [58, 76, 81].

Depending on the tribological conditions, such as the load, speed, temperature, contact geometry or surface roughness, it may be possible for two sliding surfaces to change lubricating regimes over time [76].

#### 2.2.4.4. Wear

Wear, which is generally observed as mechanical fractures, permanent (plastic) deformation, oxidation/corrosion, or combinations thereof, of engineered materials, almost always persists in application and plays a significant role on the changing geometry of the contacting surfaces, the peak and overall distribution of stresses, and the lubricating conditions at the point of contact [76]. Many types of wear exist, with the classification of them depending on the dominant mechanisms involved. Types of wear can include, but are not limited to, abrasive, adhesive, fatigue, fretting, oxidative and corrosive wear [58, 81]. Austenitic stainless steels, in general, possess poor resistance to wear and are regularly subjected to all of these

mechanisms [66]. Due to the focus of this study, only abrasive, adhesive, and oxidative wear mechanisms will be discussed in further detail.

#### 2.2.4.4.1. Abrasive Wear

Abrasive wear arises when hard asperities or particles are forced to slide against the surface of a material. To achieve abrasive damage to the surface, rather than the particle itself, it is necessary for the particles to be harder than the material it is sliding against [81]. Therefore, in metals, abrasive wear typically involves the use of ceramic surfaces or particles. Depending on the type of contact, two modes of abrasion can occur: (1) two-body and (2) three-body wear [58]. In two-body wear, the abrasive surface/abradant is found within the two interacting bodies, and consequently, wearing is achieved through sliding motion. On the other hand, in three-body wear, the abradant acts as a third body within the interaction, and is characteristically subjected to rolling during the interaction (e.g. debris rolling between two sliding surfaces) [82]. Typically, two-body abrasive wear results in 10 to 1000 times greater material loss/damage in comparison with three-body wear. Additionally, each type of abrasion can also be classed as an open (free) or closed (constrained) system (Fig. 2-14). Given the relatively low hardness of austenitic stainless steels, this form of wearing is prevalent in application [76].

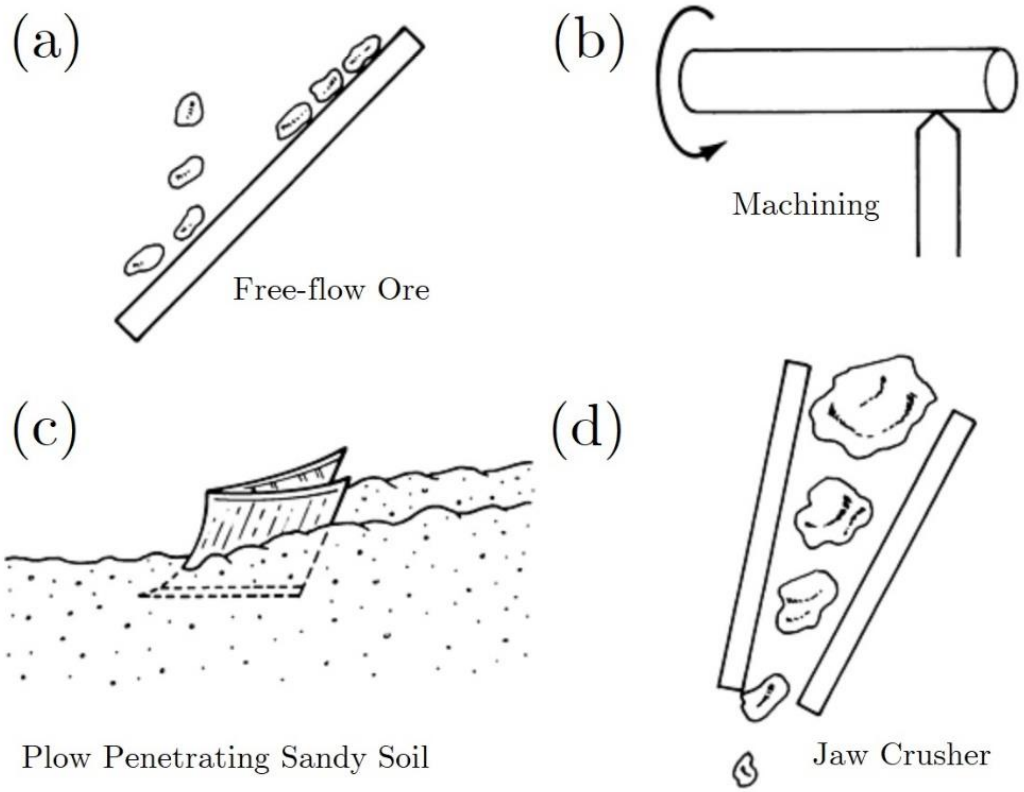



*Fig. 2-14 Contact types during abrasive wear: (a) open two-body, (b) closed two-body, (c) open three-body and (d) closed three-body [76].*

#### 2.2.4.4.2. Adhesive Wear

Adhesive wear occurs when there is localised bonding (i.e. solid-state welding) between two surfaces under relative motion, leading to plastic deformation of at least one of the surfaces. Transfer of material across the surfaces (e.g. shearing) can arise when the bonding at the interface is stronger than the bonding to the substrate. In these cases, the material is transferred from the softer surface to the harder surfaces [76, 81].

Given the need for plastic deformation and bond formation between the surfaces, soft metals such as austenitic stainless steels or aluminium alloys are particularly susceptible to this form of damage. In austenitic stainless steels, if the loads are light, then adhesive wear can be avoided due to the continuous reformation of the passive oxide layer, which acts as both a chemical barrier and a solid lubricant. However, under higher loads, this oxide layer is continuously disrupted, therefore allowing metal-on-metal contact to take place [58, 76].

Under high loads and poor lubrication, metallic materials can be subjected to galling, which is a severe form of adhesive wear. Galling typically presents with localised macroscopic material transfer through the formation of large surface fragments or protrusions. The terms scuffing and scoring are also closely related to galling, with the former characterising such damage occurring under lubricated conditions, while the latter describes similar damage in the form of long grooves [58].

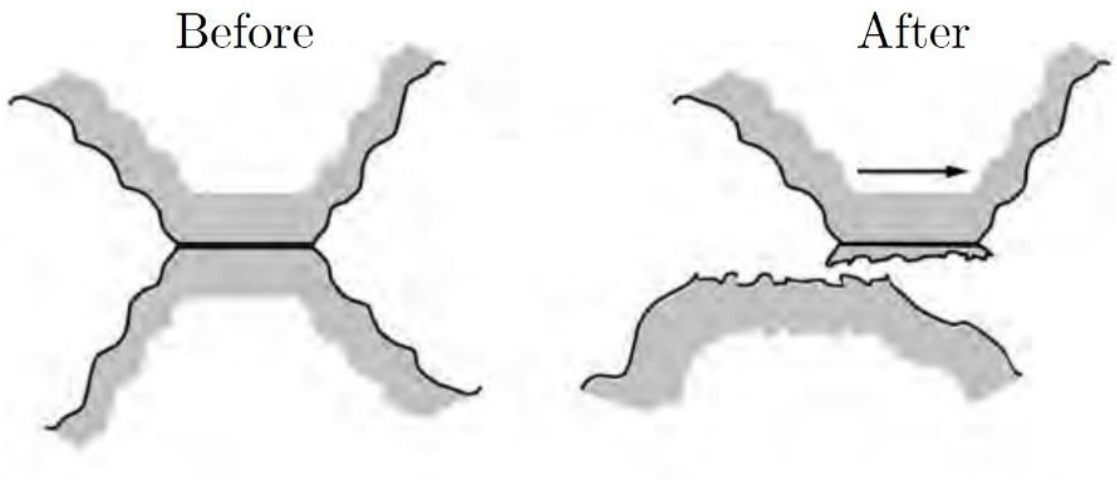



*Fig. 2-15 Adhesive wear mechanism [81].*

#### 2.2.4.4.3. Oxidative Wear

Tribo-oxidation is a common occurrence where surface oxides form in response to the elevated temperatures that develop when surfaces sliding against one another (e.g. due to friction; see section 2.2.4.2) [83]. This is a particularly prevalent phenomena on materials, such as austenitic stainless steels, that are readily oxidised or passivated. The formation and growth of these oxides increases the likelihood of break-off or delamination events, which give rise to oxidative wear [84]. However, unlike the previously described wear mechanisms, this form of wear is typically beneficial and can help to reduce both, the friction, and the volume of wear during contact [76].

### 2.2.5. Applications & Drawbacks

Resulting from their superior corrosion resistance, bio-inertness and excellent formability, austenitic stainless steels have become one of the most important materials used in the food and the medical industries [1]. They have found widespread applications as medical scalpels, bone saws, surgical sutures, bone fixation pins, pressure vessels, storage containers, cutlery, cutting tools and piping [2-6]. Although austenitic stainless steels alloys are currently the materials of choice for these applications, there are still some serious concerns with their use. The first concern relates to their relatively low hardness and poor wear resistance, which limits their longevity and requires regular in-service maintenance [7-9]. However, the largest worry is related to their high susceptibility to the attachment and growth of bacteria [4, 10, 11, 19]. It is thought that this arises due to the high surface free energy (and hydrophilic nature) of the materials, which attracts bacteria in a liquid medium to the surface and then allows chemical

and physical bonds to be formed [7]. These are obviously key issues within the food and medical industries as they lead to the contamination of foods, damage of equipment, food poisoning, infection of patients and, ultimately, death (see section 2.5.1) [19].

## 2.3. Surface Engineering

Surface engineering presents a convenient approach to overcoming one of the main concerns associated with the use of austenitic stainless steels alloys, their poor tribological performance, without compromising their advantageous bulk properties.

Surface engineering describes a group of technologies designed to alter the properties of a material at its surface, with the aim of producing long-lasting, sustainable and cost-effective engineered components. This can be achieved in a variety of ways, the three most common of which are: (1) to modify the substrate surface without altering the material chemistry (e.g. martensitic quenching), (2) to modify the surface through (thermo)chemical modification of the local chemistry of the substrate (e.g. nitriding), and (3) to introduce, or overlay, new materials to the substrate surface (e.g. diamond-like carbon coatings) [85]. The true benefit of surface engineering comes from the formation of a composite structure (bulk & surface material), with combined properties unobtainable by either material alone [86, 87].

As has been extensively discussed within this review (e.g. sections 2.2.2 & 2.2.4), it is frequently found that failure occurs due to issues with fatigue, wear, and corrosion, which can all be attributed to surface properties. The realisation of this has led to the recognition of surface engineering as a vital consideration throughout the development of engineering components [88].

One of the major strengths of surface engineering lies in the ability to alter the properties of a material to suit its application. In many situations this has helped to reduce the need for expensive bulk materials and allows them to only be used where they are essential [88]. This combination of attributes brings the potential to produce cost-effective and environmentally friendly products. The term environmentally friendly, in this case, applies to surface engineering due to the extension of the life cycle of a product, such that the extra energy necessary to treat the surface can be regained through a longer lifespan and/or more efficient energy usage during application [18, 88].

### 2.3.1. Classification

As previously mentioned, there are three main groups of surface engineering treatments. They can be categorised as: [85, 89]

1. Modification of the surface without change in chemical composition (e.g. martensitic quenching). These include thermal and mechanical hardening.
2. Modify the surface through (thermo)chemical modification of the local chemistry of the substrate. These include thermochemical treatments such as nitriding, carburising and nitrocarburising.
3. Coating of the surface. These include physical vapour deposition (PVD), chemical vapour deposition (CVD) and thermal spraying.

For the purpose of this review, only nitriding of austenitic stainless steels, with a focus on plasma nitriding, will be discussed in further detail within this review.

### 2.3.2. Nitriding of Austenitic Stainless Steel

The improvement in hardness and wear resistance of iron and steel alloys following nitriding has been known for more than 100 years. In fact, the first patent filed for a nitriding process was in 1908 by Adolph Machlet, who himself had already been working on this phenomenon for several years [90]. Since then, great effort has been put into optimising and adapting the process of nitriding. Variations of nitriding using gaseous and salt bath approaches were initially utilised, with the earliest use of plasma nitriding being in 1932 [91, 92].

Conventional nitriding involves the use of relatively high-temperatures that typically exceed 500 °C, and in some cases can reach up to 750 °C. This form of nitriding has predominantly been applied to ferritic and martensitic iron alloys, with little focus on austenitic alloys [93]. At these elevated temperatures, nitrogen in the treatment atmosphere can freely diffuse interstitially into the material to alloy the surface. Hardening is achieved through the precipitation of intermetallic nitrides (Fig. 2-16) such as γ' ($Fe_4N$), ε ($Fe_{2-3}N$), and chromium nitrides (e.g. CrN, $Cr_2N$), and unlike other hardening techniques (e.g. martensitic quenching), no phase changes take place (treatments are typically carried out below ferrite/austenite phase transformation temperature). Therefore, nitriding is a convenient surface engineering technology for the enhancement of the surface hardness of an alloy without considerable dimensional changes (due to phase changes) [58, 91].

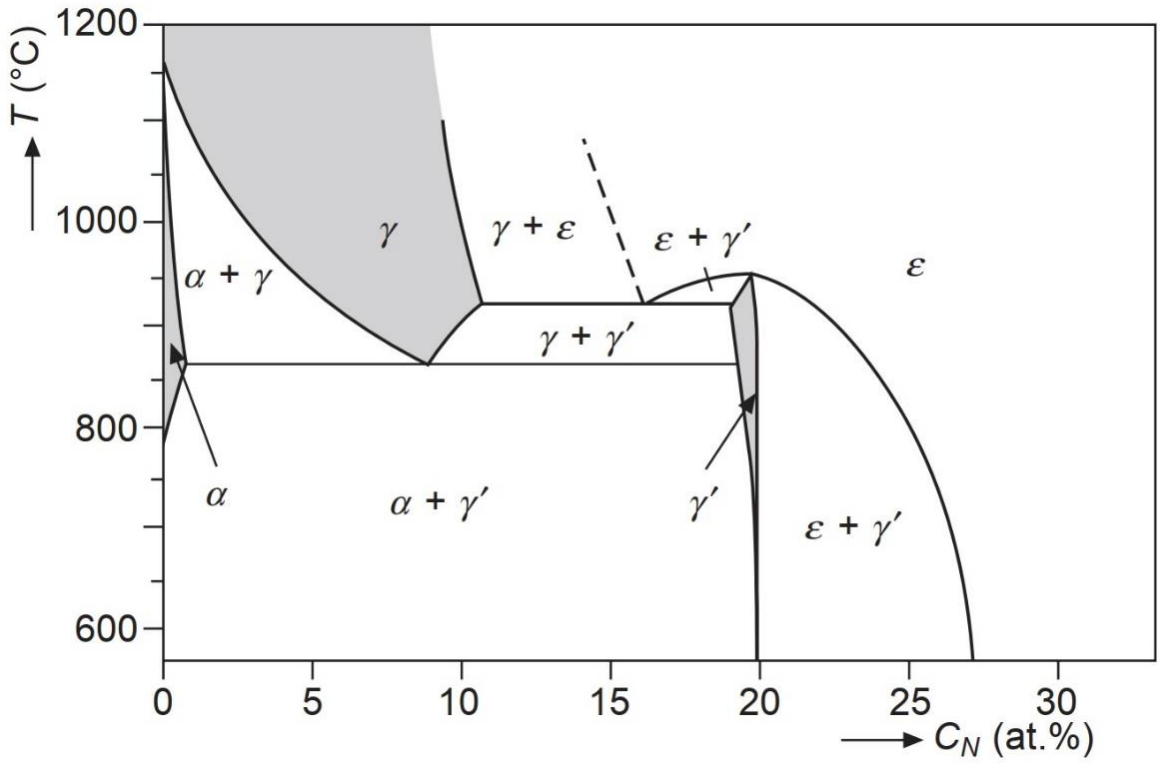



*Fig. 2-16 Fe-N phase diagram, where α is alpha ferrite, γ is austenite, γ' is $Fe_4N$ and ε is $Fe_{2-3}N$ [91].*

For ferrous alloys, other than stainless steels, nitriding can also help to improve the corrosion resistance of the surface through the formation of the stable corrosion resistant nitrides. Due to the appeal of nitriding, considerable efforts were made in the 1920s by researchers such as Adolph Fry to identify alloying elements that improved the quality and efficiency of the nitriding process. It was discovered that elements such as chromium, molybdenum, aluminium, vanadium and tungsten could improve the hardness of the treated surfaces by preferentially forming stable nitrides [92, 94].

However, given that the corrosion resistance of stainless steels comes from the retention of the chromium as a substitutional solid solution, rather than as a precipitate (as shown in Fig.

2-4), the formation, and promotion (from the high chromium content), of these nitrides presents a serious barrier to the traditional nitriding of austenitic stainless steel alloys [28, 91]. Fortunately, since the early 1980's a more promising approach to the surface treatment of austenitic stainless steel alloys has developed that involves the use of lower temperatures, typically around 400 to 450 °C, which enable the hardening of the surface without the loss of the corrosion resistance [8, 95]. In austenitic stainless steel alloys, this forms a new phase called the S phase, which will be discussed in more detail in section 2.4 [16, 17].

### 2.3.3. Plasma Nitriding

Plasma nitriding of austenitic stainless steel alloys involves the use of glow-discharge technologies, whereby surface hardening is achieved by accelerating ionised gases towards the workpiece [91]. Due to the interchangeability of the nomenclature involved in the process, plasma nitriding (as used within this study) is also regularly found to be labelled as ion nitriding or glow-discharge nitriding [92].

The first reported case of plasma treatment of materials was by Wehnheldt (first name unknown) in 1932; however, in this early nitriding work the glow-discharge formed was difficult to control. Stabilisation and improvements were subsequently made when Wehnheldt and Bernard Berghaus collaborated; eventually forming Klöckner Ionon, the first manufacturer of ion nitriding equipment (equipment from the same manufacturer used within this study; section 3.1.2) [96]. Plasma nitriding became a popular technique for German industrialists during the second world war, but it did not gain major widespread use outside of Germany until the 1970s [92].

Currently, plasma nitriding is a common place technology with specific advantages in comparison to other nitriding methods (e.g. gas & salt bath). One of the most profound benefits of plasma treatments is the ability to directly form the ionised gases necessary for the treatments using simple precursors such as nitrogen ($N_2$) gas, rather than decomposing or cracking gases (e.g. ammonia for gas nitriding) [58]. In addition to not requiring harmful gases to perform the treatments (such as the cyanides used in salt bath nitriding), plasma nitriding only requires comparatively small quantities of gases, as well as, releasing only simple, environmentally friendly, gases such as nitrogen and hydrogen as by-products into the environment; therefore, plasma nitriding is typically labelled as a green technology [91, 97]. Ultimately, the drive towards the use of "greener" and more environmentally friendly technologies has continuously increased the industrial uptake of plasma nitriding [92].

The other benefit of using plasma, as the treatment medium, comes from the bombardment of surfaces with the reactive ionised gases, which act to clean (remove grease & dirt) and activate (remove passive oxide layer) the surface during treatment, thereby bypassing many pre-processing steps associated with other techniques (e.g. surface activation and cleaning for gas nitriding). Consequently, the total processing times for plasma nitriding are often significantly lower than gas nitriding. Moreover, since the mixture of gases introduced and the electrical power used during treatments can be regulated and modified, plasma nitriding also enables more uniform treatment of the surface. Consequently, there is better control and repeatability over the final surface chemistry of plasma nitrided workpieces, therefore allowing for excellent control over the final workpiece dimensions [85, 91, 92].

Additionally, the reactive nature of ionised gases has created opportunities for potential applications aiming to form specific chemical compounds or reactions, in the treatment atmosphere or on the surface of materials, at significantly lower temperatures than other methods, or in some cases, with chemistries not possible using other techniques [98]. This advantage has recently increased the uptake of plasma surface treatments for a wide range of other materials and purposes, including the treatment of polymer materials [99], functionalisation of surfaces (e.g. carbon fibres) [100], plasma texturing [101], treatment of thermally sensitive materials using non-thermal plasma [102-104], and modification of materials using atmospheric glow-discharge plasma [105].

#### 2.3.3.1. Glow-Discharge Phenomena

The ionisation of gases to form a conductive medium between two physically separated electrodes forms the basis for all plasma treatments (Fig. 2-17). Plasma, which is generally regarded as the fourth state of matter, itself is comprised of a mixture of ionised gases, electrons, active species (e.g. radicals, excited atoms), neutral atoms, and molecules [85]. To form a stable plasma, it is necessary to both, initiate ionisation events, and maintain a constant degree of ionisation between two electrodes. This can be challenging at atmospheric pressures, since the mean free path of an ionised molecule is small, and therefore, the ion cannot gain enough momentum prior to colliding with another molecule in the atmosphere to induce another ionisation event [92]. At lower pressures, typically in the region of 0.1 to 5 mbar (10 to 500 Pa), the mean free path becomes large enough to create a sustained plasma between the electrodes (Fig. 2-18) [91, 98]. The ability to further ionise molecules and create

a cascade of ionisation events that help to form a self-sustaining plasma is known as the Townsend avalanche (Fig. 2-19) [106].

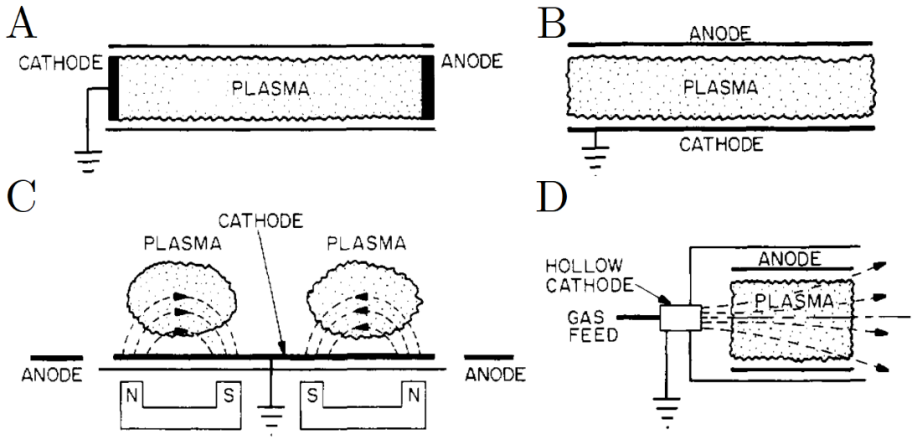



*Fig. 2-17 Types of DC glow-discharge: (A) DC electrical discharge tube, (B) parallel plate plasma reactor, (C) co-planar magnetron reactors and (D) co-axial electron bombardment discharge chamber [98].*

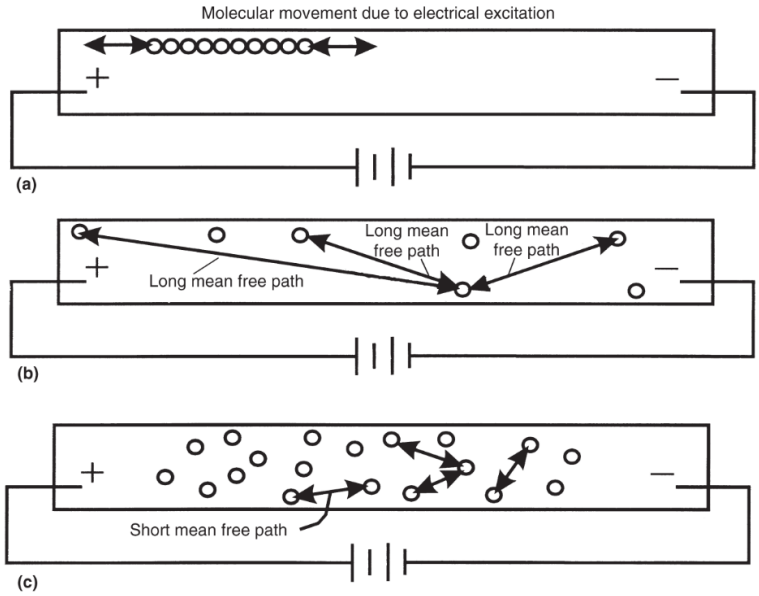



*Fig. 2-18 Influence of pressure on the formation and stabilisation of plasma. (a) At atmospheric pressure there is almost no mean free path for molecules. (b) At very low pressures (e.g. 0.0001 mbar (0.01 Pa)) there is a very long mean free path but limited gas molecules to collide with to create sustained usable plasma energy. (c) At low pressures (e.g. 0.1 mbar) the gas molecules have a sizable mean free path and plenty of molecules to collide with, and therefore form a usable plasma energy [92].*

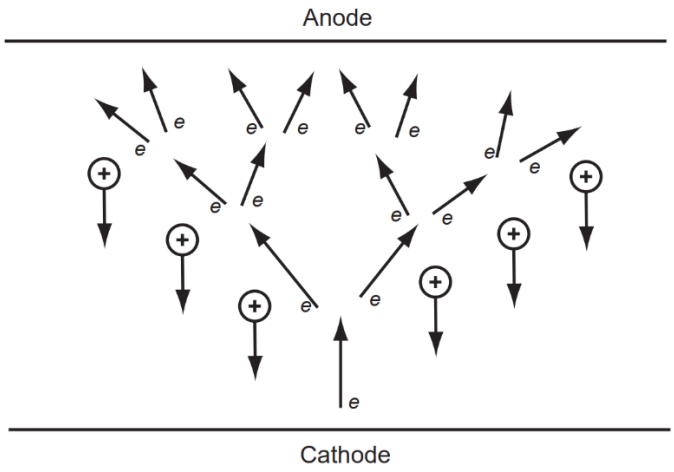



*Fig. 2-19 Townsend avalanche event with cascades of electron-induced ionisation events [106].*

Analysing the Paschen curve (Fig. 2-20) of plasma formed at low pressures can give an insight into the associated occurrences and physical principles involved. Due to the significantly lower mass of electrons, they are influenced by the electric field to a much greater extent than ions, and therefore, act as the primary source for ionisation events. Going from left to right on Fig. 2-20, reveals the mechanisms behind the formation and maintenance of the plasma. The first region is the background ionisation region (A to B), whereby free ions and electrons (largely present due to cosmic background radiation) in the working atmosphere are accelerated to the cathode and anode, respectively, once a potential difference is applied between them. At this stage, the electrons do not have enough energy to start a Townsend avalanche event, and therefore, the plasma is still not self-sustaining. In the saturation region (B to C), the effect from the free ions and electrons reaches a maximum; however, the electrons still do not possess enough energy to initiate new ionisation events within this regime. Consequently, new electrons and ions are only formed due to background cosmic radiation, and so the current

density does not increase in this region. Within the Townsend regime (C to E), the electrons begin to acquire enough energy before collisions to overcome the Townsend breakdown barrier, and therefore, an exponential increase in current density is observed (C to D). Between D and E, the electrodes voltage begins to reach the breakdown voltage ($V_B$) at asperities or sharp corners, and consequently, neutral gases in the working environment close to the electrodes are ionised directly by the electrodes (known as a corona discharge). Other than the corona discharge and individual electrical breakdown sparks, the regimes up to this point are not visible to the naked eye, and are thus labelled as dark discharges [98].

At point E, the breakdown events reach a critical quantity to enable the plasma to be visible to the naked eye, hence the name glow-discharge is given to this plasma regime. Between E and F, the ionisation events at the electrodes act to dissipate the charge that builds up on them, therefore leading to a reduction in potential difference (voltage) with increasing current density. At point F, corona discharge at the asperities of the cathode become saturated and the voltage stabilises. The saturation at the cathode, before the anode, can be explained by the distribution of the electrons and ions within the plasma leading up to this region (Fig. 2-21), whereby the ions density at the cathode outnumber the electron density at the anode. Therefore, beyond this point the regime/state of the plasma is determined by the conditions present at the cathode [106]. Further increases in current density (F to G), act to spread the breakdown events on the cathode, beyond the most profound asperities or corners, leading to the voltage remaining constant. At point G, the cathode becomes fully saturated with ionisation events and is completely covered by the plasma. Between G to H, the breakdown events at the cathode are unable to prevent charge build-up, and therefore, further increases

in current density result in an increase in potential difference (known as the abnormal glow-discharge region). Plasma nitriding is typically carried out within this abnormal glow-discharge region, which allow for complete plasma coverage on workpieces to be treated and close control of the plasma density and power throughout the treatment [92]. The regions going from F to F' to D, which completely bypass the corona regions, relate to the hysteresis (due to the plasma already being ignited at both sharp corners/asperities and flat surfaces) when reducing the current density (if starting at point F). Incandescent heating of the cathode (due to ion bombardment) is achieved at point H, and between points H and I a transition of glow-to-arc discharge begins [98].

Between points H and J, a proportional drop in voltage is seen in response to an increase in current density ($V \propto {}^{1}/_{I}$), which arises due to the occurrences of arc discharges that release significant charge build-up per discharge. While the voltage is reducing, the arc discharge plasma that forms is in a non-equilibrium state, i.e. the kinetic energy (temperature) of the working gas, ions and electrons are not the same, and therefore this region, between points H and I, is known as the non-thermal arc discharge region. Once the voltage begins to increase with increasing current density, the temperature of the gas, electrons and ions is in an equilibrium state, and the plasma is labelled as a thermal arc discharge [98, 106].

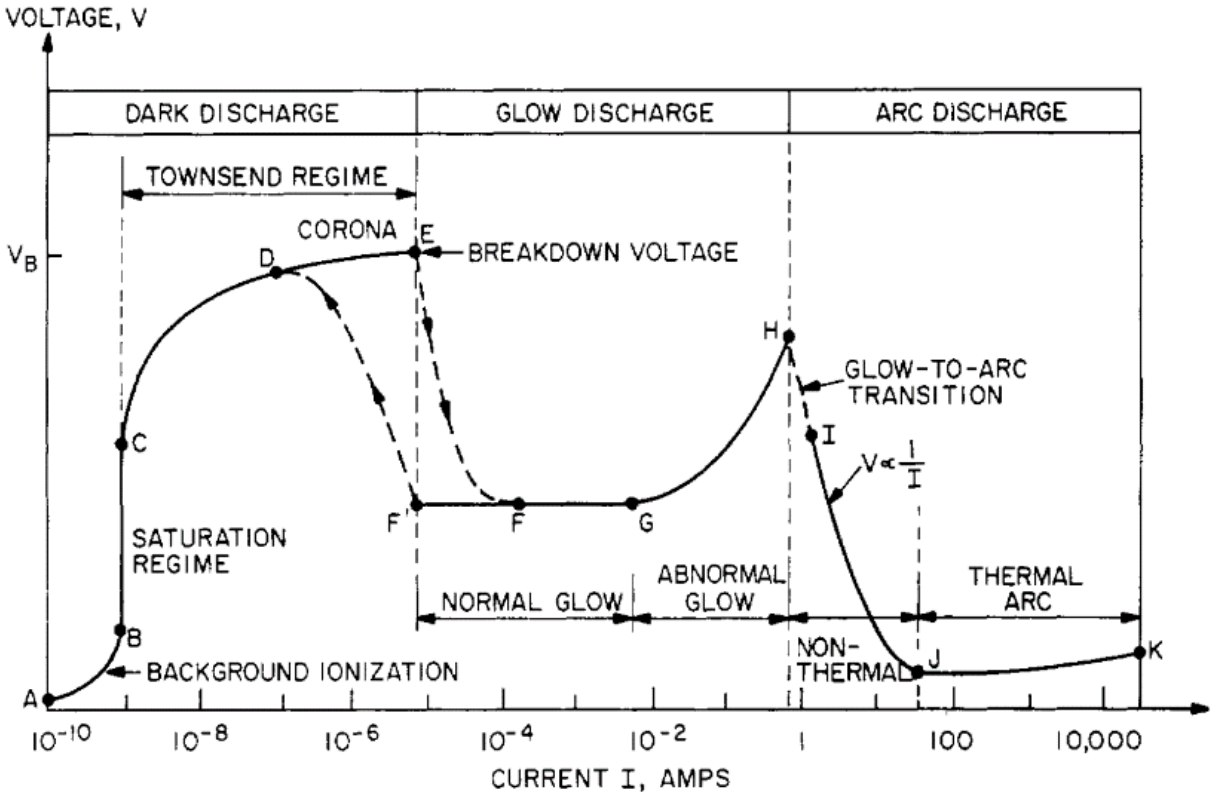



*Fig. 2-20 Paschen curve of the voltage to current density relationship for low pressure DC plasma discharge. [98].*

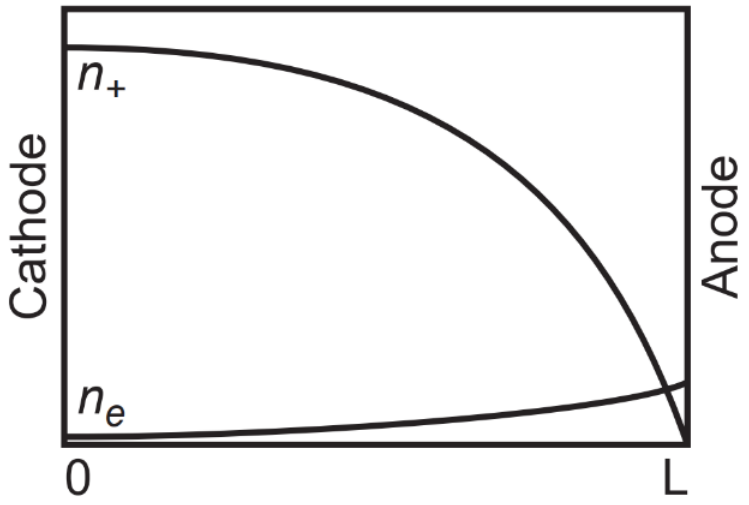



*Fig. 2-21 Electron and ion distributions across the electrodes in the dark discharge plasma regimes [106].*

#### 2.3.3.2. DC Plasma Nitriding

Under direct current (DC) plasma nitriding conditions, the heating and diffusion of interstitial elements into the sample surfaces is achieved through direct plasma bombardment (Fig. 2-22). Samples treated under these conditions are subjected to a cathodic potential, and are therefore required to be electrically conductive [85]. Heating is achieved through the transfer of kinetic energy following ion bombardment of the sample surface, which simultaneously also acts to clean the surface (section 2.3.3) and bring the nitrogen ions. The most widely accepted theory for the dominant mechanism for the adsorption and diffusion of the nitrogen ions into the surface involves the introduction of nitrogen through the formation varying forms of iron nitrides ($Fe_xN$; Koelbel's model) [92, 107, 108].

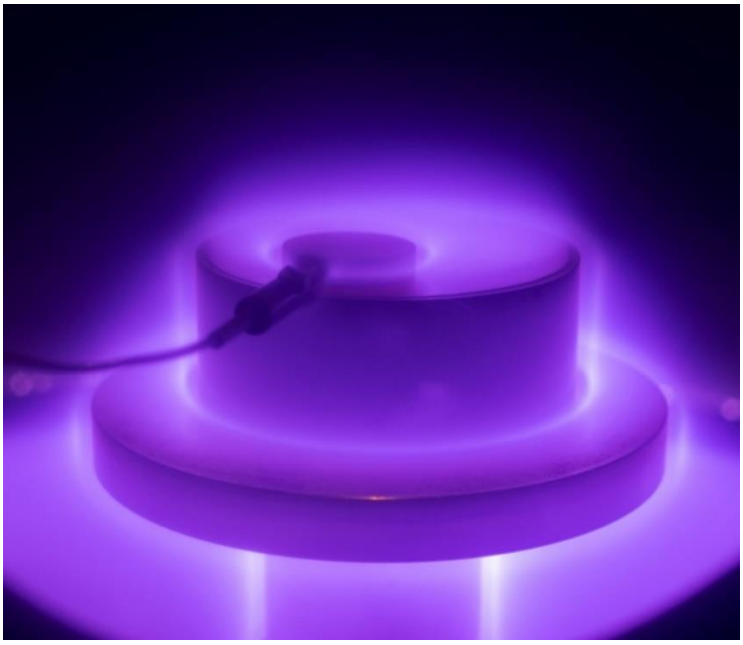


*Fig. 2-22 Glow-discharge formation in a typical DC plasma nitriding treatment.*

Koelbel's model (Fig. 2-23) follows that acceleration and bombardment of the ionised nitrogen atoms to the sample surface have the effect of dislodging material at the surface of the workpiece. The release of the matter through this process is known as sputtering, and within plasma nitriding, this has the effect of removing contaminants, as well as alloying elements at the surface of the workpiece. Vacuum pumping down then acts to remove the released matter from the furnace atmosphere. However, not all material can be removed, and some material is then back-sputtered and adsorbed as loose material onto the sample surface. Bombardment of the sputtered particles with nitrogen ions in the nearby atmosphere leads to the formation of FeN. Continuous sputtering, back-sputtering and bombardment with nitrogen ions leads to instabilities in the FeN, and breakdown to ε ($Fe_{2-3}N$) and γ' ($Fe_4N$) follows. Ultimately, nitrogen is then introduced into the surface through the formation of iron/nitrogen diffusion zones [92, 109].

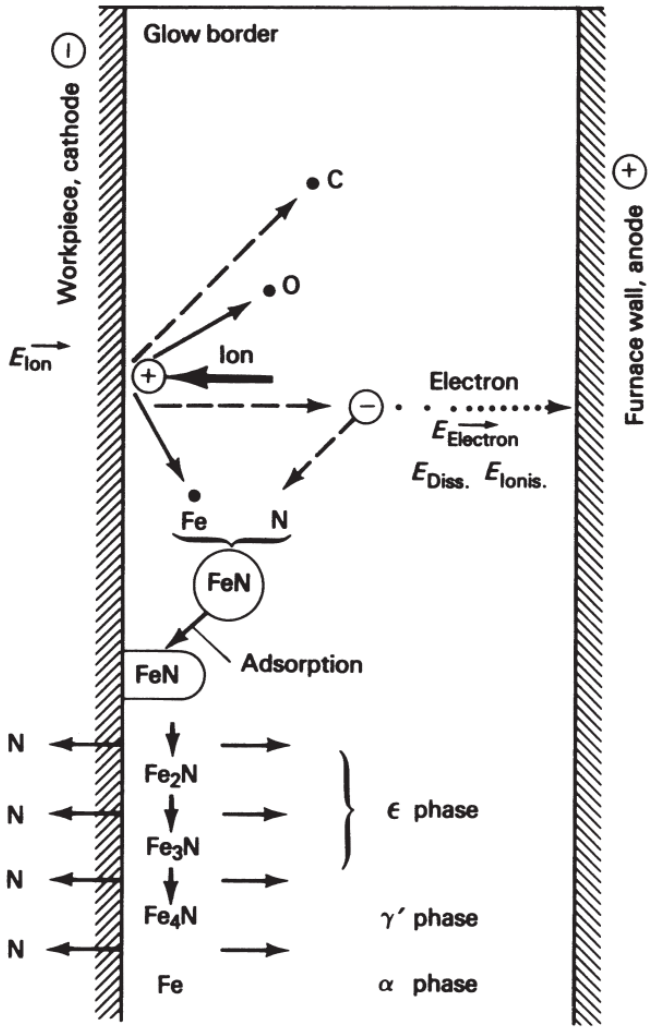



*Fig. 2-23 Koelbel's model for the DC glow-discharge plasma nitriding of ferrous alloys [92].*

### 2.3.3.3. Problems Associated with DC Plasma Nitriding

Despite possessing the already mentioned advantages of plasma nitriding (see section 2.3.3), DC plasma nitriding does suffer from some inherent shortcomings, such as direct arcing on samples (as explained in section 2.3.3.1), formation of edge effects, inhomogeneous heating of samples and hollow cathode formations [92].

Edge effects and inhomogeneous heating of samples are due to the increased current (therefore thermal energy) and bombardment density (therefore increased nitrogen diffusion) at sharp corners of material subjected to a DC glow discharge plasma (due to multiple faces of the glow-discharge contributing to the same area) [92, 94, 109, 110].

If two surfaces subjected to a glow-discharge plasma are gradually brought together, then the negative glow (Fig. 2-24) of each individual surface will eventually overlap and form an area of increased current density containing a high number of energetic electrons. The energetic electrons are produced from each cathodic surface and accelerated towards the negative glow region with limited inelastic collisions. This high density of electrons, combined with the significant photoemissions from the nearby cathodic surfaces, leads to a high level of ionisation events within the overlapping regions. Consequently, the hollow cathode region has a local temperature much higher than the normal negative glow (current densities 100-1000 times greater, with no change in voltage). The name hollow cathode originates from the formation of this effect in the hollow portion of cylindrical materials subjected to low pressure glow-discharge plasmas. However, this effect can also arise at sharp corners or blind holes, and acts to increase edge effects [92, 106, 111].

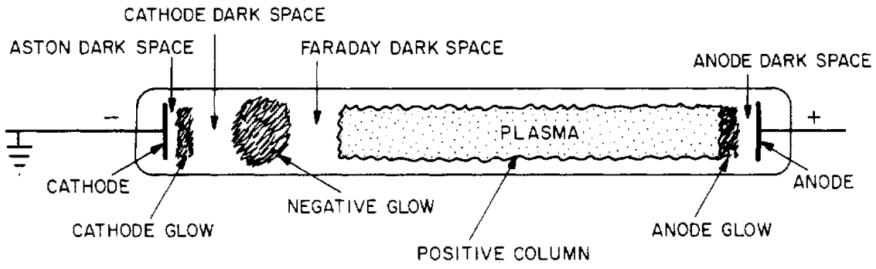



*Fig. 2-24 Schematic drawing of the regions of normal glow-discharge plasma [98].*

#### 2.3.3.4. Active Screen Plasma Nitriding

To overcome the problems associated with DC plasma nitriding of austenitic stainless steel samples, a new type of plasma treatment was discovered in the early 1990s, known as active screen plasma nitriding (ASPN) [112]. ASPN is a modified approach to DC plasma nitriding, whereby, instead of bombarding the samples directly with the ionised gases, an austenitic stainless steel mesh cage and lid (active screen; typically the same alloy as the specimens) are subjected to the cathodic potential instead (Fig. 2-26) [113, 114]. Consequently, in ASPN treatments, the workpiece is typically left at a floating potential (no charge) or is subjected to a small negative potential (bias), while the active screen is subjected to a strong cathodic (negative) potential. When the glow-discharge forms, the sputtering, edge effects and inhomogeneous treatment that the workpiece would typically undergo during DC plasma nitriding, are instead present on the active screen (Fig. 2-25). This provides multiple benefits, including: (1) surface damage of the workpiece is effectively avoided (e.g. no direct arc formations), (2) electrically insulating materials (e.g. polymers) can be treated/functionalised [99, 100], (3) inhomogeneous heating due to edge effects and hollow cathodes only occur on the active screen, and (4) the workpiece is heated more uniformly through thermal radiation from the active screen [110, 115, 116]. Active screens used in ASPN treatments typically contain mesh structures, which act to improve the heating efficiency and increase the production of active nitrogen species through the deliberate formation of hollow cathodes on the active screen (Fig. 2-27). It has been proposed that the mass transfer of nitrogen into the samples is achieved through the formation of $Fe_xN$ and active nitrogen species on the active screen (through sputtering and hollow cathode effects), and then delivery of these products

to the sample surface enables adsorption, followed by dissociation and diffusion into the workpiece [109, 113, 117-119].

The two main drawback of active screen plasma nitriding are: (1) the limited surface cleaning that is possible, especially under floating potential, which result in the need to clean/activate surfaces before treatment, and (2) some line of sight issues during treatments, especially under floating potential conditions [120].

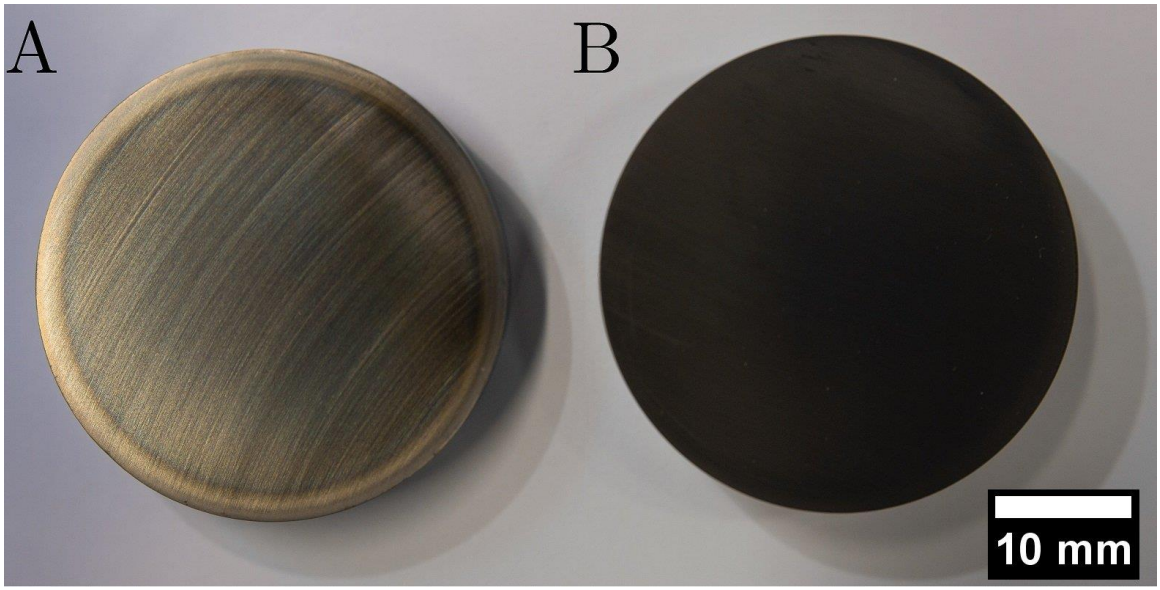



*Fig. 2-25 Typical surface morphology after (A) DC glow-discharge nitriding and (B) active screen plasma nitriding. The edge effects are prevalent in DC plasma nitriding, while uniform treatment is seen in active screen plasma nitriding. Material in image is M2 tool steel.*

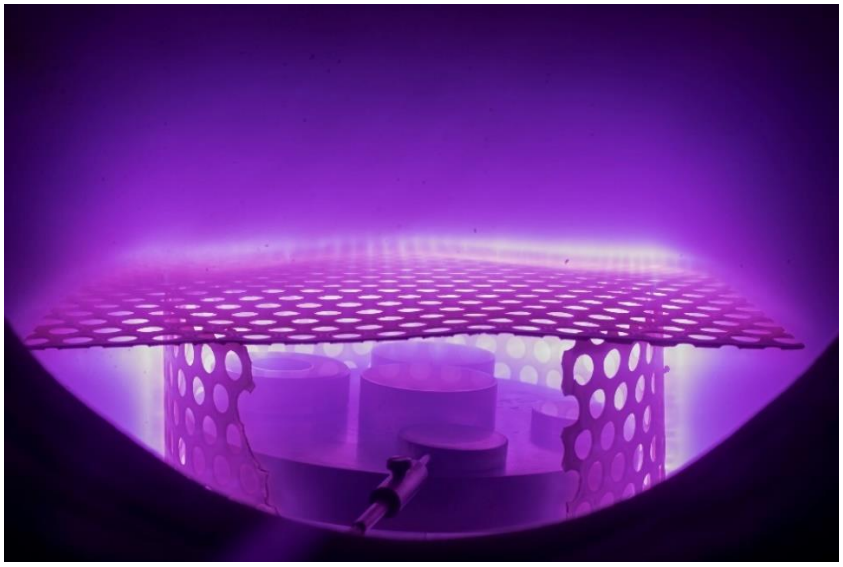


*Fig. 2-26 Active screen plasma nitriding of steels. Samples inside the mesh cage (cathodic potential) were at a floating potential. Core temperatures were measured during treatment using a thermocouple inserted into a dummy sample.*

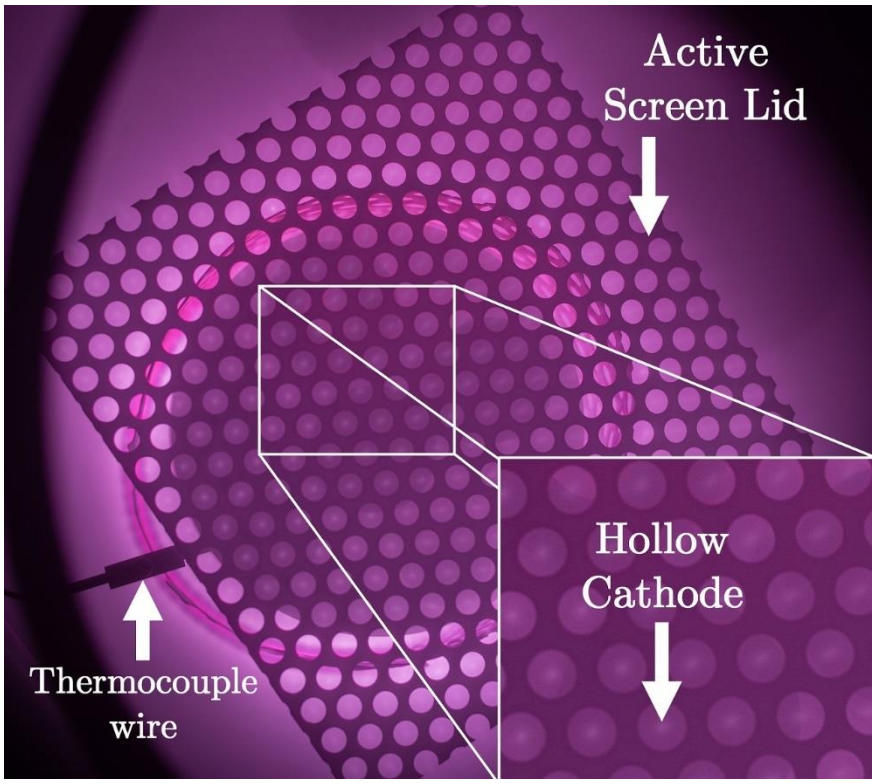



*Fig. 2-27 Hollow cathode formation on active screen.*

## 2.4. S Phase

The S phase, sometimes referred to as expanded austenite or $\gamma_N$ or $\gamma_C$, is used to describe a layer that forms on austenitic stainless steel, Co-Cr and Ni-Cr alloys following low-temperature nitriding, carburising or nitrocarburising (Fig. 2-28) [87, 121]. The discovery of the S phase dates back to the early 1980's, where the first journal articles relating to its existence were simultaneously published by Zhang and Bell [16] and Ichii *et al.* [17]. However, interest in low-temperature hardening had already begun to grow several years earlier, with work being published noting the formation of a white etchant resistant layer following low-temperature carburising by Kolster [122].

During early characterisation of the S phase layer, which was formed on AISI 316 [16] and 304 [17] ASS, it was discovered that the X-ray diffraction (XRD) patterns following nitriding treatment were shifted from the indexed austenite peaks (most notable the γ(111) and γ(200) peaks) to lower 2θ positions. Subsequently, these new peaks were, and still are, typically labelled as the S1, corresponding to γ(111), and the S2, corresponding to γ(200), peaks, respectively. Although the most profound peaks are the S1 and S2, it should be noted that the peak shifting is observed for all XRD peaks following S phase surface treatment of austenitic stainless steels (Fig. 2-29) [91].

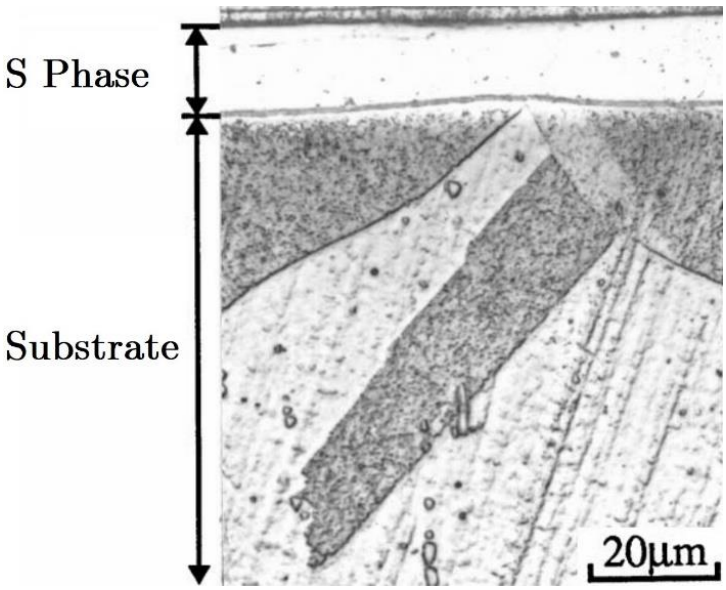



*Fig. 2-28 Optical micrograph of 450 °C plasma nitrided AISI 316 ASS for 5 hours [123].*

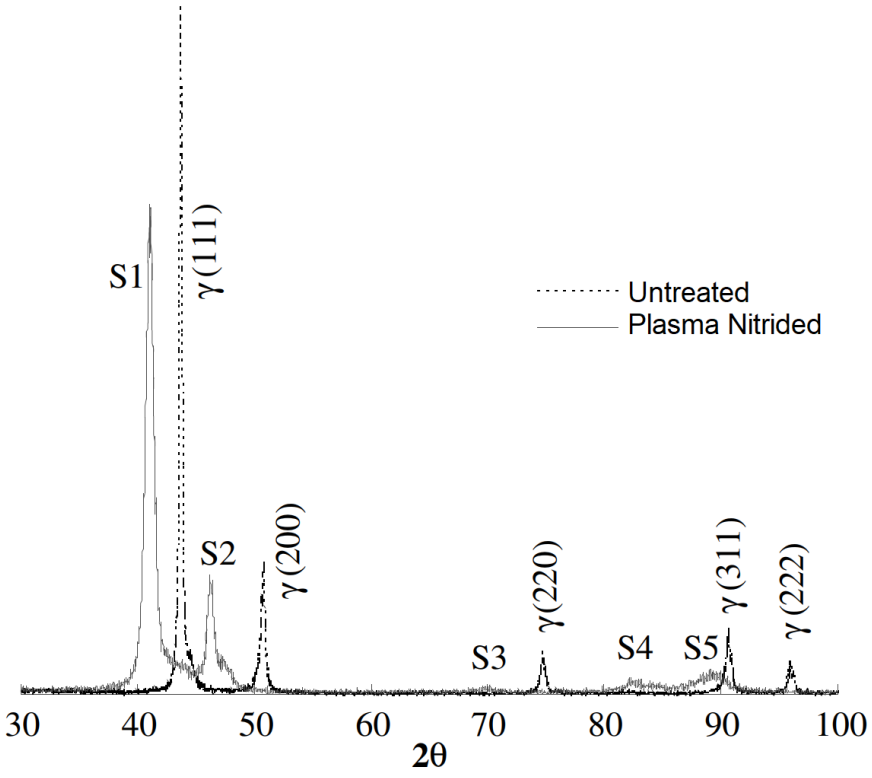



*Fig. 2-29 XRD patterns following active screen plasma nitriding of AISI 316 ASS for 20 hours at 420 °C [115].*

### 2.4.1. Formation

In principle, the S phase is a supersaturated solid solution containing nitrogen and/or carbon that work to form either a nitrogen S phase (nitriding), carbon S phase (carburising) or superficial nitrogen following by deeper carbon S phase (nitrocarburising). The major characteristic of the S phase is the significant hardening of the surface with no appreciable loss of corrosion resistance [8]. For the purposes of this study, only nitrogen S phase formed on austenitic stainless steels will be discussed; however, many of the characteristic and formation methods are similar between all forms of the S phase.

To form the S phase, it is necessary to use lower temperatures, typically below 450 °C, in comparison with traditional nitriding (typically above 500 °C), which enables the hardening of the stainless steel surface without the loss of the corrosion resistance [8, 95]. The principle behind this type of hardening is that, at lower temperatures, interstitial elements (e.g. nitrogen) can freely diffuse into the surface, but the activation energy required for substitutional elements (e.g. chromium) to move and combine to form the stable nitride (and/or carbide) precipitates is not readily achieved, and therefore these elements are essentially immobile for the duration of the treatments (i.e. paraequilibrium diffusion) [91, 124]. Subsequently, this promotes the interstitial supersaturation of the surface with nitrogen (Fig. 2-30) and leads to effective solid solution hardening [8].

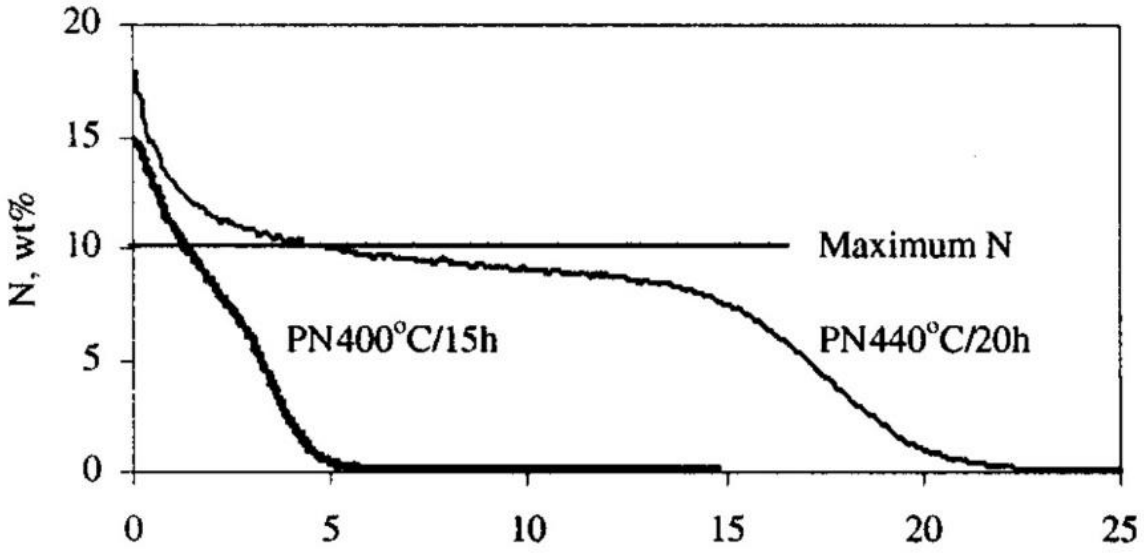



*Fig. 2-30 Elemental depth profile of nitrogen following plasma nitriding treatment of AISI 316 at 400 °C for 15 hours and 440 °C for 20 hours. Line labelled maximum N denotes the approximate maximum possible nitrogen solid solubility in austenite [125].*

The growth and supersaturation of the S phase has been a subject of intense experimental and analytical studies [87]. Although no universally agreed mechanisms have been developed thus far, the most compelling and widely used theory suggests a trapping and detrapping approach involving [126-129]: (1) the temporary locking of nitrogen atoms in the octahedral interstitial spaces of the FCC lattice as a result of the affinity between nitrogen and chromium, (2) the introduction of new nitrogen atoms that have a detrapping effect on the initial pre-existing nitrogen atoms, (3) the movement of the pre-existing nitrogen atoms into active tetrahedral interstitial spaces utilised to diffuse to new sites, and then finally (4) the occupancy of a new octahedral interstitial space. This combination of steps is assumed to play an important role on the supersaturation of the S phase (both lateral and through-depth movement of nitrogen atoms), as well as, to reduce the activation energy necessary for nitrogen mobility.

Consequently, this enables supersaturation, with up to 38 atomic percent of nitrogen, which is much greater than the maximum nitrogen equilibrium solid solubility in austenite (8.7 at%), and leads to the expansion of the lattice and formation of residual stresses and plastic deformation [123, 130-137]. The S phase can be characterised by left shifting (lattice expansion) and broadening of the austenite peaks (residual stresses and plastic deformation) within XRD patterns to lower 2θ values that correspond to ≈ 8 % expansion of the lattice parameter (Fig. 2-29) [8].

### 2.4.2. Metallurgical Characteristics

One of the most profound features of the S phase is its precipitate-free nature, which acts to retain the corrosion resistance of the alloy following surface treatment. In fact, it is generally accepted that the S phase surface layer possesses enhanced resistance in comparison with the untreated austenitic stainless steel. This phenomenon is most clearly seen following etching of a treated material, whereby the S phase treated layer presents as a featureless bright white layer, while clear topographical features are present on the untreated material (Fig. 2-28).

As previously mentioned in sections 2.1.3 and 2.3.2, the formation of chromium nitrides has the effect of developing areas of the alloy matrix depleted of chromium (Fig. 2-4), below the levels necessary for uniform surface passivation (i.e. stainlessness), and therefore a loss in corrosion resistance. Hence, it is paramount for the success of any S phase treatment to avoid the formation of such detrimental precipitates [115].

The exact structure, and degree of expansion, of the austenite phase following the formation of the S phase is still a subject of scientific debate. XRD and TEM analysis have both helped to

clarify (e.g. prove it is still an FCC austenite phase) and create new questions (inhomogeneous distortion) on the state of the S phase layer [123]. Crystallographic analysis has indicated that, unlike the untreated austenite in ASS, the S phase does not contain an ideal FCC structure. Instead, it has been found that plastic deformation, in the form of stacking faults, dislocations and microtwinning, develops during the formation of the S phase [138]. The influence of plastic deformation on the inhomogeneous distortion of different crystal planes is well documented, and assumed to play a role on the observed inhomogeneous shifting and peak broadening in S phase X-ray and electron diffraction analysis (Fig. 2-29) [139, 140].

Although the S phase was originally assumed to be an ideal solid solution (homogeneous interstitial occupancy), recent investigations in the last two decades have cast doubt on this, with findings of short range ordering (SRO; nearest neighbour positioning) between nitrogen and chromium having been observed. The chemical attraction between chromium and nitrogen, brought about by the potential formation of stable chromium nitrides (Fig. 2-31), is well-established, and thought to play an important role in both the formation (trapping and detrapping; see section 2.4.1) and ordering within the S phase [91, 140].

Studies using extended X-ray absorption fine structure (EXAFS) spectroscopy have shown non-uniform distribution (SRO) of nitrogen atoms across interstitial octahedral sites, with strong tendencies for nitrogen atoms to be found in nearest neighbour positions to substitutional chromium atoms, typically occupying 5 out of 6 of the interstitial nearest neighbour sites in S phase layers with maximum nitrogen compositions (Fig. 2-32). Additionally, denitriding of the S phase has also revealed preferential removal of nitrogen at sites adjacent to iron or nickel (Fig. 2-32) [140, 141]. X-ray photoelectron spectroscopy (XPS) measurements have also

supported this finding by revealing shifts in the chemical state of both chromium and nitrogen atoms in the S phase to new binding energies that lie between their expected elemental and CrN bonded states. Under similar examinations, no significant shift away from the metal bonding state was observed for nickel and iron within the nitrded layer [142-144]. This has also been further reinforced by a recent study by Tao *et al.* [145], which has demonstrated the presence of peaks forbidden in FCC structures at the surface of a low-temperature nitrided chromium containing ASS, which have been attributed to the high ordering (i.e. long range ordering) of the nitrogen atoms around chromium atoms. Short range ordering and random distribution were also found under varying nitrogen compositions and depths. No such ordering was observed on a chromium-free ASS (i.e. no strong nitride formers). Therefore, this suggests that to develop highly supersaturated S phase layers, the presence of chromium in the alloy is critical. However, it is still not known whether this is unique to chromium, or can also be observed with other strong nitride forming elements (e.g. Ti or Nb).

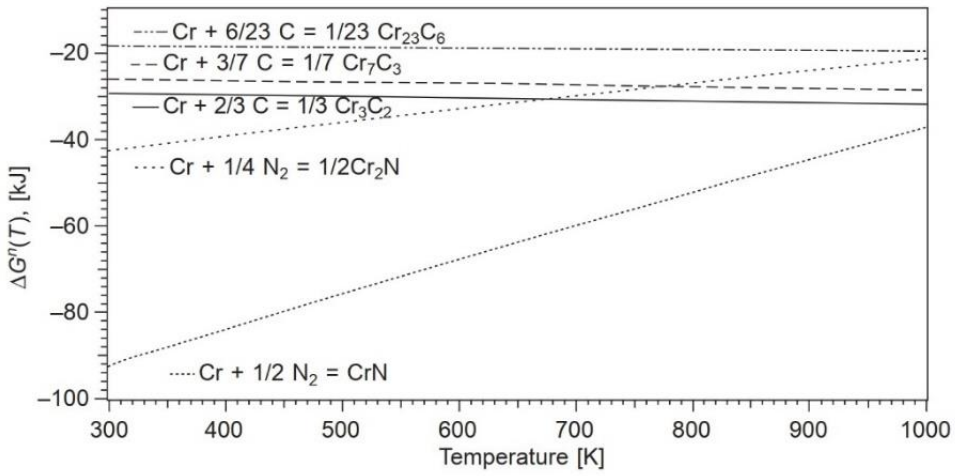



*Fig. 2-31 Gibbs free energy (per mole of chromium atoms) of chromium nitrides and carbides at different temperatures. Note the significantly lower energy and therefore thermodynamically more stable state of the CrN precipitates at all plotted temperatures [91, 146].*

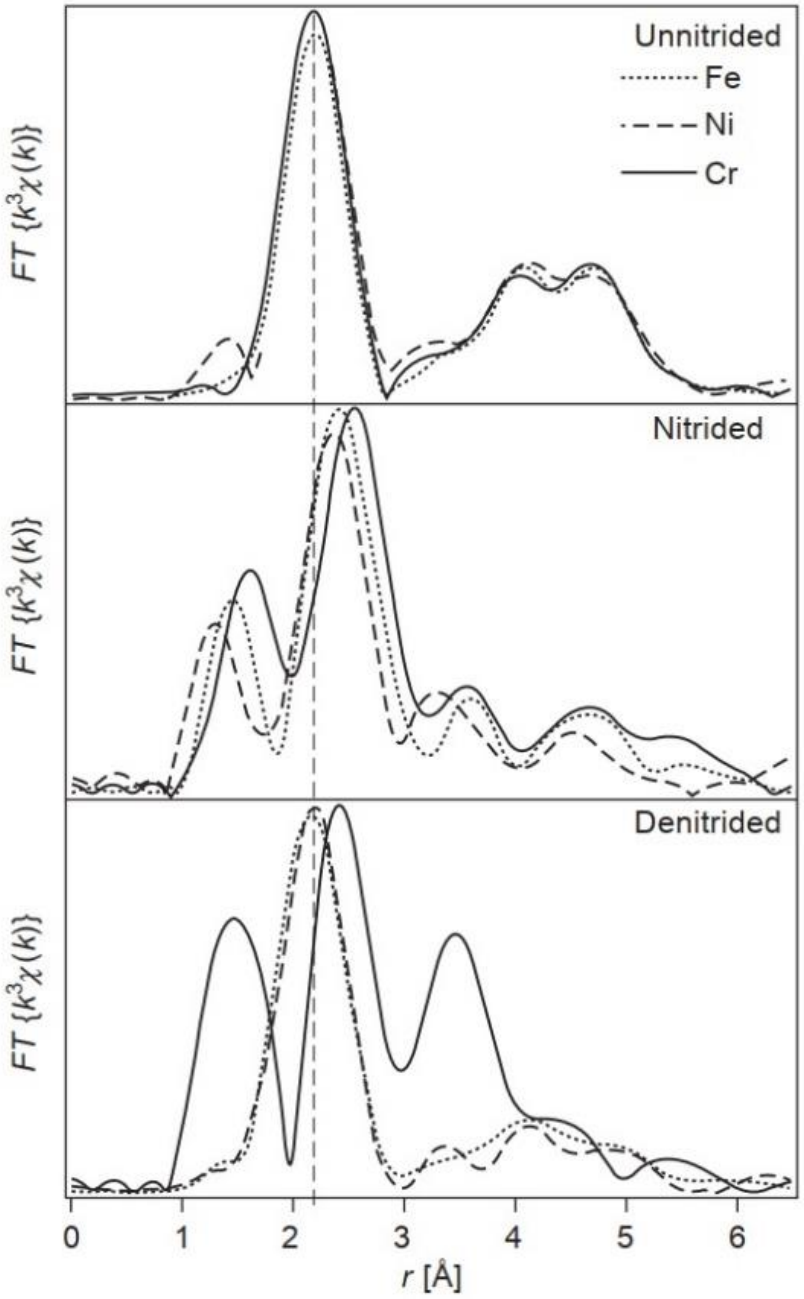



*Fig. 2-32 EXAFS study on untreated (unnitrided), S phase treated (nitrided) and denitrided S phase (using $H_2$ gas). Following nitriding, the distance to the nearest metal-metal atom (vertical dotted line) shifts for Fe, Ni and Cr in comparison to the untreated samples. Following denitriding, only shifting of the metal-metal spacing for Cr is seen. Following nitriding, all elements show somewhat similar nearest neighbour interstitial occupancy, whereas following denitriding, only Cr shows strong nearest neighbour occupancy [91, 140].*

### 2.4.3. Thermodynamic Metastability

Since the beneficial properties (hardening & corrosion resistance) of the S phase rely on the retention of the precipitate-free structure, extensive research has been dedicated to understanding and measuring the thermodynamic stability of the phase [8, 87, 91].

The chemical attraction between chromium and nitrogen is well-established, and dictates the formation of stable chromium nitrides during traditional high-temperature plasma nitriding (Fig. 2-31) [141]. Given the strong affinity between chromium and nitrogen, the SRO between them, and the general lattice inhomogeneity found within the S phase (section 2.4.2), it is not difficult to deduce that the S phase is a structure that is frozen in a metastable state.

The thermodynamic metastability of the S phase has been examined using isothermal [21, 130, 147, 148] and isochronal annealing [149] experiments (Fig. 2-33). Extrapolations of these results have shown that decomposition (nitride formation) of the S phase can be expected to begin occurring within several minutes at temperatures above 500 ˚C, with 50 % decomposition developing in the region of 1 hour. However, when kept at relatively low temperatures (under 300 ˚C), the initiation and growth of the nitrides can be expected in the order of several years. Therefore, the S phase is not recommended, or useful (for the purpose that it is treated for), for elevated temperature use above 200-250 ˚C. At these lower temperatures, decomposition of the S phase can be effective prevented, either indefinitely or of the scale of 100 years [21, 149].

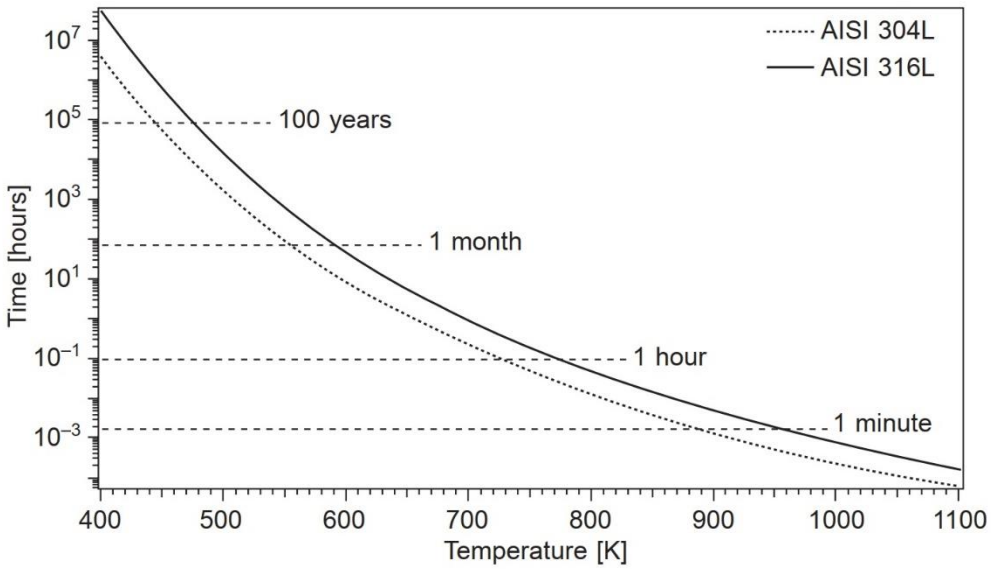



*Fig. 2-33 Isothermal stability plot (line shows 50 % decomposition) of S phase formed on AISI 304L and 316L using isochronal annealing data [91, 149].*

### 2.4.4. Properties

Following S phase surface treatment, it can be expected that there will be improvements in the mechanical strength, the fatigue strength & limit [125], the electrochemical corrosion resistance, and an increase in hydrophilicity [143, 150, 151] in comparison with the base austenitic stainless steel alloy [8, 87].

The elastic modulus of the S phase has been shown to increase in comparison with the untreated bulk. However, unlike typical FCC structures (e.g. austenite), which possess their highest elastic modulus in the <111> family of directions, the S phase has instead been shown to have its lowest values in the <111> directions (≈ 225 GPa at around 5 µm depth) and its highest values in the <001> family (≈ 260 GPa at same depth) [152]. In line with these findings,

the tensile strength of the S phase has also been found to increase, but at the cost of a decrease in ductility and toughness (lower strain until rupture under tensile testing) [125, 153].

Surface hardness values of nitrogen S phase are commonly measured to be above 1000 HV under both micro and nano hardness measurements, with surface measurements even reaching up to 1450 $HV_{0.1}$ [8, 18, 130, 154]. Hardness depth profiles have also been shown to have complementary trends to nitrogen depth profiles through the S phase (Fig. 2-30 & Fig. 2-34) [152, 155].

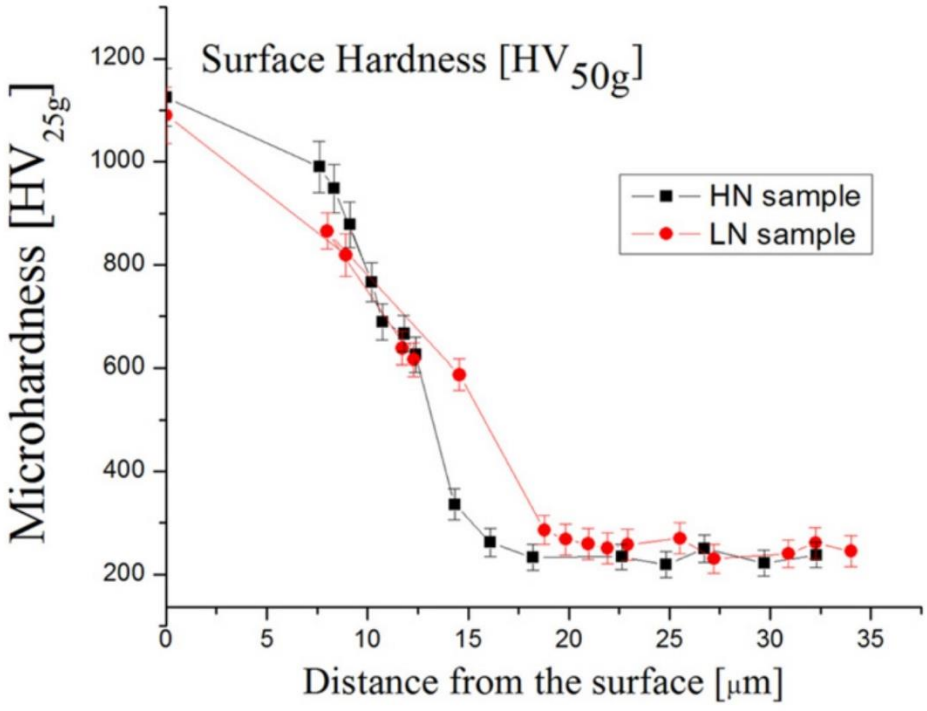



*Fig. 2-34 Hardness profiles of AISI 316L samples plasma nitrided at 400 °C for 20 hours in 25% $N_2$ (HN) and 20% $N_2$ (LN) [155].*

In agreement with the improvement in hardness, the S phase has also been shown to have significantly improved resistance to wear and changes in dominant mechanisms of wearing.

Unlike untreated austenitic stainless steels, which are typically subjected to severe adhesive wearing (section 2.2.4.4), S phase treated surfaces are more likely to undergo oxidative (when counterpart has similar hardness) or abrasive (when counterpart is significantly harder) wearing [156-159]. Under the same conditions (pin-on-disk wearing using a steel or alumina ball), a study by Sun and Bell [79] found that S phase treated surfaces dramatically reduce the wear rates (2 orders of magnitude) in comparison with untreated surfaces. Under corrosive wear conditions, the presence of a precipitate-free S phase (treated at 450 °C) resulted in an 80 % reduction in wear volume in comparison with high-temperature (550 °C) plasma nitrided equivalent surfaces (10 $mm^3$ vs 50 $mm^3$, respectively; 15 % HCl + 5 % $HNO_3$ + 85 % $H_2O$, alumina ball, 20 N of load, 1200 m sliding distance) [79].

Despite the general excellent corrosion resistance of austenitic stainless steels (AISI 316L alloy in particular), they do still suffer from issues of crevice and pitting corrosion, especially when subjected to chloride containing media (as mentioned in 2.2.2). It is known that, through various potential mechanisms (section 2.2.2.3), the addition of nitrogen into austenitic stainless steel alloy compositions has a positive effect on the corrosion resistance of the alloys, especially in regards to pitting and crevice attacks [8, 87, 160]. Therefore, if the nitrogen introduced through plasma nitriding is maintained as an interstitial solid solution, then it can be expected to possess improved corrosion resistance, even when compared to the already excellent resistance of the untreated alloy. In line with these expectations, electrochemical testing performed on S phase treated surfaces has demonstrated enhanced passivity (more cathodic potential; Fig. 2-35), resistance to pit growth (Fig. 2-35), more positive corrosion

potential (open circuit potential; Fig. 2-35) and similar current density (Fig. 2-35) when compared with untreated surfaces [115, 160-163].

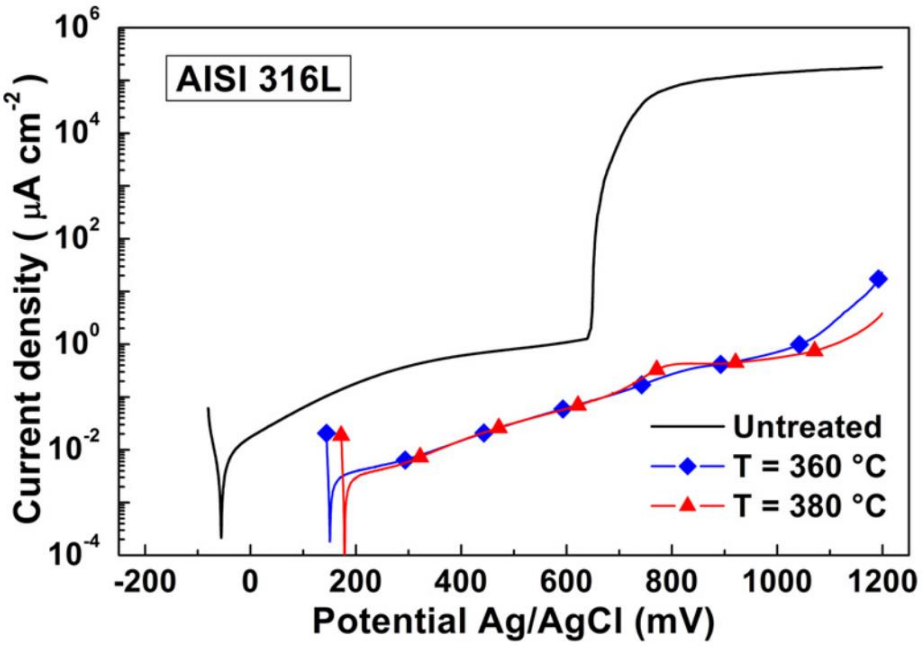



*Fig. 2-35 Anodic polarisation curve on untreated, 360 °C nitrided and 380 °C nitrided AISI 316L surfaces in 5 % NaCl media [161].*

### 2.4.5. Limitations

Given that austenitic stainless steels show poor resistance to bacterial fouling, and that they are widely used in the food and medical industries (section 2.2.5), it is therefore important that measures are taken to address this [6, 19]. Although the formation of the S phase on the surface of these alloys can improve their mechanical weaknesses, it does not however significantly enhance the antibacterial performance [164]. Therefore, it is important to use complementary surface modification technologies to address this problem. However, the most

obvious limitation of the S phase, which is its thermodynamic metastability, presents a barrier for its combination with antibacterial surface modifications, such as laser surface texturing, which are typically thermal in nature [26]. Therefore, finding solutions to this problem is both challenging and potentially highly rewarding (can form durable and antibacterial surfaces on materials already in service in the food and medical industries).

## 2.5. Antibacterial Surfaces

Antibacterial surfaces can be classified as either anti-biofouling (preventing bacterial attachment and growth) or antimicrobial (killing bacteria) [165]. Typically, physical modifications make up the bulk of anti-biofouling surfaces, with surface patterning (e.g. bio-inspired texturing) and surface grafting (e.g. with polyethylene glycol (PEG)) being the most popular choices [166, 167]. In some cases patterning, such as nanoscale rods or pillars, may also be classified as antimicrobial because of their ability to puncture/lyse (burst) bacteria (Fig. 2-36) [168, 169]. Due to their ability to effectively kill a broad spectrum of Gram-negative and Gram-positive bacteria (e.g. superbugs like MRSA), bactericidal elements such as silver or copper are currently the most common antimicrobial measure [170]. Their excellent efficacy has been measured in hospitals, where a 90 to 100 % decrease in the number of viable bacteria was observed following the replacement of touch surfaces with copper containing equivalents [171]. Other common antibacterial techniques include the changing of surface chemistry (e.g. super/ultrahydrophobic surfaces; anti-biofouling) and the incorporation/leaching of antibiotic substances on the surface (antimicrobial). Although many studies show very promising results

in the labs, it is rare to find any antibacterial products that show long lasting activity, cheap production costs and durability in practice [172].

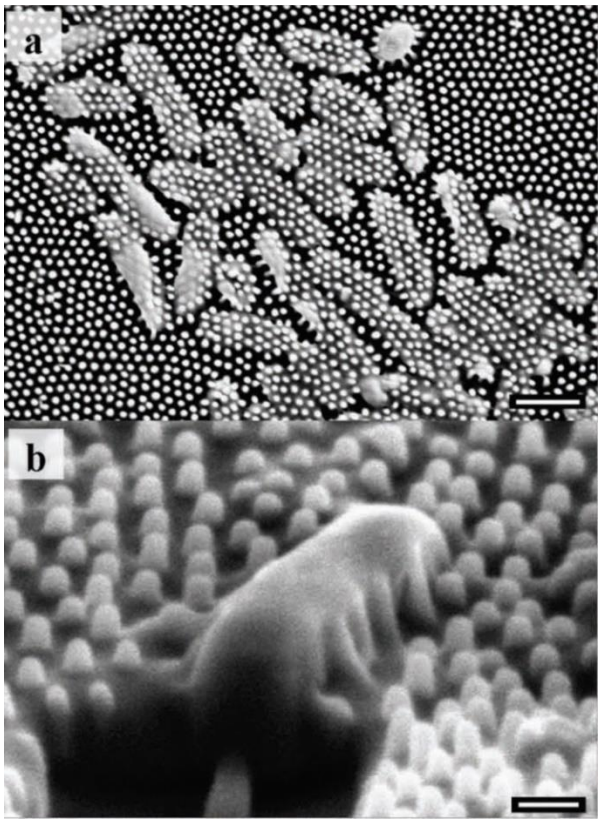



*Fig. 2-36 Electron micrographs demonstrating antimicrobial effect of nanopillars found on cicada wings. Image A (scale bar = 1 µm) shows Pseudomonas aeruginosa cells on the surface of cicada wings, with clear signs of nanopillar penetration. Image B (scale bar = 200 nm) is an angled higher magnification image showing the penetration more clearly [169].*

### 2.5.1. Demand for Antibacterial Surfaces

Healthcare-acquired infections (HAI) and cross contamination of food are two major public health and economic problems present in the food and medical industries [12]. In the UK alone, there are over 300,000 cases of HAIs and over 500,000 cases of foodborne diseases every year [13]. It is estimated to cost the NHS (National Health Service) in the UK approximately £3 billion

annually [14, 15]. The costs are even greater in the US, with the total coming over $40 billion each year [173, 174].

Cross contamination of foods, which occurs when microorganisms are unintentionally transferred between different material surfaces or foods, accounts for a significant percentage of all foodborne outbreaks, with one study attributing 39% of the cases to cross contamination (N = 231) [175]. On the other hand, hospital prevalence studies on HAIs in the US predict around 1 in every 31 hospital patients will contract at least one HAI. In many cases these are preventable HAIs, and even with inefficient approaches, the low-cost saving estimates are comparable to the financial burdens of whole diseases such as strokes, chronic obstructive pulmonary diseases and diabetes to the healthcare industry [173].

### 2.5.2. Current Control Measures & their Limitations

Currently, preventative measures do exist that are helping to reduce the number of cases of both HAIs and cross contamination of foods. Within the medical industry these measures include the increased use & education about hand hygiene [176], the use of biocidal elements (e.g. silver and copper) [177, 178], the use of antibiotics (e.g. before arthroplasty surgery) [179], and the use of disinfectants, autoclaving of tools and sterilisation of tools (e.g. with UV light) [180]. All the previously mentioned techniques can also be applied to the food industry in order clean machinery/tools and keep liquids free from sources of contamination [181]. Due to the indirect sanitation controls methods (i.e. away from the consumers) and increased variability found in the food industry, a much wider array of control measures exists in comparison to the medical industry [182]. Some common measures include the heating of

foods (e.g. pasteurisation of milk) [181], physical cleaning of tools and foods [7, 183], the use of pulsed current cleaning (e.g. to produce chloride ions) [184], the use of chlorine containing cleaning agents (e.g. sodium hypochlorite (bleach)), the use of chelating agents (e.g. ethylenediaminetetraacetic acid (EDTA)) [181] and the use of filtration/membrane systems [184].

However, many of these control methods come with major drawbacks that are creating concern for their future use, both in terms of efficacy and in relation to the new problems that they are creating. One widely publicised example of this is the ever-increasing prevalence of antibiotic resistant strains of bacteria (e.g. methicillin resistant *Staphylococcus aureus* (MRSA)) that have developed due to over-use and improper use (e.g. not completing the full course) of antibiotics [180, 185, 186]. Moreover, studies have also shown that even antibiotic susceptible bacteria (e.g. methicillin susceptible *Staphylococcus aureus* (MSSA)) can become highly resilient to the action of antibiotics through the formation of biofilms on surfaces. Bacteria within biofilms behave very differently to free-floating (planktonic) bacteria, they are able to modify their metabolic activity (e.g. through quorum sensing) and secrete an extracellular polysaccharide (EPS) matrix that acts to hold the bacterial community together and protects against external agents (e.g. antibiotics, disinfectants) [7, 182, 187]. Studies have shown that bacteria in biofilms require several hundred times higher doses of antibiotics in comparison to planktonic bacteria [188, 189]. In the food industry, some success has been observed through the combination of electrical currents and antibiotics to increase the efficacy of the antibiotics against the bacteria in the biofilm [190]. However, in many cases there are unfortunately no solutions currently available, and consequently in the US alone, there are over 2.8 million

infections each year associated with antibiotic resistant bacteria, with over 35,000 of those resulting in deaths [185].

### 2.5.3. Future Preventative Measures

Given the limitations of current control methods stated in section 2.5.2, it is therefore apparent that other measures are necessary to address the current situation, with preventative approaches implemented & acting before problems arise being the ideal solution [181, 191].

For the most part, addressing this need has been predominantly attempted through more materials or engineering based strategies in both the medical and food industries. An example within the food industry would be the enforcements of good design, regular maintenance and general good manufacturing practices [183]. These requirements include the use of sanitary materials (e.g. corrosion resistant ASS alloys) for all food contacting surfaces, regularly scheduled & recorded cleaning of equipment and improved machine/equipment/tool designs that enable easier cleaning (e.g. few sharp corners or hard to reach areas) [183]. Similarly, in the medical industry this approach has been observed with the uptake of copper incorporated hospital door handles (as mentioned in section 2.5) or the use of silver embedded urinary catheters to prevent the potential infections before they arise [178, 191].

### 2.5.4. Anti-Biofouling Surfaces

The trend towards these preventative approaches have created a demand for equipment and surfaces that are inherently antibacterial. In particular, the demand for anti-biofouling surfaces

that repel or resist the attachment and spread of bacteria has dramatically increased [192]. The potential for such surfaces to, instantaneously and repeatedly, prevent the attachment of bacteria and formation of biofilms onto them is clearly an appealing quality. By reducing the need for regular cleaning, whilst increasing the efficacy of other sanitation control methods, such as antibiotics (e.g. increasing susceptibility of MSSA, as mentioned in section 2.5.2), these surfaces can increase the production yield, reduce costs & improve overall hygiene [193]. Moreover, since these anti-biofouling surfaces do not specifically target individual species or strains of bacteria, these surfaces would not be expected to increase the prevalence of antibiotic resistant strains. Overall, this driving force has created a lot of scientific interest in the field of functional surfaces, and it has now become an important subject area with new innovative ideas being regularly published [19, 167, 194].

Research into the production of functional anti-biofouling surfaces has, in one form or another, existed for several decades, although the awareness and importance of the subject has only recently gained wider attention. Research has evolved from the modifications of macro- and microscale surface topography, to the modification of surface chemistry and more recently to the utilisation of biomimetic (e.g. lotus leaf) and nanoscale structures [167, 195-197]. The scientific understanding of the anti-biofouling functional performance of surfaces has also advanced over time, from the belief that it was directly related to the surface hydrophobicity to a more complex, not yet fully understood, theory that is influenced by a mixture of the surface wettability (Cassie-Baxter state in particular), surface free energy and surface structure. It should be noted that none of these terms are fully characterised yet, and there are still ongoing scientific discussions regarding them [167, 198, 199].

In terms of performance related to surface structures, it is generally accepted that smaller features provide better functionality. The current consensus is that the anti-biofouling performance of a surface is related with the periodicity of the surface structures (Fig. 2-37), i.e. if the periodicity is smaller than the dimensions of the bacteria then the strength of the attachment and migration is limited and mitigated, respectively [200, 201]. Coincidentally, micro- to nanoscale features tend to give rise to physical hydrophobicity through the formation of trapped pockets or air (i.e. creating a gap between the surface and the liquid) [198].

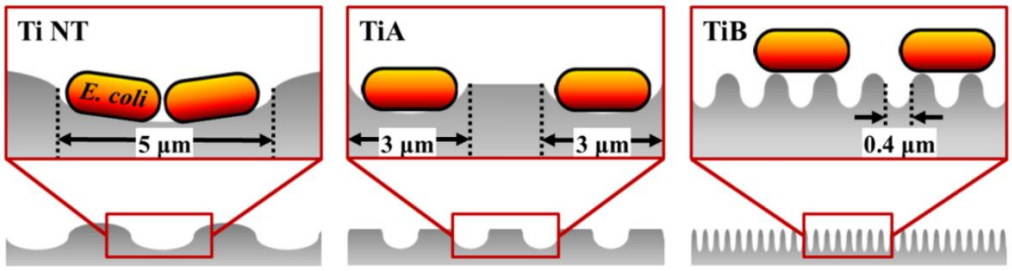



*Fig. 2-37 Periodicity and aspect ratio effect on the available surface area for bacterial (E. coli) attachment on untreated (Ti NT), Hydrothermally treated A (TiA) and hydrothermally treated B (TiB) commercially pure titanium [201].*

## 2.6. Surface Texturing

All surface structuring approaches can be broadly categorised as either adding material, removing material or re-organising existing material. There are a wide variety of techniques available for achieving this, including etching, selective milling, laser melting, laser ablation and photolithography. Each technique comes with its own advantages and disadvantages, which can include the maximum precision achievable, speed of formation, scalability, cost, and reproducibility [167, 202-204].

Due to the rapid processing times, excellent reproducibility and ease of scaling, laser surface texturing has become an industrially attractive approach for the production of functional anti-biofouling surfaces [22]. Therefore, for the purposes of this study, only methods utilising lasers will be explored.

### 2.6.1. Ultrashort Pulsed Laser Texturing

With the development of pulsed laser technologies, faster fabrication and more precise control over the final surface topography has become possible. In particular, the progress into ultrashort pulsed laser texturing has enabled rapid micro- and nanoscale texturing of surfaces [20]. In pulsed laser texturing (even down to nanosecond durations), localised melting is achieved through rapid heating and self-quenching using significantly higher laser intensities than non-pulsed lasers [25]. Additionally, since 1965, unique self-forming repetitive textures, known as laser-induced periodic surface structures (LIPSS), have been found to form on surfaces when processing close to the ablation threshold of the materials. It has been hypothesised that this phenomena (periodic self-formation structures) arises due to the interactions of electromagnetic waves from the laser with the surface topography of the material, as well as the formation and excitation of surface plasmon polaritons [24]. In most cases this results in the formation of ripple like textures that are parallel to each other, with a periodicity of the order of the wavelength of the laser source (typically 100-200 nm smaller than the wavelength) and are usually referred to as low spatial frequency LIPSS (LSFL; Fig. 2-38) [205-207].

Textures comprised of LIPSS are known to have antibacterial properties. Research findings have revealed increased antibacterial efficacy for stainless steels containing LIPSS, in comparison to their untextured counterparts, against all types of bacteria, regardless of the bacterial surface structuring. Consequently, this non-specific resistance to both Gram positive (single thick cell wall) and Gram negative (thin cell wall that resides within a periplasmic space between an inner (plasma membrane) and outer lipopolysaccharide layer) bacteria such as *Staphylococcus aureus* (*S. aureus*) and *Escherichia coli* (*E. coli*), respectively, has attracted significant research attention for biomedical and food industry related applications [208-210].

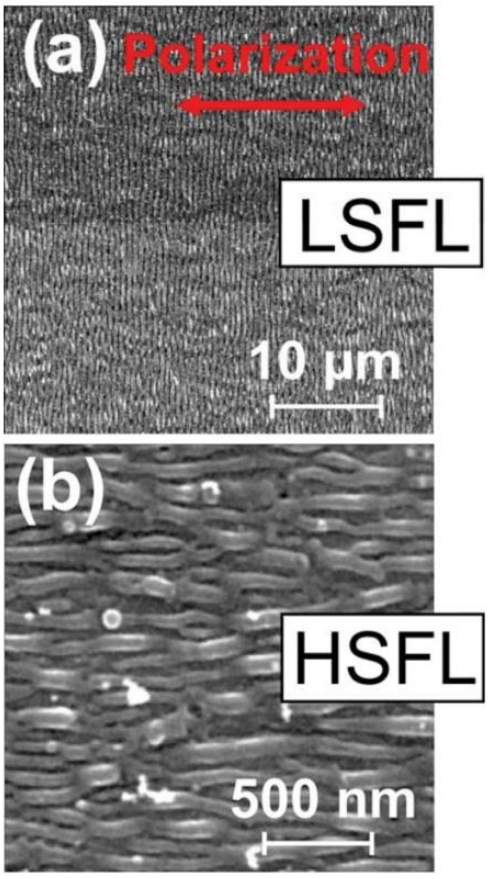



*Fig. 2-38 Scanning electron microscope image showing both (a) low spatial frequency LIPSS and (b) high spatial frequency LIPSS formed on the surface of titanium samples [205].*

#### 2.6.1.1. Limitations of Laser Texturing

The main limitation to the uptake of laser texturing arises due to the thermal effect that it typically has on the targeted material, thereby limiting the suitable materials and applications it can be utilised for. Due to the effect that heating has on the surface chemistry, microstructure and properties, temperature sensitive/thermodynamically metastable materials have traditionally not been viable for laser processing [198, 211]. Although the introduction of nano- and picosecond pulsed laser technologies have minimised many of the problems associated with laser heating, there are still many materials unable to retain their structural and chemical integrity or tolerate the thermal shock induced by the rapid heating and cooling [212, 213].

In addition to the development of surface cracking, recasting of molten materials, re-organisation of adjacent material (due to the formed shock waves) and damage to structures within the vicinity of thermal laser pulses (Fig. 2-39), the development of microstructural changes within the solid material has also traditionally limited the uptake of laser texturing [213]. Even under nanosecond laser texturing, significant surface damage (melting and formation of burrs) and microstructural changes (coarsening and equiaxed grains) can readily develop due to the thermal nature of the processing (Fig. 2-40). However, such surface damage or microstructural change can be avoided through careful use of athermal femtosecond laser processing (Fig. 2-40). In such cases, it is possible to ablate surface matter, even with high aspect ratios, without the development of thermal effects [214]. This advantage has allowed for the development and uptake of femtosecond laser texturing, alongside focus

ion beam (FIB) milling, for the lamella sample preparation of transmission electron microscopy (TEM) specimen [212].

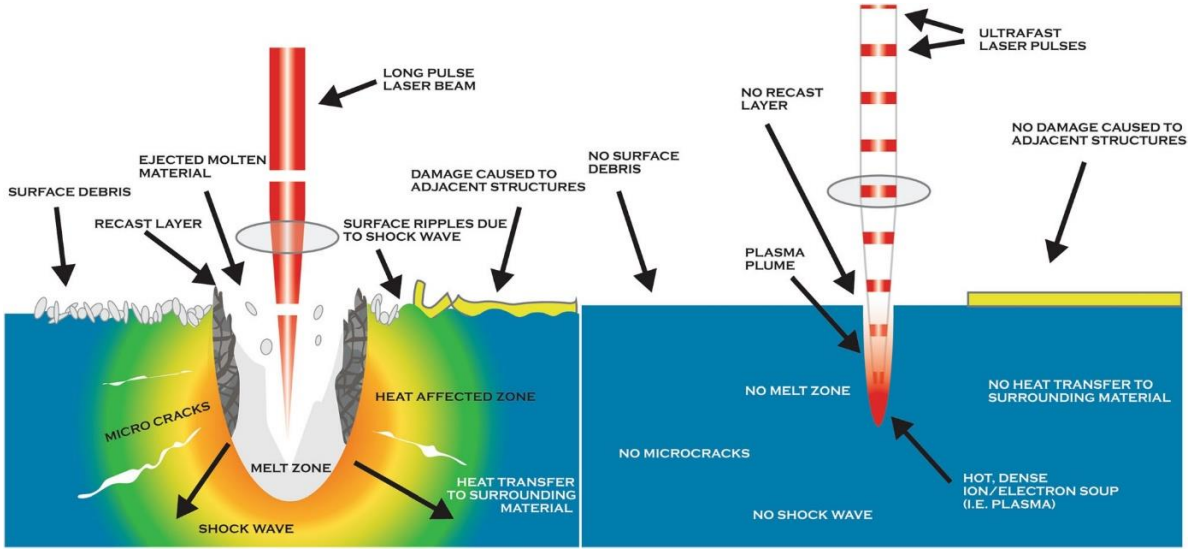



*Fig. 2-39 Schematic diagram of the phenomena observed in long pulsed thermal laser machining and athermal femtosecond laser ablation. Original diagram from Clark-MXR Inc (original source material not available) [213].*

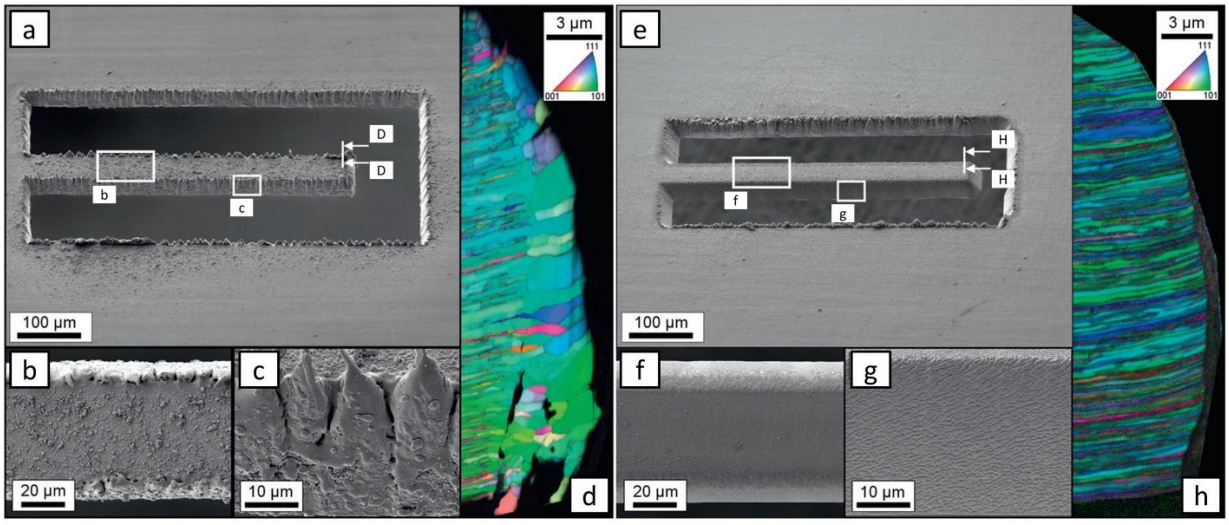



*Fig. 2-40 Fabrication of a cantilever through nanosecond (a-d) and femtosecond (e-h) laser processing. The scan patterns (a and e), magnified top views (b and f), magnified cut edges (c and g) and electron backscatter diffraction analysis of the cross sections (d and h) at positions D-D and H-H, respectively, are shown. The inset at the top right corresponds to the colour coding of the grain orientation with respect to an external reference. Note the lack of coarsening and variation in the grain structure following femtosecond laser processing (h) in comparison with nanosecond laser processing (d) [212].*

### 2.6.2. Femtosecond Pulsed Laser Texturing

It was not until the introduction and more widespread application of femtosecond (fs) laser texturing that many more barriers were removed [23, 26]. Laser pulses in the femtosecond ($10^{-15}$ s) range deliver energy to a surface (valence electrons) faster than can be dissipated away to the surrounding matter (≈ $1x10^{-12}$ s; electron-phonon coupling time) [215]. Therefore, if the delivered energy during the pulse can exceed the ablation threshold of the target material, it is possible to athermally sputter away surface matter [26].

LIPSS formed using fs pulses present with unique features, the most profound of which is the formation of secondary structures with periodicity much smaller than the wavelength of the laser source, known as high spatial frequency LIPSS (HSFL; Fig. 2-38). These HSFL typically overlay and arrange perpendicular to the LSFL [205]. In addition to these structures, it is also possible to generate more complex and new forms of LIPSS by varying the laser polarisation. A particularly interesting and useful pattern is observed when circularly polarised light is used. Under the right conditions, instead of ripple-like features, triangular shaped and hexagonally organised pillars, resembling the surface of springtails, are formed with similar periodicity to LSFL in 3 different directions (Fig. 2-41) [206, 216]. Due to the near nanoscale features and high hydrophobicity, these new structures, named triangular LIPSS, are promising for anti-biofouling applications, and studies on similar structures have produced excellent results [208].

However, it should be noted that since the functional properties are directly related to the structure integrity of the nano-scale triangular LIPSS, there are major concerns over the

longevity of the properties. Durability is of concern within the food and medical industries, where surface interaction-induced wear is expected to occur on medical tools and body implants as well as for food equipment during processing and pre-&-post-cleaning [167].

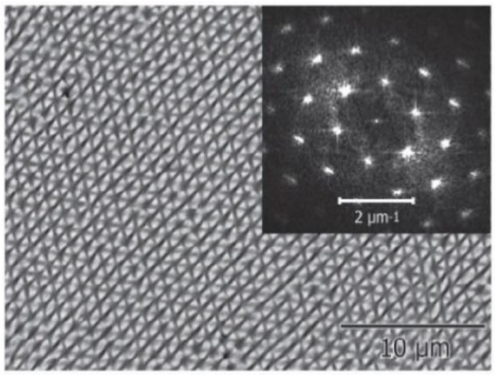



*Fig. 2-41 Electron microscope image (main image) showing triangular LIPSS formed on steel using femtosecond pulsed laser texturing (310 fs, 500 kHz). Top right image is a fast Fourier transform taken of the same image, showing the multi-directional ordering in the texture [206].*

#### 2.6.2.1. Potential Use with S Phase Surfaces

Due to the metastable nature of the S phase, laser texturing (even using ultrashort pulses) has traditionally been avoided since the associated heating leads to the decomposition of the phase and loss of corrosion resistance. A recent industrial report also discovered a similar issue (nitride precipitation) following the heating of low-temperature nitrocarburised AISI 316L stainless steel during laser welding [211]. Therefore, the challenge faced when attempting to combine surface texturing and low-temperature nitriding is to introduce the desirable textures on the thermodynamically metastable S phase without damaging or decomposing it. Given the above barriers, very little research has been carried out thus far on the surface functionalisation via texturing of S phase treated stainless steel surfaces.

However, the development and availability of potentially athermal fs pulsed laser texturing of metallic surfaces [205, 217] has created new opportunities for the functionalisation of S phase treated surfaces [23, 218]. It should be noted that as of the beginning of this study no research had been published on the response of the metastable S phase to texturing using these ultrashort pulsed lasers.

## 2.7. Summary

Owing to their bio-inert nature and superior corrosion resistance, even within the stainless steel family, austenitic stainless steels have already found widespread applications throughout the food and medical industries (sections 2.1 and 2.2). However, further uptake of these alloys requires their limitations of poor wear resistance and susceptibility to bacterial colonisation to be addressed. Surface engineering (section 2.3) has produced successful approaches to overcome these challenges individually, through low temperature plasma nitriding to form the hard and corrosion resistant S phase (section 2.4), or through antibacterial surface modifications (section 2.5) using laser surface texturing (section 2.6). However, given the traditional thermal nature of laser patterning and the thermodynamic metastability of the S phase, no research has been reported, thus far, to have successfully combined these technologies. Fortunately, the recent development and increased availability of athermal ultrashort femtosecond pulsed laser texturing has created new opportunities to engineer surfaces capable of simultaneously overcoming the poor wear resistance and susceptibility to bacterial fouling of austenitic stainless steel alloys, such as the widely used AISI 316L alloy (section 2.2).

# CHAPTER 3 MATERIALS & METHODS

## 3.1. Materials and Sample Preparation

5 mm thick AISI 316L austenitic stainless steel cylindrical coupons, with composition as listed in Table 3-1, were cut from hot rolled bars (25 mm diameter) using SiC cutting wheels. Coupons were initially ground to 1200 grit size and then polished using 6 µm, 3 µm and finally 1 µm diamond suspensions to achieve a mirror finish ($R_a$ = 22.1 $\pm$ 3.6 nm). Ultrasonic cleaning with Teepol and acetone were carried out between each step.

*Table 3-1 Chemical composition of AISI 316L coupons measured using average glow-discharge optical emission spectroscopy depth readings*

| Element | Cr | Ni | Mo | Mn | Si | S | N | C | Fe |
|---|---|---|---|---|---|---|---|---|---|
| **Composition (wt%)** | 16.22 ± 0.06 | 12.35 ± 0.04 | 2.02 ± 0.01 | 1.90 ± 0.001 | 0.34 ± 0.01 | 0.02 ± 0.006 | 0.07 ± 0.02 | 0.01 ± 0.0004 | Bal |

### 3.1.1. Cross-Section Preparation

Cross-sections were prepared by cutting and mounting samples in conductive Bakelite. Microstructures of samples were revealed for scanning electron microscope (SEM) imaging by etching (50% HCl + 25% $HNO_3$ + 25% $H_2O$) for up to ten seconds on untreated samples, and up to thirty seconds for S phase treated samples. For the UntΔ sample type (triangular LIPSS textured on untreated AISI 316L coupons; see section 3.1.4 for more detailed labelling information), nickel plating was necessary to protect the textured surface from damage during

cross-sectional sample preparation. Nickel plating (Sifco ASC, part No. 2086) was carried out for approximately 10 minutes using a Skytronic DC power supply set at a controlled current of 0.1 A (<10 V).

### 3.1.2. Plasma Surface Treatment

Interstitial solid solution hardening of the surface was carried out using low-temperature active screen plasma nitriding (ASPN) in an adapted DC Klöckner Ionon 40 kW plasma furnace (Fig. 3-1). Freshly polished samples were treated for 20 hours at 400 °C in a gas pressure of 3 mbar and gas mixture of 25 % $N_2$: 75 % $H_2$. Samples were kept at a floating potential and enclosed in an AISI 316 ASS active screen. Samples were separated from the AISI 316 ASS active screen lid by 20 mm. Brief re-polishing using a 1 µm diamond suspension was carried out following treatment to return samples to a mirror finish ($R_a$ = 25.3 ± 2.8 nm).

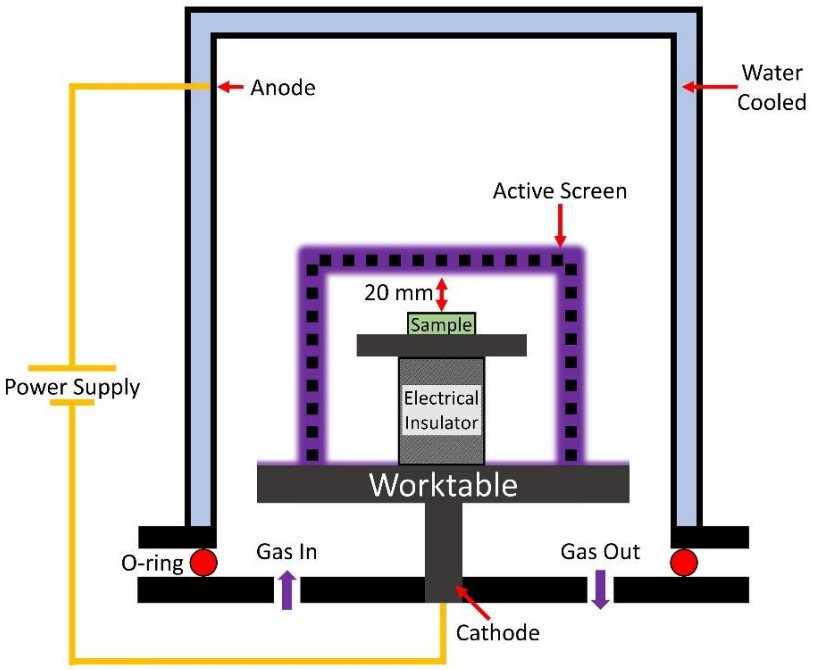



*Fig. 3-1 Schematic diagram of active screen plasma treatment setup.*

### 3.1.3. Laser Texturing

To examine the feasibility of laser texturing of S phase treated surfaces, both femtosecond (fs) and nanosecond (ns) ultrashort pulsed laser texturing were initially attempted. Based on the results obtained (section 4.2), optimisation and further analysis of specifically antibacterial textures were only carried out using the femtosecond laser source. Femtosecond pulsed laser texturing was performed using a femtosecond laser source (Satsuma from Amplitude Systems) with a wavelength of 1032 nm and a pulse duration of 310 fs. Nanosecond pulsed laser texturing was performed using a MOPA-based Yb-doped fibre on a SPI G4 50W HS-S set up with a laser source wavelength of 1064 nm. A gaussian beam spot of 15 µm radius ($\omega_0$) was used for both lasers.

#### 3.1.3.1. Channel Textures

Channel textures were chosen to examine the response of the S phase to the different laser sources and settings. Large horizontal spacing (300 µm; Fig. 3-2) was used to separate adjacent channels to minimise/eliminate potential thermal interactions (e.g. from heat affected zones). These textures were chosen for their structural simplicity, ease of comparison (i.e. controlled moving energy density), and that they were not subjected to secondary phenomena (e.g. HSFL). Three different laser settings were used to create channel textures on ASPN treated samples (see Table 3-2): 310 fs textured (310 fs), 15 ns textured (15 ns) and 220 ns textured (220 ns). By altering the frequency and speed of the laser, the theoretical amount of energy delivered to the surface per unit distance travelled by the laser (moving energy density =

single pulse energy/$\frac{\text{speed of laser}}{\text{frequency}}$) was kept constant between all textures. Details of the laser settings are listed in Table 3-2.

*Table 3-2 Pulsed laser texturing settings for channel textured sample types.*

| Sample Code | 310 fs | 15 ns | 220 ns |
|---|---|---|---|
| **Pulse Duration (s)** | $3.1 \times 10^{-13}$ | $1.5 \times 10^{-8}$ | $2.2 \times 10^{-7}$ |
| **Frequency (kHz)** | 500 | 100 | 70 |
| **Single Pulse Energy (µJ)** | 4.68 | 30.89 | 50.14 |
| **Speed of Laser (mm/s)** | 100 | 132 | 150 |
| **Moving Energy Density (µJ/µm)** | 23.4 | 23.4 | 23.4 |
| **Hatch Spacing (µm)** | 300 | 300 | 300 |

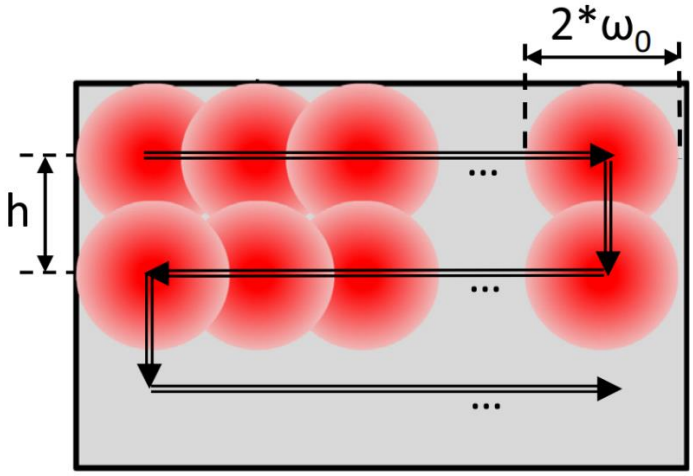



*Fig. 3-2 Schematic diagram of the rastering strategy used during the laser texturing. With labels for grid/hatch spacing (h) and Gaussian spot beam diameter ($2*\omega_0$) [206].*

#### 3.1.3.2. Antibacterial Textures

Four different bio-inspired antibacterial textures were formed using femtosecond pulsed laser texturing on ASPN treated samples: low aspect ratio lotus (ASPNL1), high aspect ratio lotus (ASPNL2), shark skin (ASPNS) and triangular LIPSS (ASPNΔ).

Both lotus-inspired textures (ASPNL1 & ASPNL2) were formed by rastering a circularly-polarised beam across the sample surface with a velocity of 500 mm/s, frequency of 500 kHz and grid spacing of 25 µm (Fig. 3-2). Identical settings were used for both textures, but with different repetition rates. The ASPNL1 texture settings were repeated 4 times, whereas the ASPNL2 texture settings were repeated 9 times.

The shark skin inspired texture (ASPNS) was created by rastering a circularly-polarised beam across the sample surface with a velocity of 500 mm/s and frequency of 500 kHz. Three different rastering patterns (Fig. 3-2) were used: (1) the first was a full power raster with grid spacing of 25 µm, (2) the second was a half power raster at 45 ° to step 1 and grid spacing of 106.1 µm, and (3) the third was the same as step 2 but at 135 ° to step 1. These three steps were repeated 10 times to achieve the texture.

Triangular LIPSS textures were achieved by rastering a circularly-polarised beam across the sample surface with a velocity of 500 mm/s, pulse frequency of 250 kHz, and grid spacing of approximately 2 µm, both horizontally and vertically (Fig. 3-2). Overall, the effective accumulated fluence was 92 mJ/cm$^2$. Triangular LIPSS were also performed on polished untreated AISI 316L coupons (UntΔ).

### 3.1.4. Sample Coding

In total, 10 different surfaces were used within this study: (1) untreated AISI 316L ASS (Unt), (2) S phase treated AISI 316L ASS (ASPN), (3) ASPN samples with 310 fs channel textures (310 fs), (4) ASPN samples with 15 ns channel textures (15 ns), (5) ASPN samples with 220 ns channel textures (220 ns), (6) ASPN samples with low aspect ratio lotus textures (ASPNL1), (7) ASPN samples with high aspect ratio lotus textures (ASPNL2), (8) ASPN samples with shark skin textures (ASPNS), (9) ASPN samples with triangular LIPSS textures (ASPNΔ), and (10) Unt samples with triangular LIPSS textures (UntΔ). A list of the different sample codes, including their treatment and texturing conditions, can be found in Table 3-3.

*Table 3-3 Sample codes, treatment condition and texturing condition of all sample types.*

| Sample Code | Treatment Condition | Laser Source | Texture Morphology |
|---|---|---|---|
| **Unt** | Untreated | - | - |
| **ASPN** | ASPN Treated | - | - |
| **310 fs** | ASPN Treated | fs | Channel |
| **15 ns** | ASPN Treated | ns | Channel |
| **220 ns** | ASPN Treated | ns | Channel |
| **ASPNL1** | ASPN Treated | fs | Low Aspect Ratio Lotus |
| **ASPNL2** | ASPN Treated | fs | High Aspect Ratio Lotus |
| **ASPNS** | ASPN Treated | fs | Shark Skin |
| **ASPNΔ** | ASPN Treated | fs | Triangular LIPSS |
| **UntΔ** | Untreated | fs | Triangular LIPSS |

## 3.2. Characterisation

### 3.2.1. Material Characterisation

Before texturing of the Unt and ASPN samples, surface roughness measurements were taken using an AMBIOS XP-200 surface profilometer (tip radius 2 µm) to demonstrate similar surface conditions. The elemental depth profiles of treated surfaces were measured and analysed using a glow-discharge optical emission spectrometer (GDOES; GDA 650 Spectruma Analytic Gmbh). GDOES was also utilised to determine the as-received untreated AISI 316L alloy semi-quantitative composition. GDOES measurements were carried out with a crater spot diameter of 2.5 mm, excitation potential of 1000 V and current of approximately 12 mA. Due to limitations with the availability of standard specimens containing nitrogen (maximum of 2 wt% nitrogen), only semi-quantitative data was possible for nitrided specimens that characteristically contain much higher concentrations of nitrogen. However, the main purpose of the GDOES measurements within this study were for the determination of the treatment layer thickness. Confirmation of the crater depth formed following GDOES etching was performed using surface profilometry over the crater (AMBIOS XP-200).

Hardness measurements were taken to demonstrate the depth of S phase treatments, as well as, to quantify changes in hardness following triangular LIPSS texturing of S phase treated surfaces. Surface hardness (and Unt hardness depth profile) measurements were taken using a Mitutoyo MVK-H1 Vicker's microhardness tester with a load of 50 gram-force (gf). Hardness depth profiles were taken using nanoindentation (MicroMaterials NanoTest Vantage) with a Berkovich indenter and a depth control of 200 nm. Raman spectroscopy, using a Renishaw

inVia Raman Microscope fitted with a 488 nm excitation laser and a Raman shift range of 250 to 2000 $cm^{-1}$, was performed to show surface contamination (e.g. oxidation) following laser texturing. X-ray diffraction (XRD; Bruker D8 Advanced or Proto AXRD) analysis using a Cu radiation source (Kα = 0.145 nm) was used to confirm the formation and nature of the S phase layer on samples.

SEM imaging (JEOL 7000F; accelerating voltage 20 kV) was used to reveal signs of material thermal shock, melting, sputtering or cracking, the response of the S phase to the different textures, and the layer structure of the S phase. Energy dispersive X-ray spectroscopy (EDS; Oxford Instruments Ultim Max 40) of point spots and area maps were used to determine the chemical composition of samples, to confirm sites of chromium nitride precipitation, and to detect sites of elemental segregation. EDS spot analysis was carried out at identical accelerating voltage (20 kV) to imaging, for 3 minutes on each spot, and X-ray spectrum range of 0-20 keV. For EDS mapping, a dwell time of 1000 µs (1 ms), processing time of 5 s, and energy spectrum range of 0-20 keV was used, resulting in an approximate total mapping time of 3 hours per map (1 full scan). Although long EDS scanning times were used to account for the difficulty related to the accurate measurement of light elements such as nitrogen and oxygen, quantitative data from these measurements were still deemed to not be quantitative, but rather qualitative/comparative.

Transmission electron microscopy (TEM) was used to accurately observe the surface condition of 310 fs channel textured samples to confirm the precipitate- and damage-free state of the surface. Cross-sections of the 310 fs textured samples were prepared for TEM analysis using manual sample preparation (cutting and grinding) and a focussed ion beam milling (FIB; FEI

Quanta 3D) approach to produce samples of ≈ 50 nanometre thickness. Prior to milling, a protective platinum coating was deposited using the gas injection system to shield the textured areas. A JEOL 2100 TEM was used to study the surface microstructure (imaging) and phase characterisation (selected area diffraction) of the 310 fs channel textured S phase layer.

### 3.2.2. Texture Characterisation

Scanning electron microscope imaging (JEOL 7000F) was used to examine the surface morphology, cross-sectional morphology/structure, texture channel spacing and laser-induced damage of the textured samples. Optical camera imaging was used to demonstrate the light scattering effect of the triangular LIPSS textured samples (UntΔ & ASPNΔ). Periodicity and symmetry of the triangular LIPSS textured samples were determined using fast Fourier transforms (FFT; ImageJ) of low magnification surface SEM images.

## 3.3. 1-D Surface Temperature Modelling

Analytical models were used to predict the temperatures immediately following single and multiple pulse nanosecond laser texturing. These values were then combined with diffusion data to determine the feasibility of S phase decomposition (i.e. chromium nitride precipitation) during the nanosecond laser texturing of the channels. Surface temperatures (where depth = 0) during and following the nanosecond pulses (15 ns & 220 ns) were calculated analytically using Fourier's second law [219]. Temperatures for the femtosecond laser pulses were not examined as they follow different mechanisms (non-equilibrium excitation of valence electrons) that are beyond the reach of this study [23, 217]. Also, since the maximum

temperature achieved with the laser was the main purpose of the calculation, material loss and phase changes (i.e. latent heats) were not taken into consideration for the heat flow. Additionally, since the maximum temperature is achieved at the laser spot, only one-dimensional heat flow was used for the calculation. The following heating (equation 3-1) and cooling (equation 3-2) equations were used to calculate the temperature during and after each laser pulse [219].

$$T(t < \tau) = \frac{2I_0(1-R)}{k}.\sqrt{\alpha t}.\sqrt{\frac{1}{\pi}} + T_0 \qquad \text{(equation 3-1)}$$

$$T(t > \tau) = \frac{2I_0(1-R)}{k}.\sqrt{\frac{1}{\pi}}.\sqrt{\alpha}.\left[\sqrt{t} - \sqrt{t-\tau}\right] \qquad \text{(equation 3-2)}$$

where $t$ is the time since the last pulse started (s), $\tau$ is the pulse duration (s), $I_0$ is the calculated laser intensity (equation 3-3); W.m$^{-2}$), $R$ is the surface reflectivity at the wavelength of the laser source (value used is 0.6352), $k$ is the thermal conductivity (16.3 W.m$^{-1}$.K$^{-1}$), $\alpha$ is the calculated thermal diffusivity (equation 3-4; m$^2$.s$^{-1}$) and $T_0$ is the starting temperature before the pulse begins (25 °C) [220].

$$I_0 = \frac{E}{\tau \pi r^2} \qquad \text{(equation 3-3)}$$

$$\alpha = \frac{k}{C_p \rho} \qquad \text{(equation 3-4)}$$

where $E$ is the energy of the pulse (J), $r$ is the Gaussian spot radius (m), $C_p$ is the specific heat of the material (500 J.Kg$^{-1}$.K$^{-1}$) and $\rho$ is the material density (8000 Kg.m$^{-3}$).

The accumulation of heat with successive pulses was accounted for by re-calculating how long a pulse duration would have to be from the starting temperature to reach the temperature at the end of the last pulse (equation 3-5). The new pulse duration was then directly inserted into equation 3-2 to calculate each cooling cycle.

$$t(T) = \frac{\left[\frac{k(T - T_0)}{2I_0(1 - R)\sqrt{\frac{1}{\pi}}}\right]^2}{\alpha} \quad \text{(equation 3-5)}$$

where T is the temperature reached just before the laser turns off (°C).

## 3.4. Electrochemical Corrosion Testing

Potentiodynamic anodic polarisation and electrochemical impedance spectroscopy were performed to examine the effect of the different types of laser patterning on the corrosive behaviour of S phase treated surfaces. For both testing conditions, electrochemical testing was carried out under room temperature conditions and using a standard three electrode setup. A platinum plated rod, a saturated calomel electrode and sample surface acted as the counter electrode, reference electrode and working electrode, respectively.

### 3.4.1. Potentiodynamic Anodic Polarisation

Potentiodynamic anodic polarisation was performed using Ringer's solution (9 g/L NaCl, 0.64 g/L $CaCl.2H_20$, 0.42 g/L KCl and 0.2 g/L $NaHCO_3$), which closely resembles bodily fluid, as the

electrolyte media [221]. A Gamry Interface 1000 instrument was used to measure current changes during the experiments. An open circuit potential test was initially performed for 3600 seconds to stabilise the surface voltage and obtain an estimated open circuit corrosion potential ($E_{OC}$). Anodic polarisation was then performed between -0.5 mV and 1.5 mV of the obtained $E_{OC}$ at a scan rate of 2 mV/s.

Following the tests, SEM imaging of the surfaces were used to look at the morphology of the samples as well as measure the total length of laser created channels within the tested areas for each sample. Cross-section SEM imaging was also used to roughly measure the extra surface area provided by the channels. By multiplying this extra surface by the total length of the channels in the test area it was possible to approximate the surface area tested for each electrochemical test performed. Tafel curve fitting (equation 3-6) was then utilised to determine the corrosion potential ($E_{Corr}$), corrosion current density ($I_{Corr}$) and corrosion rates of each sample type.

$$I = I_{Corr} \cdot \left[ e^{\frac{2.303(E-E_{Corr})}{\beta_A}} - e^{\frac{2.303(E-E_{Corr})}{\beta_C}} \right] \quad \text{(equation 3-6)}$$

where $I$ is the measured cell current (A), $I_{Corr}$ is the corrosion current (A), $E$ is the electrode potential (V), $E_{Corr}$ is the corrosion potential (V), $\beta_A$ is the anodic Tafel coefficient (V/decade) and $\beta_C$ is the cathodic Tafel coefficient (V/decade).

### 3.4.2. Electrochemical Impedance Spectroscopy

Electrochemical impedance spectroscopy (EIS) analysis was carried out using a Gamry Interface 1000 instrument. EIS testing was carried out following an open circuit potential test performed

for approximately 5400 seconds. The EIS test was performed using Ringer's solution (see section 3.4.1), an AC amplitude of ±10 mV and a frequency range between $10^{-2}$ and $10^{5}$ Hz with 10 points per decade. Automated computer extrapolation of the impedance magnitude and phase angle (between the voltage and current) from each decade of frequency tested were obtained using Lissajous plots.

## 3.5. Wettability Testing

Calculated surface energies and wetting properties of different sample surfaces were measured using 6 µl sessile drops of diiodomethane and Milli-Q water. Average contact angle measurements were taken using an Attension Theta Optical Tensiometer over a 15 s period after the drops had stabilised. Prior to testing, samples were cleaned using Teepol and allowed to fully dry. To account for the influence of ageing, treated and/or textured samples were prepared 3 months in advance. Surface free energy calculations were carried out according to Fowkes theory (as described by Rulison [222]).

## 3.6. Tribological Testing

### 3.6.1. Reciprocating Sliding Wearing

Sliding wear testing was carried out to obtain comparable surface wear resistance data, obtain texture structural integrity information, and to give insights into wear mechanisms present. Reciprocating sliding ball-on-plate wear testing was performed using a Phoenix TE79 tribometer and an 8 mm diameter alumina ball counterpart. Both dry and Ringer's (see section 3.4.1) lubricated conditions were tested. A total sliding distance of 5 m was used (5 mm/cycle

x 1000 cycles) with varying loads (50 gf, 300 gf, 500 gf) and maximum Hertzian contact pressures (Table 3-4). The volume of removed material was measured by multiplying the stroke length (5 mm) by the average cross-sectional surface area removed through wearing (measured using an AMBIOS XP-200 surface profilometer). Wear factor ($m^3$/Nm) was then calculated using the volume of material removed ($m^3$), the applied load (N) and the total sliding distance (m). Surface morphology of the wear tracks and damage to the textures were observed using SEM (JEOL 7000F) imaging.

*Table 3-4 Load and maximum Hertzian contact pressures during reciprocating sliding wear testing.*

| Load (gf) | Load (N) | Maximum Hertzian Contact Pressure (GPa) | |
|---|---|---|---|
| | | Unt | ASPN |
| 50 | 0.5 | 0.49 | 0.51 |
| 300 | 3.0 | 0.88 | 0.93 |
| 500 | 5.0 | 1.05 | 1.10 |

### 3.6.2. Pattern Durability Testing

To simulate real contact conditions, large area wear testing was carried out on an automated polishing machine (Struers LaboPol-5/LaboForce-3) using 3 µm diamond suspension and a polishing cloth (Struers MD-Dac). The LaboPol-5 and the LaboForce-3 were both kept at constant rotational speeds of 50 rpm and 250 rpm, respectively (Fig. 3-3). Throughout testing, the diamond suspension was reapplied every 15 seconds to replenish any counterpart particles that were lost due to the rotations. Samples were kept under a constant load of 10 N, while the amount of wearing was varied with time (Table 3-5). Samples were subjected to a total

sliding distance of 900 mm (90 mm x 5 (lines) x 2 (slide up/down)) per rotation of the LaboPol-5 (Fig. 3-3). Following testing, samples were ultrasonically cleaned (Teepol and acetone) and then imaged using an SEM (JEOL 7000F) to observe the damage to the surface and the textures.

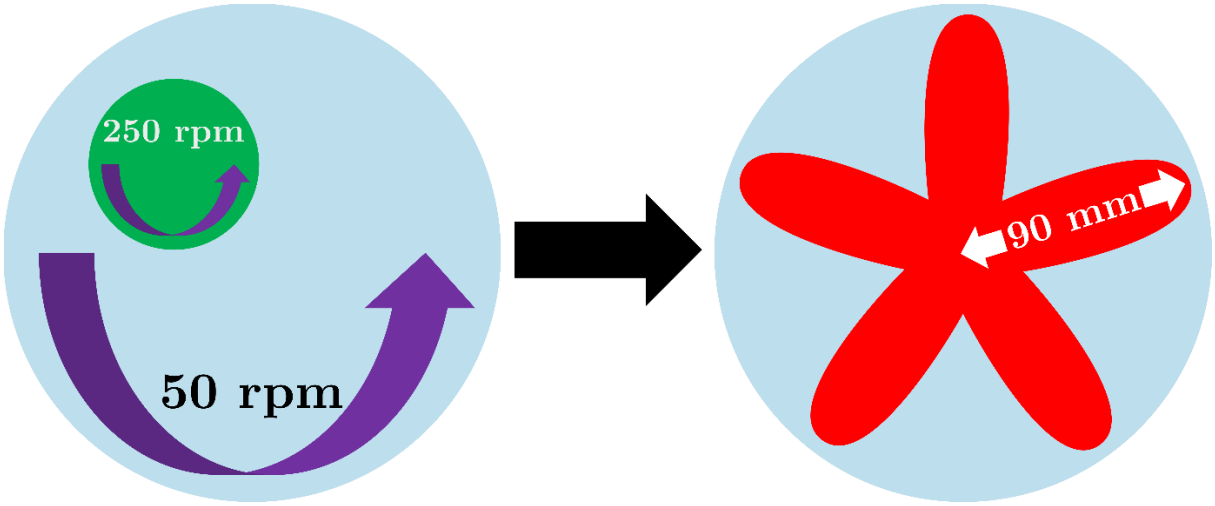



*Fig. 3-3 Illustration of the large area wear testing. Image on the left shows the setup for the test. Image on the right shows the sliding trajectory and distance travelled per rotation.*

*Table 3-5 Total sliding distances of the large area wear testing with changing cycle counts.*

| Cycle Name | Distance Per Rotation (m/rotation) | Rotations Per Minute (rotation/min) | Time (min) | Total Sliding Distance (m) |
|---|---|---|---|---|
| **Low** | 0.9 | 50 | 0.5 | 22.5 |
| **Medium** | 0.9 | 50 | 1.0 | 45.0 |
| **High** | 0.9 | 50 | 2.0 | 90.0 |

## 3.7. Antimicrobial Testing

Antimicrobial testing (shown in Fig. 3-4) against both Gram-positive *Staphylococcus aureus* (*S. aureus*) and Gram-negative *Escherichia coli* (*E. coli*) was carried out similar to the Japanese JIS Z 2801:2000 spread plate protocol previously described by Suzuki *et al.* [223]. Each bacterium was tested separately and from a single colony. Initially, the bacteria were put into 10 ml of sterile tryptone soya broth (TSB; Oxoid) and then cultured overnight in a mixing incubator at 100 rpm and 37 °C. Before testing, serial dilutions were made from the overnight cultured bacteria to achieve a bacterial suspension concentration of the order of $10^4$ cells/ml for *S. aureus* and $10^5$ cells/ml for *E. coli*. Freshly steam autoclaved (121 °C, 100 kPa, 15 minutes) and sterilised samples (3 of each sample type) were inoculated with 20 µl of the diluted bacterial suspension and then covered with a glass coverslip to stop the liquid drying. Samples were then place into an empty petri dish and incubated for 6 hours at 37 °C. Following incubation, samples were placed into 50 ml MD Falcon tubes containing 10 ml of sterile phosphate buffered saline (PBS; Sigma-Aldrich) and vortexed for 20 s to release bacteria into the solution. 100 µl aliquots of the PBS suspension were transferred and spread onto tryptone soya agar (TSA; Oxoid) filled petri dishes. 3 repeats were performed for each individual coupon (i.e. 9 dishes per sample type), before overnight incubation at 37 °C. Within this time, every viable bacterial cell was able to grow into colonies visible by eye.

Counting of the colony forming units (CFU) was performed using ImageJ (Trainable Weka Segmentation plugin). In situations where colonies had overlapped with each other, the number of CFU was determined by dividing the total area covered by the colonies by an

average colony size (N = 10). To determine the antimicrobial efficacy, comparisons were made to the control (equation 3-7). The control for this test was a 20 µl inoculate of the original $10^4/10^5$ cells/ml bacterial suspension directly inserted and vortexed into a 50 ml MD Falcon tube containing 10 ml of PBS. All the other steps were carried out in the same way as the samples (with 3 repeats).

$$Efficacy\ (\%) = \left[\frac{N_0 - N}{N_0}\right] x\ 100 \qquad \text{(equation 3-7)}$$

where N is the CFU count from the sample and $N_0$ is the CFU count from the control.

## 3.8. Statistical Analysis

Statistical analysis was carried out using one-way analysis of variance (ANOVA) with a Holm-Sidak post-hoc test. Differences were considered statistically significant when $p < 0.05$. In all cases without statistical analysis, the means and standard deviations are reported instead.

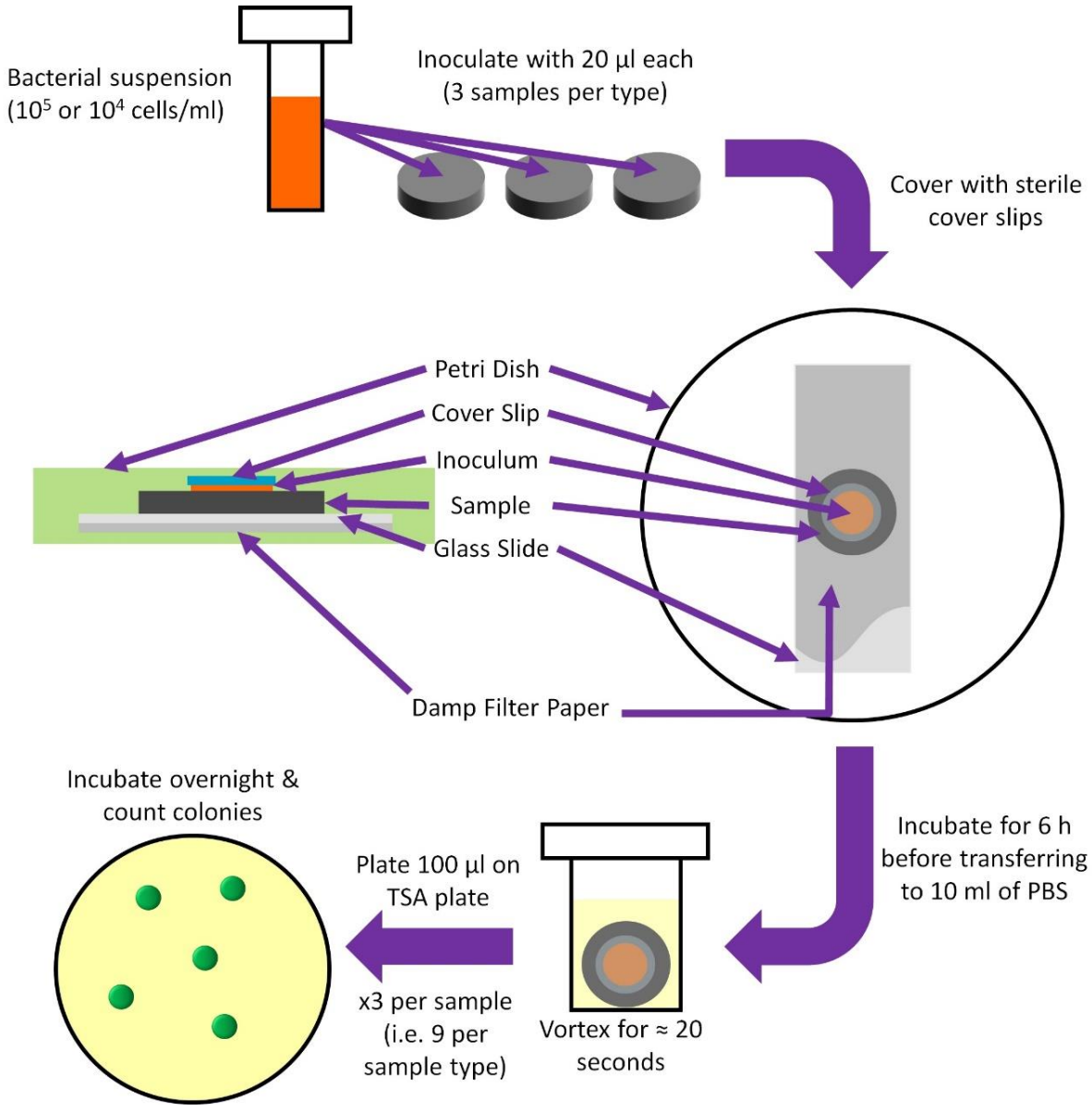



*Fig. 3-4 Overview of antimicrobial testing procedure.*

# CHAPTER 4 EXPERIMENTAL RESULTS

To examine the feasibility and capability of combining S phase surface hardening and ultrashort pulsed laser texturing, as outlined in the aims and objectives of this study (section 1), comparisons were initially made for different ultrashort pulsed laser texturing parameters (310 fs, 15 ns and 220 ns; section 4.2) against as-treated surfaces (ASPN; section 4.1). Following confirmation of the feasibility of femtosecond pulsed laser texturing of the S phase surface layer, various bio-inspired antibacterial surface textures were produced using the femtosecond laser texturing (section 4.3) under different rastering strategies (section 3.1.3). Due to the superior antibacterial performance of the triangular LIPSS, further detailed examinations were carried out to determine the surface characteristics, electrochemical performance and antibacterial efficacy of the triangular LIPSS (section 4.4). Finally, the mechanical performance and antibacterial durability of the triangular LIPSS produced on S phase treated surfaces are characterised and compared against untreated equivalent surfaces (section 4.5).

## 4.1. ASPN Surface Layer

The ASPN sample type was used to determine the conditions of the surface layer prior to texturing. Elemental depth profiling by GDOES revealed an approximately 8 µm deep nitrided surface layer following the 20 hours treatment at 400 ˚C. Semi-quantitative measurements from GDOES also demonstrated a maximum nitrogen content at the surface of approximately

35 wt% (Fig. 4-1A), with an improvement in hardness from 200 to 1130 (HV0.05) following treatment, which are all typical for an S phase surface treatment [8]. Cross-section SEM micrographs (Fig. 4-1B) confirmed the presence of a precipitate free S phase surface layer measuring approximately 8.17 ± 0.4 µm deep, which agrees with the depth profiling data (Fig. 4-1A). X-ray diffraction data (Fig. 4-2) further confirmed the formation of the S phase on the ASPN samples with characteristic left shifted austenite (ϒ) peaks at 42 ° (S1) and 47 ° (S2) without any appreciable peaks for chromium nitrides. Additionally, the ϒ(111) peak, present from the underlying bulk material, can also be seen at a 2θ angle of 44 °.

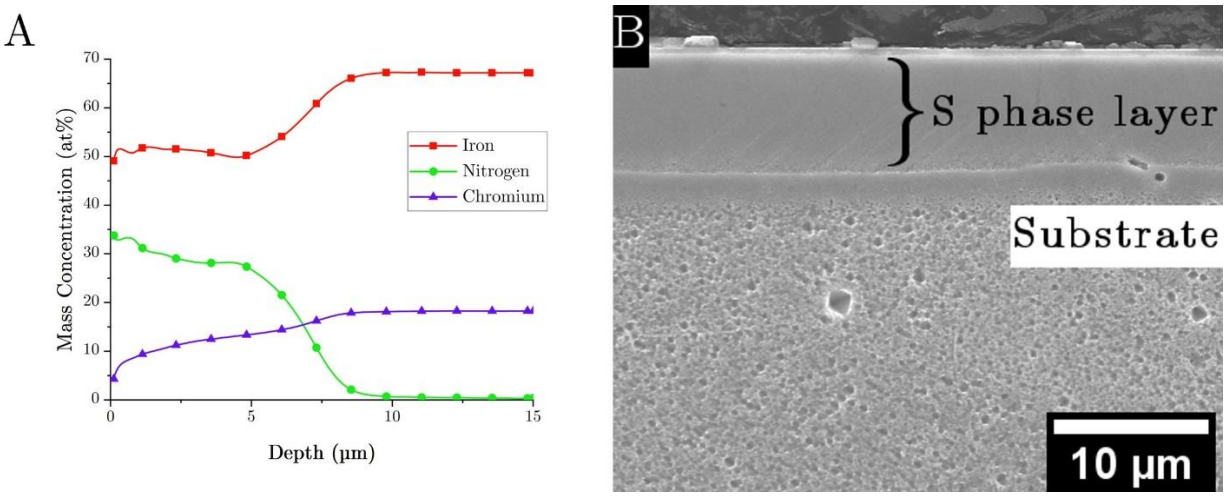



*Fig. 4-1 Characterisation of the ASPN sample type. (A) shows elemental depth profiling and (B) shows the cross sectional morphology of the S phase. Although only three elements are displayed in the elemental depth profiling, all elements present in the alloy were measured.*

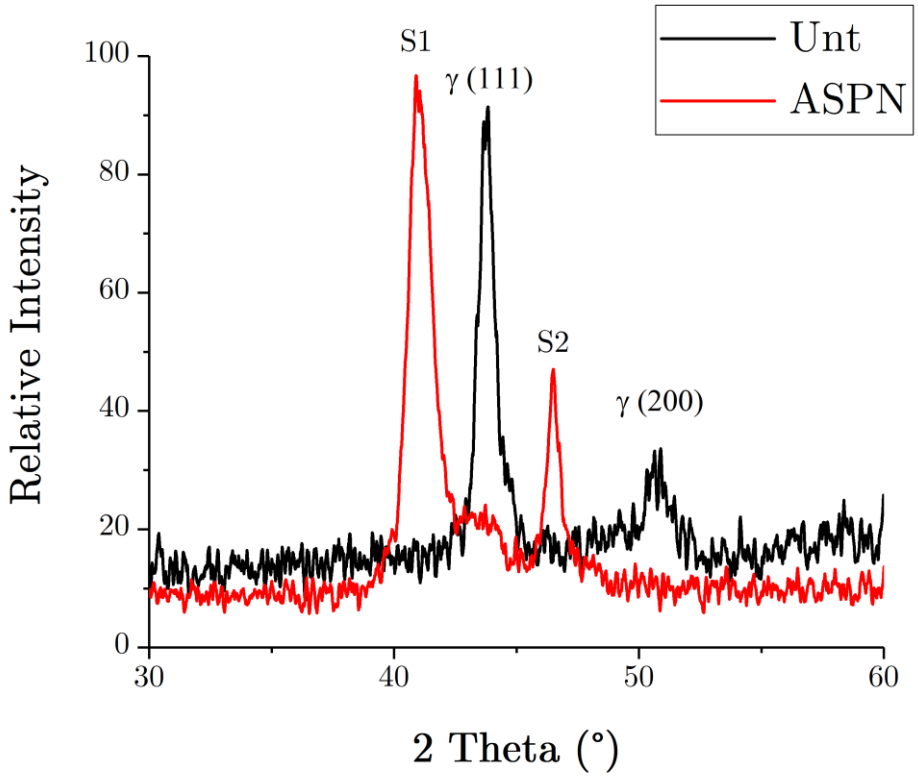



*Fig. 4-2 XRD phase comparison of Unt and ASPN samples.*

## 4.2. Nano- and Femtosecond Pulsed Channel Textures

The primary aim of this work was to ascertain whether decomposition of the S phase occurred, following channel texturing (310 fs, 15 ns & 220 ns) with either femtosecond or nanosecond laser sources (see section 3.1.3.1). Confirmation of the condition of the S phase following texturing were carried out using morphological analysis, compositional mapping, phase analysis and electrochemical corrosion behaviour. Analytical modelling of maximum surface temperatures following nanosecond laser texturing were also carried out to support and explain the observed S phase decomposition.

### 4.2.1. Morphology of Textured Surfaces

ASPN treated samples were textured using nanosecond and femtosecond pulsed laser texturing. From the electron micrographs (Fig. 4-3) it is clear to see that the spacing of the channels are consistent with the set hatch spacing of 300 µm. However, it is also obvious that the width of the channels varies between sample types. The channel widths become larger with increasing pulse duration, going from 29.97 ± 1.4 µm for the 310 fs sample type, to 52.44 ± 3.3 µm for the 220 ns sample type. The morphology of the tracks and the surrounding areas also varies greatly. Clear signs of melting and recasting are visible in both of the 15 ns and the 220 ns samples, with re-solidified metal droplets being spread within and around each channel (Fig. 4-3B3 & C3) [198]. The 15 ns textured samples display a smooth and perpendicularly layered inner track with regular surface cracking. The 220 ns textured samples demonstrate the most significant change in surface morphology, with the presence of vast amounts of droplets, especially within each channel. Additionally, the 220 ns tracks appear to have segments whereby the channels close in on themselves.

The 310 fs textured samples, on the other hand, present with minimal change in surface morphology to the surrounding areas of the channels. Fine nanoscale debris and particulates are present adjacent to channels, which most likely arise due to the ablation and back sputtering that occurs during the texturing process (Fig. 4-4B) [224]. No obvious signs of melting or cracking can be deduced from the surface images. Also, typical sub-micron ripple-like LIPSS textures can be clearly seen within the channels (Fig. 4-4A). Altered periodicity, changing orientation and presence of holes can be seen within the channels, which are likely

to be due to incomplete optimisation of the laser source and should be considered for the morphology of the surface following electrochemical corrosion testing.

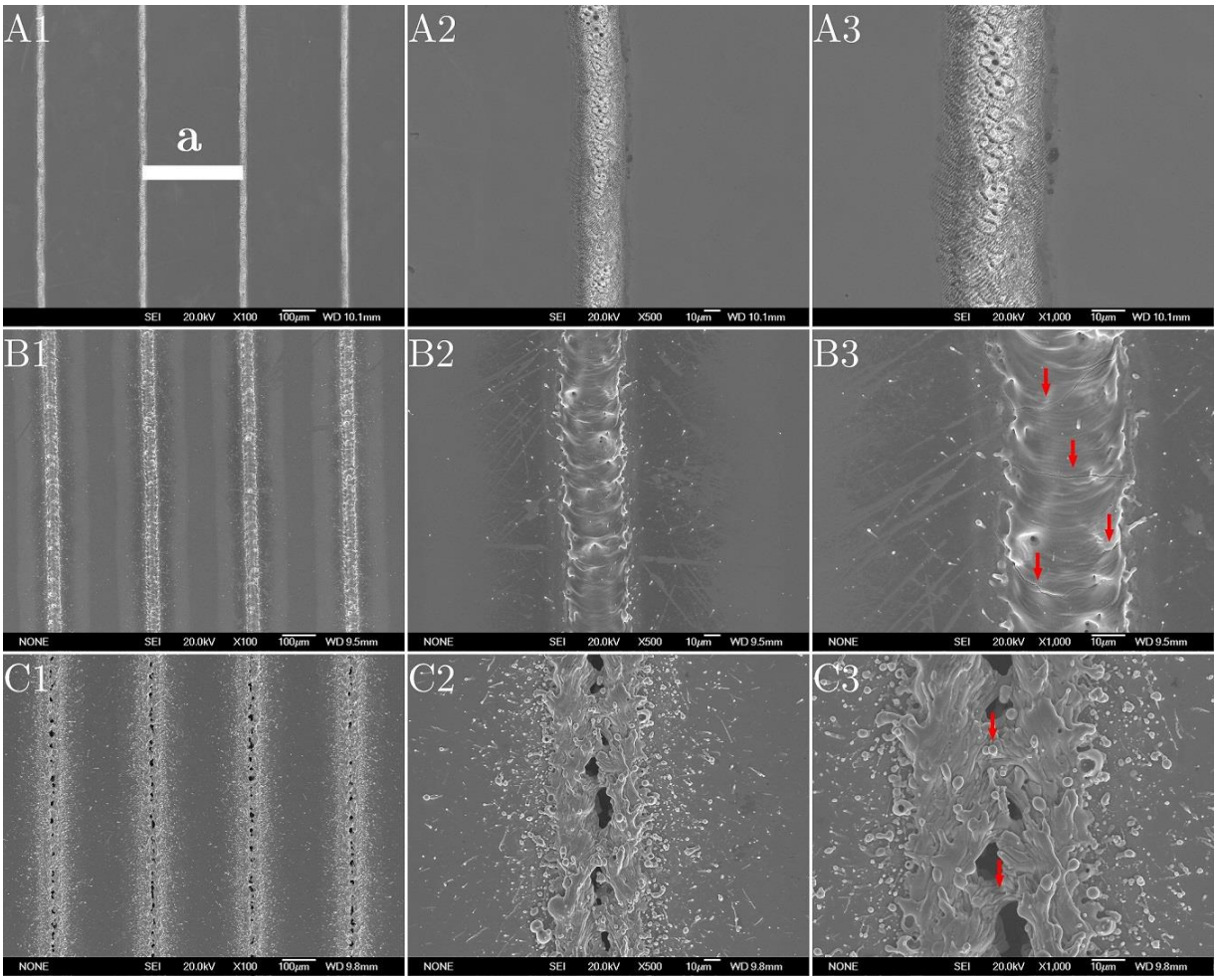



*Fig. 4-3 Surface morphology of the ASPN treated and channel textured samples. (A1-3) 310 fs samples, (B1-3) 15 ns samples and (C1-3) 220 ns samples. Hatch spacing (a) was also measured to be 300.6 ± 1.1 µm. Arrows indicate areas where cracks are present and where channels have closed in on themselves.*

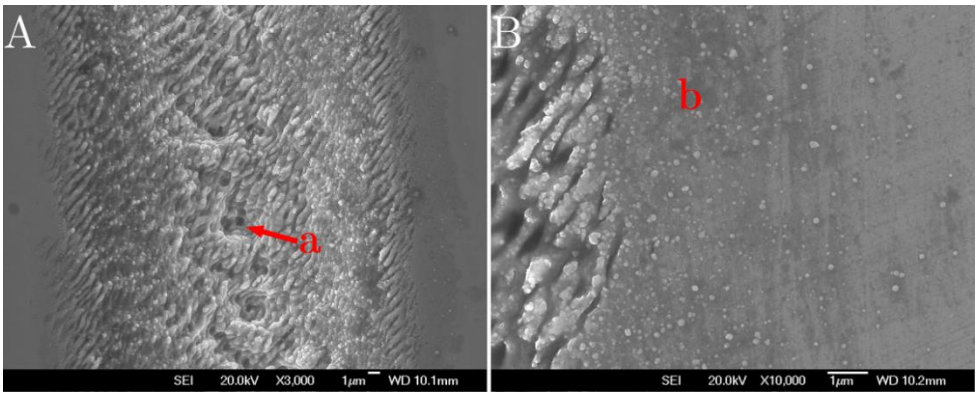



*Fig. 4-4 Surface morphology of 310 fs textured samples. The fine sub-micron ripple textures along each channel can be seen in image A, with some inconsistencies in the texturing process (a). Image B shows the back-sputtered particulates (b) found adjacent to the channels.*

### 4.2.2. Cross-Sectional Layer Structure

Comparisons of the structures underneath and around the laser textured channels were made with the as-treated sample type (ASPN, Fig. 4-1B) to determine any changes or damage to the S phase. Other than the addition of the channels and LIPSS textures, no visible changes can be distinguished in the cross-sections of the 310 fs treated samples (Fig. 4-5A1-3). Even under backscattered electron imaging, no variation in contrast density can be seen (Fig. 4-5A3). EDS mapping (Fig. 4-6A & B) also helped to show no discernible changes to the elemental profile across the 310 fs channels. On the other hand, both nanosecond laser textured samples displayed clear signs of damage to the surface layer. Obvious cracks can be seen near the surface of the 15 ns textured samples (Fig. 4-5B2-3), while complete loss of the S phase is observed within and atop of the channels in the 220 ns textured samples (Fig. 4-5C1 & 6D). Moreover, EDS mapping of the cross-sectional areas of the nanosecond textured samples conclusively show the altered elemental profile (Fig. 4-6B & C). In particular, the formation of localised areas of high chromium, high nitrogen, low iron and low nickel in the superficial

regions of the textures (as indicated in Fig. 4-6) help to confirm the presence of chromium nitrides. Additionally, both nanosecond textured samples also present clear signs of general compositional changes at the surface (Fig. 4-5B3 & C3) and initiations of the formation of lamellar structures (Fig. 4-5B2-3 & C2-3). Confirmation of the composition of these formations was made using EDS spot analysis (Table 4-1).

Table 4-1 shows the changing chemistry within these regions in comparison to surface composition data from ASPN samples. A clear increase of Cr, N and Mo was detected on the 15 and 220 ns textures samples, with the latter showing the greatest increase. However, the concentration of Fe and Ni were reduced following both ns textures (also found under EDS mapping (Fig. 4-6)). Again, the most profound changes were observed following the 220 ns texturing. On the other hand, the only observable changes found with the 310 fs textured samples were with the detected compositions of S and Mn, which were both only slightly altered.

The formation of the lamellar structures (Fig. 4-5) and compositional changes (Table 4-1 & Fig. 4-6) on the nanosecond textured samples have already demonstrated the formation of chromium nitride precipitates, and hence TEM analysis was not carried out on these sample types [225]. Instead, TEM analysis was carried out to conclusively confirm whether the S phase on the 310 fs samples had remained precipitate free. As the textured surface was directly in contact with the femtosecond laser beam, a protective layer of Pt was deposited before ion beam cutting and milling (Fig. 4-7A). Cross-sectional TEM microstructures shown in Fig. 4-7B and C revealed the contours of the texture at the top surface. Observations at the areas just beneath the contour line confirmed no CrN precipitation (Fig. 4-7B & C). Selected area

diffractions taken from the S phase area showed FCC structured patterns (Fig. 4-7D) with expanded austenite d-spacing, consistent with expected XRD data [8]. High density microstructure defects, such as micro-twins (Fig. 4-7B) and dislocations, were presented within the layer, which are the characteristic of the S phase layer [8, 131].

*Table 4-1 Elemental concentrations (wt%) from the location shown in Fig. 4-5. ASPN spots were taken from the surface.*

| Sample | Cr | Fe | N | Ni | Mo | Mn | Si | S |
|---|---|---|---|---|---|---|---|---|
| **ASPN** | 16.73 | 65.08 | 4.32 | 9.73 | 1.75 | 1.88 | 0.48 | 0.03 |
| **310 fs** | 16.40 | 66.34 | 4.10 | 9.52 | 1.66 | 1.58 | 0.36 | 0.04 |
| **15 ns** | 21.10 | 61.45 | 5.77 | 7.49 | 2.01 | 1.88 | 0.25 | 0.05 |
| **220 ns** | 24.86 | 51.17 | 10.08 | 8.95 | 2.99 | 1.54 | 0.41 | 0.00 |

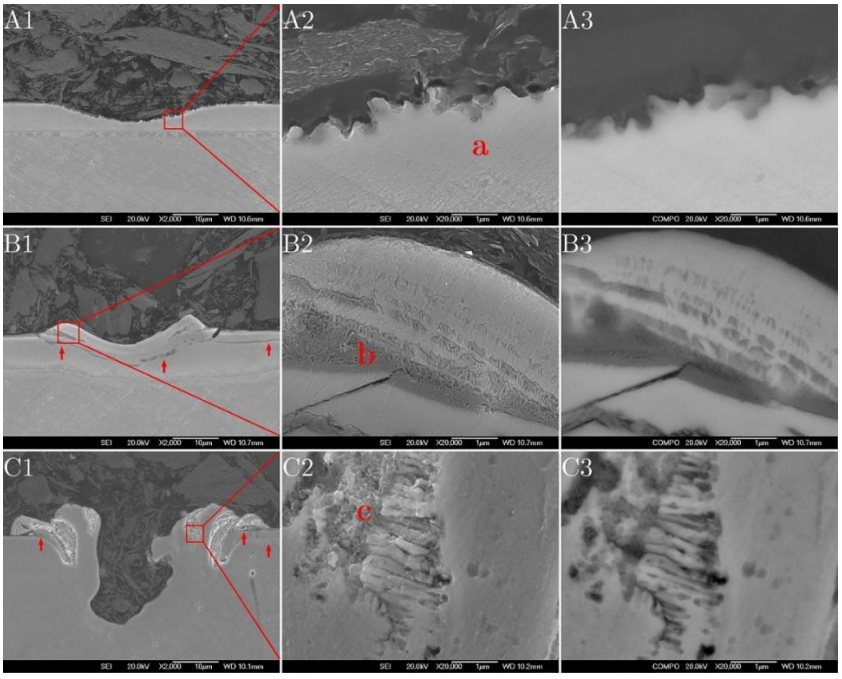



*Fig. 4-5 Secondary (A1-A2, B1-B2 and C1-C2) and backscattered (A3, B3 and C3) electron images of cross-sectional layer structures of the channel textured samples. (A1-A3) 310 fs samples, (B1-B3) 15 ns samples and (C1-C3) 220 ns samples. Areas of material cracking are indicated with an arrow. Labels (a, b and c) indicate locations of elemental spot analysis listed in Table 4-1.*

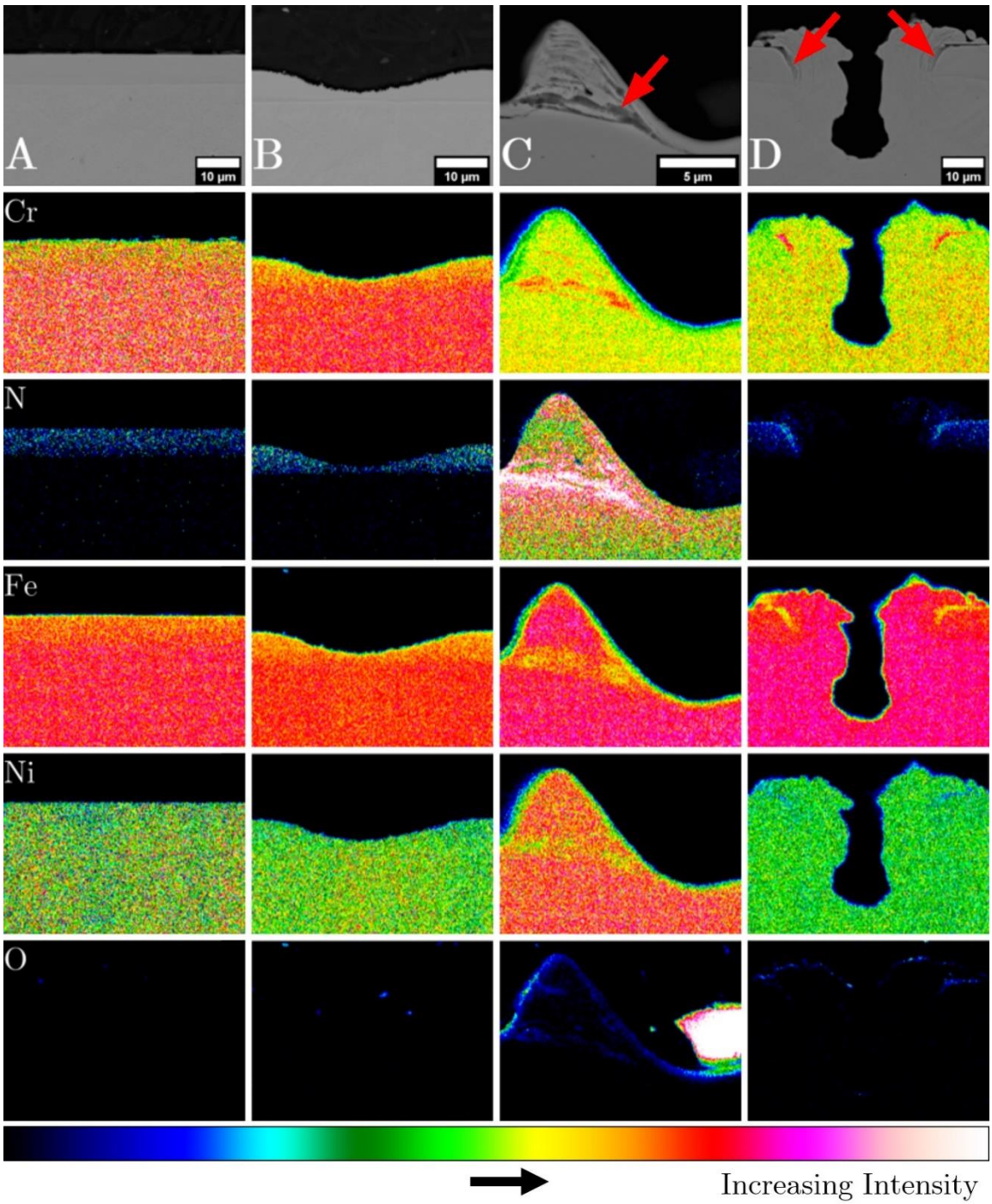



*Fig. 4-6 Backscattered electron imaging (top row) and EDS elemental mapping through the cross-sectional areas of each sample type: (A) ASPN samples, (B) 310 fs textured samples, (C) 15 ns textured samples and (D) 220 ns textured samples. Samples are organised in columns, with each row representing a different element (as labelled). Colour intensity mapping used is relative to each individual element map. Arrows correspond to sites of precipitation that match elemental composition changes in the related maps.*

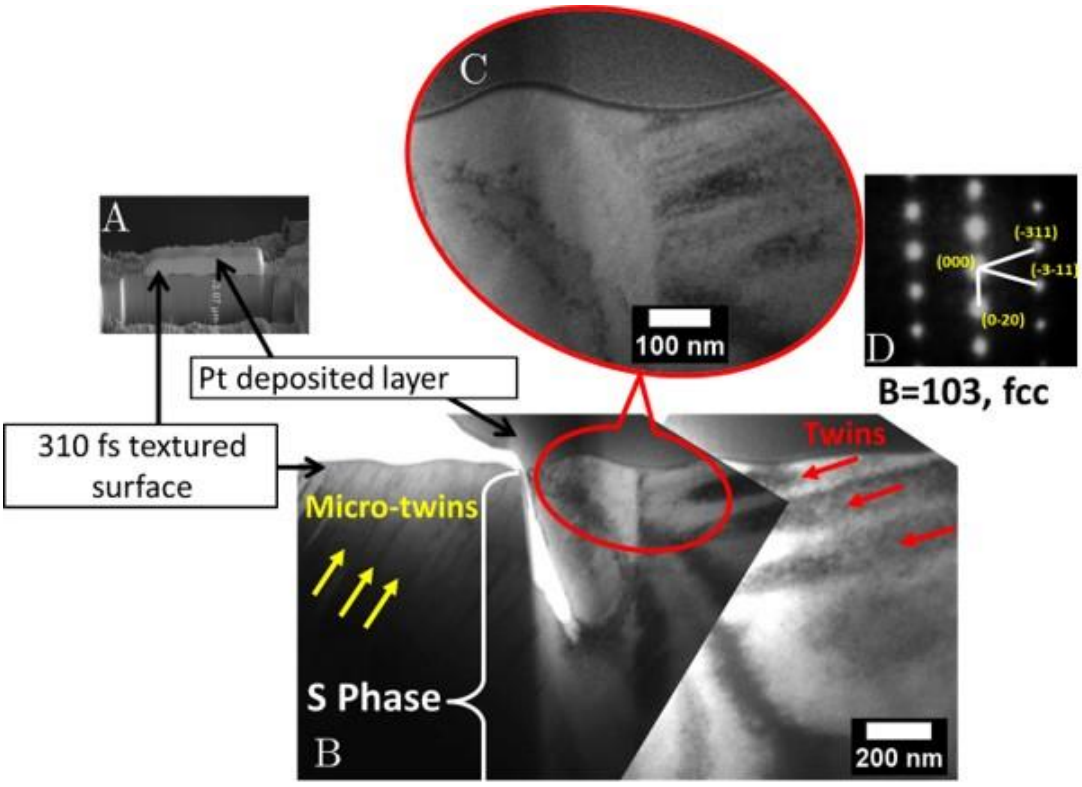



*Fig. 4-7 Cross-sectional TEM sample preparation and characterisation of the 310 fs textured sample: (A) SEM image of FIB cutting and milling of the sample for thin TEM specimen preparation; (B) TEM image of the S phase layer, showing the surface texture contour line; (C) enlarged 310 fs textured top surface, and (D) selected area diffraction pattern from S phase area shown in (C).*

### 4.2.3. Predicted Surface Temperatures

To attribute the rapid deterioration of the S phase following nanosecond texturing, 1D heat conduction modelling was carried out to predict the maximum possible temperatures at the surfaces of the samples following single (Fig. 4-8) and multiple (Fig. 4-9) pulses from the laser source. No sources of heat loss (e.g. phase changes & material loss) other than conduction have been accounted for in the model. Therefore, in both cases (single and multiple pulses) it can be regarded as the maximum possible temperature following laser heating. Due to the

significantly different inherent mechanism of action, a temperature model for femtosecond laser texturing was possible within this study (as previously explained in section 3.3).

The calculated peak temperatures ($T_{peak}$)were found to vary greatly between the two laser settings, with the 15 ns pulses achieving approximately 18000 °C after a single laser pulse, while the 220 ns pulse reaching a much lower, but still incredibly high, temperature of around 8000 °C (Fig. 4-8). Following multiple pulses, only a limited amount of heat accumulation occurs before an equilibrium between the heating and cooling rates is achieved (Fig. 4-9). Although counterintuitive, the higher temperatures reached following a shorter pulse can be explained as a result of the much greater laser intensity of the 15 ns pulse ($2.91 \times 10^{12}$ $Wm^{-2}$) in comparison to the 220 ns pulse ($3.22 \times 10^{11}$ $Wm^{-2}$).

The cooling rates of both pulse durations follow a similar trend, leading to a saturation temperature ($T_{sat}$) of 390 °C for the 15 ns pulses and 577 °C for the 220 ns pulses. Additionally, by taking an average temperature across the data in Fig. 4-9 and then calculating the time taken for the laser to move the distance of one spot diameter (Table 3-2) it is possible to approximate the temperature (757.24 °C (15ns) and 1111.45 °C (220 ns)) and length of time (227.27 µs (15 ns) and 200 µs (220 ns)) any one spot on the sample will be subjected to. Similarly, using extended version of the data presented in Fig. 4-8, it is also possible to predict average temperatures for single pulses of each laser (729.2 °C (15 ns) and 981.8 °C (220 ns)).

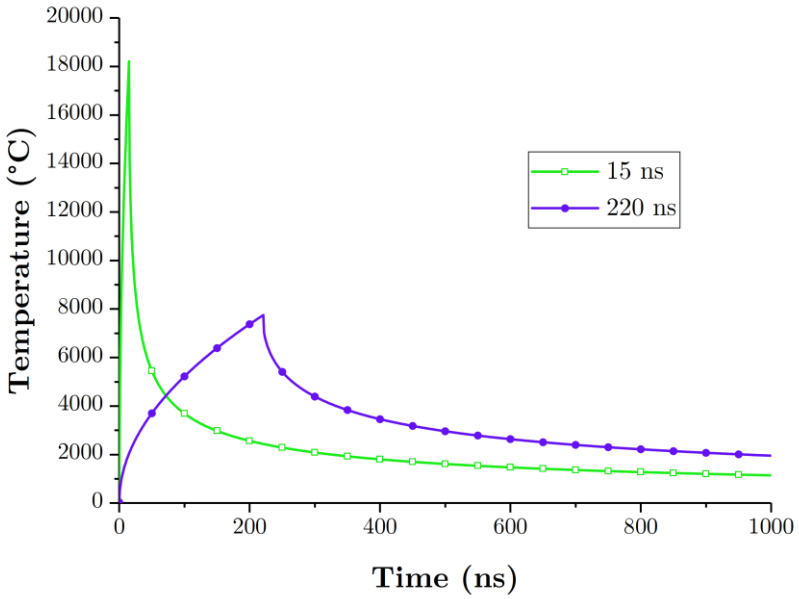



*Fig. 4-8 Single pulse surface temperature modelling following 15 ns and 220 ns laser pulses.*

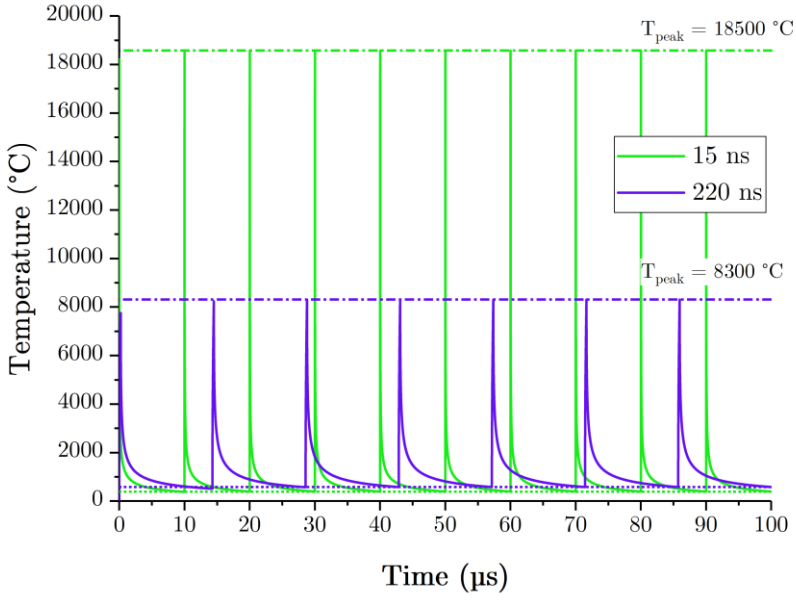



*Fig. 4-9 Multiple pulse surface temperature modelling following 15 ns and 220 ns laser pulses. Dash and dot lines indicate the peak temperatures, while the dotted lines show the saturation temperatures.*

## 4.2.4. Corrosion Behaviour

### 4.2.4.1. Potentiodynamic Anodic Polarisation

The calculated corrosion rates (Table 4-2) demonstrate that the as-treated (ASPN) and 310 fs textured samples possess the best average resistance to corrosion (4.5 and 30.2 µm/year, respectively) across the tested area. Both sample types displayed significantly better predicted corrosion rates than the 15 ns (264.4 µm/year) and 220 ns (685 µm/year) textured samples. Correspondingly, the corrosion current density ($I_{Corr}$) follows the same trend for all sample types. Corrosion potential ($E_{Corr}$) data revealed that the ASPN and femtosecond textured samples (-206 and -218 mV/SCE, respectively) were the most noble. On the other hand, the 15 ns textured samples showed the most negatively charged corrosion potential (-567 mV/SCE). The 220 ns textured surface displayed a more noble corrosion potential (-294 mV/SCE), which can be attributed to the extensive oxidation that occurs during thermal laser texturing [198].

*Table 4-2 Quantitative corrosion measurements of the channel textured sample types.*

| | **ASPN** | **310 fs** | **15 ns** | **220 ns** |
|---|---|---|---|---|
| **$I_{corr}$ (µA/cm²)** | 0.392 | 2.61 | 22.8 | 59.1 |
| **$E_{corr}$ (mV/SCE)** | -206 | -218 | -567 | -294 |
| **Corrosion Rate (µm/year)** | 4.5 | 30.2 | 264.4 | 685.0 |

The polarisation curves (Fig. 4-10) match up clearly to the calculated corrosion potentials. As expected, multiple signs of re-passivation are obvious on the ASPN samples. The 15 ns textured samples also show signs of current density stagnation between the potentials of approximately

-0.3 and 0.2 mV/SCE. Almost no signs of passivation can be observed with the 220 ns textured samples, while only limited passivation is present on the femtosecond textured samples.

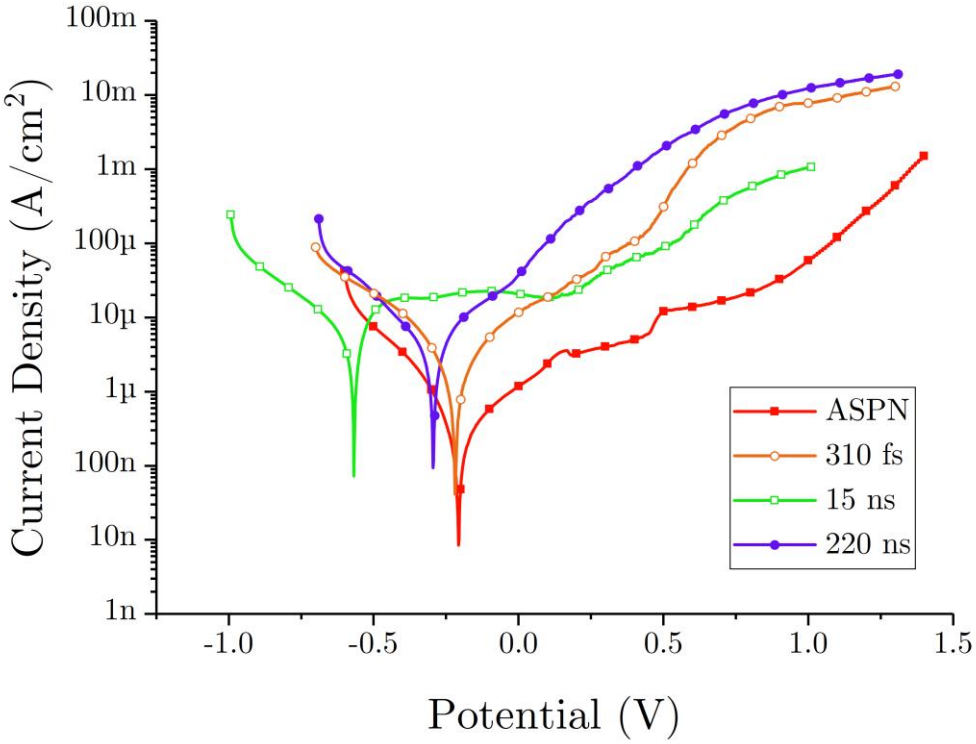



*Fig. 4-10 Polarisation curves of the different channel textured sample types in Ringer's solution.*

Surface SEM imaging was carried out following anodic polarisation testing in order to observe the condition of the textured surfaces (Fig. 4-11). Extensive damage to the surface structure can be seen on both nanosecond textured samples. On the surface of the 15 ns samples, grain boundary corrosion related to the precipitation of chromium nitrides can be clearly distinguished (Fig. 4-11B1-2) [8]. Whereas, the surface of the 220 ns samples reveals large amounts of cracks perpendicular to the channels as a result of the thermal shock following the

rapid heating and cooling cycles [198]. On both nanosecond textured samples there are signs of partial (15 ns) and complete (220 ns) removal of the bulges at the sides of the channels (Fig. 4-11B & C). On the other hand, the 310 fs channels show almost no change or damage to the surface, even under backscattered electron imaging (Fig. 4-11A1-2). In particular, the fine LIPSS textures within the channels demonstrate excellent resistance to the Ringer's solution, despite the vastly greater surface area.

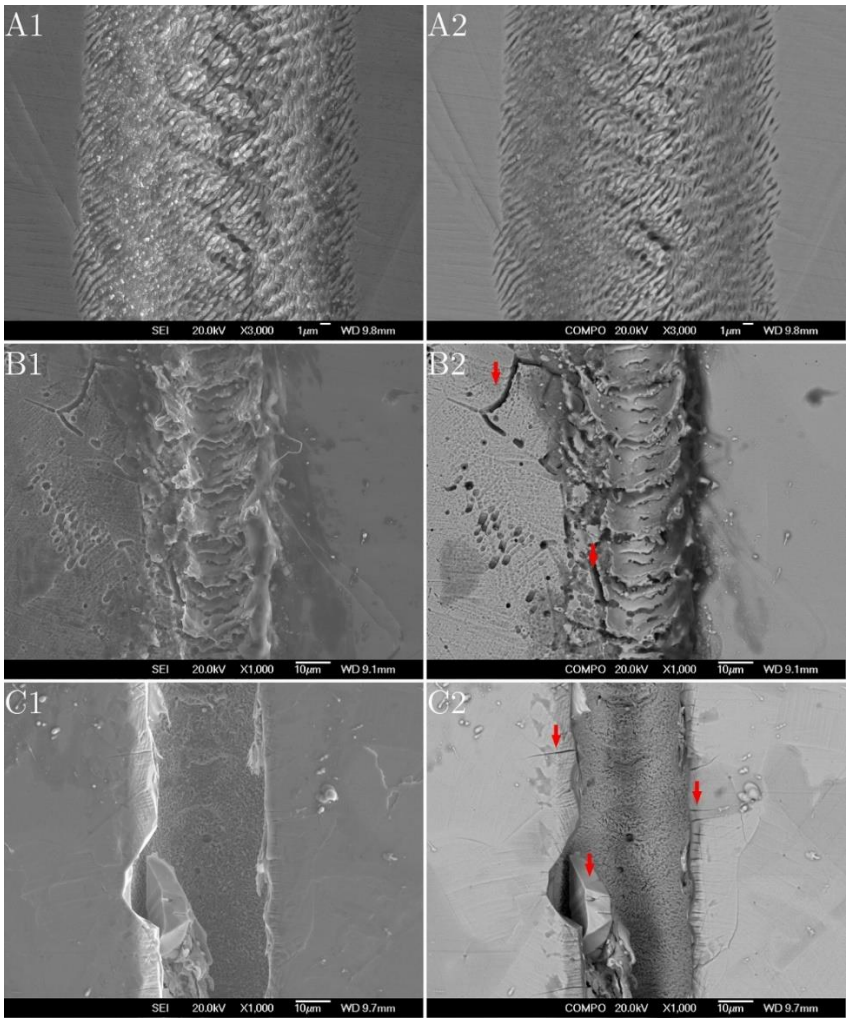



*Fig. 4-11 Secondary and backscattered electron imaging following anodic polarisation testing of (A) 310 fs, (B) 15 ns and (C) 220 ns textured samples. Arrows indicate areas of material damage or profound corrosion attack.*

#### 4.2.4.2. Electrochemical Impedance Spectroscopy

The Bode (Fig. 4-12) and Nyquist (Fig. 4-13) plots both demonstrate correlating results to the data obtained through anodic polarisation testing, with the best total resistance to polarisation ($R_f + R_p$; see Fig. 4-14 for explanation of terms) being found in the ASPN and 310 fs textured samples (Table 4-3). The superior impedance (real component, imaginary component and total magnitude) of these surfaces over the nanosecond textured surfaces can be further discerned from the data obtained at the lowest frequency ($10^{-2}$ Hz). Additionally, the phase angle differences in the bode plots (Fig. 4-12) indicate a change in surface structure with the nanosecond textured surfaces, whereas almost identical trends are captured with the ASPN and 310 fs textured samples. This is particularly highlighted by the different equivalent circuits used for each sample type fitting (Fig. 4-14), with both nanosecond textured surfaces demonstrating some form of diffusion based impedance (Warburg impedance) that can be attributed to the formation of a thick porous surface oxide layer as a result of the rapid heating and cooling laser texturing process (Fig. 4-6; Fig. 4-15). This is also clearly demonstrated by the slope of the Nyquist plot of the 220 ns textured sample (Fig. 4-13 inset) [198, 226].

Furthermore, data collected from Raman spectroscopy (Fig. 4-15) also help to confirm the presence, and increased thickness, of the surface oxides (as well as the presence of some carbon deposits) following laser texturing [227, 228]. From Fig. 4-15, a significant increase in overall surface oxides is observed for all textured surfaces, with both nanosecond textured surfaces undergoing the most extensive surface oxidation, with particularly significant increases of $CrO_2$ ($\approx 680$ $cm^{-1}$) [229, 230]. This rapid increase of the oxide layer following

nanosecond laser texturing likely contributes to the significantly larger $R_f$ values measured for the 15 ns and 220 ns samples, in comparison with the ASPN and 310 fs samples (Table 4-3).

The large disparity in $R_f$ values between the 15 ns and 220 ns can be attributed to the depth of texturing (i.e. whether the S phase surface layer is penetrated; Fig. 4-5 & Fig. 4-6). For 15 ns textured samples, the S phase surface layer is not fully penetrated, and therefore, the rapidly formed and porous oxide develops on the S phase layer, which forms the outer electrolyte-S phase interface, and gives rise to the large resistance to polarisation ($R_f$). On the other hands, for the 220 ns laser textured samples, the S phase layer is fully penetrated, and therefore, the rapidly formed and porous oxide can develop on both the S phase surface, and the exposed untreated surfaces. Consequently, this creates a situation whereby there is potential to bypass the S phase surface layer (electrolyte-S phase interface) to a large extent, through the exposed untreated surface (electrolyte-untreated bulk interface), and therefore results in the significantly larger $R_p$ value. No such disparity, or change in absolute measured value, of the Rf and Rp value are observed for the 310 fs samples, in comparison with the ASPN treated surface (Table 4-3).

*Table 4-3 Measurements of resistance (Ω) to polarisation of the channel textured sample types.*

| | **ASPN** | **310 fs** | **15 ns** | **220 ns** |
|---|---|---|---|---|
| **$R_f$** | 58.98 | 43.80 | $1.93 \times 10^5$ | 2096 |
| **$R_p$** | $3.202 \times 10^6$ | $3.203 \times 10^6$ | 404.8 | $1.97 \times 10^4$ |
| **$R_{Total}$** | $3.202 \times 10^6$ | $3.203 \times 10^6$ | $1.93 \times 10^5$ | $2.18 \times 10^4$ |

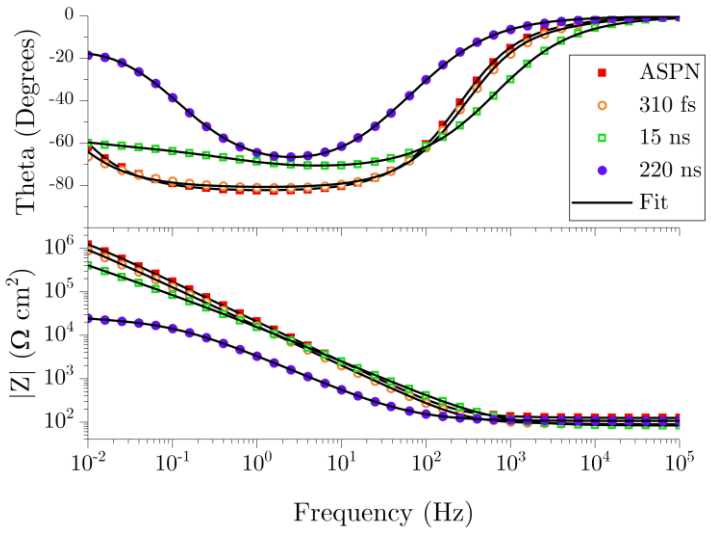



*Fig. 4-12 Bode phase (top) and magnitude (bottom) plots of the channel textured sample types. Fitted lines were made according to the equivalent circuit models in Fig. 4-14.*

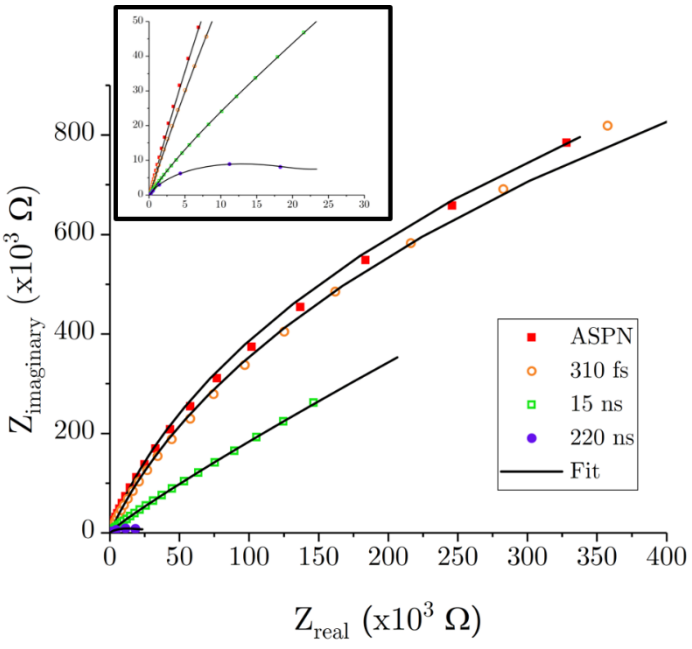



*Fig. 4-13 Nyquist plot of impedance of the channel textured sample types. Fitted lines were made according to the equivalent circuit models in Fig. 4-14. Inset magnifies the $Z_{real}$ region between 0-30 $x10^3$ Ω to show the 220 ns plot more clearly.*

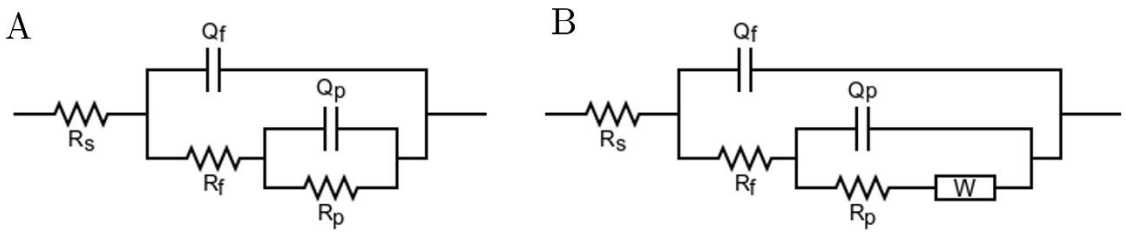



*Fig. 4-14 Equivalent circuit models used for EIS analysis where $R_s$ is solution resistance, $R_f$ (resistance to polarisation) & $Q_f$ (double layer capacitance) relate to the outer electrolyte-sample interface layer, $R_p$ & $Q_p$ relate to the S phase-untreated bulk interface, and W relates to the Warburg impedance associated with diffusion resistance. Model A was used for ASPN and 310 fs textured samples. Model B was used for 15 ns and 220 ns textured samples.*

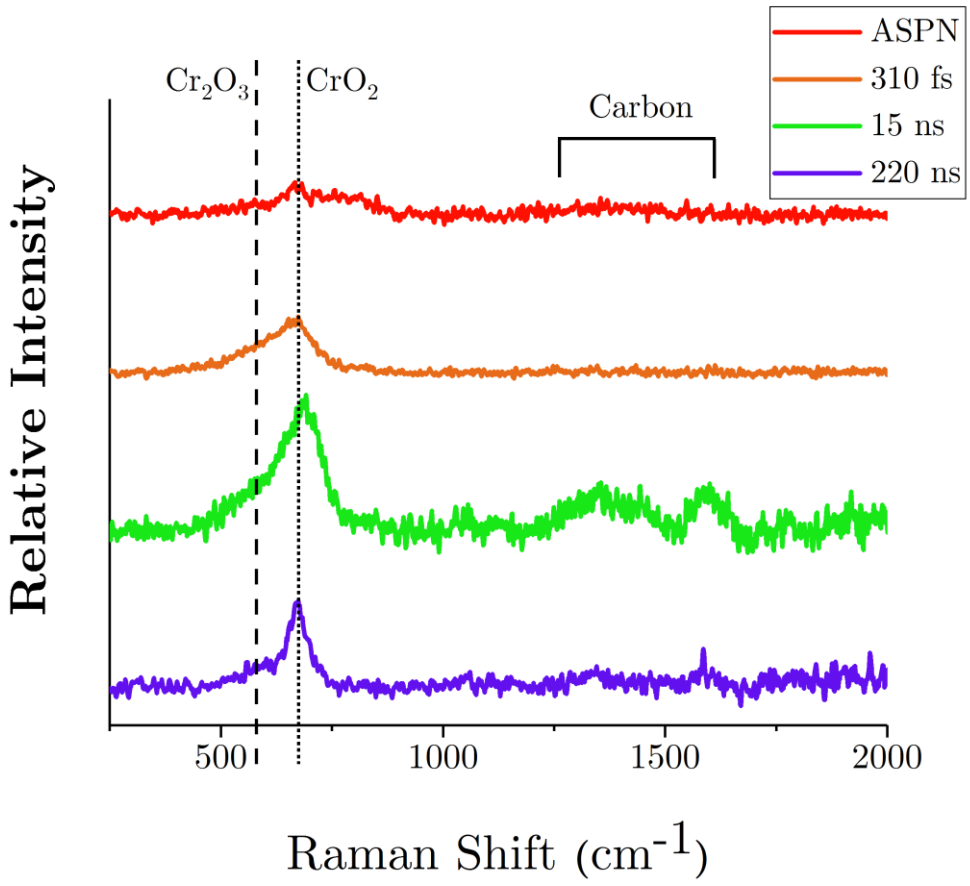



*Fig. 4-15 Raman spectroscopy of all the channel textured sample types. Peaks relating to surface carbon deposition and surface oxidation ($Cr_2O_3$ and $CrO_2$) are labelled accordingly.*

## 4.3. Antibacterial S Phase Texturing

Based on the findings of section 4.2, only femtosecond laser texturing was deemed viable for use with S phase treated surfaces. In response, multiple bio-inspired antibacterial textures (see section 3.1.3.2) formed using femtosecond pulsed laser texturing were characterised. In addition to describing the surface morphology and layer structure, composition mapping was also carried out to confirm the precipitate-free nature of the S phase. Finally, the antibacterial efficacy of the textures, including the 310 fs channel texture from section 4.2, were compared to determine an optimal texture for further characterisation (section 4.4) and durability analysis (section 4.5).

### 4.3.1. Texture Morphology

The surface morphology of four distinct types of textures formed using femtosecond laser texturing on S phase treated surfaces are shown in Fig. 4-16 & Fig. 4-17. Detailed analysis of the morphology & features of the ASPNΔ sample type can be found in section 4.4. Both ASPNL1 and ASPNL2 samples present with cross-hatched textures with similar vertical/horizontal peak spacings (a; 23.7 ± 1.1 µm and 25.1 ± 1.6 µm, respectively) and 45 ° diagonal peak spacing (b; 34.6 ± 0.9 µm and 35.4 ± 1.1 µm, respectively). Moreover, the peak tip diameter (c) for both samples are comparable as well (Table 4-4). The surface morphology of the ASPNS samples are significantly different to the lotus leaf inspired textures (ASPNL1 & ASPNL2; Fig. 4-17), with minimal peaks and valleys present. Instead, shallow channels with similar widths to the laser spot size (c; 27.2 ± 0.8 µm) separate the square/diamond shark skin features. From Table 4-4,

it can be observed that the horizontal/vertical spacing (a) of the ASPNS sample type is also much larger than both of the lotus-like textures.

Severe re-deposition and back-sputtering are visible within the valleys of the ASPNL2 samples in the higher magnification imaging found in Fig. 4-16B2, which consequently have caused roughening and rounding of the surface. This effect can be attributed to the extra repeated laser runs over for the generation of the higher aspect ratio of the ASPNL2 sample type in comparison with the ASPNL1 sample type (described in section 3.1.3.2). Aside from the re-deposition, only ripple LIPSS features are present on the ASPNL2 samples, whereas nanoscale pillars can be seen on the surface of the ASPNL1 samples. As a result of this, the channel spacing (S1; Table 4-4) between the two textures differ, with the ASPNL2 showing smaller channel spacing. Similar channel spacing is found on the ASPNS samples, but with more shallow appearing valleys (Fig. 4-17A2).

*Table 4-4 Pattern spacing, tip diameter and channel spacing of the ASPNL1, ASPNL2 and ASPNS textures.*

| Sample | a (µm) | b (µm) | c (µm) | S1 (nm) |
|---|---|---|---|---|
| **ASPNL1** | 23.7 ± 1.1 | 34.6 ± 0.9 | 7.1 ± 1.2 | 553.9 ± 61.3 |
| **ASPNL2** | 25.1 ± 1.6 | 35.4 ± 1.1 | 7.2 ± 1.0 | 430.2 ± 103.9 |
| **ASPNS** | 111.3 ± 2.3 | 22.2 ± 3.1 | 27.2 ± 0.8 | 547.6 ± 216.7 |

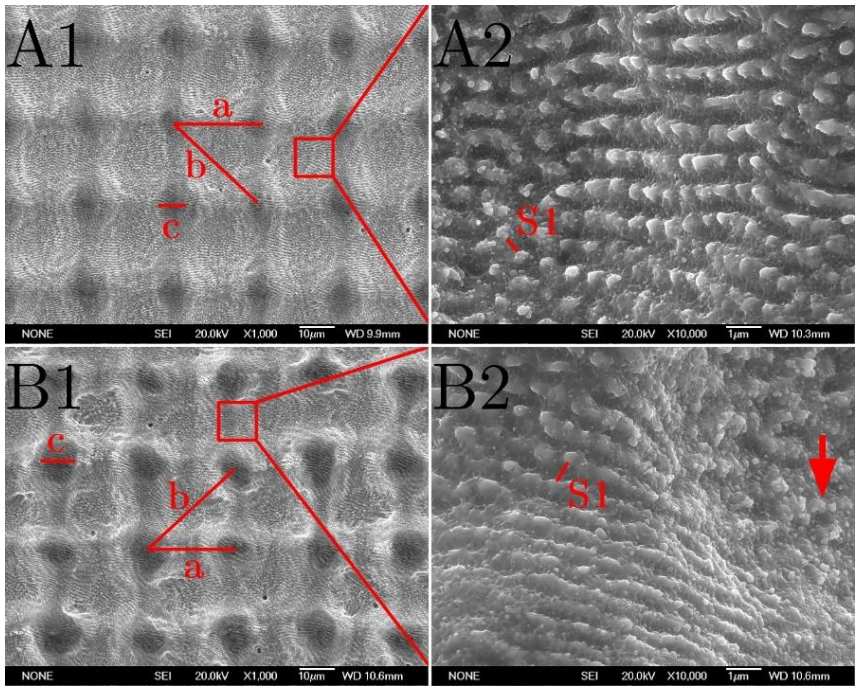



*Fig. 4-16 Surface morphology of the (A) ASPNL1 and (B) ASPNL2 textures. Labels (also used in Table 4-4) correspond to the 90 ° peak spacing (a), 45 ° peak spacing (b), tip diameter (c) and channel spacing (S1). Arrow indicates location of severe back-sputtering.*

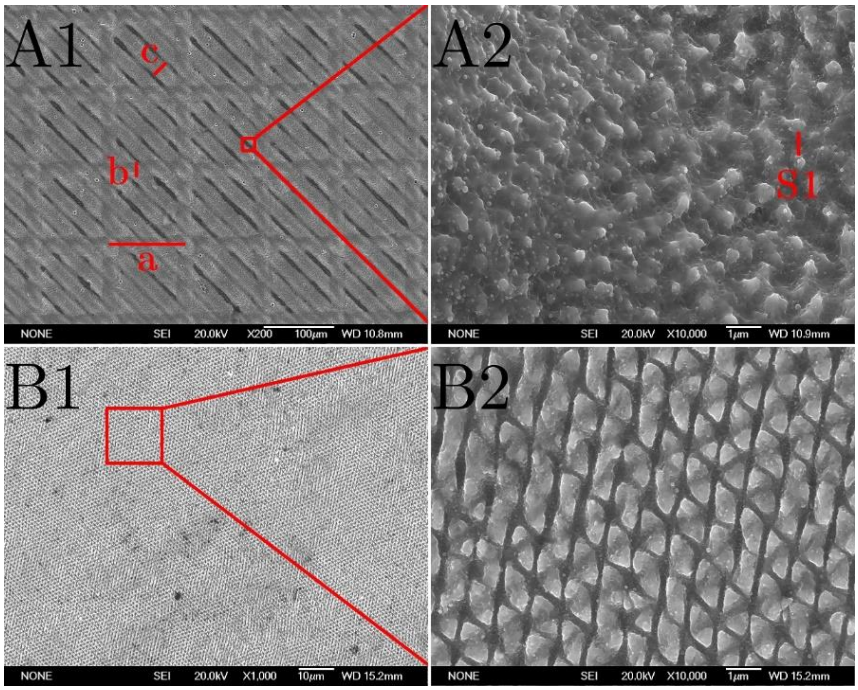



*Fig. 4-17 Surface morphology of the (A) ASPNS and (B) ASPNΔ textures. Labels (also used in Table 4-4) correspond to the 90 ° spacing (a), 45 ° inner spacing (b), channel width (c) and channel spacing (S1). Labelling and in-depth detail of the ASPNΔ sample can be found in section 4.4.*

### 4.3.2. Cross-Sectional Layer Structure

The most notable difference between the cross-sectional layer structure of the different textures is the depth of the valleys (Fig. 4-18 & Table 4-5), with the textures on the ASPNL2 samples frequently penetrating through the S phase treated layer by approximately 5.1 ± 2.1 µm. On the other hand, the depth of the S phase layer at the peaks of both lotus-inspired textures (ASPNL1 & ASPNL2) are quite similar (Table 4-5), while the depth is slightly reduced on the ASPNS sample peaks (5.1 ± 0.6 µm). The difference between the peak and valley of the ASPNL1 and ASPNS textures are quite similar (3.4 & 2.9 µm, respectively), while the difference is much larger for the ASPNL2 samples (11.2 µm). Details of the ASPNΔ sample type can be found in section 4.4, but it should be noted that there were no discernible peaks or valleys within this texture, and the depth of the S phase layer was consistent (6.93 ± 0.11 µm) and comparable to the as-treated (ASPN; 7.07 ± 0.07 µm) material.

Both cross-sectional imaging (Fig. 4-18) and elemental mapping (Fig. 4-19) revealed no signs of S phase decomposition following femtosecond laser texturing on all sample types. No signs of element segregation or contrast density variation could be distinguished. The only measurable change between the as-treated (ASPN) sample type and the textured sample type was the development of a thin surface oxide layer, which likely develops from the oxidation of sputtered and re-deposited matter during the texturing process.

*Table 4-5 S phase layer thickness on textured peaks and valleys .*

| Sample | Textured S Phase Layer Thickness (µm) | |
|---|---|---|
| | Peak | Valley |
| **ASPNL1** | 6.5 ± 1.2 | 3.1 ± 1.0 |
| **ASPNL2** | 6.3 ± 1.5 | - 5.1 ± 2.1 |
| **ASPNS** | 5.1 ± 0.6 | 2.2 ± 0.4 |

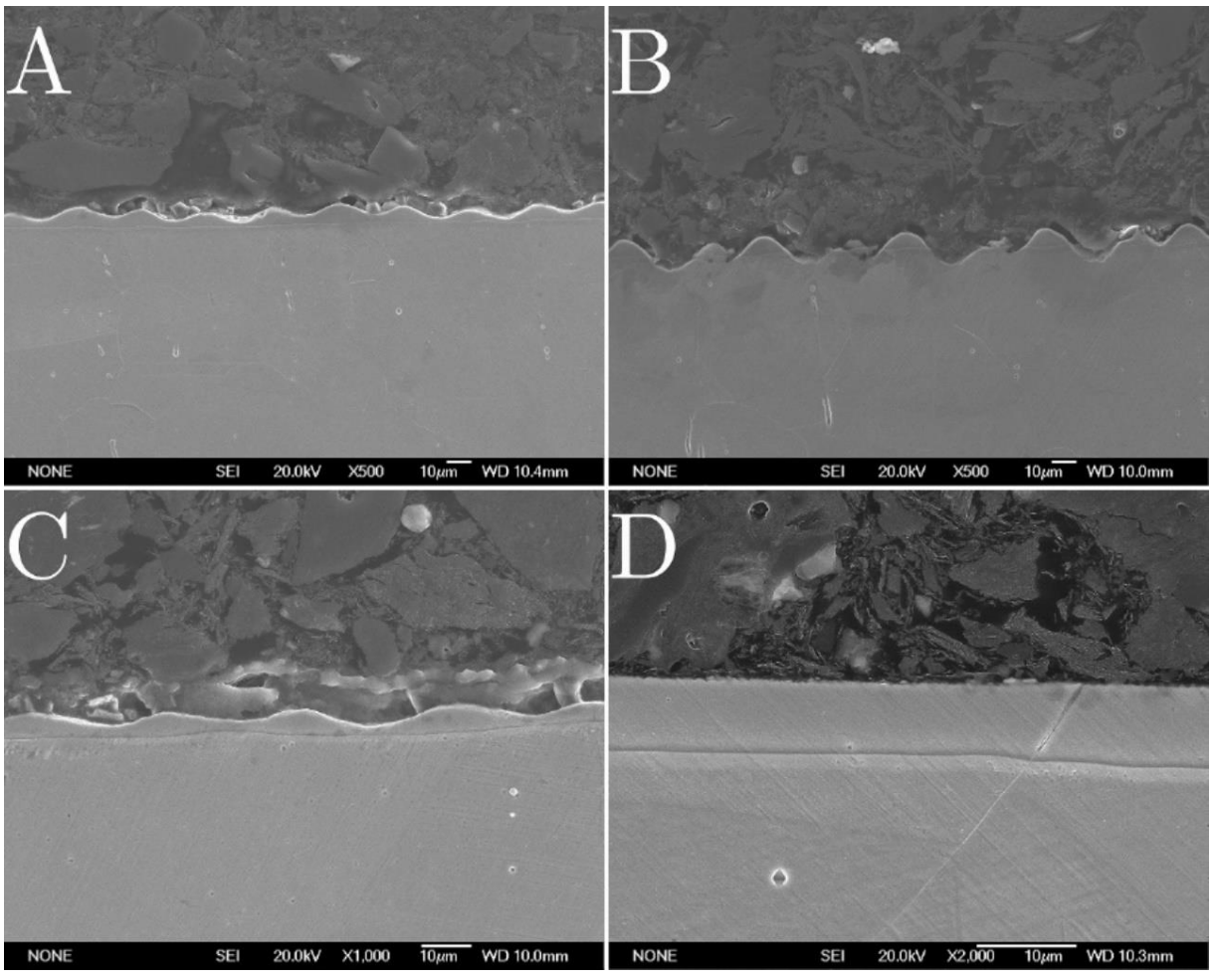



*Fig. 4-18 Cross-sectional electron microscopy imaging of the (A) ASPNL1, (B) ASPNL2, (C) ASPNS and (D) ASPNΔ sample types.*

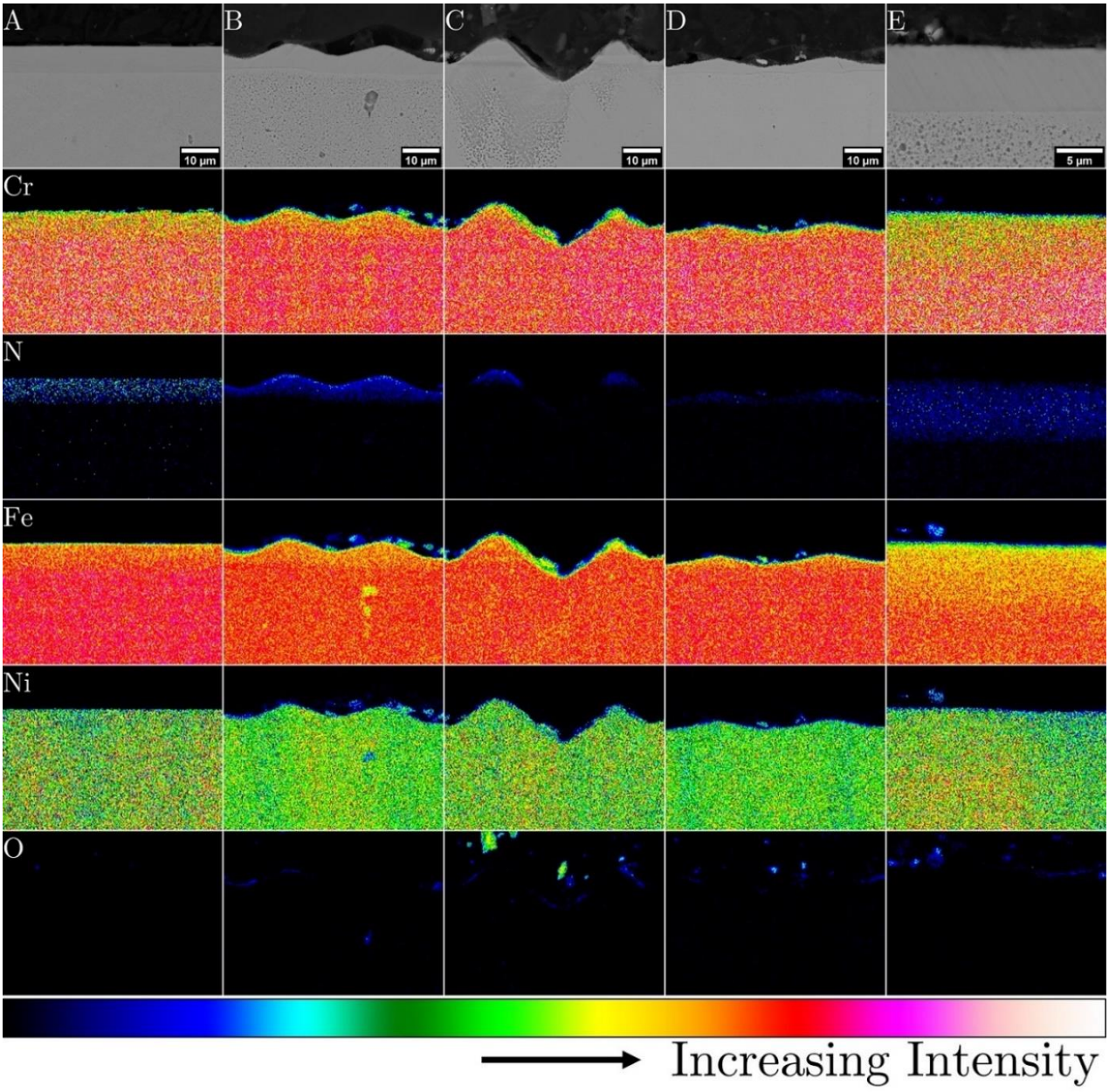



*Fig. 4-19 Backscattered electron imaging (top row) and EDS elemental mapping through the cross-sectional areas of the (A) ASPN, (B) ASPNL1, (C) ASPNL2, (D) ASPNS and (E) ASPNΔ sample types. Samples are organised in columns, with each row representing a different element (as labelled). Colour intensity mapping is relative to each individual element map. It should be noted that a different magnification was used in E.*

### 4.3.3. Antimicrobial Efficacy

For comparison, the 310 fs channel textures shown in section 4.2 were also analysed against the four texture types introduced in this section. It can be seen from Fig. 4-20 that the ASPNΔ sample type was the most effective texture at reducing the number of colony forming units of *S. aureus* following contact with the surface (91.4 ± 4.7 % reduction), and was statistically superior to all other texture types ($p<0.001$). The ASPNL1 sample type showed the next highest resistance (76.5 ± 1.8 % reduction), and like the ASPNΔ sample type, possessed significantly higher antimicrobial resistance ($p<0.001$) than the other texture types. The ASPNL2, ASPNS and 310 fs channel textured samples showed antimicrobial efficacies in the range of 55.3 % (310 fs) and 62.7 % (ASPNL2), and in some cases were not statistically different to one another ($p>0.05$; Fig. 4-20). The difference in antibacterial performance between the lotus-like textures of varying aspect ratios (ASPNL1 and ASPNL2) can be attributed to the penetration of the S phase layer (Fig. 4-18 & Fig. 4-19), therefore reducing resistance due to the exposure of the untreated surface.

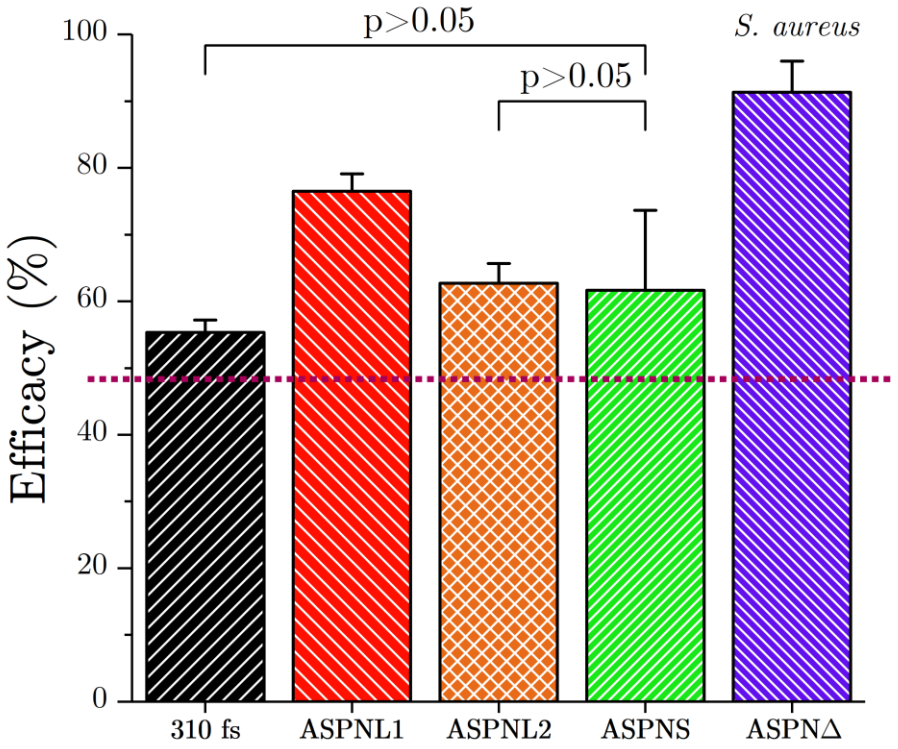



*Fig. 4-20 Antimicrobial efficacy of the different textured sample types against S. aureus. Dotted line corresponds to the efficacy for the ASPN sample type. Other than the labelled comparisons, all other comparison were found to be significantly different to each other (p<0.05).*

## 4.4. Triangular LIPSS Textures

Based on their superior antibacterial efficacy (section 4.3.3), the triangular LIPSS textures were chosen for further analysis. In-depth characterisation of the surface morphology, layer structure, electrochemical corrosion behaviour, antibacterial efficacy against *S. aureus* and *E. coli*, and surface wettability were carried out. To differentiate the effect of ASPN treatment and triangular LIPSS texturing, comparisons were made between untextured and triangular LIPSS textured surfaces formed on untreated and S phase treated samples.

### 4.4.1. Texture Morphology

Optical camera imaging (Fig. 4-21A & C) and electron microscopy (Fig. 4-22A & C) helped to reveal that both the Unt and ASPN sample types had smooth, almost featureless, surfaces. Measurements of the surface roughness, $R_a$ (Table 4-6), before surface texturing confirmed the similar surface condition of the Unt and ASPN samples (22.1 ± 3.6 nm & 25.3 ± 2.8 nm, respectively).

Fast Fourier transformations (FFT) of the surface micrographs (Fig. 4-23) quantified the pattern periodicity (Table 4-6), which revealed the repetitive nature of the triangular LIPSS textured surfaces in varying directions. Both textured (UntΔ and ASPNΔ) sample types were found to have 3 orders of symmetry at angles 0 ° (direction a), 60 ° ($\alpha_1$) and 120 ° ($\alpha_1 + \alpha_2$) with overall hexagonal structuring. In agreement with previously published triangular LIPSS literature, the periodicity of the textures were measured to be slightly smaller (≈ 2-6 $nm^{-1}$) than the wavelength of the texturing laser (1032 nm) [205-207]. Almost identical periodicity was measured for the UntΔ and ASPNΔ sample types in each direction, with the highest frequency being found in direction b (≈ 885-889 nm; Table 4-6). As a result of the pattern periodicity, scattering of white light was seen with optical camera imaging for both UntΔ and ASPNΔ sample types (Fig. 4-21). Additionally, due to the 3 orders of symmetry (Fig. 4-23), white light becomes scattered in multiple directions upon interaction with the textures and leads to the appearance of different colours across the surface (Fig. 4-21), as well as, at different viewing angles [231].

Other than periodicity, the effective widths of the valleys within the textures (named channel spacing) were also measured. Two types of valleys were found on the textured surfaces (S1 & S2; Fig. 4-22), with both UntΔ and ASPNΔ samples possessing similar channel spacing for S1 (230.6 ± 63.9 and 239.5 ± 76.3 nm respectively) and S2 (732.0 ± 78.9 and 734.9 ± 108.4 nm respectively).

*Table 4-6 Pattern periodicity, channel spacing and surface roughness (pre-texturing) for the Unt, UntΔ, ASPN & ASPNΔ samples.*

| Sample code | $R_a$ (nm) | Pattern Periodicity ($nm^{-1}$) | | | Channel Spacing (nm) | |
|---|---|---|---|---|---|---|
| | | a | b | c | S1 | S2 |
| **Unt** | 22.1 ± 3.6 | - | - | - | - | - |
| **UntΔ** | - | 930.0 ± 4.3 | 889.2 ± 2.7 | 936.3 ± 10.5 | 230.6 ± 63.9 | 732.0 ± 78.9 |
| **ASPN** | 25.3 ± 2.8 | - | - | - | - | - |
| **ASPNΔ** | - | 924.1 ± 4.7 | 885.4 ± 2.8 | 934.0 ± 5.6 | 239.5 ± 76.3 | 734.9 ± 108.4 |

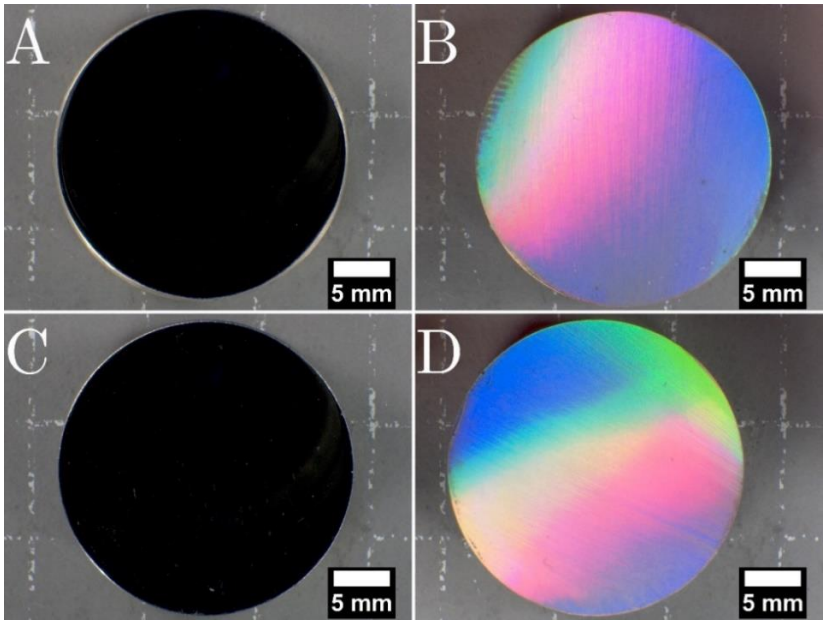



*Fig. 4-21 Camera pictures of the surface colours and uniformity of Unt (A), UntΔ (B), ASPN (C) and ASPNΔ (D) samples.*

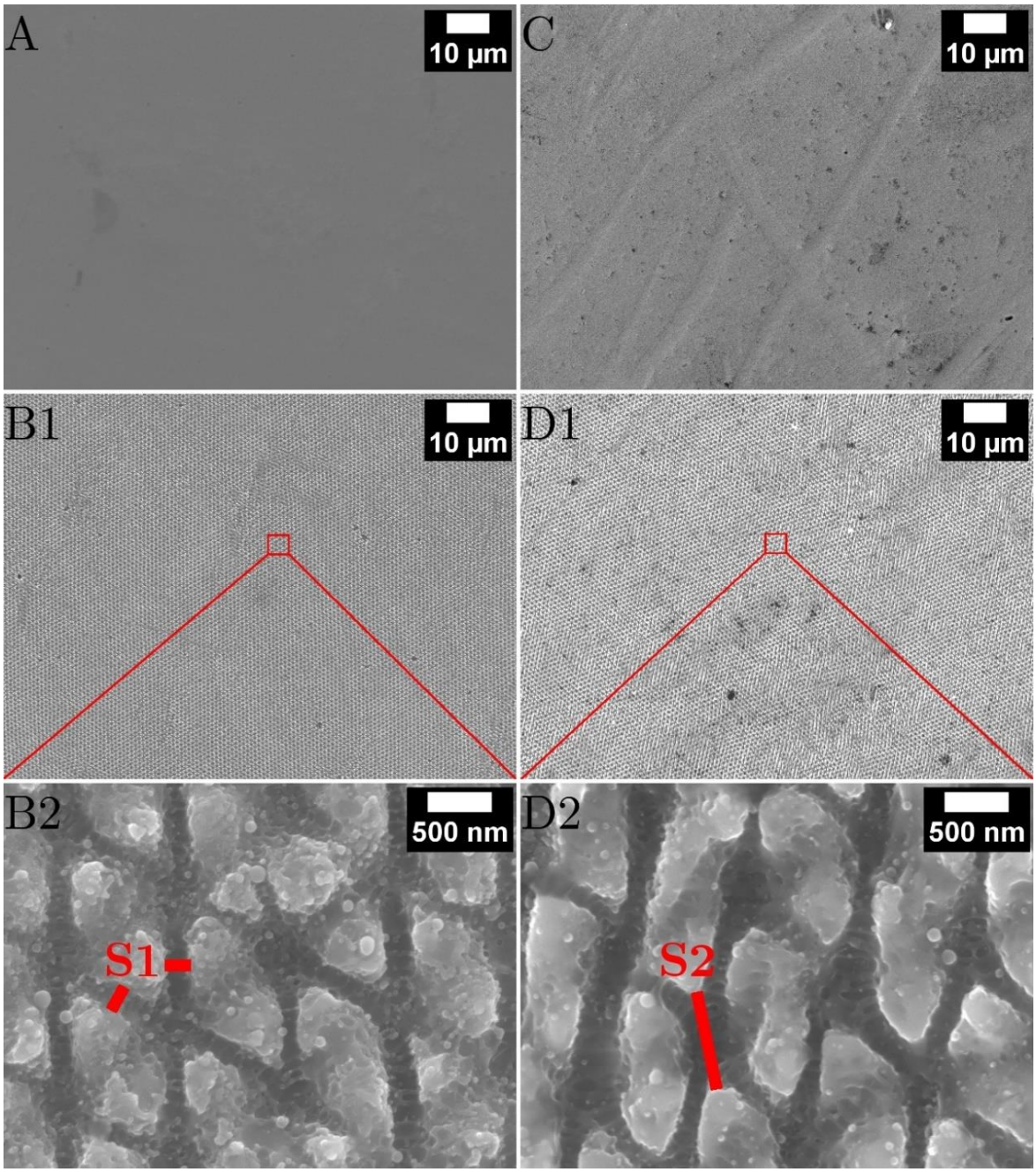



*Fig. 4-22 Surface morphology of the different sample types: Unt (A), UntΔ (B1-2), ASPN (C) and ASPNΔ (D1-2). Lines labelled S1 and S2 depict the two types of channel spacing present within the textured surface.*

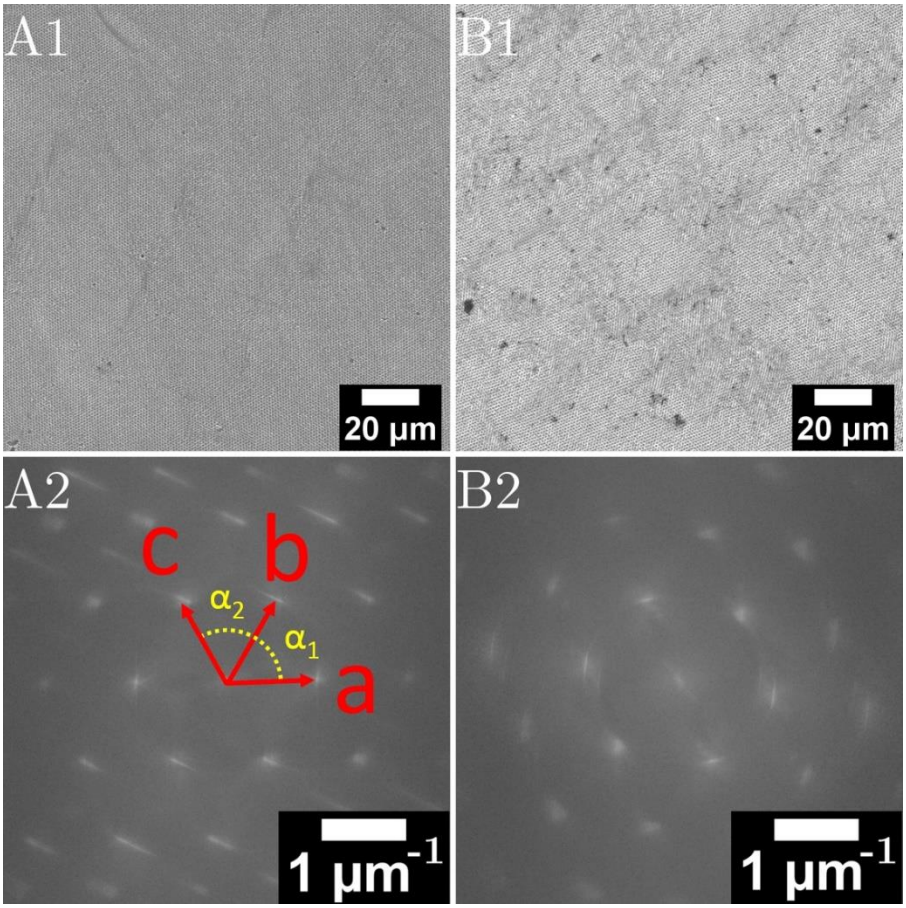



*Fig. 4-23 Pattern periodicity (labelled as a, b and c) of UntΔ (A) and ASPNΔ (B) sample types revealed by surface micrographs (labelled 1) and image FFTs (labelled 2). Hexagonal structuring is demonstrated by both sample types, and consequently, 3 orders of symmetry are found with angles α1 and α2 (where α1 = α2 = 60 °).*

### 4.4.2. Cross-Sectional Layer Structure

Following on from previous results in section 4.2 of this study on the response of the S phase to ultrashort pulsed laser texturing [26], testing and analysis was also performed on the triangular LIPSS (Δ) textures to confirm that no changes arose in the structure of the nitrided surface layer following treatment and/or texturing. Particular attention was paid to the ASPNΔ samples to detect potential precipitation of new phases (Fig. 4-24 & Fig. 4-19), changes to the

existing crystal structure (Fig. 4-25) or changes in the mechanical properties (Fig. 4-26) of the treated layer.

Cross-sectional imaging (Fig. 4-24) revealed no discernible signs of S phase decomposition on the ASPNΔ samples. Instead, a clear 6.93±0.11 μm thick precipitate-free S phase, similar with the ASPN sample type (7.07±0.07 μm), was observed. The only noticeable difference was the presence of the triangular LIPSS textures on the surface, which were also found on the UntΔ sample type (Fig. 4-24D). In both UntΔ and ASPNΔ samples, the depth of the texturing (peak to valley) was measured to be less than 300 nm. Due to the poor mechanical properties of the UntΔ samples, a nickel surface coating (Fig. 4-24B) was necessary to protect against damage to the fine surface textures during sample preparation. Whereas, with the ASPNΔ samples (Fig. 4-24D), such a protective coating was not required due to the vastly improved hardness (Fig. 4-26). Another noteworthy difference between the untreated (Unt, UntΔ) and treated (ASPN, ASPNΔ) sample types was with the presence of pores in the bulk of the treated surfaces (Fig. 4-24C & D). However, this was not due to any change to the bulk material, but instead, due to the significantly longer etching time required to reveal the S phase.

Elemental mapping (Fig. 4-19) of the layer structure of the treated samples further demonstrated the homogeneous S phase surface treated layer on both the ASPN and ASPNΔ sample types. Other than the boundary between the S phase and the underlying bulk, no signs of element segregation could be detected within the material. Backscattered electron imaging also supported this finding, with no discernible change in contrast density between the samples (Fig. 4-19A & E). A thin heterogeneous surface oxide was noticeable on the ASPNΔ sample type (Fig. 4-19), which likely arose as a result of the ablation and back-sputtering

process involved with the athermal femtosecond laser texturing process (similar to the findings of the other textures in section 4.3.2).

Left shifting (increased d-spacing) of austenite peaks (ϒ) in XRD phase analysis (Fig. 4-25) verified the formation of the S phase. An approximately 3 ° and 4 ° shift was measured in the S1 and S2 peaks of the ASPN treated samples, respectively. The mechanical superiority of the S phase over the untreated material (Unt) was observable within the hardness depth profiling (Fig. 4-26). An approximately 5-fold increase in surface hardness was found between the S phase (1200-1300 HV) and the untreated 316L material (≈ 250 HV; Unt). No change in hardness across the depth of the S phase was detected following texturing (ASPNΔ). The recorded drop in hardness at the surface of both treated samples was attributed to the interaction volume of the indent overlapping into the softer adjacent Bakelite. The difference between the bulk hardness of the treated (ASPN & ASPNΔ) samples in comparison to the untreated (Unt) samples was due to the different measuring techniques used (nanoindentation vs. microhardness).

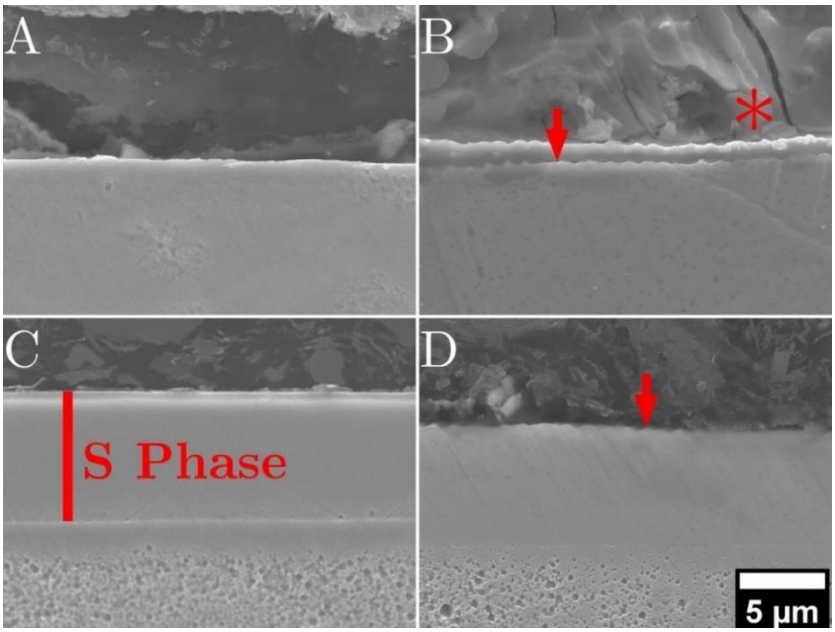



*Fig. 4-24 Cross-sectional secondary electron micrographs of the different sample types: Unt (A), UntΔ (B), ASPN (C) and ASPNΔ (D). Arrows indicate the surface of the texture, while the * represents the nickel protective plating layer on the UntΔ sample type. Scale bar is the same for all images.*

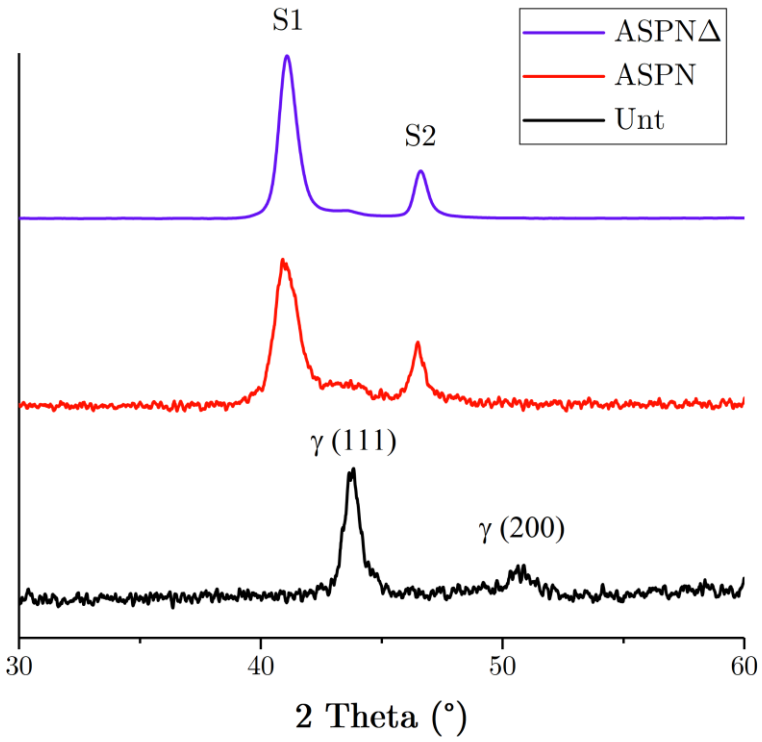



*Fig. 4-25 XRD phase analysis of Unt, ASPN and ASPNΔ samples.*

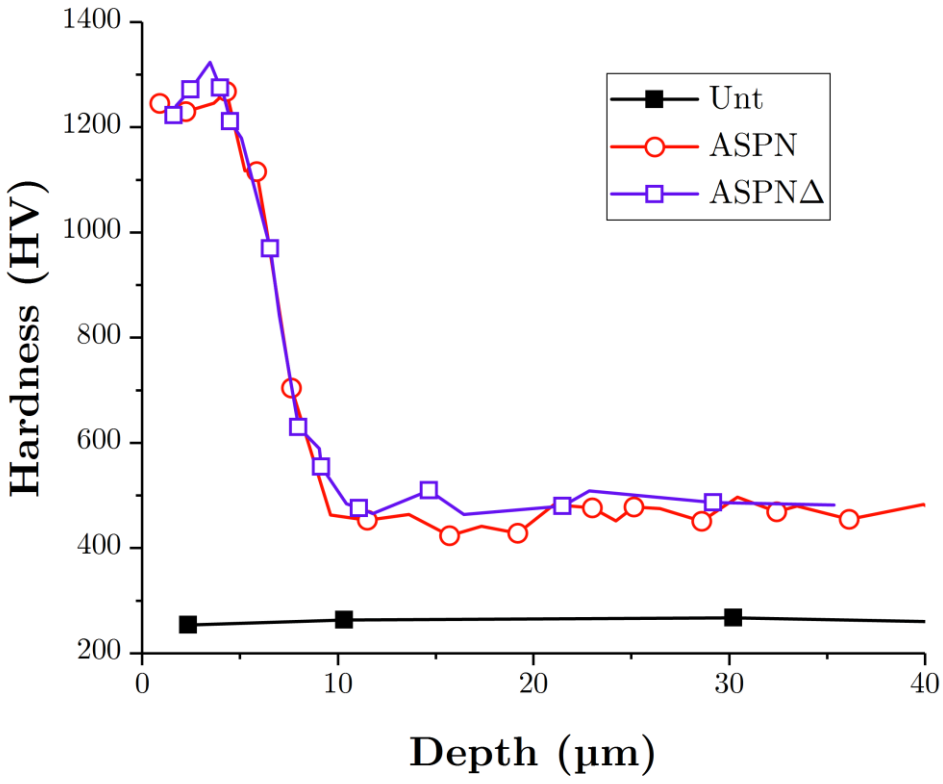



*Fig. 4-26 Hardness depth profiling of Unt, ASPN and ASPNΔ samples.*

### 4.4.3. Corrosion Behaviour

In addition to the detection methods used to determine the precipitate-free nature of the surface layer following S phase surface treatment and triangular LIPSS texturing (ASPNΔ; Fig. 4-18, Fig. 4-19, Fig. 4-24 & Fig. 4-25), electrochemical impedance spectroscopy was also performed and compared against the 310 fs textured samples from section 4.2. Whilst the UntΔ sample type shows a slight reduction in total resistance to polarisation in comparison with the Unt sample type, the ASPNΔ sample, instead shows a slight improvement despite the increased surface area introduced during the texturing process (Table 4-7). Fig. 4-27 & Fig. 4-28

reveal no increase in corrosion susceptibility of the ASPNΔ sample type on either the Bode or Nyquist plots, even at the lowest frequencies. The most significant differences observed in Table 4-7 relate to the $R_f$ values of the electrolyte-S phase interface layer on the 310 fs, ASPN and ASPNΔ sample types. The difference in $R_f$ resistance between the ASPN and ASPNΔ samples can be attributed to the difficulties associated with measuring (or representing) the true surface area of the samples following the triangular LIPSS texturing. However, despite an expected increase in surface area in comparison with the 310 fs samples, the ASPNΔ were found to have a significantly higher $R_f$ resistance. This increase is likely to be due to the difference in depth of the textures, with the 310 fs samples displaying regions of thin S phase layers within the channels (Fig. 4-5), whereas a thick S phase layer is found across the whole surface of the ASPNΔ samples (Fig. 4-18 & Fig. 4-24).

*Table 4-7 Measurements of resistance (Ω) to polarisation of the 310 fs, Unt, UntΔ, ASPN and ASPNΔ sample types. The lack of $R_p$ value for the Unt and UntΔ samples related to the equivalent circuit models in Fig. 4-29.*

| | **310 fs** | **Unt** | **UntΔ** | **ASPN** | **ASPNΔ** |
|---|---|---|---|---|---|
| **$R_f$** | 43.80 | $3.8 \times 10^6$ | $1.84 \times 10^6$ | $3.11 \times 10^6$ | $5.33 \times 10^4$ |
| **$R_p$** | $3.203 \times 10^6$ | - | - | $2.19 \times 10^3$ | $8.10 \times 10^6$ |
| **$R_{Total}$** | $3.203 \times 10^6$ | $3.8 \times 10^6$ | $1.84 \times 10^6$ | $3.1 \times 10^6$ | $8.15 \times 10^6$ |

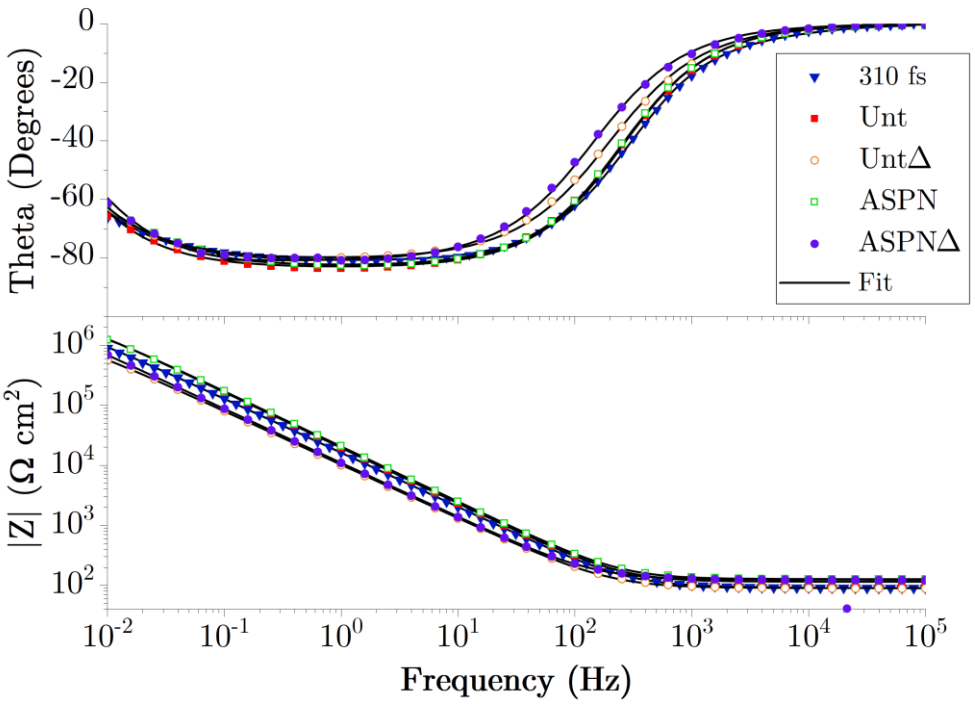



*Fig. 4-27 Bode phase (top) and magnitude (bottom) plots of the Unt, UntΔ, ASPN and ASPNΔ sample types. Fitted lines were made according to the equivalent circuit models in Fig. 4-29.*

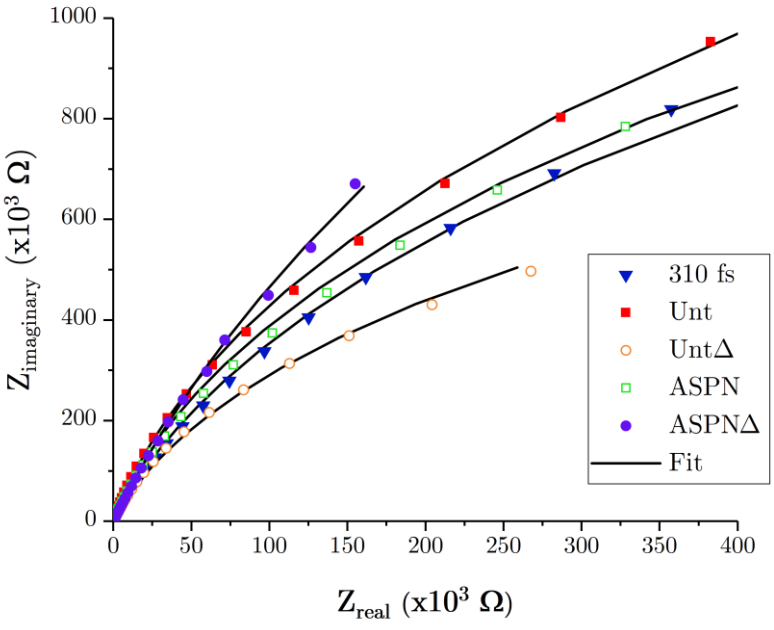



*Fig. 4-28 Nyquist plot of impedance of the Unt, UntΔ, ASPN and ASPNΔ sample types. Fitted lines were made according to the equivalent circuit models in Fig. 4-29.*

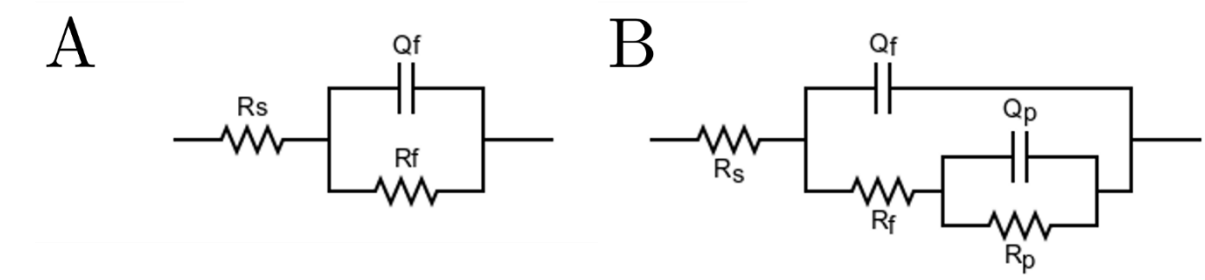



*Fig. 4-29 Equivalent circuits models used for EIS analysis where $R_s$ is solution resistance, $R_f$ (resistance to polarisation) & $Q_f$ (double layer capacitance) relate to the outer electrolyte-S phase interface, and $R_p$ & $Q_p$ relate to the S phase-untreated bulk interface. Model A was used for Unt & UntΔ samples. Model B was used for ASPN & ASPNΔ samples.*

### 4.4.4. Surface Wettability

Wettability testing (Table 4-8) revealed a decrease in the contact angle readings going from the untreated sample type (Unt) to the treated sample type (ASPN). This change is likely to be caused by the introduction of nitrogen to the surface of the ASPN sample type [232, 233]. This is also supported by the increase in the calculated surface free energy; particularly, the increase in the polar component (Fig. 4-30). A more pronounced difference was observed between the textured samples, with the ASPNΔ sample type demonstrating a 56.8 ° increase in the water contact angle when compared with the UntΔ sample type. The reason for this change is likely to be due to a mixture of physical and chemical differences between the sample types (see section 5.3.2 for further details). On the other hand, negligible differences were found between the textured samples when using diiodomethane (Table 4-8). Both textured sample types (UntΔ, ASPNΔ) were found to have an increase in surface free energy (polar component, dispersive component and total) when compared to their untextured counterparts (Unt, ASPN). When compared with each other, the total surface free energy was

found to be similar for the UntΔ and ASPNΔ sample types (45.8 ± 2.0 and 43.9 ± 3.1 mJ/m$^2$, respectively; Fig. 4-30).

*Table 4-8 Contact angle measurements of the Unt, UntΔ, ASPN and ASPNΔ sample types.*

| Liquid | Contact Angle (°) | | | |
|---|---|---|---|---|
| | Unt | UntΔ | ASPN | ASPNΔ |
| **Water** | 99.1 ± 3.5 | 66.9 ± 4.4 | 80.3 ± 4.8 | 123.7 ± 4.4 |
| **Diiodomethane** | 60.2 ± 3.1 | 44.9 ± 2.9 | 51.3 ± 1.6 | 42.1 ± 2.4 |

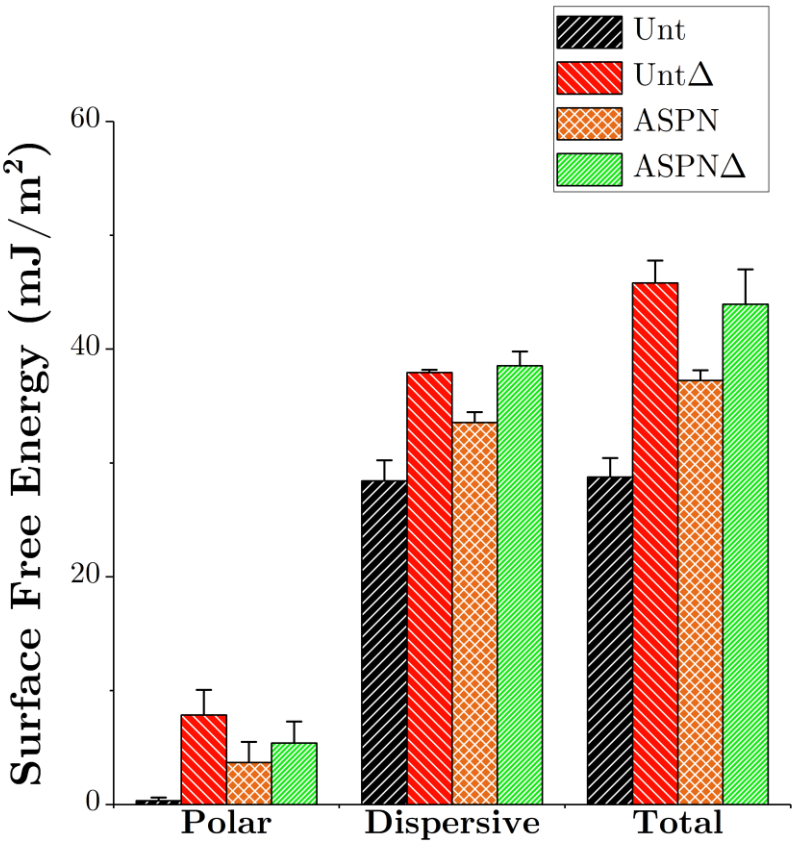



*Fig. 4-30 Surface free energy calculations of the Unt, UntΔ, ASPN and ASPNΔ sample types.*

### 4.4.5. Antimicrobial Efficacy

Excellent antimicrobial efficacy against *S. aureus* (Fig. 4-31) was measured for both textured samples, with reductions of CFUs by 96.5 ± 2.5 % and 92.2 ± 1.0 % (against control; section 3.7) for the UntΔ and ASPNΔ samples types, respectively. Although not significantly different to each other ($p=0.44$), both sample types possessed significantly improved efficacy in comparison to the Unt and ASPN sample types ($p<0.001$). Likewise, plasma treatment alone (ASPN) also was effective in improving the antimicrobial efficacy of the surface from 32.0 ± 4.3 % (Unt) to 48.3 ± 3.1 % ($p<0.001$). Similar results were found with the textured surfaces following testing against *E. coli* (Fig. 4-32), with CFU reductions of 85.1 ± 7.1 % and 75.6 ± 10.9 % for the ASPNΔ and UntΔ samples types, respectively ($p<0.001$ against Unt and ASPN). However, unlike testing against *S. aureus*, a significant difference was observed between the efficacy of the UntΔ and ASPNΔ surfaces against *E. coli* ($p<0.05$). ASPN samples also showed a significant, and more pronounced, improvement in efficacy in comparison to the Unt samples ($p<0.001$). Fig. 4-33 shows the optical images of the viable CFUs following 6-hour exposure to each surface type.

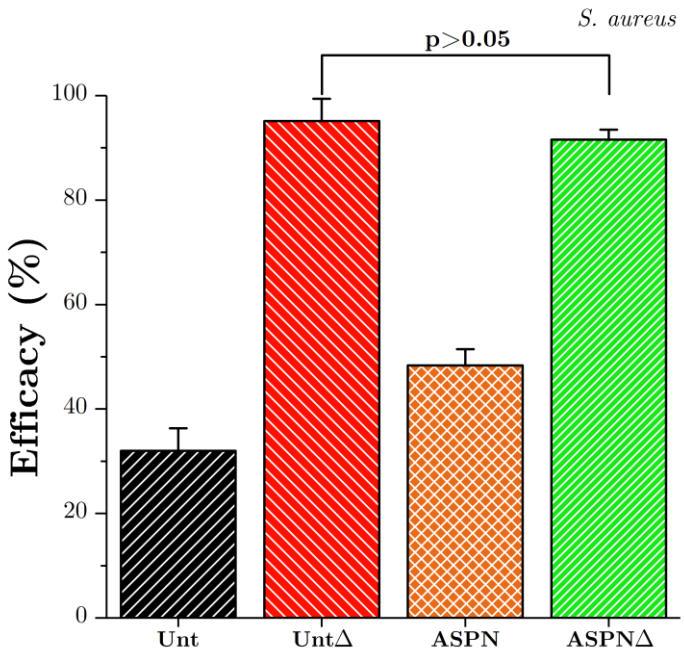



*Fig. 4-31 Antimicrobial efficacy of the Unt, UntΔ, ASPN and ASPNΔ sample types against S. aureus. Other than the labelled comparisons, all other comparison were found to be significantly different to each other.*

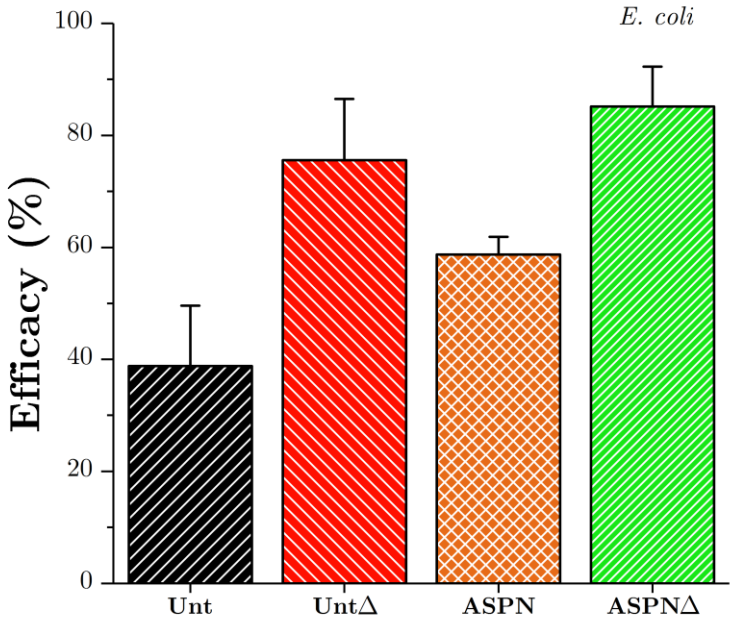



*Fig. 4-32 Antimicrobial efficacy of the Unt, UntΔ, ASPN and ASPNΔ sample types against E. coli. All samples were found to be significantly different to each other.*

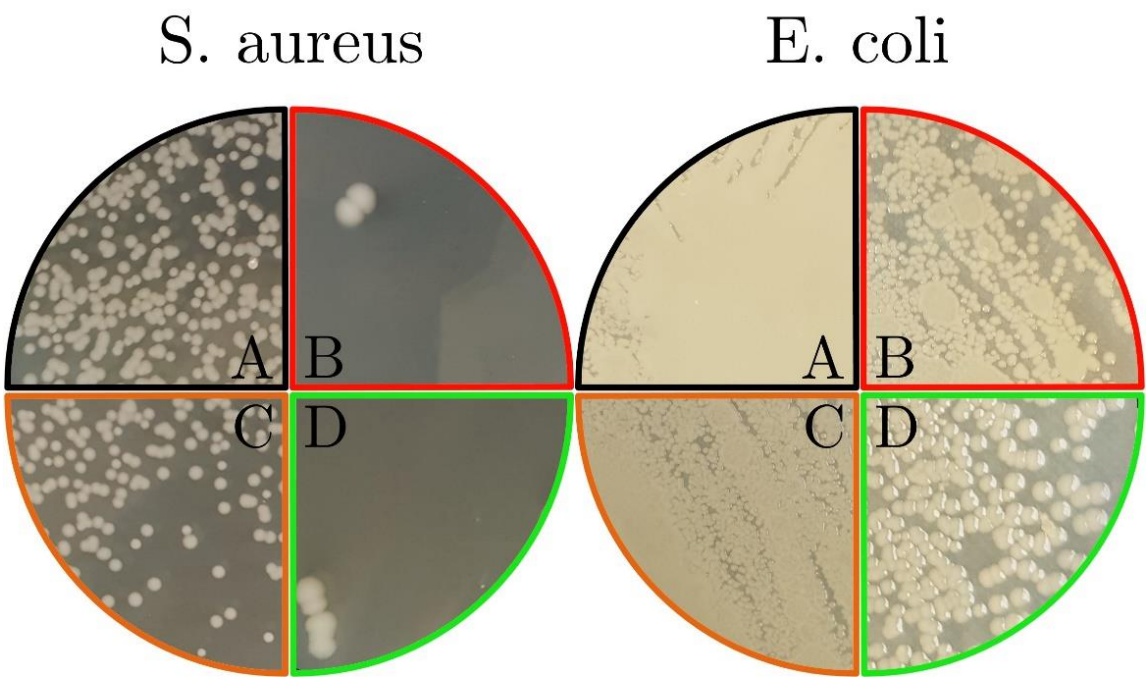



*Fig. 4-33 Camera pictures demonstrating the number of colony forming units of S. aureus (images on the left) and E. coli (images on the right) present following contact with each sample type: Unt (A), UntΔ (B), ASPN (C) and ASPNΔ (D).*

## 4.5. Texture Durability

Reciprocating sliding wear testing (under dry and lubricated conditions) and large area wearing of triangular LIPSS textures on untreated and S phase treated surfaces were carried out to examine the structural durability of the textures, as well as the functional durability (antibacterial efficacy).

### 4.5.1. Dry Sliding Reciprocating Wear

Significantly reduced wear factors (also known as wear coefficients) were measured on both treated samples in comparison to their untreated counterparts (Fig. 4-34). The wear resistance

of the ASPN sample type was found to be 60 to 220 times better than the Unt sample type. Similar wear rates as the ASPN sample type were measured on the ASPNΔ samples, with a maximum recorded wear factor difference of $1.3x10^{-14}$ $m^3/Nm$ (50 gf load). The UntΔ sample type demonstrated excellent improvement in wear resistance under 50 gf of loading in comparison to the Unt sample type. The improvement likely arises mainly due to the deposition of wear debris into the valleys of the texture during the early cycles, thereby limiting severe abrasive wear induced by wear debris at the point of contact [202]. In addition, the formation of a thin oxide film during laser texturing in air could also have contributed to the improved wear resistance (promoting mild oxidative wearing). At higher loads the wear resistance dramatically dropped, which can be explained due to the quicker loss of the textures, as well as the very thin oxide film, and eventual return to properties of the bulk material.

No appreciable texture features could be identified within the wear tracks of the UntΔ samples, even under the lowest load. In contrast, texture features were easily recognisable within the tracks of the ASPNΔ sample types, even under the highest load (Fig. 4-35). Additionally, only signs of abrasive and possibly oxidative wear mechanisms could be identified from the imaging of the ASPNΔ wear tracks. On the other hand, clear signs of severe adhesive and abrasive wear were visible on the UntΔ sample types.

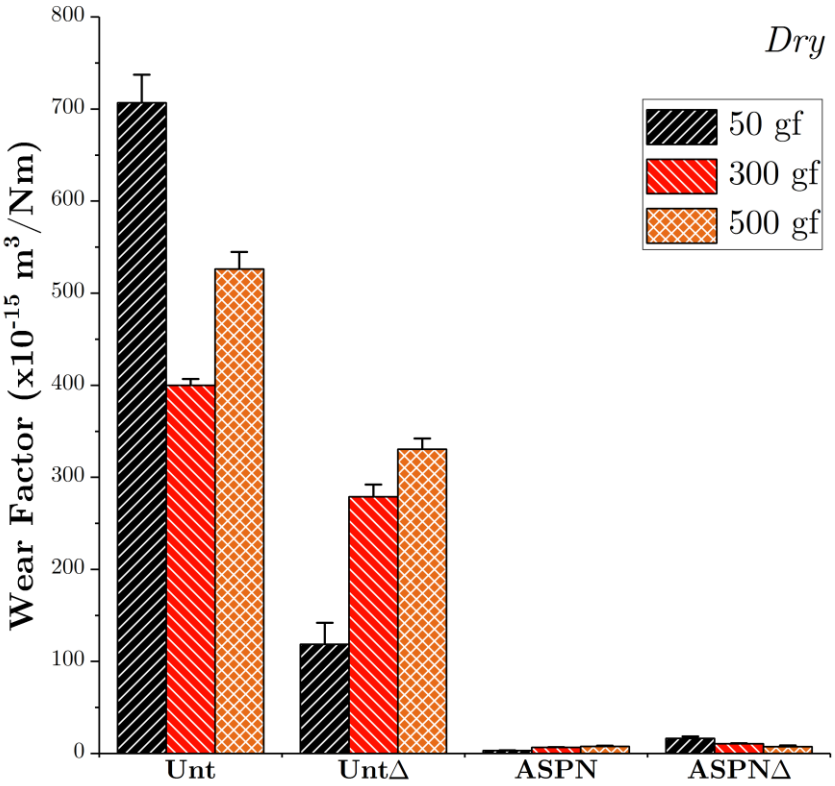



*Fig. 4-34 Wear Factor of the Unt, UntΔ, ASPN and ASPNΔ surfaces following dry sliding reciprocating wear testing under 3 different loads: 50 gf, 300 gf and 500 gf.*

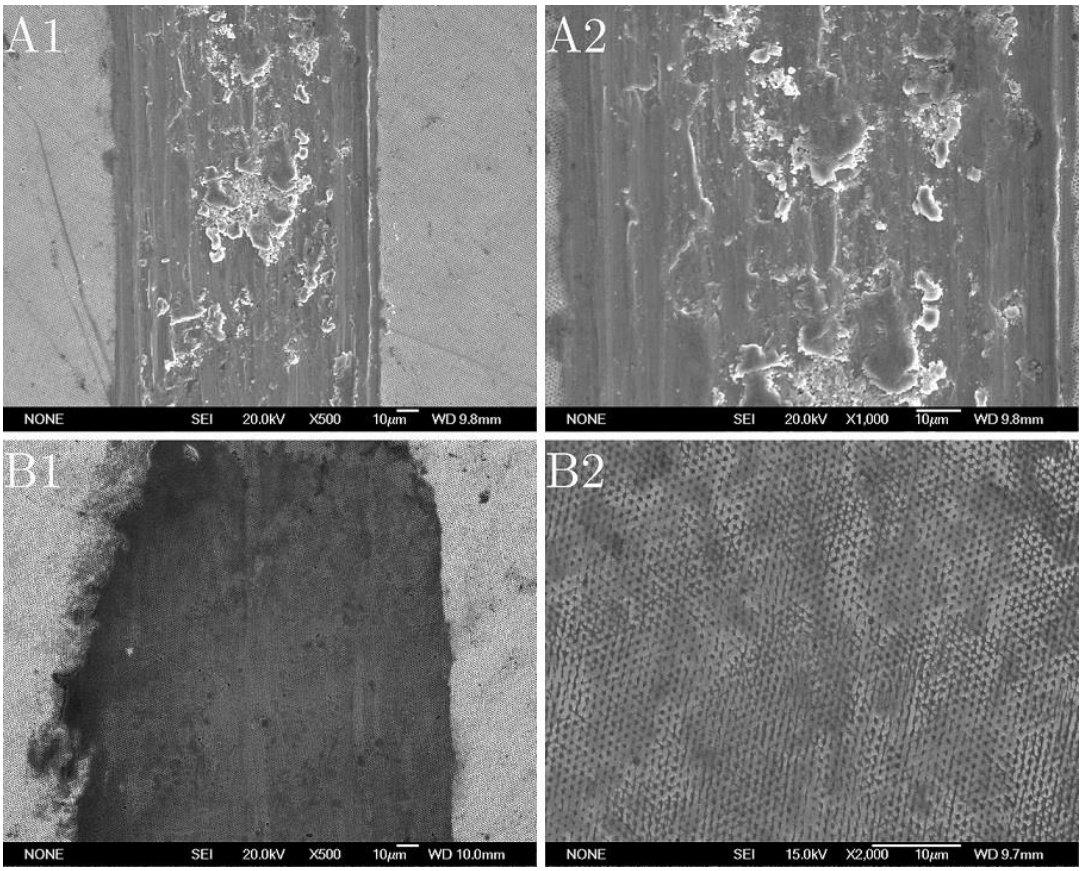



*Fig. 4-35 Electron micrographs of the resulting wear tracks following dry sliding wear of the UntΔ surface under a load of 50 gf (A) and ASPNΔ surface under a load of 500 gf (B).*

### 4.5.2. Ringer's Lubricated Reciprocating Wear

Both treated samples types (ASPN & ASPNΔ) demonstrated excellent wear resistance, with a maximum absolute wear factor difference of 4.84 $x10^{-15}$ $m^3$/Nm between them (Fig. 4-36). In line with the dry testing data (section 4.5.1), the UntΔ was measured to have significantly improved wear resistance at a load of 50 gf in comparison to the Unt sample type. At higher loads the difference dropped dramatically, and the average wear factor of the UntΔ samples

were indeed larger than that of Unt samples; although the difference was negligible at 500 gf of loading.

Fig. 4-37 shows the wear track morphology following the Ringer's lubricated wearing. In contrast to the dry surface wearing (Fig. 4-35), the triangle LIPSS textures are shown to remain on the UntΔ samples under 50 gf of loading, which is likely to have contributed to the excellent wear factor (Fig. 4-36). At higher loads the textures are removed, and the wear tracks become wider and deeper. On the other hand, no loss of the textures can be found with the ASPNΔ sample types, even under the highest loading.

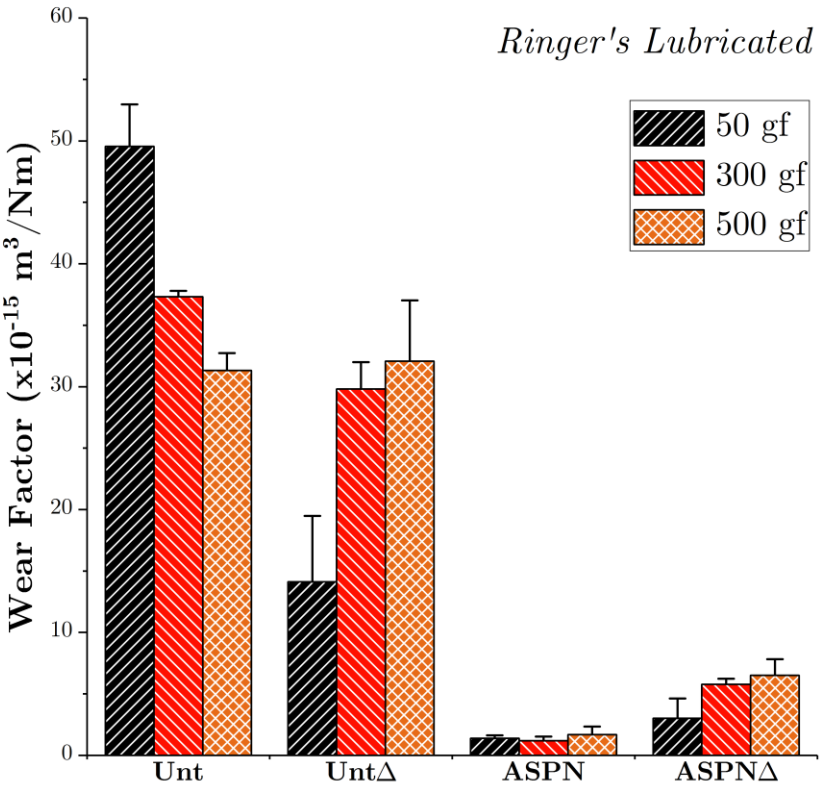



*Fig. 4-36 Wear Factor of the Unt, UntΔ, ASPN and ASPNΔ surfaces following Ringer's lubricated sliding reciprocating wear testing under 3 different loads: 50 gf, 300 gf and 500 gf.*

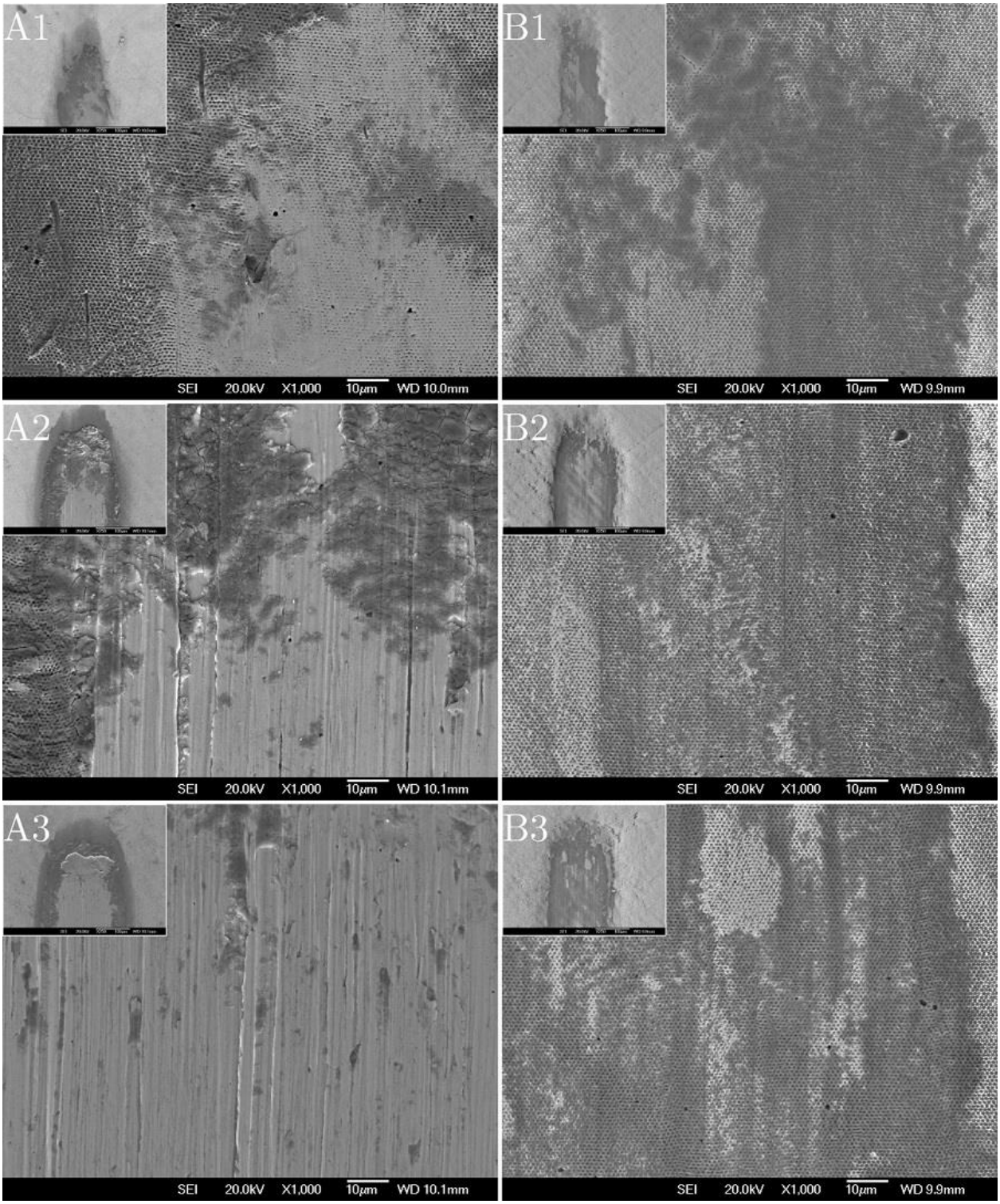



*Fig. 4-37 Electron micrographs of the resulting wear tracks following Ringer's lubricated wearing of the UntΔ (A) and ASPNΔ (B) surfaces under loads of 50 gf (1), 300 gf (2) and 500 gf (3). Insets at the top left of each image are lower magnification micrographs taken at the same spot.*

## 4.5.3. Antibacterial Durability

### 4.5.3.1. Large Area Surface Wearing

Fig. 4-38 and Fig. 4-39 demonstrate the surface morphology after large area wearing of the UntΔ and ASPNΔ sample types, respectively. Almost complete removal of the triangular LIPSS textures are found on the UntΔ sample type following low cycle wearing (Fig. 4-38B). In contrast, a similar level of damage to the textures of the ASPNΔ sample type is only found following high cycle wearing, which is equivalent to a four-fold increase in distance travelled in comparison to low cycle wearing (Fig. 4-39D). Almost no loss of texture features or homogeneity are apparent under low cycle wearing of the ASPNΔ sample type (Fig. 4-39B), with the flattening of the top-most surface being the only distinguishable change. After medium cycle wearing, areas of complete texture removal and areas of retained triangle LIPSS textures are found on the ASPNΔ sample type. Finally, almost complete removal of the textures is observed following high cycle wearing of the ASPNΔ sample types (Fig. 4-39D). Additionally, similar with the low cycle wearing of the UntΔ sample, only faint, sparsely spread, remnants of the triangle LIPSS patterns can be seen across the surface of the ASPNΔ samples after high cycle wearing.

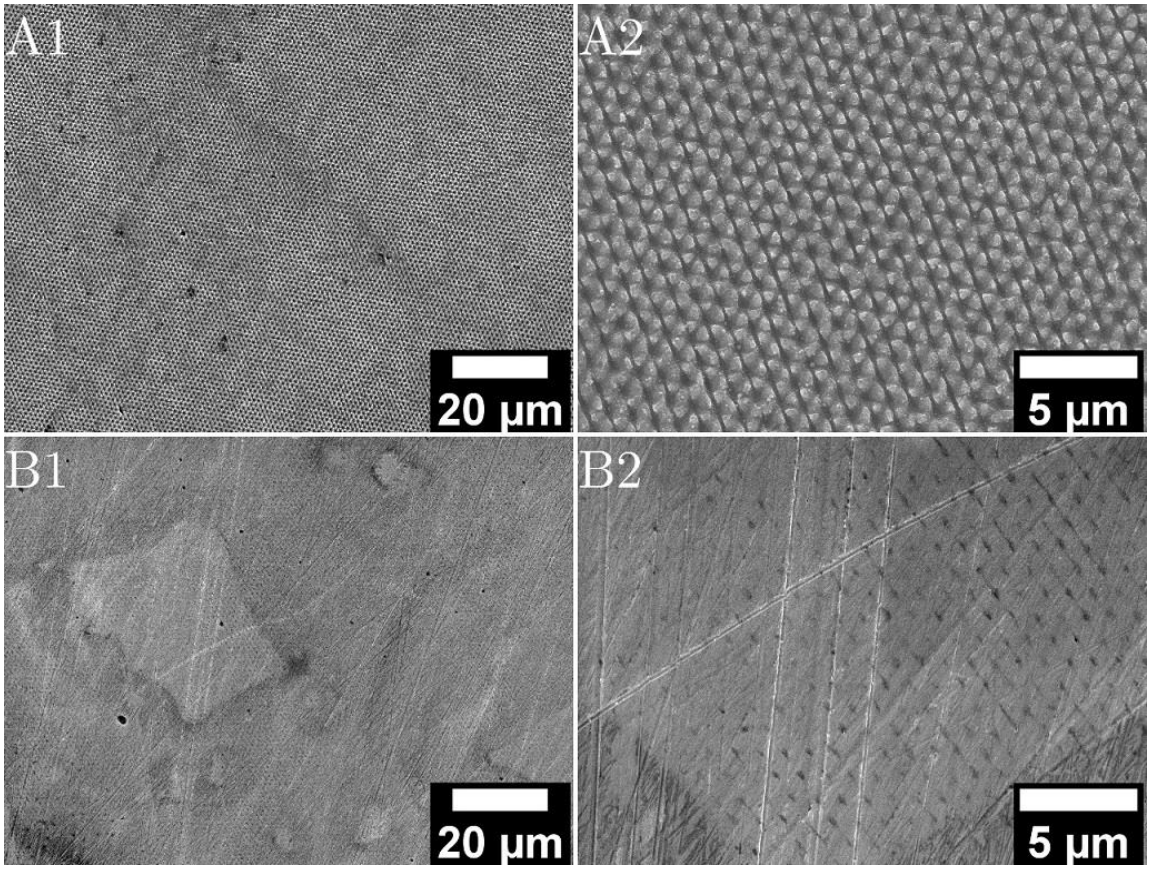



*Fig. 4-38 Surface morphology of UntΔ surfaces at different stages of large area wearing: untouched surface (A1-2) and low cycle wearing (B1-2).*

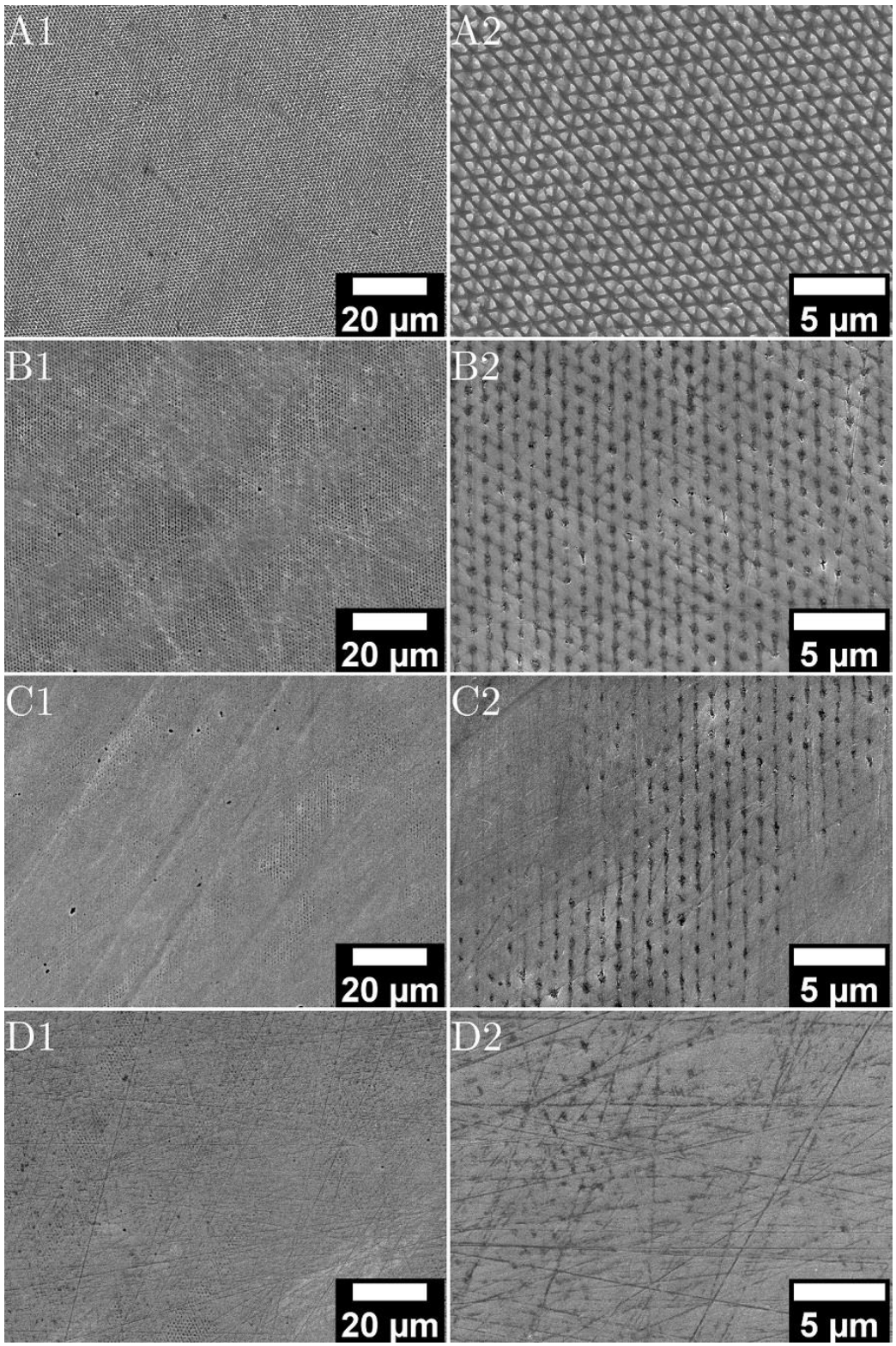



*Fig. 4-39 Surface morphology of ASPNΔ at different stages of large area wearing: untouched surface (A1-2), low cycle wearing (B1-2), medium cycle wearing (C1-2) and high cycle wearing (D1-2).*

#### 4.5.3.2. Worn Surface Antimicrobial Efficacy

Results of antimicrobial testing of the worn surfaces (Fig. 4-38 & Fig. 4-39) against *S. aureus* and *E. coli* are shown in Fig. 4-40 and Fig. 4-41, respectively. In the case of the UntΔ sample type a significant drop in antimicrobial efficacy against both *S. aureus* and *E. coli* was observed after large area low cycle wearing ($p<0.001$ for both), dropping to 38.2 ± 1.7 % (from 95.1 ± 4.3 %) and 24.5 ± 10.5 % (from 75.6 ± 10.9 %), respectively. In contrast, the ASPNΔ sample type was not found to have a statistically significant change of its antimicrobial efficacy against both *S. aureus* and *E. coli* after large area low cycle wearing ($p=0.88$ and $p=0.12$, respectively). Significant loss of antimicrobial properties (against untouched ASPNΔ) was found after large area medium cycle and high cycle wearing. Even under more severe wearing, the antimicrobial efficacy of the ASPNΔ (medium cycle) sample type was found to be significantly higher than the UntΔ (low cycle) sample type for both *S. aureus* and *E. coli* testing ($p<0.001$). Higher efficacy against *E. coli* was found even after large area high cycle wearing of ASPNΔ samples in comparison to low cycle worn UntΔ samples ($p<0.001$; Fig. 4-41). The only comparison that revealed significantly higher antimicrobial efficacy for the large area low cycle worn UntΔ sample type was with high cycle wearing of the ASPNΔ against *S. aureus* ($p<0.001$; Fig. 4-40).

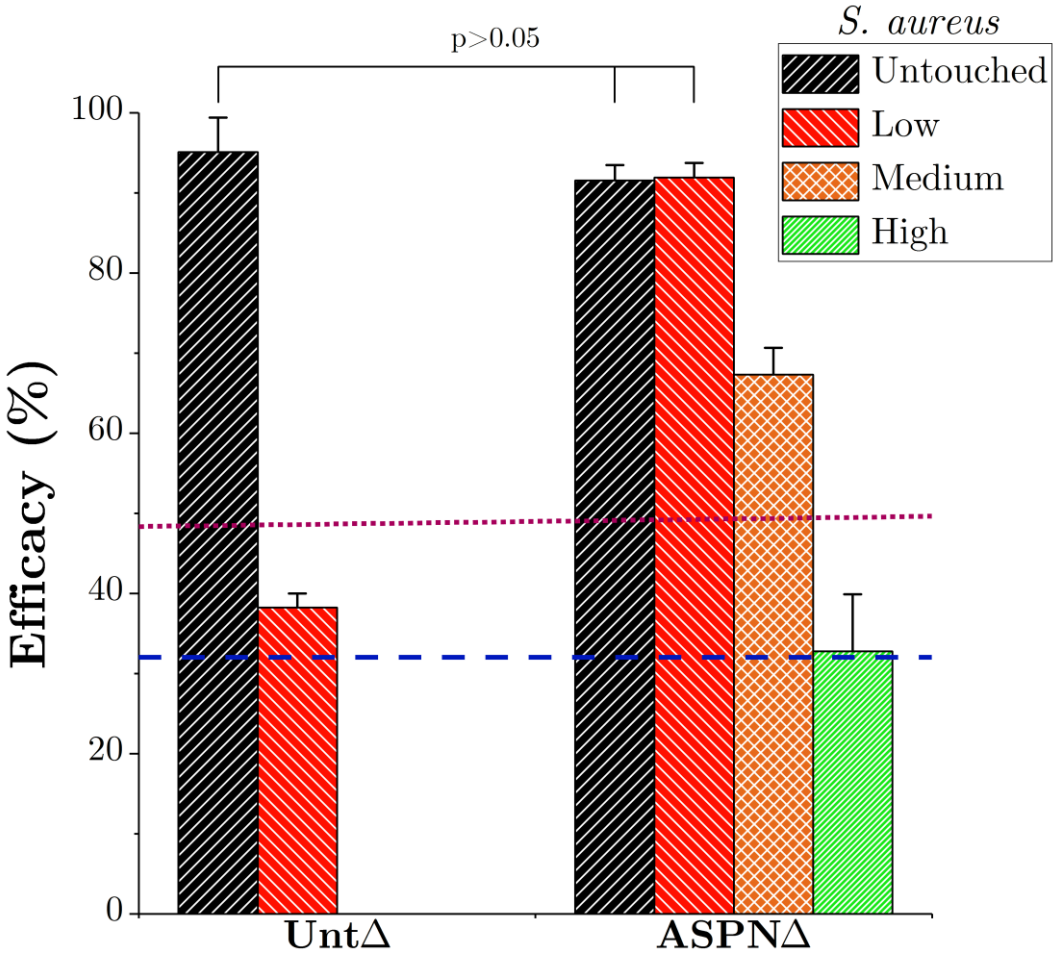



*Fig. 4-40 Antimicrobial efficacy against S. aureus before and after large area wearing of the triangular LIPSS textured surfaces. Other than the three labelled ones, the antimicrobial efficacy was found to be significantly different ($p<0.05$) for all comparisons. Efficacy of the untextured surfaces are represented by dashed (Unt) and dotted (ASPN) lines.*

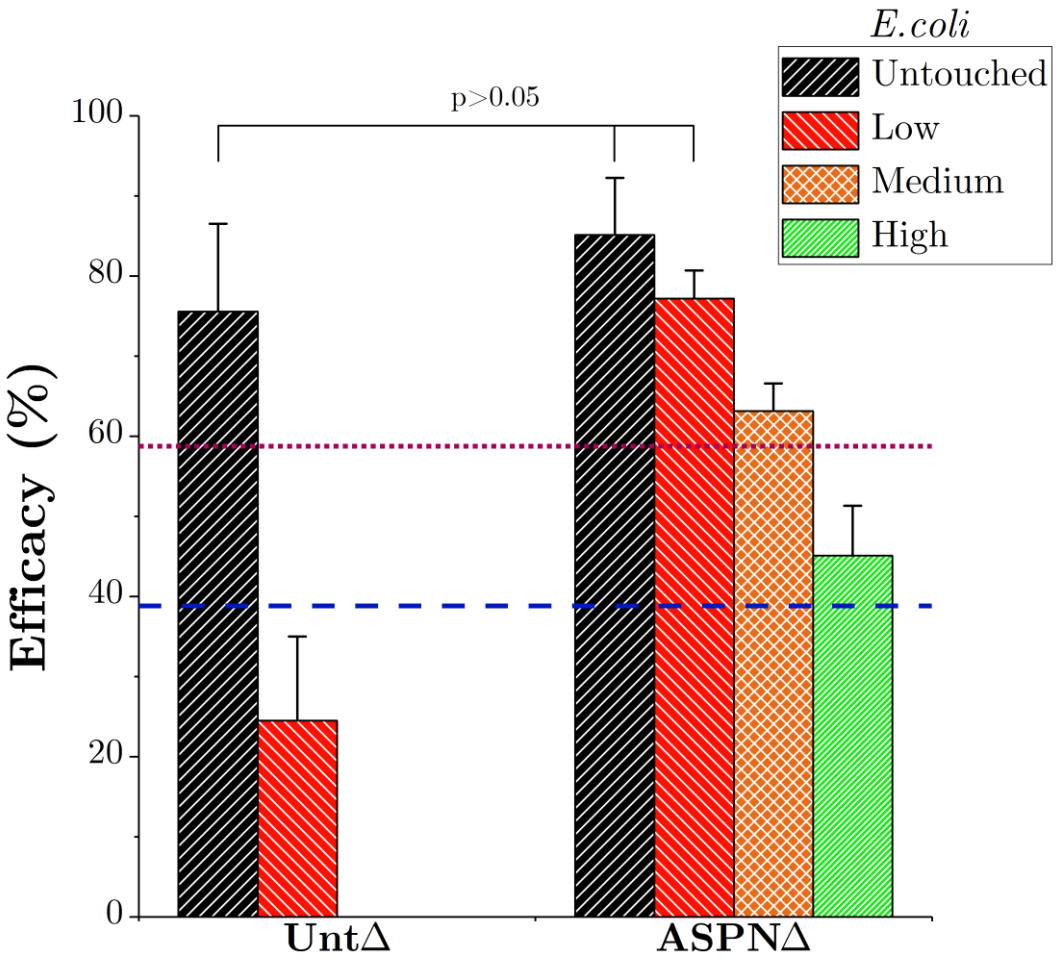



*Fig. 4-41 Antimicrobial efficacy against E. coli before and after large area wearing of the triangular LIPSS textured surfaces. Other than the three labelled ones, the antimicrobial efficacy was found to be significantly different ($p<0.05$) for all comparisons. Efficacy of the untextured surfaces are represented by dashed (Unt) and dotted (ASPN) lines.*

# CHAPTER 5 DISCUSSION

Within this chapter, an analysis of the structure and properties of the as-treated S phase layer (ASPN) produced on the AISI 316L alloys is given, along with explanations for the thermostability and traditional incompatibility with thermal laser texturing (section 5.1). An overview and discussion of the findings following ultrashort nanosecond and femtosecond laser texturing on S phase treated surfaces is provided, especially with respect to their subsequently changes in corrosion resistance (section 5.2). This is then followed by a review of the different bio-inspired textures produced on S phase treated surfaces using femtosecond laser texturing, before more in-depth evaluation of the characteristic morphology/structure and antibacterial performance of the optimised triangular LIPSS textures are given (section 5.3). Subsequently, the antibacterial durability of the triangular LIPSS textures formed on untreated and S phase treated surfaces are discussed, along with the difficulties related to accurate assessment of this property (section 5.4). Finally, some suggestions are made for future research opportunities, and the scientific and industrial insight that they may provide (section 5.5).

## 5.1. S Phase & Its Thermostability

### 5.1.1. Characterisation & Properties of S Phase

A mixture of cross-sectional layer structure (Fig. 4-1B), cross-sectional elemental mapping (Fig. 4-6) and crystallographic phase analysis (Fig. 4-2) helped to confirm the precipitate-free nature

of the as-treated S phase (ASPN). The lack of any variable etching resistance, composition variance or formation of nitride peaks demonstrated the successful S phase low-temperature plasma nitridation of the AISI 316L. Both the measured XRD peak left shifting (Fig. 4-2) and the S phase layer thickness (8.17 ± 0.4 µm; Fig. 4-1B) were found to agree with previously published work on AISI 316L alloys [8, 154, 155]. As expected, a significantly harder (1130 HV) and more wear resistant (Fig. 4-34 & Fig. 4-36) surface layer was formed, with hardening depth (Fig. 4-26) in accordance with the nitrogen elemental depth profile (Fig. 4-1A).

### 5.1.2. Thermostability & Laser Texturing of S Phase

The precipitation of chromium nitrides following low-temperature plasma nitriding of stainless steels is usually used as an indicator for a poor or failed treatment. Much of the literature states that this formation has detrimental effects on the corrosion resistance of the surface [234]. Although chromium nitrides themselves possess excellent corrosion resistance, the issue with the formation of these precipitates is the effect that they have on the surrounding material (as previously mentioned in section 2.1.3). In stainless steel, the corrosion resistance is obtained through the formation of a continuous passive chromium oxide ($Cr_2O_3$) film [235, 236]. When the distribution of chromium becomes inhomogeneous and localised areas contain levels below the minimum value required for stainlessness, like it does within adjacent areas to chromium nitrides, it leads to the breakdown of the protective layer, which subsequently causes the deterioration of the corrosion resistance [123, 237, 238]. This has been supported by the electrochemical test results (Fig. 4-10 to Fig. 4-14, Table 4-2 & Table 4-3). Therefore, it is important to avoid precipitation of chromium nitrides and the

decomposition of the S phase during laser surface texturing, especially at grain boundaries, which give rise to sensitisation [31].

Laser energy transfer onto material surfaces is known to predominantly occur through absorption by valence electrons [215, 217]. Significant transfer of energy between the electrons and the surrounding lattice has also been shown to take approximately 1 picosecond ($10^{-12}$ s). Therefore, pulsed laser texturing, even down to nanosecond ($10^{-9}$ s) pulse durations, always involves the heating of surface matter to create textures. This obviously involves high local ("flash") temperatures that increase the risk of decomposition of the S phase.

Alternatively, it is possible to texture stainless steel surfaces prior to low-temperature plasma nitriding of the samples; however, the rounding effect that the deposition of matter has on the surface effectively coats and negates any nanoscale features present on the surface. On the other, this can be a useful approach, and has been previously attempted by other studies, for creating macroscale textured S phase surface for applications such as wear resistant or reduced friction coefficient surfaces (dry conditions) [101, 239].

## 5.2. Response of S Phase to Ultrashort Pulsed Laser Texturing

### 5.2.1. Effect of Nanosecond Laser Texturing

Kinetic analysis is a common approach that can be utilised to analyse the response of a material to heating. Additionally, it has already been implemented successfully to predict the degree of precipitation that can be expected following heating and annealing of an S phase through-treated material [149]. Due to the success of this approach it is only natural to also apply the

same technique to predict whether decomposition of the S phase will arise following nanosecond laser texturing. Owing to the rapid heating and cooling of the patterned areas (Fig. 4-8 & Fig. 4-9), laser texturing can be regarded as a non-isothermal heat treatment of the surface. Therefore, following on from the work by Christiansen and Somers [149], calculations were carried out to determine the expected degrees of precipitation following laser texturing using equations for non-isothermal isochronal annealing (equations 5-1 & 5-2).

The results suggest that, in both 15 ns and 220 ns textured surfaces, there should be complete decomposition ($f$ = 1) of the S Phase. Seemingly, this does not directly match the observed outcomes following the texturing (Fig. 4-5). However, upon more careful analysis of the results, the calculated transformed fractions are likely to be true. Firstly, as predicted through the simulations (Fig. 4-8 & Fig. 4-9), the immediate surface temperatures (18000 and 8000°C for 15 and 220 ns pulses respectively) expected during the texturing are comfortably above the melting point of the 316L stainless steel. This implies that the superficial S phase material is melted then vapourised (ablated), and can easily be pushed away or removed during the texturing. This is evidenced by the pile-up of material along both sides of the laser channels as shown in Fig. 4-3B1 and the key-hole shown in Fig. 4-3C1. By combining both arguments it is easy reach the conclusion that the missing material, that physically leaves the voids that form the textures, would have been decomposed. Therefore, if we consider a scenario whereby the melted/ablated matter remained in position, it would be expected that this S phase material would be fully decomposed, and hence, in accordance with the calculated fractions transformed.

$$f = 1 - \exp[-\beta^n] \quad \text{(equation 5-1)}$$

$$\beta^n\ (non - isothermal) \approx \left[\frac{k_0 \cdot \varphi \cdot R \cdot \left[t + \frac{T_0}{\varphi}\right]^2}{Q} \cdot exp\left[\frac{-Q}{R \cdot \varphi \cdot \left[t + \frac{T_0}{\varphi}\right]}\right]\right]^n \quad \text{(equation 5-2)}$$

where $f$ is the fraction transformed, $\beta$ is the path variable, $n$ is the Johnson-Mehl-Avrami equation for heterogeneous reactions, $k_0$ is the pre-exponential factor ($s^{-1}$), $\varphi$ is the heating rate ($K.s^{-1}$; 4.88 $x10^{10}$ $K.s^{-1}$ for 15 ns and 4.94 $x10^9$ $K.s^{-1}$ for 220 ns), $R$ is the gas constant (8.31 $J.mol^{-1}.K^{-1}$), $t$ is the time held at this temperature (s; 227.27 µs for 15 ns and 200 µs for 220 ns), $T_0$ is the starting temperature (298 k) and $Q$ is the overall activation energy (139 $kJ.mol^{-1}$).

The observed decomposition of the S phase material adjacent to the laser channel or beneath the 15 ns and 220 ns textured surfaces can be explained using the predicted average temperature (section 4.2.3). Since nanosecond laser texturing is known to be a thermal process it is possible to apply Fourier's second law (heat conduction) in order to predict whether enough mobility is introduced into the surface to initiate the formation of precipitates [217]. Chromium nitrides that form within nitrided surfaces of stainless steels predominantly have the empirical formula of CrN that grows with a face-centred cubic (FCC) crystal structure [225, 240]. It is already known that interstitial elements such as nitrogen can move significantly more freely through the metallic crystalline lattice than substitutional elements such as chromium. Therefore, it can be deduced that the determining step for the initial formation of chromium nitrides is directly related to the mobility of chromium atoms. The minimum amount of

diffusion necessary to initiate the precipitation of a chromium nitride would require the movement of one chromium atom at least the distance of one lattice parameter of CrN (0.414 nm) [130, 225]. In this case, it is assumed that all the other randomly distributed elements, by chance, already occupy the necessary positions to initiate the formation of CrN [8, 241].

Combining this logic with the data from the models allows for the prediction of whether, in theory, it is feasible to form chromium nitrides following nanosecond texturing. By using diffusion coefficient calculations (D; equations 5-3 & 5-4) for Cr in austenite with the average temperatures and durations predicted in section 4.2.3, it is possible to estimate the expected distance that Cr atoms are able to move during the time that the surface is heated (equation 5-5). The diffusion equations are based on experimental data obtained from radiotracer (equation 5-3) and microprobe analysis (equation 5-4) [242]. Table 5-1 shows that in both nanosecond laser texturing settings it is more than feasible for chromium nitrides to precipitate. In fact, even when repeating the same process for a single pulse of each laser setting it was still found to provide much greater than the minimum movement (355-546 nm (220 ns) and 41-61 nm (15 ns)) required for the chromium atoms to form nitrides (0.414 nm) (Table 5-1). Although the values for the Cr distance travelled within Table 5-1 appear extraordinary, it should be noted that within this kinetic analysis, the material would retain its solid metallic crystalline structure, without any phase changes or melting of the material. Moreover, the limitations stated in sections 3.3 and 4.2.3, are likely to play an important role in increasing the calculated diffusion distance values (particularly the effect of latent heats and material transfer away from the laser spot) [215].

$$D = [10.8] \cdot exp\left[\frac{-69700}{R \cdot T}\right] \quad \text{(equation 5-3)}$$

$$D = [4.08] \cdot exp\left[\frac{-68500}{R \cdot T}\right] \quad \text{(equation 5-4)}$$

$$x = \sqrt{D \cdot t} \quad \text{(equation 5-5)}$$

where $D$ is the diffusion coefficient ($m^2.s^{-1}$), $R$ is the gas constant (8.31 $J.mol^{-1}.K^{-1}$), $T$ is the temperature (K), $x$ is the distance travelled (m) and $t$ is the time (s).

*Table 5-1 Total distance of chromium diffusion for any surface spot following nanosecond laser texturing.*

| | Average Temperature (°C) | Diffusion Coefficient of Cr in γ-Fe ($x10^{-7}$ $m^2s^{-1}$) | Time (µs) | Distance Travelled (nm) | Equation |
|---|---|---|---|---|---|
| **220 ns** | 1111.45 | 25.30 | 227.27 | 23980 | 5-3 |
| | | 10.61 | | 15528 | 5-4 |
| **15 ns** | 757.24 | 3.16 | 200.00 | 7946 | 5-3 |
| | | 1.37 | | 5238 | 5-4 |

In agreement with both kinetic analysis and the Cr diffusion predictions, both nanosecond texturing processes were found to cause decomposition of the S phase. This is most clearly demonstrated with the presence of chemically altered regions under cross-section SEM imaging (Fig. 4-5B3 & C3) and EDS mapping (Fig. 4-6C & D). In both cases, the precipitated areas formed at the lips of the channels present with rod and lamellar structures that arise from the formation of nitrides interlaced with chromium depleted austenite [225]. Additionally, the increasing concentrations of Cr, N and Mo (Table 4-1 & Fig. 4-6) within these

darkened areas following chemical etching of the material further confirmed the presence of precipitates (Fig. 4-5).

Electrochemical corrosion results (Fig. 4-10 & Table 4-2) emphasised the decomposition of the S phase and the presence of the precipitates by demonstrating significant increases in the corrosion rates of both of the nanosecond textured samples [16]. Additionally, this is highlighted by the significant reductions in impedance (Fig. 4-12 & Fig. 4-13) & total resistance to polarisation (Table 4-3) following nanosecond texturing, which occur due to the decomposition of the surface S phase layer. Moreover, the development of an altered electrochemical circuit model (Fig. 4-14), increased presence of surface oxides (Fig. 4-15 & Fig. 4-6) and change in phase angles across the EIS study (Fig. 4-12) following nanosecond texturing further demonstrate the change in surface structure of the nanosecond textured samples in comparison to the as-treated (ASPN) sample type [229]. The rapid formation of the thick porous surface oxide layer (300-500 nm for 15 ns, and 600-700 nm for 220 ns; Fig. 4-6) also exhibits the heating effect of the nanosecond laser texturing. The presence of intergranular damage and quench cracking (Fig. 4-11) on the samples also outline the thermal shock effect of the laser on the surface, and may also play a role in the development of Warburg (diffusion based) impedance observed on the nanosecond textured surfaces [57, 243, 244].

As already discussed in section 4.2.4.2, a change in the dominating interface responsible for the measured resistance to polarisation of the nanosecond textured surfaces is observed between the 15 ns and 220 ns textured surfaces. Under 15 ns texturing, the S phase surface layer is not fully penetrated (Fig. 4-5B), and therefore, the rapidly formed and porous oxides grown superficial to the S phase layer (i.e. electrolyte-sample surface interface; Fig. 4-14) can

act as the rate determining step in the electrochemical cell ($R_f$; Table 4-3). On the other hand, the complete penetration of the S phase layer under 220 ns laser texturing (Fig. 4-5C) leads to a change in the dominating step within the electrochemical circuit, through the formation of a new route (electrolyte-untreated bulk interface) for the transfer of electrons [57].

### 5.2.2. Effect of Femtosecond Laser Texturing

Based on the data obtained, it can be deduced that the femtosecond laser texturing is suitable for use in combination with the S phase. No discernible change in composition (Table 4-1 & Fig. 4-6), morphology (Fig. 4-5) or presence of CrN precipitates (Fig. 4-7) could be detected following the texturing. In particular, the lack of other crystal structures, such as hexagonal closed packing (HCP; $Cr_2N$), or nanocrystalline phases, under TEM electron diffraction conclusively confirmed the precipitate-free nature of the S phase [225]. Additionally, the femtosecond texturing also did not lead to the development of detrimental defects such as the cracking observed with the nanosecond laser channels (Fig. 4-3) or the pile-up of materials along the sides of the laser channels (Fig. 4-5) [212].

This is ultimately because during femtosecond laser texturing enough energy is provided within the extremely short pulse duration to cause evaporation of the irradiated surface. The consequence of this is that fine evaporation (ablation) occurs at the laser spot without, in theory, any opportunity for heat to be transferred to the surrounding material [20, 23, 217]. This idea is supported by the limited increase observed in the thickness of the surface oxide layer (Fig. 4-6 & Fig. 4-15), that would be expected to form had the surface been exposed to heat, on the femtosecond textured samples. Application of the same 1-D surface temperature

modelling equations used for the nanosecond pulsed laser (section 3.3) to the femtosecond pulsed laser further prove the difference in energy transfer mechanisms, with calculated maximum temperatures exceeding 600,000 °C (at the 310 fs time point), which are clearly invalid, and indicate the incompatibility of the mechanisms between such varying pulse durations ($10^6$ s difference) [23, 217, 245]. Hence, femtosecond laser texturing provides a promising route for the patterning of S phase treated surfaces to produce wear resistant, corrosion resistant and functionalised stainless steel surfaces capable of being used in the food and medical industries.

As previously discussed (sections 2.4.5 & 2.6.2.1), the lack of research into laser texturing of S phase surfaces has been due to the damaging effect it is thought to have on the corrosion resistance of the surface. Therefore, to confirm the viability of femtosecond laser texturing for use with S phase surfaces, it is necessary to demonstrate the retained corrosion properties. As evidenced in Fig. 4-10, no appreciable change in corrosion potential was observed following 310 fs texturing. Although the corrosion rate and current density did increase slightly, this is likely due to the difficulties associated with the accurate quantification of sub-micron textured surface areas (Fig. 4-4) [246]. If the increased surface area could be accounted for, then both the current density and corrosion rate would be expected to match the values for the as-treated (ASPN) surfaces. Indeed, the lack of any observable damage (e.g. formation of pits; Fig. 4-11) following the anodic polarisation testing also suggests the retention of the precipitate-free homogeneous S phase [8]. Furthermore, the similarities between the total resistance to polarisation, impedance (real, imaginary, and total magnitude) and phase angle all suggest that no significant change occurred to the surface chemical structure following

femtosecond texturing (when compared to the ASPN treated surfaces). Additionally, no such disparity, as seen with nanosecond textured samples (section 5.2.1), or change in absolute measured value of the $R_f$ and $R_p$ value (Table 4-3) are observed for the 310 fs samples, in comparison with the ASPN treated samples.

## 5.3. Antibacterial Texturing

### 5.3.1. Optimising Femtosecond Textures

The first step towards the development and characterisation of durable antibacterial surfaces is the initial introduction of antibacterial features onto the hardened S phase surfaces without detrimental decomposition. Therefore, given the successful response of the S phase to femtosecond pulsed laser texturing (section 5.2), only textures utilising this range of pulse durations were used. Cross-sectional elemental mapping (Fig. 4-19), which was used as a precautionary measure, revealed no elemental segregation on any of the textured samples, thereby demonstrating feasibility of all the different femtosecond pulsed laser textures used within this study.

The initial study of the spaced apart adjacent channel textures was chosen to only examine the influence of each 2D overlapping LIPSS setting (enabled accumulation of fluence on single spots), with minimal interaction between channels (hence 300 μm hatch spacing). Antibacterial efficacy was not intended or hoped for with these textures; however, given that the textures were feasible and that the samples had already been produced, the 310 fs channel textures were also examined for antibacterial performance.

All other textures chosen for the comparison and optimisation were inspired by naturally occurring biological structures (biomimetic) which have previously been known to possess antibacterial functionality. The lotus leaf (*N. nucifera*), which is one of the most widely known antibacterial structures, is thought to gain its properties from a mixture of micro- and nano-scale features (Fig. 4-16) that enable super hydrophobicity and strong anti-biofouling properties [247]. Both functions act to enable the leaves to limit the available surface for attachment by, either trapping air in the microscale grooves, or by physically limiting surface available to bacteria (nanoscale features) [248]. Consequently, two forms of lotus leaf structures were utilised (ASPNL1 & ASPNL2), with one possessing deeper and more prominent microscale features (ASPNL2, Fig. 4-16B). In relation to the shark skin inspired texture (ASPNS), which possess anti-biofouling properties amongst other functional properties (e.g. drag reduction and self-cleaning), the most prominent influence on their antibacterial efficacy is thought to be due to the diamond-like interlaced structures (Fig. 4-17A), which can successfully disturb the migration of bacteria and suppress the build-up of biofilms on the surface [249-251]. The triangular LIPSS, which closely resemble features found on springtails (Collembola), are built almost exclusively with nanoscale structures (Fig. 4-17B & Fig. 4-22) [216]. Although not extensively explored for their antibacterial performance, the springtail cuticular morphology is known for its strong omniphobic liquid repellence, and has therefore, stimulated significant scientific interest [252-255]. Similar structures have also been shown to have potential for strong antibacterial performance [208]. Overall, textures ranging from largely microscale (ASPNS) to almost completely nanoscale (ASPNΔ) structures were chosen for comparison.

Since the antibacterial performance of these textures are largely assumed to arise as a result of anti-biofouling properties, only antimicrobial efficacy against *S. aureus* (the smaller of the two bacterial species typically tested) was used as the determinant for choosing the optimal texture to continue further analysis and durability testing on. As expected, all textures (including the channel texture) had a positive effect on the antimicrobial efficacy of the surfaces against *S. aureus* (Fig. 4-20). The most significant improvement was found with the triangular LIPSS, which were subsequently chosen as the texture to analyse and characterise further. Therefore, analysis for the effect of triangular LIPSS texturing will not be discussed in this section, instead, detailed analysis of this can be found in sections 5.3.2 and 0. The antibacterial performance of the rest of the textures follows according to the scale of their structures, with smaller featured structures possessing the best properties (ASPNL1 > ASPNL2 > ASPNS > 310 fs channels > ASPN; Fig. 4-20). This trend follows widely accepted and expected results for anti-biofouling textures, in which finer features produce the best resistance, which is largely attained through the limitation of the surface area available for attachment [198, 201, 256-258]. Interestingly, the comparison between the channel spacings (S1; Table 4-4) of the two lotus-inspired textures would initially promote the idea that, since the measured channel spacing is smaller on the ASPNL2 samples (≈ 120 nm smaller), the antibacterial efficacy should be better for this texture. However, this is not the case for these textures, and this can be attributed to the change in texture morphology (Fig. 4-16). The ASPNL2 samples present with ripple LIPSS structures that produce large continuous top-most surface areas that bacteria can adhere to. Alternatively, the ASPNL1 surface morphology more closely resembles the

triangular LIPSS (ASPNΔ) structures, with significantly reduced available surface area for bacterial attachment.

Aside from the antibacterial performance, another noteworthy characteristic of the textures was related to the depth of the valleys of the textures (Fig. 4-18). With regards to the S phase treatments, it can be observed that with the deep lotus leaf structures (ASPNL2), it was possible to penetrate through the S phase surface layer and into the bulk matter. Therefore, even in the absence of the antibacterial performance, it can be deduced that such a texture is incompatible for use with the S phase produced within this study, since it negates the intended value that the treated layers brings to the material surface (although it may find future use for thicker S phase layers). Additionally, even though the other textures (not including triangular LIPSS) do not penetrate through the S phase layer (Fig. 4-18), they do remove significant portions of the treated layer, and therefore, may be more suited to a dual texturing approach, whereby microscale textures are introduced prior to S phase treatment, with nanoscale features (like the triangular LIPSS) being further incorporated through a secondary texturing step after plasma nitriding.

### 5.3.2. Properties of Triangular LIPSS Textures

As has been reported within this study, the novel duplex treatment combining S phase plasma pre-hardening with athermal femtosecond laser texturing can produce stable hydrophobic properties (section 4.4.4) with strong antibacterial performance against *S. aureus* and *E. coli* due to the formation of triangular LIPSS patterns (section 4.4.5). Most importantly, the S phase pre-hardening can significantly improve the wear resistance (Fig. 4-34 & Fig. 4-36) and the

structural integrity of triangular LIPSS textures (Fig. 4-35 & Fig. 4-37), and therefore, effectively increase the durability of the antibacterial properties (section 4.5). Additionally, in line with previous 310 fs channel texturing (section 5.2.2), no signs of deterioration of the corrosion resistance of the S phase surface layer is seen following triangular LIPSS texturing (Fig. 4-27 & Fig. 4-28).

Triangular LIPSS are a new form of LIPSS patterns that have recently been discovered to occur when using femtosecond pulsed circularly polarised light under specific conditions (e.g. frequency, pulse energy, scanning speed). In the founding study by Romano *et al.* [206] in 2018, the triangular LIPSS textures were shown to have long-range ordering with three directions of periodicity that were each approximately at a 60 ° angle to neighbouring directions. Functionally, the triangular LIPSS textures have been found to be superhydrophobic and highly antibacterial [208], which has attracted attention for applications within the food and medical industries.

Although the substrate material from this study differs from the study by Romano *et al.* [206] (which used an X6Cr17 ferritic stainless steel), the physical properties, such as texture periodicity, symmetry and general morphology, appear almost identical, therefore, suggesting similar functional performance is to be expected (Fig. 4-22 & Fig. 4-23). However, wettability testing (functional property) does not follow the same trend, with water contact angle readings decreasing following triangular LIPSS texturing of the untreated 316L ASS samples (Table 4-8). Although the findings of this study initially appear to contradict the literature, the true reasoning for this change is more likely to be due to the prolonged time gap between the formation of the textures and the testing of the properties [259, 260]. It is already

well-established that surfaces undergo changes in chemistry, which are thought to be due to the introduction and then annihilation of active species, deoxidation of the surface and alterations of functional groups at the surface following laser texturing [261-263]. Therefore, since the testing within this study was carried out after a 3 month period of rest, it is more likely that the results represent the stabilised properties of the surfaces [259]. The S phase treated and triangular LIPSS textured samples (ASPNΔ), on the other hand, demonstrated water contact angles that were almost two times bigger than their untreated counterparts (UntΔ; Table 4-8). This increase in water contact angle is likely to be due to a mixture of reduced periodicity (slight but consistent reduction across all directions; Table 4-6), lack of surface tension breaking nanoparticles/nano roughness (Fig. 4-22) and increased surface stability over time in comparison to the UntΔ samples. Although not the main objective of this study, the interesting retention of the large water contact angle on the ASPNΔ sample type provides hope for future production of long-lasting hydrophobic surfaces (e.g. for anti-icing applications) [264].

The surface morphology of the UntΔ and ASPNΔ samples differs greatly at the nanoscale (Fig. 4-22). A typical rough surface with ablated and re-deposited particles can be found on the UntΔ sample type (Fig. 4-22B2), whereas a much smoother surface is observed on the ASPNΔ (Fig. 4-22D2) samples. This change in surface morphology is likely to be due to the formation of finer sputtered individual atoms or clusters of atoms from the surface of the ASPNΔ sample type as a consequence of the increased ablation threshold in comparison with the UntΔ sample type, which can then be re-deposited further away from the laser spot due to their lower mass [198, 260, 265]. As expected with femtosecond LIPSS textures, HSFL running perpendicular to

the LSFL directions can be found within the channels of both UntΔ and ASPNΔ samples [205]. Additionally, at the microscale, consistently smaller periodicity has been measured on the ASPNΔ sample type (Table 4-6), which is likely to arise due to residual stress relaxation that follows removal of surface matter during laser texturing. Furthermore, this relaxation over time could also help to explain the increase in deviation measured in the channel spacing (S1 and S2) of the ASPNΔ sample type in comparison with the UntΔ sample type. Since the Young's modulus, and therefore residual stress, of the S phase varies with grain orientation; non-uniform relaxation is expected for different grains (due to different orientations), which leads to bigger variance in channel spacing [266, 267]. At the macro scale, the triangular LIPSS textures appear almost identical for both S phase treated and untreated sample types, with similar homogeneous & multi directional scattering of light (Fig. 4-21).

Although surface texturing primarily aims to introduce anti-biofouling properties, and not antimicrobial properties (which the test in section 4.4.5 is measuring), it does however lead to a similar effect of reducing the number of colony forming units present following contact with the surface [200]. This occurs due to a greater number of bacteria remaining in the planktonic state, which typically has a slower growth rate, and consequently results in the reduction of viable bacterial cells following contact with the textured surface (as would be expected from an antimicrobial surface) [268].

S phase treated surfaces showed slight improvements in antibacterial efficacy against *S. aureus* and *E. coli*, in comparison to the untreated surfaces (Fig. 4-31 & Fig. 4-32). Previous studies have attributed this enhancement to the increased dissolution of chromium and/or iron ions from the metastable S phase surface (in comparison to untreated surfaces), which can then

affect the bacteria through mechanisms such as promotion of reactive oxygen species formation and displacement of catalytic or structural cations in enzymes [164, 269, 270].

A clear and significant improvement in antibacterial efficacy was observed for the textured (UntΔ and ASPNΔ) sample types. Unlike the study by Lutey *et al.* [208], which used a texture similar to the triangular LIPSS (called nano-pillars), the triangular LIPSS within this study were found to be effective against both *S. aureus* and *E. coli*; with the strongest activity against *S. aureus*. The overall significant improvement in antibacterial efficacy can be attributed to the channel spacing (Table 4-6) of the triangular LIPSS, which were predominantly smaller than the *S. aureus* (500 nm) & *E. coli* (500 nm x 2000 nm) being tested against; therefore, effectively reducing the available surface area for attachment and growth [194, 257, 258]. Additionally, since more bacteria stay in the planktonic state, they also remain more susceptible to external factors (e.g. hydrodynamic forces, antimicrobial agents, chemical agents) [188, 268]. This improvement in antibacterial performance was achieved despite increasing surface free energy (Fig. 4-30), which is widely accepted to increase surface fouling susceptibility [257].

The slightly stronger resistance (in terms of quantity) against *S. aureus*, in comparison to *E. coli*, can be explained by the motility of the bacteria. Unlike *S. aureus*, *E. coli* bacteria typically present with protruding flagellae that can drive the cells to surfaces, and therefore, enable more bacteria to adhere and grow [271-274].

## 5.4. Assessing Antibacterial Durability of Triangular LIPSS

### 5.4.1. Difficulties Associated with Assessing Texture Durability

One of the biggest contributors to the lack of publications on the durability of functional properties related to textures results from the difficulties associated with carrying out repeatable tests with controlled homogeneous wearing of large surfaces. To wear a texture, it is necessary to use a material that is harder than the textured sample, in order to inflict damage [76]. This is trivial for a point contact test (e.g. ball-on-plate; Fig. 4-35), where there is no need for levelling of the point of interaction, but this only provides a small contact point and at most it can only create a single line of wear (Fig. 5-1A). It is exponentially harder to carry out line and 2D area contacts (plane/surface-on-surface contact; Fig. 5-1B). The difficulty arises from the lack of deformation (conformation) in the harder counterpart, thereby, only permitting the most protruding asperities to make contact (see section 2.2.4.1). Therefore, to overcome this issue, the counterpart and the textured surface are required to be complementary in surface asperity shape prior to testing to enable equal spread of forces and homogeneous wearing of the entire contact line/2D surface area. In practice, this is extremely difficult to achieve on both the counterpart and the textured surface (especially when both materials are mechanically hard). Multiple unsuccessful attempts were made during the development of this study to find suitable approaches to large area wearing, including various line contact & 2D surface contact testing approaches (similar to Fig. 5-1B). Progress was only made once liquid suspended counterparts were attempted (Fig. 5-1C). The success of these approaches comes from: (1) the conformation of the essentially liquid counterparts, which enables even force

exertion (similar to section 2.2.4.3) and (2) homogeneous suspension of the harder counterpart particles, allowing for uniform wearing. Additionally, the ability to choose the size of the counterpart particles, speed of sliding and distance of sliding allows for the rate of surface damage/wearing to be made bespoke to the material and/or application. Essentially, this forms a closed three-body abrasive wear scenario (as described in section 2.2.4.4.1), and at its core, this approach to large area wearing is just a repurposing of the identical automated diamond suspension polishing regularly performed in any metallurgical lab (and also regularly used within this work) [76, 77]. However, under controlled conditions this can become a repeatable, reliable and readily accessible approach for assessing the durability and functional performance of often nanoscale textures (Fig. 4-38 & Fig. 4-39).

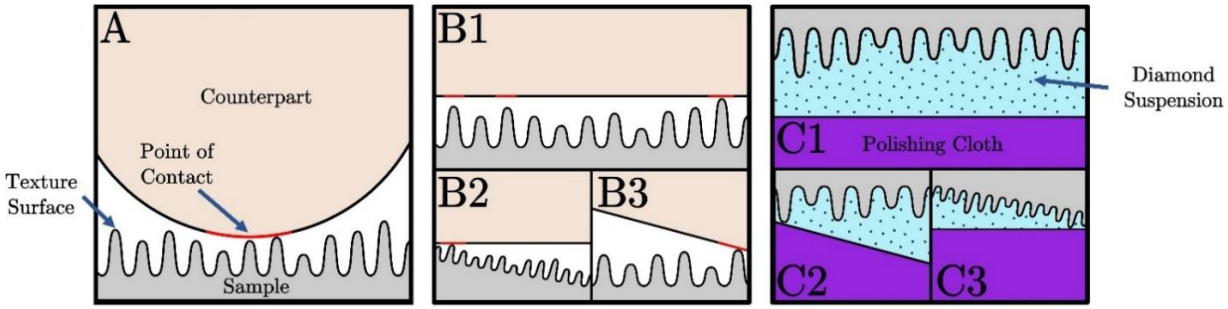



*Fig. 5-1 Different set ups for wear testing. Image A represents ball-on-plate contact (e.g. Fig. 4-35) with a single point/small area of contact. Image B represents plane/surface-on-surface contact with localised points of contact due to irregularities in the texture (B1), uneven surface on the sample (B2) and uneven counterpart surface (B3). Image C represents diamond suspension large area wearing where conformation of the liquid allows for equal pressure and the homogeneous spread of the diamond particles for controlled damage of the texture under all conditions (irregularities in the texture (C1), uneven counterpart surface (C2) and uneven surface on the sample (C3)).*

### 5.4.2. Antimicrobial Durability of Textured Surfaces

With the growing demand for, and use of, functional surfaces, it is now more important than ever before to expand our understanding of the longevity of properties associated with textured surfaces [275]. Durable textures are intentionally added surface features with high structural integrity (i.e. resistant to damage). They differ from textures that improve wear resistance of surfaces through mechanisms such as sacrificial wearing or wear debris entrapment (e.g. high aspect ratio pits/channels) [276, 277]. There are very few published papers that have examined the durability of textures, and even less that have studied the functional durability [257, 260, 275, 278-280]. This is particularly alarming as most functional textures rely on the preservation of fragile nanoscale features. To date, no other published works have analysed the antibacterial durability of surfaces.

As has been shown in Fig. 4-40 and Fig. 4-41, triangular LIPSS texturing can introduce similar high antibacterial performance on both untreated AISI 316L surfaces (UntΔ) and S phase treated surfaces (ASPNΔ). However, the antibacterial efficacy of the UntΔ sample type against both *S. aureus* and *E. coli* was shown to drop by 56.9 and 51.1 %, respectively, after low distance large area wearing. This demonstrated a need for the susceptibility of such surfaces to the loss of functionality, and the need for both, the production of durable textures, and the characterisation of long lasting antibacterial properties, thereby enabling determination of safe long-term use.

A clear increase in antibacterial durability (both *S. aureus* and *E. coli*) was found with the ASPNΔ sample type against the UntΔ sample type (Fig. 4-40 & Fig. 4-41). After both low and medium

distance large area wearing, the ASPNΔ samples were still shown to possess significantly better antimicrobial efficacy than low distance large area worn UntΔ surfaces. A more prominent drop in efficacy was found for the ASPNΔ samples against *S. aureus* than *E. coli*, which is likely due to the differing bacterial cell sizes [208, 281]. During surface wearing the initially shielded texture valleys (described in Section 5.3.2) become available sooner for attachment for *S. aureus* than for *E. coli*. Within the parameters of this study, no such phenomenon could not be observed with the UntΔ samples as the texture features were rapidly lost.

The significantly enhanced antibacterial durability of the textured surfaces can be attributed to the effective increase of surface hardness through S phase hardening, as evidenced by the nanoindentation hardness depth profiling (Fig. 4-26). In line with previous findings of this study [26], the lack of any crystallised nitride peaks (Fig. 4-25), over-etched areas (Fig. 4-24) or localised aggregation of elements (Fig. 4-19) allowed confirmation of the precipitate-free nature (unchanged chemistry) of the textured S phase surface (ASPNΔ). This hardening, therefore, predominantly arises due to interstitial (N) supersaturation, increased dislocation density and increased deformation twin density at the surface [8, 282]. Additionally, no change in the mechanical properties across the depth of the S phase layer could be found following the triangular LIPSS texturing, which reflects one of the key advantages of athermal fs laser texturing [23].

The successfully improved durability of textured surfaces through the novel synergetic combination of S phase hardening and laser texturing can pave the way towards long-lasting high efficacy antibacterial surfaces for high performance medical devices and food processing equipment. Equally, such an approach will be valuable for generating durable functional

properties, such as anti-icing [283], anti-biofouling [284] and anti-wetting [257], that are frequently finding industrial applications.

## 5.5. Future Perspective

### 5.5.1. Proposed Future Work on Antibacterial Textures

The findings of this study have helped to demonstrate the successful use of laser texturing on thermodynamically metastable S phase treated surfaces. Additionally, it has been shown that this novel synergetic combination can produce long-lasting antibacterial properties throughout various stages of surface damage. Going forward, it would be scientifically valuable to explore the following areas:

(1) Expand the understanding of the functional durability of these surfaces with regards to the other properties (e.g. hydrophobicity) that they possess. This can be performed using the strategy outlined within this study (section 3.6.2). The findings of this can help to characterise and optimise future generations of durable antibacterial and hydrophobic/hydrophilic surfaces. To obtain accurate representations of these properties, it is necessary for close control and regulation to be kept over the surface ageing (following texturing) and quality/cleanliness (ambient storage condition) of the surfaces to be measured.

(2) Examine the changes in bacterial attachment following texturing, with focus on the location of attachment. The findings of this work can help to further characterise the antibacterial functional performance of the triangular LIPSS textures, as well as,

enabling the examination of “cleanability” of the textures (as would be expected to be performed on a long-lasting antibacterial surface).

(3) Examine in further detail the surface structures and chemistry present on both nanosecond and femtosecond textured surfaces in more detail. Given the initial findings within this study, that modification of the oxide layer and state arises during laser texturing, it would be scientifically valuable to examine in detail, using Raman and XPS analysis, the subsequent surface characteristics.

(4) Since untreated surfaces succumb to significantly greater wear than S phase treated surfaces, it can be expected, and shown in this study, that under the same wearing conditions, the surface morphology of the two sample types varies greatly. Consequently, the functional properties of the two surfaces are also vastly different. For application purposes, this demonstrates the need to produce durable textured surfaces. However, to expand scientific understanding on the mechanism behind the change in functional property during wearing, it would be interesting to explore the difference between equally worn triangular LIPSS textures on untreated and S phase treated samples (i.e. identical morphology following large area wearing). The findings of this can help to differentiate the influence of chemistry and topography on the functional properties.

(5) The combination of more advanced plasma treatment technologies, such as triple-glow plasma nitriding, with these triangular LIPSS textures can potentially produce highly multifunctional and durable surfaces [285]. In particular, the combination of silver and S phase co-alloyed surface layers, produced through triple-glow plasma nitriding, with

these triangular LIPSS textures, have the potential to produce surfaces that possess both highly anti-biofouling (from texture) and antimicrobial (from bactericidal effect of silver) properties. Moreover, early indications of these novel triple-glow plasma nitriding treatments (unpublished work) reveal that, despite the relatively weak mechanical properties of pure silver, such silver containing co-alloyed layers can possess mechanical properties that are even superior to the already hard nitrogen S phase, and therefore, are expected to have even higher resistance to wearing. Additionally, the silver that resides in these co-alloyed layers can also act as a solid lubricant, and thus, help to further reduce both the wear and friction of the subsequent surfaces.

### 5.5.2. Future Use of Texture Channel Spacing

Currently, there is a lack of general parameters available for the description and comparison of functional textures. Periodicity is the most widely used descriptor for textures, and although it does provide valuable information about the patterns, it falls short when used to explain antibacterial properties. Finer periodic structures are typically associated with antibiofouling properties; however, this is not always the case [258, 281, 286]. Fig. 5-2 highlights the pitfalls of using periodicity as a functional descriptor, with increasingly smaller periodicities being both beneficial (Fig. 5-2B1) and detrimental (Fig. 5-2B2) to the functional performance. Tip diameter, which describes the top-most available surface of a texture, is another parameter that is regularly found within the literature [201]. It has been successfully used to describe the antimicrobial properties introduced as a result of needle or nano-spike textures (through

penetration and lysing of bacteria) [169]. However, like periodicity, tip diameter also fails to capture the functional performance of textures, with larger tip diameters leading to both beneficial (Fig. 5-2C1) and detrimental effects (Fig. 5-2C2). Additionally, the shortcomings are also apparent when the antibacterial performance changes while the periodicity or tip diameter are kept constant (Fig. 5-2).

It is therefore recommended that in the future, channel spacing, a much less commonly used parameter, should be used in combination with tip diameter and periodicity when describing antibacterial textures. From Fig. 5-2 it can be deduced that channel spacing is a function of both tip diameter and periodicity (i.e. changes in response to both variables). In particular, the combination of tip diameter and channel spacing can comprehensively describe the physical availability of the top-most surface (tip diameter) and the valleys (channel spacing) of the texture to the attachment of bacteria.

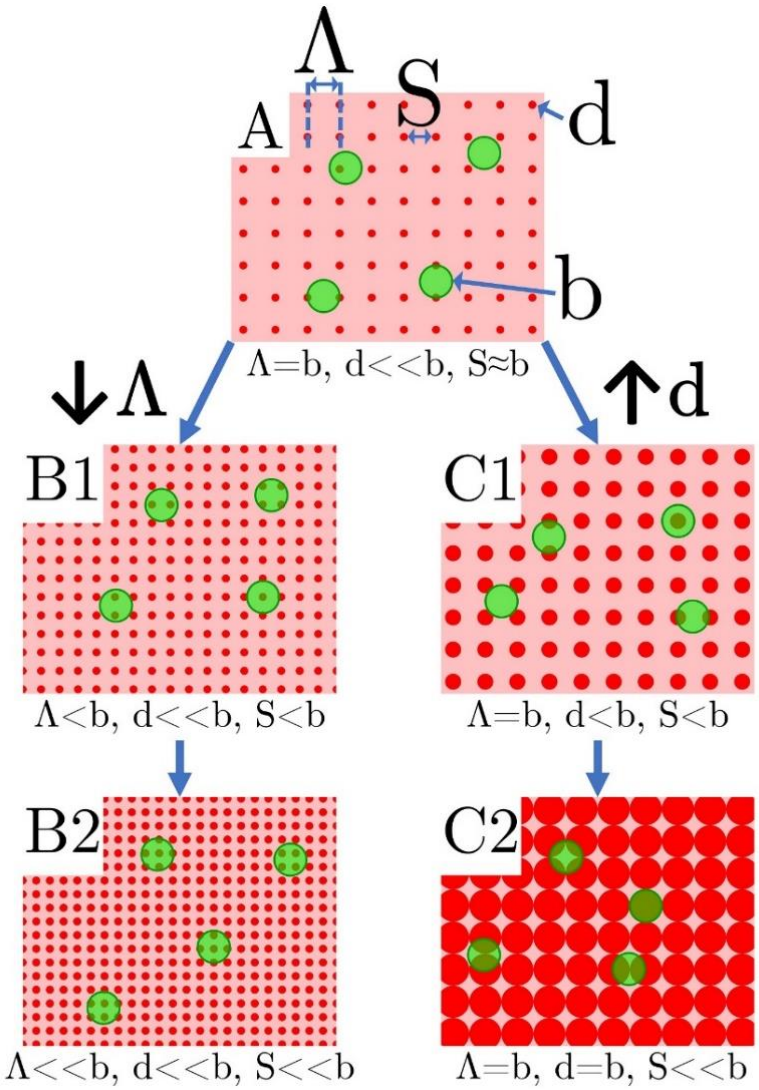



*Fig. 5-2 Changing surface morphology and availability for bacterial (b) attachment. Images B1 and B2 describe the available surface with reducing periodicity (Λ). Images C1 and C2 describe the available surface with increasing tip diameter (d). Note that only channel spacing (S) changes with both periodicity and tip diameter.*

# CHAPTER 6 CONCLUSIONS

The findings of this study can be summarised as follows [26]:

1. Feasibility studies of laser texturing on S phase surfaces was performed by forming channel textures on untreated and nitrogen S phase treated AISI 316L surfaces using nanosecond (ns) and femtosecond (fs) pulsed laser texturing.
2. Surface texturing using laser pulses within the nanosecond regime (15 and 220 ns) led to severe damage of the S phase surface, decomposition of the metastable S phase, and formation of precipitates. Subsequently, distinct losses in corrosion resistance were revealed through anodic polarisation testing & electrochemical impedance spectroscopy.
3. Heat conduction modelling revealed that nanosecond pulsed laser texturing provided significantly higher temperatures than is necessary for decomposition of the metastable S phase layer. Well-established kinetic analysis also predicted similar outcomes.
4. Femtosecond laser texturing within the kHz frequency range did not cause any appreciable decomposition of nitrogen supersaturated metastable S phase surfaces. This was largely attributed to the athermal nature of fs pulse laser texturing via rapid evaporation/ablation without appreciable heat diffusion.
5. No discernible changes in chemical composition, cross-sectional layer structure or electrochemical corrosion properties could be found in the S phase following fs

texturing. Hence, it was concluded to be feasible to texture metastable S phase surfaces using fs lasers without causing undue deterioration of the S-phase layers.

6. Femtosecond laser texturing of S phase treated surfaces was expanded to produce different bio-inspired surface structures (springtails, lotus leaves and shark skin). Brief analysis of the response of the S phase following the formation of the different textures revealed no change in chemical composition or layer structure.
7. Textures characterised by larger proportions of nanoscale features were found to possess better antibacterial efficacy against *S. aureus*, with the triangular LIPSS, which closely resembling springtails, demonstrating the strongest resistance.
8. Triangular LIPSS textures were found to consist of hexagonally organised peaks with periodicity in three different directions. As a result of the periodicity of approximately 900 nm, multi directional scattering of light was observed from the triangular LIPSS textures.
9. Due to the fine periodic structures and small channel spacing associated with the triangular LIPSS, strong antibacterial performance against *S. aureus* and *E. coli* was measured following texturing of both untreated and S phase treated AISI 316L stainless steel surfaces.
10. Following a stabilisation period of 3 months, hydrophobic properties were found to be retained on S phase treated and triangular LIPSS textured surfaces, while hydrophilic properties developed on identical untreated surfaces.
11. Rapid removal of triangular LIPSS textures through severe adhesive wearing, even under light loading, was observed on untreated AISI 316L surfaces.

12. Improved wear resistance and structural integrity were found following duplex S phase hardening and triangular LIPSS texturing of AISI 316L surfaces. Therefore, the durability of the antibacterial properties were discovered to be effectively improved (at least two fold).

# REFERENCES


[1] Davis, J.R. (1994) **Stainless steels**. ASM international: Materials Park, OH.

[2] Dewangan, A., Patel, A. and Bhadania, A. (2015) Stainless steel for dairy and food industry. **Research Journal of Animal Husbandry and Dairy Science**; 6(1): 66-71.

[3] Kathuria, Y.P. (2004) An overview on laser microfabrication of bicompatible metallic stent for medical therapy. **Laser-Assisted Micro-and Nanotechnologies 2003**; 5399: 234-245.

[4] Verran, J. and Whitehead, K. (2005) Factors affecting microbial adhesion to stainless steel and other materials used in medical devices. **The International journal of artificial organs**; 28(11): 1138-1145.

[5] Ren, Y., Yang, K., Zhang, B., Wang, Y. and Liang, Y. (2004) Nickel-free stainless steel for medical applications. **Journal of Materials science and technology**; 20(5): 571-573.

[6] Decléty, P. (2003) Metals used in the food industry. **Ecyclopaedia of Food Science, Food Technology and Nutrition**: 3869-3876.

[7] Chmielewski, R. and Frank, J. (2003) Biofilm formation and control in food processing facilities. **Comprehensive reviews in food science and food safety**; 2(1): 22-32.

[8] Dong, H. (2010) S-phase surface engineering of Fe-Cr, Co-Cr and Ni-Cr alloys. **International Materials Reviews**; 55(2): 65-98.

[9] Menthe, E. and Rie, K.-T. (1999) Further investigation of the structure and properties of austenitic stainless steel after plasma nitriding. **Surface and Coatings Technology**; 116: 199-204.

[10] Wong, A.C.L. (1998) Biofilms in food processing environments. **Journal of dairy science**; 81(10): 2765-2770.

[11] Kusumaningrum, H., Riboldi, G., Hazeleger, W. and Beumer, R. (2003) Survival of foodborne pathogens on stainless steel surfaces and cross-contamination to foods. **International journal of food microbiology**; 85(3): 227-236.

[12] Jones, A.K., Cross, P., Burton, M., Millman, C., O'Brien, S.J. and Rigby, D. (2017) Estimating the prevalence of food risk increasing behaviours in UK kitchens. **PloS one**; 12(6).

[13] Tam, C., Larose, T. and O'Brien, S.J. (2014) Costed extension to the Second Study of Infectious Intestinal Disease in the Community: Identifying the proportion of foodborne disease in the UK and attributing foodborne disease by food commodity. **Food Standards Agency**; UK.

[14] Mantle, S. (2015) Reducing HCAI-What the Commissioner needs to know. **NHS England**.

[15] Food Standards Agency (2013) **Annual Report of the Chief Scientist 2012/13. Safer food for the nation**. Food Standards Agency: UK.

[16] Zhang, Z.L. and Bell, T. (1985) Structure and Corrosion Resistance of Plasma Nitrided Stainless Steel. **Surface Engineering**; 1(2): 131-136.

[17] Ichii, K., Fujimura, K. and Takase, T. (1986) Structure of the ion-nitrided layer of 18-8 stainless steel. **Technology Reports of Kansai University**; 27: 135-144.

[18] Bell, T. (2002) Surface engineering of austenitic stainless steel. **Surface Engineering**; 18(6): 415-422.

[19] Barish, J.A. and Goddard, J.M. (2013) Anti-fouling surface modified stainless steel for food processing. **Food and Bioproducts processing**; 91(4): 352-361.

[20] Nolte, S., Momma, C., Jacobs, H., Tünnermann, A., Chichkov, B.N., Wellegehausen, B. and Welling, H. (1997) Ablation of metals by ultrashort laser pulses. **JOSA B**; 14(10): 2716-2722.

[21] Li, X. (2001) Joint second prize low temperature plasma nitriding of 316 stainless steel–nature of S phase and its thermal stability. **Surface Engineering**; 17(2): 147-152.

[22] Yilbas, B.S. and Shuja, S.Z. (2013) **Laser surface processing and model studies**. Springer: Berlin, Germany.

[23] Sundaram, S. and Mazur, E. (2002) Inducing and probing non-thermal transitions in semiconductors using femtosecond laser pulses. **Nature materials**; 1(4): 217.

[24] Bonse, J., Höhm, S., Kirner, S.V., Rosenfeld, A. and Krüger, J. (2017) Laser-induced periodic surface structures—a scientific evergreen. **IEEE Journal of Selected Topics in Quantum Electronics**; 23(3): 1-15.

[25] Bechtel, J. (1975) Heating of solid targets with laser pulses. **Journal of Applied Physics**; 46(4): 1585-1593.

[26] Dashtbozorg, B., Li, X., Romano, J.M., Garcia–Giron, A., Sammons, R.L., Dimov, S. and Dong, H. (2020) A study on the effect of ultrashort pulsed laser texturing on the microstructure and properties of metastable S phase layer formed on AISI 316L surfaces. **Applied Surface Science**; 511: 145557.

[27] Cramer, S.D., Covino, B.S. and Moosbrugger, C. (2005) **ASM handbook volume 13b: corrosion: materials**. ASM International: Materials Park, OH.

[28] McGuire, M.F. (2008) **Stainless steels for design engineers**. ASM International: Materials Park, OH.

[29] Lozano-Perez, S., Saxey, D.W., Yamada, T. and Terachi, T. (2010) Atom-probe tomography characterization of the oxidation of stainless steel. **Scripta Materialia**; 62(11): 855-858.

[30] Bhadeshia, H. and Honeycombe, R. (2017) **Steels: microstructure and properties**. Butterworth-Heinemann.

[31] Dossett, J.L. and Totten, G.E. (2013) **ASM Handbook: Steel Heat Treating, Fundamentals and Processes. Volume 4A**. ASM International: Materials Park, OH.

[32] Prager, M. (1984) Cast High Alloy Metallurgy. **Steel Casting Metallurgy**: 221.

[33] Davis, J.R. (2000) **Corrosion: Understanding the basics**. ASM International: Materials Park, OH.

[34] ASM (1994) **ASM Handbook Vol. 5: Surface Engineering**. ASM International: Materials Park, OH. 345-347 p.

[35] Khatak, H.S. and Raj, B. (2002) **Corrosion of austenitic stainless steels: mechanism, mitigation and monitoring**. Woodhead publishing.

[36] Durand-Charre, M. (2004) **Microstructure of steels and cast irons**. Springer Science & Business Media.

[37] Davis, J.R. (2000) **Alloy digest sourcebook: stainless steels**. ASM international: Materials Park, OH.

[38] Narayan, R. (2012) **ASM Handbook, Volume 23, Materials for Medical Devices**. ASM International: Materials Park, OH.

[39] Llewellyn, D. and Hudd, R. (1998) **Steels: metallurgy and applications**. Elsevier.

[40] Nilsson, J. (2018) **Precipitation Hardened Stainless Steels** [Online]. Accessed From: https://www.materials.sandvik/en-gb/materials-center/expert-columns/archive/2018/02/precipitation-hardened-stainless-steels/ (02/11/2020)

[41] Alderliesten, R. (2018) **Introduction to Aerospace Structures and Materials**. Delft University of Technology.

[42] Davis, J.R. (2003) **Handbook of materials for medical devices**. ASM International: Materials Park, OH.

[43] Casarin, L.S., de Oliveira Casarin, F., Soares, T.P., Aguzzoli, C., Figueroa, C.A., Soares, G.V., Brandelli, A. and Tondo, E.C. (2016) Effect of plasma nitriding surface modification on the adhesion of food pathogens to stainless steel AISI 316 and AISI 304. **Journal of Food Safety**; 36(3): 341-347.

[44] World Material (2020) **AISI 304 Grade Stainless Steel Properties, Tensile Yield Strength, Thermal Conductivity** [Online]. Accessed From: https://www.theworldmaterial.com/type-304-grade-stainless-steel/ (05/11/2020)

[45] Maciejewski, J. (2015) The effects of sulfide inclusions on mechanical properties and failures of steel components. **Journal of Failure Analysis and Prevention**; 15(2): 169-178.

[46] Aalco (2019) **Alloying Elements in Stainless Steel** [Online]. Accessed From: http://www.aalco.co.uk/datasheets/Stainless-Steel_Alloying-Elements-in-Stainless-Steel_98.ashx (05/11/2020)

[47] Cobb, H.M. (2010) **The history of stainless steel**. ASM International.

[48] Hashimoto, K., Asami, K., Kawashima, A., Habazaki, H. and Akiyama, E. (2007) The role of corrosion-resistant alloying elements in passivity. **Corrosion Science**; 49(1): 42-52.

[49] Sugimoto, K. and Sawada, Y. (1977) The role of molybdenum additions to austenitic stainless steels in the inhibition of pitting in acid chloride solutions. **Corrosion Science**; 17(5): 425-445.

[50] Clayton, C. and Lu, Y. (1986) A bipolar model of the passivity of stainless steel: the role of Mo addition. **Journal of the Electrochemical Society**; 133(12): 2465.

[51] Nishimoto, M., Muto, I., Sugawara, Y. and Hara, N. (2019) Morphological characteristics of trenching around MnS inclusions in type 316 stainless steel: the role of molybdenum in pitting corrosion resistance. **Journal of The Electrochemical Society**; 166(11): C3081.

[52] Ilevbare, G. and Burstein, G. (2001) The role of alloyed molybdenum in the inhibition of pitting corrosion in stainless steels. **Corrosion Science**; 43(3): 485-513.

[53] Henderson, J.D., Li, X., Shoesmith, D.W., Noël, J.J. and Ogle, K. (2019) Molybdenum surface enrichment and release during transpassive dissolution of Ni-based alloys. **Corrosion Science**; 147: 32-40.

[54] Maurice, V., Peng, H., Klein, L.H., Seyeux, A., Zanna, S. and Marcus, P. (2015) Effects of molybdenum on the composition and nanoscale morphology of passivated austenitic stainless steel surfaces. **Faraday discussions**; 180: 151-170.

[55] BomBač, D., Brojan, M., Fajfar, P., Kosel, F. and Turk, R. (2007) Review of materials in medical applications Pregled materialov v medicinskih aplikacijah. **RMZ–Materials and Geoenvironment**; 54(4): 471-499.

[56] Lo, K.H., Shek, C.H. and Lai, J. (2009) Recent developments in stainless steels. **Materials Science and Engineering: R: Reports**; 65(4-6): 39-104.

[57] McCafferty, E. (2010) **Introduction to corrosion science**. Springer Science & Business Media.

[58] Davis, J.R. (2001) **Surface engineering for corrosion and wear resistance**. ASM international.

[59] Newman, R. and Shahrabi, T. (1987) The effect of alloyed nitrogen or dissolved nitrate ions on the anodic behaviour of austenitic stainless steel in hydrochloric acid. **Corrosion Science**; 27(8): 827-838.

[60] Olsson, C.-O.A. (1995) The influence of nitrogen and molybdenum on passive films formed on the austenoferritic stainless steel 2205 studied by AES and XPS. **Corrosion Science**; 37(3): 467-479.

[61] Ghanem, W.A., Hussein, W., Saeed, S., Bader, S. and Abou Shahba, R. (2015) Effect of nitrogen on the corrosion behavior of austenitic stainless steel in chloride solutions. **Modern Applied Science**; 9(11): 119.

[62] Kadowaki, M., Saengdeejing, A., Muto, I., Chen, Y., Frankel, G.S., Doi, T., Kawano, K., Sugawara, Y. and Hara, N. (2020) Roles of Interstitial Nitrogen, Carbon, and Boron in Steel Corrosion: Generation of Oxyanions and Stabilization of Electronic Structure. **Journal of The Electrochemical Society**; 167(8): 081503.

[63] Féron, D. (2007) **Corrosion behaviour and protection of copper and aluminium alloys in seawater**. Elsevier.

[64] Smith, A. (1984) The friction and sliding wear of unlubricated 316 stainless steel at room temperature in air. **Wear**; 96(3): 301-318.

[65] Popov, V.L. (2018) Is tribology approaching its golden age? Grand challenges in engineering education and tribological research. **Frontiers in Mechanical Engineering**; 4: 16.

[66] Hsu, K.-L., Ahn, T. and Rigney, D. (1980) Friction, wear and microstructure of unlubricated austenitic stainless steels. **Wear**; 60(1): 13-37.

[67] Dong, Y.C., Li, X.Y., Sammons, R. and Dong, H.S. (2010) The Generation of Wear-Resistant Antimicrobial Stainless Steel Surfaces by Active Screen Plasma Alloying with N and Nanocrystalline Ag. **Journal of Biomedical Materials Research Part B-Applied Biomaterials**; 93B(1): 185-193.

[68] Outokumpu (2013) **Handbook of Stainless Steels**. Outokumpu Oyj.

[69] Skoczen, B.T. (2004) **Compensation systems for low temperature applications**. Springer Science & Business Media.

[70] Han, W., Liu, Y., Wan, F., Liu, P., Yi, X., Zhan, Q., Morrall, D. and Ohnuki, S. (2018) Deformation behavior of austenitic stainless steel at deep cryogenic temperatures. **Journal of Nuclear Materials**; 504: 29-32.

[71] Mallick, P., Tewary, N., Ghosh, S. and Chattopadhyay, P. (2017) Effect of cryogenic deformation on microstructure and mechanical properties of 304 austenitic stainless steel. **Materials Characterization**; 133: 77-86.

[72] Weiss, B. and Stickler, R. (1972) Phase instabilities during high temperature exposure of 316 austenitic stainless steel. **Metallurgical and Materials Transactions B**; 3(4): 851-866.

[73] Stellwag, B. (1998) The mechanism of oxide film formation on austenitic stainless steels in high temperature water. **Corrosion science**; 40(2-3): 337-370.

[74] Takadoum, J. (2013) **Materials and surface engineering in tribology**. John Wiley & Sons.

[75] Mang, T., Bobzin, K. and Bartels, T. (2011) **Industrial tribology: Tribosystems, friction, wear and surface engineering, lubrication**. John Wiley & Sons.

[76] Totten, G.E. (1992) **ASM handbook, Volume 18: friction, lubrication, and wear technology**. ASM International.

[77] Phoenix Tribology (2020) **Sliding Hertzian point contact tests** [Online]. Accessed From: http://www.phoenix-tribology.com/wp-content/uploads/guidance/Guidance-Sliding-Hertzian-Point-Contact.pdf (20/11/2020)

[78] Holmberg, K. and Erdemir, A. (2017) Influence of tribology on global energy consumption, costs and emissions. **Friction**; 5(3): 263-284.

[79] Sun, Y. and Bell, T. (1998) Sliding wear characteristics of low temperature plasma nitrided 316 austenitic stainless steel. **Wear**; 218(1): 34-42.

[80] Yetim, A., Yildiz, F., Alsaran, A. and Celik, A. (2008) Surface modification of 316L stainless steel with plasma nitriding. **Kovove Materialy**; 46(2): 105.

[81] Holmberg, K. and Matthews, A. (2009) **Coatings tribology: properties, mechanisms, techniques and applications in surface engineering**. Elsevier.

[82] Adachi, K. and Hutchings, I. (2003) Wear-mode mapping for the micro-scale abrasion test. **Wear**; 255(1-6): 23-29.

[83] Wei, M., Chen, K., Wang, S. and Cui, X. (2011) Analysis for wear behaviors of oxidative wear. **Tribology Letters**; 42(1): 1-7.

[84] Straffelini, G., Trabucco, D. and Molinari, A. (2001) Oxidative wear of heat-treated steels. **Wear**; 250(1-12): 485-491.

[85] Xu, Z., Fang, B., Zheng, W., Wang, C. and Tang, B. (1990) A novel plasma surface metallurgy: Xu-Tec process. **Surface and Coatings Technology**; 43: 1065-1073.

[86] Bell, T. (1987) Surface Engineering: a rapidly developing discipline. **European Journal of Engineering Education**; 12(1): 27-32.

[87] Borgioli, F. (2020) From austenitic stainless steel to expanded austenite-S phase: Formation, characteristics and properties of an elusive metastable phase. **Metals**; 10(2): 187.

[88] Bell, T. (1992) Surface Engineering - Its Current and Future Impact on Tribology. **Journal of Physics D-Applied Physics**; 25(1A): A297-A306.

[89] Burakowski, T. and Wierzchon, T. (1998) **Surface engineering of metals: principles, equipment, technologies**. CRC press.

[90] Machlet, A.W. (1914) Hardening or treatment of steel, iron, &c. **US Patents:** 1092925

[91] Mittemeijer, E.J. and Somers, M.A. (2014) **Thermochemical surface engineering of steels: improving materials performance**. Elsevier.

[92] Pye, D. (2003) **Practical nitriding and ferritic nitrocarburizing**. ASM international.

[93] Sato, N., Ojima, M., Tomota, Y. and Inaba, K. (2008) Surface Modification by Nitriding-Quenching for Steels. **Proc of the 17th International Federation on Heat Treatment and Surface Engineering Congress**: 220.

[94] Davis, J.R. (2002) **Surface hardening of steels: understanding the basics**. ASM international.

[95] Buhagiar, J. (2010) 25 years of S-phase. 26(4): 229-232.

[96] Berghaus, B. (1932) Process for surface treatment of metallic elements. **German Patent DRP**; 668639.

[97] Bell, T. and Dearnley, P. (1994) Environmental issues in surface engineering and related industrial sectors. **Surface engineering**; 10(2): 123-128.

[98] Roth, J. (2002) **Industrial Plasma Engineering: Volume 1: Principles**. Taylor & Francis.

[99] Kaklamani, G., Mehrban, N., Chen, J., Bowen, J., Dong, H., Grover, L. and Stamboulis, A. (2010) Effect of plasma surface modification on the biocompatibility of UHMWPE. **Biomedical Materials**; 5(5): 054102.

[100] Liang, Y., Li, X., Semitekolos, D., Charitidis, C.A. and Dong, H. (2020) Enhanced properties of PAN‐derived carbon fibres and resulting composites by active screen plasma surface functionalisation. **Plasma Processes and Polymers**; 17(4): 1900252.

[101] Czerwiec, T., Marcos, G., Thiriet, T., Guo, Y. and Belmonte, T. (2009) Austenitic stainless steel patterning by plasma assisted diffusion treatments. **IOP Conference Series: Materials Science and Engineering**; 5: 012012.

[102] Fridman, A., Chirokov, A. and Gutsol, A. (2005) Non-thermal atmospheric pressure discharges. **Journal of Physics D: Applied Physics**; 38(2): R1.

[103] Ghosh, S., Yang, R., Kaumeyer, M., Zorman, C.A., Rowan, S.J., Feng, P.X.-L. and Sankaran, R.M. (2014) Fabrication of electrically conductive metal patterns at the surface of polymer films by microplasma-based direct writing. **ACS applied materials & interfaces**; 6(5): 3099-3104.

[104] Liu, F., Liu, Y., Lu, Y., Wang, Z., Shi, Y., Ji, L. and Cheng, J. (2019) Electrical analysis of triboelectric nanogenerator for high voltage applications exampled by DBD microplasma. **Nano energy**; 56: 482-493.

[105] Staack, D., Farouk, B., Gutsol, A. and Fridman, A. (2008) DC normal glow discharges in atmospheric pressure atomic and molecular gases. **Plasma Sources Science and Technology**; 17(2): 025013.

[106] Fridman, A. (2008) **Plasma chemistry**. Cambridge university press.

[107] Rembges, W. and Oppel, W. (1993) Process control of plasma nitriding and plasma nitrocarburizing in industry. **Surface and coatings technology**; 59(1-3): 129-134.

[108] Kölbel, J. (2013) **Die Nitridschichtbildung bei der Glimmnitrierung**. Springer-Verlag.

[109] Saeed, A., Khan, A., Jan, F., Abrar, M., Khalid, M. and Zakaullah, M. (2013) Validity of “sputtering and re-condensation” model in active screen cage plasma nitriding process. **Applied Surface Science**; 273: 173-178.

[110] Li, C.X., Bell, T. and Dong, H. (2002) A study of active screen plasma nitriding. **Surface Engineering**; 18(3): 174-181.

[111] Fridman, A. and Kennedy, L.A. (2004) **Plasma physics and engineering**. CRC press.

[112] Georges, J. (1999) Nitriding process and nitriding furnace therefor. **US Patent:** 5,989,363

[113] Zhao, C., Li, C.X., Dong, H. and Bell, T. (2006) Study on the active screen plasma nitriding and its nitriding mechanism. **Surface & Coatings Technology**; 201(6): 2320-2325.

[114] Gallo, S.C. and Dong, H. (2011) Corrosion behaviour of direct current and active screen plasma carburised AISI 316 stainless steel in boiling sulphuric acid solutions. **Corrosion Engineering Science and Technology**; 46(1): 8-16.

[115] Li, C. and Bell, T. (2004) Corrosion properties of active screen plasma nitrided 316 austenitic stainless steel. **Corrosion Science**; 46(6): 1527-1547.

[116] Nishimoto, A., Nagatsuka, K., Narita, R., Nii, H. and Akamatsu, K. (2010) Effect of the distance between screen and sample on active screen plasma nitriding properties. **Surface and Coatings Technology**; 205: S365-S368.

[117] Fraczek, T., Ogorek, M., Skuza, Z. and Prusak, R. (2020) Mechanism of ion nitriding of 316L austenitic steel by active screen method in a hydrogen-nitrogen atmosphere. **The International Journal of Advanced Manufacturing Technology**; 109(5): 1357-1368.

[118] Gallo, S.C. and Dong, H. (2009) On the fundamental mechanisms of active screen plasma nitriding. **Vacuum**; 84(2): 321-325.

[119] Lin, K., Li, X., Dong, H., Guo, P. and Gu, D. (2018) Nitrogen mass transfer and surface layer formation during the active screen plasma nitriding of austenitic stainless steels. **Vacuum**; 148: 224-229.

[120] Biró, A.S. (2014) Active Screen Plasma Nitriding State of the Art. 7: 103-114.

[121] Leyland, A., Lewis, D., Stevenson, P. and Matthews, A. (1993) Low temperature plasma diffusion treatment of stainless steels for improved wear resistance. **Surface and Coatings Technology**; 62(1-3): 608-617.

[122] Kolster, B. (1983) Verschleiß-und korrosionsfeste Schichten auf austenitischen Stählen. **VDI-Berichte**; 506: 107-113.

[123] Sun, Y., Li, X. and Bell, T. (1999) X-ray diffraction characterisation of low temperature plasma nitrided austenitic stainless steels. **Journal of Materials Science**; 34(19): 4793-4802.

[124] Cao, Y., Ernst, F. and Michal, G. (2003) Colossal carbon supersaturation in austenitic stainless steels carburized at low temperature. **Acta Materialia**; 51(14): 4171-4181.

[125] Thaiwatthana, S., Li, X., Dong, H. and Bell, T. (2002) Comparison studies on properties of nitrogen and carbon S phase on low temperature plasma alloyed AISI 316 stainless steel. **Surface Engineering**; 18(6): 433-437.

[126] Williamson, D., Ivanov, I., Wei, R. and Wilbur, P. (1991) Role of chromium in high-dose, high-rate, elevated temperature nitrogen implantation of austenitic stainless steels. **MRS Online Proceedings Library Archive**; 235.

[127] Parascandola, S., Möller, W. and Williamson, D. (2000) The nitrogen transport in austenitic stainless steel at moderate temperatures. **Applied Physics Letters**; 76(16): 2194-2196.

[128] Christiansen, T.L., Drouet, M., Martinavičius, A. and Somers, M.A. (2013) Isotope exchange investigation of nitrogen redistribution in expanded austenite. **Scripta Materialia**; 69(8): 582-585.

[129] Christiansen, T., Dahl, K.V. and Somers, M.A. (2008) Nitrogen diffusion and nitrogen depth profiles in expanded austenite: experimental assessment, numerical simulation and role of stress. **Materials Science and Technology**; 24(2): 159-167.

[130] Li, X., Sun, Y. and Bell, T. (1999) The stability of the nitrogen S-phase in austenitic stainless steel. **Zeitschrift fur Metallkunde(Germany)**; 90(11): 901-907.

[131] Brink, B., Ståhl, K., Christiansen, T.L. and Somers, M.A. (2014) Thermal expansion and phase transformations of nitrogen-expanded austenite studied with in situ synchrotron X-ray diffraction. **Journal of Applied Crystallography**; 47(3): 819-826.

[132] Christiansen, T. and Somers, M.A. (2004) On the crystallographic structure of S-phase. **Scripta Materialia**; 50(1): 35-37.

[133] Peng, Y., Liu, Z., Jiang, Y., Wang, B., Gong, J. and Somers, M.A. (2018) Experimental and numerical analysis of residual stress in carbon-stabilized expanded austenite. **Scripta Materialia**; 157: 106-109.

[134] Blawert, C., Mordike, B., Collins, G., Short, K., Jiraskova, Y., Schneeweiss, O. and Perina, V. (2000) Characterisation of duplex layer structures produced by simultaneous implantation of nitrogen and carbon into austenitic stainless steel X5CrNi189. **Surface and Coatings Technology**; 128: 219-225.

[135] Christiansen, T. and Somers, M.A. (2006) Characterisation of low temperature surface hardened stainless steel. **Struers Journal of Materialography**; 9: 1-17.

[136] Tao, X., Liu, X., Matthews, A. and Leyland, A. (2019) The influence of stacking fault energy on plasticity mechanisms in triode-plasma nitrided austenitic stainless steels: Implications for the structure and stability of nitrogen-expanded austenite. **Acta Materialia**; 164: 60-75.

[137] Christiansen, T. and Somers, M.A. (2006) Controlled dissolution of colossal quantities of nitrogen in stainless steel. **Metallurgical and Materials Transactions A**; 37(3): 675-682.

[138] Paterson, M.S. (1952) X‐ray diffraction by face‐centered cubic crystals with deformation faults. **Journal of Applied Physics**; 23(8): 805-811.

[139] Oddershede, J., Christiansen, T.L. and Ståhl, K. (2008) Modelling the X-ray powder diffraction of nitrogen-expanded austenite using the Debye formula. **Journal of Applied Crystallography**; 41(3): 537-543.

[140] Oddershede, J., Christiansen, T.L., Ståhl, K. and Somers, M.A. (2010) Extended X-ray absorption fine structure investigation of nitrogen stabilized expanded austenite. **Scripta Materialia**; 62(5): 290-293.

[141] Tong, K., Ye, F. and Wang, Y.K. (2019) Short-range ordered structure and phase stability of supersaturated nitrided layer on austenitic stainless steel. **Acta Materialia**; 175: 314-323.

[142] Liang, W., Xiaolei, X., Jiujun, X. and Yaqin, S. (2001) Characteristics of low pressure plasma arc source ion nitrided layer on austenitic stainless steel at low temperature. **Thin Solid Films**; 391(1): 11-16.

[143] Lin, Y.-H., Lan, W.-C., Ou, K.-L., Liu, C.-M. and Peng, P.-W. (2012) Hemocompatibility evaluation of plasma-nitrided austenitic stainless steels at low temperature. **Surface and Coatings Technology**; 206(23): 4785-4790.

[144] Riviere, J., Méheust, P., Villain, J., Templier, C., Cahoreau, M., Abrasonis, G. and Pranevicius, L. (2002) High current density nitrogen implantation of an austenitic stainless steel. **Surface and Coatings Technology**; 158: 99-104.

[145] Tao, X., Matthews, A. and Leyland, A. (2020) On the Nitrogen-Induced Lattice Expansion of a Non-stainless Austenitic Steel, Invar 36®, Under Triode Plasma Nitriding. **Metallurgical and Materials Transactions A**; 51(1): 436-447.

[146] Christiansen, T. and Somers, M.A. (2005) Low temperature gaseous nitriding and carburising of stainless steel. **Surface Engineering**; 21(5-6): 445-455.

[147] Jirásková, Y., Blawert, C. and Schneeweiss, O. (1999) Thermal stability of stainless steel surfaces nitrided by plasma immersion ion implantation. **physica status solidi (a)**; 175(2): 537-548.

[148] Li, X. and Dong, H. (2003) Effect of annealing on corrosion behaviour of nitrogen S phase in austenitic stainless steel. **Materials science and technology**; 19(10): 1427-1434.

[149] Christiansen, T. and Somers, M.A. (2006) Decomposition kinetics of expanded austenite with high nitrogen contents. **Zeitschrift für Metallkunde**; 97(1): 79-88.

[150] Buhagiar, J., Bell, T., Sammons, R. and Dong, H. (2011) Evaluation of the biocompatibility of S-phase layers on medical grade austenitic stainless steels. **Journal of Materials Science: Materials in Medicine**; 22(5): 1269-1278.

[151] Braz, J.K., Martins, G.M., Sabino, V., Vitoriano, J.O., Barboza, C.A.G., Soares, A.K.M., Rocha, H.A., Oliveira, M.F., Júnior, C.A. and Moura, C.E.B. (2019) Plasma nitriding under low temperature improves the endothelial cell biocompatibility of 316L stainless steel. **Biotechnology letters**; 41(4-5): 503-510.

[152] Tromas, C., Stinville, J.-C., Templier, C. and Villechaise, P. (2012) Hardness and elastic modulus gradients in plasma-nitrided 316L polycrystalline stainless steel investigated by nanoindentation tomography. **Acta Materialia**; 60(5): 1965-1973.

[153] Stinville, J., Cormier, J., Templier, C. and Villechaise, P. (2014) Monotonic mechanical properties of plasma nitrided 316L polycrystalline austenitic stainless steel: Mechanical behaviour of the nitrided layer and impact of nitriding residual stresses. **Materials Science and Engineering: A**; 605: 51-58.

[154] Fossati, A., Borgioli, F., Galvanetto, E. and Bacci, T. (2006) Glow-discharge nitriding of AISI 316L austenitic stainless steel: influence of treatment time. **Surface and Coatings Technology**; 200(11): 3511-3517.

[155] De Las Heras, E., Ybarra, G., Lamas, D., Cabo, A., Dalibon, E.L. and Brühl, S.P. (2017) Plasma nitriding of 316L stainless steel in two different N2-H2 atmospheres-Influence on microstructure and corrosion resistance. **Surface and Coatings Technology**; 313: 47-54.

[156] Lu, S., Zhao, X., Wang, S., Li, J., Wei, W. and Hu, J. (2017) Performance enhancement by plasma nitriding at low gas pressure for 304 austenitic stainless steel. **Vacuum**; 145: 334-339.

[157] Hoshiyama, Y., Mizobata, R. and Miyake, H. (2016) Mechanical properties of austenitic stainless steel treated by active screen plasma nitriding. **Surface and Coatings Technology**; 307: 1041-1044.

[158] De Las Heras, E., Santamaría, D.G., García‐Luis, A., Cabo, A., Brizuela, M., Ybarra, G., Mingolo, N., Brühl, S. and Corengia, P. (2007) Microstructure and wear behavior of DC‐pulsed plasma nitrided AISI 316L austenitic stainless steel. **Plasma Processes and Polymers**; 4(S1): S741-S745.

[159] Baranowska, J., Franklin, S. and Kochmańska, A. (2007) Wear behaviour of low-temperature gas nitrided austenitic stainless steel in a corrosive liquid environment. **Wear**; 263(1-6): 669-673.

[160] Zhu, X. and Lei, M. (2000) Pitting corrosion resistance of high nitrogen fcc phase in plasma source ion nitrided austenitic stainless steel. **Surface and Coatings Technology**; 131(1-3): 400-403.

[161] Borgioli, F., Galvanetto, E. and Bacci, T. (2018) Corrosion behaviour of low temperature nitrided nickel-free, AISI 200 and AISI 300 series austenitic stainless steels in NaCl solution. **Corrosion Science**; 136: 352-365.

[162] Flis-Kabulska, I., Sun, Y. and Flis, J. (2013) Monitoring the near-surface pH to probe the role of nitrogen in corrosion behaviour of low-temperature plasma nitrided 316L stainless steel. **Electrochimica Acta**; 104: 208-215.

[163] Fossati, A., Galvanetto, E., Bacci, T. and Borgioli, F. (2011) Improvement of corrosion resistance of austenitic stainless steels by means of glow-discharge nitriding. **Corrosion Reviews**; 29(5-6): 209-221.

[164] Li, J., He, X., Zhang, G., Zhang, X. and Tang, B. (2018) Effect of Nitriding on Antibacterial Performance of 8Cr17 and 4Cr13 Martensitic Stainless Steel. **Materials Performance and Characterization**; 7(1): 70-77.

[165] Vaterrodt, A., Thallinger, B., Daumann, K., Koch, D., Guebitz, G.M. and Ulbricht, M. (2016) Antifouling and antibacterial multifunctional polyzwitterion/enzyme coating on silicone catheter material prepared by electrostatic layer-by-layer assembly. **Langmuir**; 32(5): 1347-1359.

[166] Cheng, G., Li, G., Xue, H., Chen, S., Bryers, J.D. and Jiang, S. (2009) Zwitterionic carboxybetaine polymer surfaces and their resistance to long-term biofilm formation. **Biomaterials**; 30(28): 5234-5240.

[167] Cheng, Y., Feng, G. and Moraru, C.I. (2019) Micro-and nanotopography sensitive bacterial attachment mechanisms: A review. **Front Microbiol**; 10.

[168] Lichter, J.A., Van Vliet, K.J. and Rubner, M.F. (2009) Design of antibacterial surfaces and interfaces: polyelectrolyte multilayers as a multifunctional platform. **Macromolecules**; 42(22): 8573-8586.

[169] Ivanova, E.P., Hasan, J., Webb, H.K., Truong, V.K., Watson, G.S., Watson, J.A., Baulin, V.A., Pogodin, S., Wang, J.Y. and Tobin, M.J. (2012) Natural bactericidal surfaces: mechanical rupture of Pseudomonas aeruginosa cells by cicada wings. **Small**; 8(16): 2489-2494.

[170] Noyce, J., Michels, H. and Keevil, C. (2006) Potential use of copper surfaces to reduce survival of epidemic meticillin-resistant Staphylococcus aureus in the healthcare environment. **Journal of Hospital Infection**; 63(3): 289-297.

[171] Casey, A., Adams, D., Karpanen, T., Lambert, P., Cookson, B., Nightingale, P., Miruszenko, L., Shillam, R., Christian, P. and Elliott, T. (2010) Role of copper in reducing hospital environment contamination. **Journal of Hospital Infection**; 74(1): 72-77.

[172] Bazaka, K., Jacob, M., Chrzanowski, W. and Ostrikov, K. (2015) Anti-bacterial surfaces: natural agents, mechanisms of action, and plasma surface modification. **Rsc Advances**; 5(60): 48739-48759.

[173] Scott, R.D. (2009) The direct medical costs of healthcare-associated infections in US hospitals and the benefits of prevention. **Centers for Disease Control and Prevention**; Atlanta.

[174] Hoffmann, S., Batz, M.B. and Morris Jr, J.G. (2012) Annual cost of illness and quality-adjusted life year losses in the United States due to 14 foodborne pathogens. **Journal of food protection**; 75(7): 1292-1302.

[175] Evans, H., Madden, P., Douglas, C., Adak, G., O'Brien, S., Djuretic, T., Wall, P. and Stanwell-Smith, R. (1998) General outbreaks of infectious intestinal disease in England and Wales, 1995 and 1996. **Communicable Disease and Public Health**; 1: 165-175.

[176] Centers for Disease Control and Prevention (2016) **HAI Data and Statistics** [Online]. Accessed From: https://www.cdc.gov/hai/surveillance/index.html (06/08/2017

[177] Moriarty, T.F., Zaat, S.A. and Busscher, H.J. (2012) **Biomaterials associated infection: immunological aspects and antimicrobial strategies**. Springer Science & Business Media: New York, US. 355-378 p.

[178] Borkow, G. (2014) **Use of biocidal surfaces for reduction of healthcare acquired infections**. Springer: Cham, Switzerland. 59-84 p.

[179] McNeil, J.C., Campbell, J.R. and Crews, J.D. (2019) **Healthcare Associated Infections in Children: A Guide to Prevention and Management**. Springer: Cham, Switzerland. 3-16 p.

[180] McDonnell, G.E. and Sheard, D. (2012) **A practical guide to decontamination in healthcare**. John Wiley & Sons: Chichester, UK. 101-129 p.

[181] Marriott, N.G. and Gravani, R.B. (2006) **Sanitation and the Food Industry**. Springer: New York, US.

[182] Srey, S., Jahid, I.K. and Ha, S.-D. (2013) Biofilm formation in food industries: a food safety concern. **Food control**; 31(2): 572-585.

[183] Cramer, M.M. (2013) **Food plant sanitation: design, maintenance, and good manufacturing practices**. CRC Press. 109-134 p.

[184] Stanga, M. (2010) **Sanitation: cleaning and disinfection in the food industry**. John Wiley & Sons: Darmstadt, Germany. 499-554 p.

[185] Centers for Disease Control and Prevention (2019) **Antibiotic resistance threats in the United States, 2019**. Department of Health and Human Services: Atlanta, US.

[186] Giaouris, E., Heir, E., Hébraud, M., Chorianopoulos, N., Langsrud, S., Møretrø, T., Habimana, O., Desvaux, M., Renier, S. and Nychas, G.-J. (2014) Attachment and biofilm formation by foodborne bacteria in meat processing environments: causes, implications, role of bacterial interactions and control by alternative novel methods. **Meat Sci**; 97(3): 298-309.

[187] Sharma, D., Misba, L. and Khan, A.U. (2019) Antibiotics versus biofilm: an emerging battleground in microbial communities. **Antimicrobial Resistance & Infection Control**; 8(1): 76.

[188] Caubet, R., Pedarros-Caubet, F., Chu, M., Freye, E., de Belem Rodrigues, M., Moreau, J. and Ellison, W. (2004) A radio frequency electric current enhances antibiotic efficacy against bacterial biofilms. **Antimicrobial agents and chemotherapy**; 48(12): 4662-4664.

[189] Nickel, J., Wright, J., Ruseska, I., Marrie, T., Whitfield, C. and Costerton, J. (1985) Antibiotic resistance ofPseudomonas aeruginosa colonizing a urinary catheter in vitro. **European journal of clinical microbiology**; 4(2): 213-218.

[190] Kumar, C.G. and Anand, S.K. (1998) Significance of microbial biofilms in food industry: a review. **International Journal of Food Microbiology**; 42(1-2): 9-27.

[191] Curtis, L. (2008) Prevention of hospital-acquired infections: review of non-pharmacological interventions. **Journal of Hospital Infection**; 69(3): 204-219.

[192] Zhang, H. and Chiao, M. (2015) Anti-fouling coatings of poly (dimethylsiloxane) devices for biological and biomedical applications. **Journal of medical and biological engineering**; 35(2): 143-155.

[193] Krishnan, S., Weinman, C.J. and Ober, C.K. (2008) Advances in polymers for anti-biofouling surfaces. **Journal of Materials Chemistry**; 18(29): 3405-3413.

[194] Hasan, J. and Chatterjee, K. (2015) Recent advances in engineering topography mediated antibacterial surfaces. **Nanoscale**; 7(38): 15568-15575.

[195] Hasan, J., Crawford, R.J. and Ivanova, E.P. (2013) Antibacterial surfaces: the quest for a new generation of biomaterials. **Trends in biotechnology**; 31(5): 295-304.

[196] Skoulas, E., Manousaki, A., Fotakis, C. and Stratakis, E. (2017) Biomimetic surface structuring using cylindrical vector femtosecond laser beams. **Scientific reports**; 7(1): 1-11.

[197] Stratakis, E., Bonse, J., Heitz, J., Siegel, J., Tsibidis, G., Skoulas, E., Papadopoulos, A., Mimidis, A., Joel, A.-C. and Comanns, P. (2020) Laser engineering of biomimetic surfaces. **Materials Science and Engineering: R: Reports**; 141: 100562.

[198] Garcia-Giron, A., Romano, J.-M., Liang, Y., Dashtbozorg, B., Dong, H., Penchev, P. and Dimov, S. (2018) Combined surface hardening and laser patterning approach for functionalising stainless steel surfaces. **Applied Surface Science**; 439: 516-524.

[199] Crawford, R.J., Webb, H.K., Truong, V.K., Hasan, J. and Ivanova, E.P. (2012) Surface topographical factors influencing bacterial attachment. **Advances in colloid and interface science**; 179: 142-149.

[200] Feng, G., Cheng, Y., Wang, S.-Y., Borca-Tasciuc, D.A., Worobo, R.W. and Moraru, C.I. (2015) Bacterial attachment and biofilm formation on surfaces are reduced by small-diameter nanoscale pores: how small is small enough? **NPJ biofilms and microbiomes**; 1(1): 1-9.

[201] Lorenzetti, M., Dogša, I., Stošicki, T.a., Stopar, D., Kalin, M., Kobe, S. and Novak, S.a. (2015) The influence of surface modification on bacterial adhesion to titanium-based substrates. **ACS applied materials & interfaces**; 7(3): 1644-1651.

[202] Arslan, A., Masjuki, H., Kalam, M., Varman, M., Mufti, R., Mosarof, M., Khuong, L. and Quazi, M. (2016) Surface texture manufacturing techniques and tribological effect of surface texturing on cutting tool performance: a review. **Critical Reviews in Solid State and Materials Sciences**; 41(6): 447-481.

[203] Kusiński, J., Kac, S., Kopia, A., Radziszewska, A., Rozmus-Górnikowska, M., Major, B., Major, L., Marczak, J. and Lisiecki, A. (2012) Laser modification of the materials surface layer-a review paper. **Bulletin of the polish academy of sciences Technical sciences**; 60(4): 711-728.

[204] Steen, W.M. and Mazumder, J. (2010) **Laser material processing**. springer science & business media.

[205] Bonse, J., Krüger, J., Höhm, S. and Rosenfeld, A. (2012) Femtosecond laser-induced periodic surface structures. **Journal of Laser Applications**; 24(4): 042006.

[206] Romano, J.-M., Garcia-Giron, A., Penchev, P. and Dimov, S. (2018) Triangular laser-induced submicron textures for functionalising stainless steel surfaces. **Applied Surface Science**; 440: 162-169.

[207] Borowiec, A. and Haugen, H. (2003) Subwavelength ripple formation on the surfaces of compound semiconductors irradiated with femtosecond laser pulses. **Applied Physics Letters**; 82(25): 4462-4464.

[208] Lutey, A.H., Gemini, L., Romoli, L., Lazzini, G., Fuso, F., Faucon, M. and Kling, R. (2018) Towards laser-textured antibacterial surfaces. **Scientific reports**; 8(1): 1-10.

[209] Alberts, B., Bray, D., Lewis, J., Raff, M., Roberts, K., Watson, J.D. and Grimstone, A. (2008) **Molecular Biology of the Cell**. 3rd ed. Garland Science. 1-45 p.

[210] Beveridge, T.J. and Davies, J.A. (1983) Cellular-Responses of Bacillus subtilis and Escherichia coli to the Gram Stain. **Journal of Bacteriology**; 156(2): 846-858.

[211] Bodycote (2018) **Laser welding of $s^3p$-treated components** [Online]. Accessed From: https://www.bodycote.com/wp-content/uploads/2018/12/Spotlight_S3P_LaserWelding_EN_02-S.pdf (16/05/2019)

[212] Pfeifenberger, M.J., Mangang, M., Wurster, S., Reiser, J., Hohenwarter, A., Pfleging, W., Kiener, D. and Pippan, R. (2017) The use of femtosecond laser ablation as a novel tool for rapid micro-mechanical sample preparation. **Materials & Design**; 121: 109-118.

[213] McCulloch, Q., Gigax, J. and Hosemann, P. (2020) Femtosecond laser ablation for mesoscale specimen evaluation. **JOM**; 72(4): 1694-1702.

[214] Barnett, R., Mueller, S., Hiller, S., Perez-Willard, F., Strickland, J. and Dong, H. (2020) Rapid production of pillar structures on the surface of single crystal CMSX-4 superalloy by femtosecond laser machining. **Optics and Lasers in Engineering**; 127: 105941.

[215] Bauer, F., Michalowski, A., Kiedrowski, T. and Nolte, S. (2015) Heat accumulation in ultra-short pulsed scanning laser ablation of metals. **Optics express**; 23(2): 1035-1043.

[216] Romano, J.-M., Helbig, R., Fraggelakis, F., Garcia-Giron, A., Werner, C., Kling, R. and Dimov, S. (2019) Springtail-inspired triangular laser-induced surface textures on metals using MHz ultrashort pulses. **Journal of Micro and Nano-Manufacturing**; 7(2).

[217] Chichkov, B.N., Momma, C., Nolte, S., Von Alvensleben, F. and Tünnermann, A. (1996) Femtosecond, picosecond and nanosecond laser ablation of solids. **Applied Physics A**; 63(2): 109-115.

[218] Bonse, J., Kirner, S., Koter, R., Pentzien, S., Spaltmann, D. and Krüger, J. (2017) Femtosecond laser-induced periodic surface structures on titanium nitride coatings for tribological applications. **Applied Surface Science**; 418: 572-579.

[219] Alshaer, A., Rogers, B. and Li, L. (2017) Smoothed Particle Hydrodynamics (SPH) modelling of transient heat transfer in pulsed laser ablation of Al and associated free-surface problems. **Computational Materials Science**; 127: 161-179.

[220] Williams, E. and Brousseau, E. (2016) Nanosecond laser processing of Zr41. 2Ti13. 8Cu12. 5Ni10Be22. 5 with single pulses. **Journal of Materials Processing Technology**; 232: 34-42.

[221] Saji, V.S. and Choe, H.C. (2009) Electrochemical corrosion behaviour of nanotubular Ti–13Nb–13Zr alloy in Ringer's solution. **Corrosion Science**; 51(8): 1658-1663.

[222] Rulison, C. (1999) So you want to measure surface energy: A tutorial designed to provide basic understanding of the concept solid surface energy, and its many complications. **Kruss**: 1-16.

[223] Suzuki, S., Imai, S. and Kourai, H. (2006) Background and evidence leading to the establishment of the JIS standard for antimicrobial products. **Biocontrol Science**; 11(3): 135-145.

[224] Tsubaki, A.T., Koten, M.A., Lucis, M.J., Zuhlke, C., Ianno, N., Shield, J.E. and Alexander, D.R. (2017) Formation of aggregated nanoparticle spheres through femtosecond laser surface processing. **Applied surface science**; 419: 778-787.

[225] Peng, D., Kim, T.-H., Chung, J.-H. and Park, J.-K. (2010) Development of nitride-layer of AISI 304 austenitic stainless steel during high-temperature ammonia gas-nitriding. **Applied Surface Science**; 256(24): 7522-7529.

[226] Mohan, L., Anandan, C. and Grips, V.W. (2013) Investigation of electrochemical behavior of nitrogen implanted Ti–15Mo–3Nb–3Al alloy in Hank's solution. **Journal of Materials Science: Materials in Medicine**; 24(3): 623-633.

[227] Fleischer, K., Caffrey, D., Farrell, L., Norton, E., Mullarkey, D., Arca, E. and Shvets, I.V. (2015) Raman spectra of p-type transparent semiconducting Cr2O3: Mg. **Thin Solid Films**; 594: 245-249.

[228] Bokobza, L., Bruneel, J.-L. and Couzi, M. (2014) Raman spectroscopy as a tool for the analysis of carbon-based materials (highly oriented pyrolitic graphite, multilayer

graphene and multiwall carbon nanotubes) and of some of their elastomeric composites. **Vibrational Spectroscopy**; 74: 57-63.

[229] Mohammadtaheri, M., Yang, Q., Li, Y. and Corona-Gomez, J. (2018) The effect of deposition parameters on the structure and mechanical properties of chromium oxide coatings deposited by reactive magnetron sputtering. **Coatings**; 8(3): 111.

[230] Sousa, P., Silvestre, A.J., Popovici, N. and Conde, O. (2005) Morphological and structural characterization of CrO2/Cr2O3 films grown by Laser-CVD. **Applied surface science**; 247(1-4): 423-428.

[231] Yao, J., Zhang, C., Liu, H., Dai, Q., Wu, L., Lan, S., Gopal, A.V., Trofimov, V.A. and Lysak, T.M. (2012) Selective appearance of several laser-induced periodic surface structure patterns on a metal surface using structural colors produced by femtosecond laser pulses. **Applied Surface Science**; 258(19): 7625-7632.

[232] Vesel, A., Junkar, I., Cvelbar, U., Kovac, J. and Mozetic, M. (2008) Surface modification of polyester by oxygen ‐ and nitrogen ‐ plasma treatment. **Surface and Interface Analysis: An International Journal devoted to the development and application of techniques for the analysis of surfaces, interfaces and thin films**; 40(11): 1444-1453.

[233] Talha, M., Behera, C. and Sinha, O. (2014) Promising in vitro performances of nickel-free nitrogen containing stainless steels for orthopaedic applications. **Bulletin of Materials Science**; 37(6): 1321-1330.

[234] Knyazeva, M. and Pohl, M. (2013) Duplex steels. Part II: carbides and nitrides. **Metallography, Microstructure, and Analysis**; 2(5): 343-351.

[235] Butzke, C.E. (2010) **Winemaking problems solved**. Elsevier.

[236] Wang, J., Li, Z., Wang, D., Qiu, S. and Ernst, F. (2017) Thermal stability of low-temperature-carburized austenitic stainless steel. **Acta Materialia**; 128: 235-240.

[237] Gil, L., Brühl, S., Jimenez, L., Leon, O., Guevara, R. and Staia, M.H. (2006) Corrosion performance of the plasma nitrided 316L stainless steel. **Surface and Coatings Technology**; 201(7): 4424-4429.

[238] Yuan, X., Zhao, Y., Li, X. and Chen, L. (2017) Effects of Gas Nitriding Temperature on the Surface Properties of a High Manganese TWIP Steel. **Metals**; 7(3): 102.

[239] Dong, Y., Svoboda, P., Vrbka, M., Kostal, D., Urban, F., Cizek, J., Roupcova, P., Dong, H., Krupka, I. and Hartl, M. (2016) Towards near-permanent CoCrMo prosthesis surface by combining micro-texturing and low temperature plasma carburising. **Journal of the mechanical behavior of biomedical materials**; 55: 215-227.

[240] Christiansen, T.L. and Somers, M.A. (2009) Low-temperature gaseous surface hardening of stainless steel: the current status. **International Journal of Materials Research**; 100(10): 1361-1377.

[241] Williamson, D., Ozturk, O., Wei, R. and Wilbur, P.J. (1994) Metastable phase formation and enhanced diffusion in fcc alloys under high dose, high flux nitrogen implantation at high and low ion energies. **Surface and Coatings Technology**; 65(1-3): 15-23.

[242] Bowen, A. and Leak, G. (1970) Solute diffusion in alpha-and gamma-iron. **Metallurgical Transactions**; 1(6): 1695-1700.

[243] Vedalakshmi, R., Saraswathy, V., Song, H.-W. and Palaniswamy, N. (2009) Determination of diffusion coefficient of chloride in concrete using Warburg diffusion coefficient. **Corrosion Science**; 51(6): 1299-1307.

[244] Wang, Z., Yin, C., Li, J., Yang, Y., Chen, L., Luo, Y., Liu, Y., He, C. and Fang, P. (2018) Electrochemical impedance study of water transportation in corona-aged silicone rubber: effect of applied voltage. **Journal of Materials Science**; 53(18): 12871-12884.

[245] Chowdhury, I.H. and Xu, X. (2003) Heat transfer in femtosecond laser processing of metal. **Numerical Heat Transfer: Part A: Applications**; 44(3): 219-232.

[246] Melchers, R. and Jeffrey, R. (2004) Surface “Roughness” effect on marine immersion corrosion of mild steel. **Corrosion**; 60(7): 697-703.

[247] Cheng, Y.T., Rodak, D., Wong, C. and Hayden, C. (2006) Effects of micro-and nano-structures on the self-cleaning behaviour of lotus leaves. **Nanotechnology**; 17(5): 1359.

[248] Ensikat, H.J., Ditsche-Kuru, P., Neinhuis, C. and Barthlott, W. (2011) Superhydrophobicity in perfection: the outstanding properties of the lotus leaf. **Beilstein journal of nanotechnology**; 2(1): 152-161.

[249] Sakamoto, A., Terui, Y., Horie, C., Fukui, T., Masuzawa, T., Sugawara, S., Shigeta, K., Shigeta, T., Igarashi, K. and Kashiwagi, K. (2014) Antibacterial effects of protruding and recessed shark skin micropatterned surfaces of polyacrylate plate with a shallow groove. **FEMS Microbiology letters**; 361(1): 10-16.

[250] Reddy, S.T., Chung, K.K., McDaniel, C.J., Darouiche, R.O., Landman, J. and Brennan, A.B. (2011) Micropatterned surfaces for reducing the risk of catheter-associated urinary tract infection: an in vitro study on the effect of sharklet micropatterned surfaces to inhibit bacterial colonization and migration of uropathogenic Escherichia coli. **Journal of endourology**; 25(9): 1547-1552.

[251] Jaggessar, A., Shahali, H., Mathew, A. and Yarlagadda, P.K. (2017) Bio-mimicking nano and micro-structured surface fabrication for antibacterial properties in medical implants. **Journal of nanobiotechnology**; 15(1): 64.

[252] Fraggelakis, F., Mincuzzi, G., Lopez, J., Manek-Hönninger, I. and Kling, R. (2019) Controlling 2D laser nano structuring over large area with double femtosecond pulses. **Applied Surface Science**; 470: 677-686.

[253] Schroeder, T.B., Houghtaling, J., Wilts, B.D. and Mayer, M. (2018) It's not a bug, it's a feature: functional materials in insects. **Advanced Materials**; 30(19): 1705322.

[254] Hensel, R., Neinhuis, C. and Werner, C. (2016) The springtail cuticle as a blueprint for omniphobic surfaces. **Chemical Society Reviews**; 45(2): 323-341.

[255] Helbig, R., Nickerl, J., Neinhuis, C. and Werner, C. (2011) Smart skin patterns protect springtails. **PloS one**; 6(9): e25105.

[256] Chenab, K.K., Sohrabi, B. and Rahmanzadeh, A. (2019) Superhydrophobicity: advanced biological and biomedical applications. **Biomaterials science**; 7(8): 3110-3137.

[257] Pan, Q., Cao, Y., Xue, W., Zhu, D. and Liu, W. (2019) Picosecond laser-textured stainless steel superhydrophobic surface with an antibacterial adhesion property. **Langmuir**; 35(35): 11414-11421.

[258] Helbig, R., Günther, D., Friedrichs, J., Rößler, F., Lasagni, A. and Werner, C. (2016) The impact of structure dimensions on initial bacterial adhesion. **Biomaterials science**; 4(7): 1074-1078.

[259] Gregorčič, P., Conradi, M., Hribar, L. and Hočevar, M. (2018) Long-term influence of laser-processing parameters on (super) hydrophobicity development and stability of stainless-steel surfaces. **Materials**; 11(11): 2240.

[260] Garcia-Giron, A., Romano, J.-M., Batal, A., Dashtbozorg, B., Dong, H., Solanas, E.M., Angos, D.U., Walker, M., Penchev, P. and Dimov, S. (2019) Durability and wear

resistance of laser-textured hardened stainless steel surfaces with hydrophobic properties. **Langmuir**; 35(15): 5353-5363.

[261] Chang, F.-M., Cheng, S.-L., Hong, S.-J., Sheng, Y.-J. and Tsao, H.-K. (2010) Superhydrophilicity to superhydrophobicity transition of CuO nanowire films. **Applied Physics Letters**; 96(11): 114101.

[262] Zhang, Y., Zou, G., Liu, L., Zhao, Y., Liang, Q., Wu, A. and Zhou, Y.N. (2016) Time-dependent wettability of nano-patterned surfaces fabricated by femtosecond laser with high efficiency. **Applied Surface Science**; 389: 554-559.

[263] Schnell, G., Polley, C., Bartling, S. and Seitz, H. (2020) Effect of Chemical Solvents on the Wetting Behavior Over Time of Femtosecond Laser Structured Ti6Al4V Surfaces. **Nanomaterials**; 10(6): 1241.

[264] Guo, P., Zheng, Y., Wen, M., Song, C., Lin, Y. and Jiang, L. (2012) Icephobic/anti‐icing properties of micro/nanostructured surfaces. **Advanced Materials**; 24(19): 2642-2648.

[265] Cangueiro, L.T., Cavaleiro, A.J., Morgiel, J. and Vilar, R. (2016) Mechanisms of the formation of low spatial frequency LIPSS on Ni/Ti reactive multilayers. **Journal of Physics D: Applied Physics**; 49(36): 365103.

[266] Sun, Y. and Chin, L. (2002) Residual stress evolution and relaxation in carbon S phase layers on AISI 316 austenitic stainless steel. **Surface engineering**; 18(6): 443-446.

[267] Somers, M. and Mittemeijer, E. (1990) Development and relaxation of stress in surface layers; Composition and residual stress profiles in $\gamma'$ -Fe 4 N 1− x layers on α-Fe substrates. **Metallurgical Transactions A**; 21(1): 189-204.

[268] Donlan, R.M. (2002) Biofilms: microbial life on surfaces. **Emerging infectious diseases**; 8(9): 881.

[269] Lemire, J.A., Harrison, J.J. and Turner, R.J. (2013) Antimicrobial activity of metals: mechanisms, molecular targets and applications. **Nature Reviews Microbiology**; 11(6): 371-384.

[270] Lin, L.-H., Chen, S.-C., Wu, C.-Z., Hung, J.-M. and Ou, K.-L. (2011) Microstructure and antibacterial properties of microwave plasma nitrided layers on biomedical stainless steels. **Applied surface science**; 257(17): 7375-7380.

[271] Friedlander, R.S., Vlamakis, H., Kim, P., Khan, M., Kolter, R. and Aizenberg, J. (2013) Bacterial flagella explore microscale hummocks and hollows to increase adhesion. **Proceedings of the National Academy of Sciences**; 110(14): 5624-5629.

[272] Chai, H., Guo, L., Wang, X., Fu, Y., Guan, J., Tan, L., Ren, L. and Yang, K. (2011) Antibacterial effect of 317L stainless steel contained copper in prevention of implant-related infection in vitro and in vivo. **Journal of Materials Science: Materials in Medicine**; 22(11): 2525-2535.

[273] Monte, J., Abreu, A.C., Borges, A., Simões, L.C. and Simões, M. (2014) Antimicrobial activity of selected phytochemicals against Escherichia coli and Staphylococcus aureus and their biofilms. **Pathogens**; 3(2): 473-498.

[274] Khalid, S., Gao, A., Wang, G., Chu, P.K. and Wang, H. (2020) Tuning surface topographies on biomaterials to control bacterial infection. **Biomaterials Science**.

[275] Han, J., Cai, M., Lin, Y., Liu, W., Luo, X., Zhang, H., Wang, K. and Zhong, M. (2018) Comprehensively durable superhydrophobic metallic hierarchical surfaces via tunable micro-cone design to protect functional nanostructures. **RSC advances**; 8(12): 6733-6744.

[276] Liu, Z., Wang, H., Lin, N. and Duan, R. (2020) Combined Plasma Nitriding And Surface Texturing For Improving Tribological Performance Of 316 Stainless Steel. **Surface Review and Letters**: 1950226.

[277] Roessler, F. and Lasagni, A.F. (2018) Protecting Sub-Micrometer Surface Features in Polymers from Mechanical Damage Using Hierarchical Patterns. **Journal of Laser Micro Nanoengineering**; 13(2): 68-75.

[278] Romano, J.-M., Gulcur, M., Garcia-Giron, A., Martinez-Solanas, E., Whiteside, B.R. and Dimov, S.S. (2019) Mechanical durability of hydrophobic surfaces fabricated by injection moulding of laser-induced textures. **Applied Surface Science**; 476: 850-860.

[279] Ahlawat, S., Singh, A., Sharma, S.K., Mukhopadhyay, P.K., Singh, R. and Bindra, K. (2020) Mechanical abrasion resistant candle soot based superhydrophobic coating over nanosecond laser textured stainless steel. **Surface Topography: Metrology and Properties**; 8(2): 025007.

[280] Romano, J.-M., Fantova Sarasa, J., Concheso, C., Gulcur, M., Dashtbozorg, B., Garcia-Giron, A., Penchev, P., Dong, H., Whiteside, B.R. and Dimov, S. (2020) Effects of mould wear on hydrophobic polymer surfaces replicated using plasma-treated and laser-textured stainless steel inserts. **Tribology-Materials, Surfaces & Interfaces**: 1-13.

[281] Lazzini, G., Romoli, L., Lutey, A. and Fuso, F. (2019) Modelling the interaction between bacterial cells and laser-textured surfaces. **Surface and Coatings Technology**; 375: 8-14.

[282] Stróż, D. and Psoda, M. (2010) TEM studies of plasma nitrided austenitic stainless steel. **Journal of microscopy**; 237(3): 227-231.

[283] Kietziga, A.-M., Mirvakilia, M.N., Kamalb, S., Englezosa, P. and Hatzikiriakosa, S.G. (2011) Nanopatterned metallic surfaces: their wettability and impact on ice friction. **Journal of adhesion science and technology**; 25(12): 1293-1303.

[284] Medilanski, E., Kaufmann, K., Wick, L.Y., Wanner, O. and Harms, H. (2002) Influence of the surface topography of stainless steel on bacterial adhesion. **Biofouling**; 18(3): 193-203.

[285] Tian, L., Li, X. and Dong, H. (2017) Novel wear-resistant anti-bacterial stainless steel surfaces. **Surface Engineering**: 1-11.

[286] Krsko, P., Kaplan, J.B. and Libera, M. (2009) Spatially controlled bacterial adhesion using surface-patterned poly (ethylene glycol) hydrogels. **Acta Biomaterialia**; 5(2): 589-596.